US

University of Sussex

University of Sussex

Development and Implementation of an Yb$^+$ Ion Trap Experiment Towards Coherent Manipulation and Entanglement

by

James McLoughlin

Submitted for the degree of Doctor of Philosophy

University of Sussex

May 2011

Declaration

I hereby declare that this thesis has not been and will not be submitted in whole or in part to another University for the award of any other degree.

Signature:

James McLoughlin

UNIVERSITY OF SUSSEX

James McLoughlin, Doctor of Philosophy

Development and Implementation of an Yb$^+$ Ion Trap Experiment
Towards Coherent Manipulation and Entanglement

Abstract

Trapped ions are currently one of the most promising architectures for realising the quantum information processor. The long lived internal states are ideal for representing qubit states and, through controlled interactions with electromagnetic radiation, ions can be manipulated to execute coherent logic operations. In this thesis an experiment capable of trapping Yb^+ ions, including $^{171}Yb^+$, is presented.

Since ion energy can limit the coherence of qubit manipulations, characterisation of an ion trap heating rate is vital. Using a trapped $^{174}Yb^+$ ion a heating rate consistent with previous measurements of other ion species in similar ion traps is obtained. This result shows abnormal heating of Yb^+ does not occur, further solidifying the suitability of this species for quantum information processing.

Efficient creation, and cooling of trapped ions requires exact wavelengths for the ionising, cooling and repump transitions. A simple technique to measure the $^1S_0 \leftrightarrow {}^1P_1$ transition wavelengths, required for isotope selective photoionisation of neutral Yb, is developed. Using the technique new wavelengths, accurate to 60 MHz, are obtained and differ from previously published results by 660 MHz. Through a simple modification the technique can also predict Doppler shifted transition frequencies, which may be required in non-perpendicular atom-laser interactions. Using trapped ions, the $^2S_{1/2} \leftrightarrow {}^2P_{1/2}$ Doppler cooling and $^2D_{3/2} \leftrightarrow {}^2D[3/2]_{1/2}$ repump transitions are also measured to a greater accuracy than previously reported.

Many experiments require wavelengths which can only be obtained using complex expensive laser systems. To remedy this a simple cost effective laser is developed to enable laser diodes to be operated at sub zero temperatures, extending the range of obtainable wavelengths. Additional diode modulation capabilities allow for the manipulation of atoms and ions with hyperfine structures. The laser is shown to be suitable for manipulating Yb^+ ions by cooling a diode from 372 nm to 369 nm and simultaneously generating 2.1 GHz frequency sidebands.

Coherent manipulation such as arbitrary qubit rotations, motional coupling and ground

state cooling, are required for trapped ion quantum computing. Two photon stimulated Raman transitions are identified as a suitable technique to implement all of these requirements and an investigation into implementing this technique with ^{171}Yb$^+$ is conducted. The possibility of exciting a Raman transition via either a dipole or quadrupole transitions in ^{171}Yb$^+$ is analysed, with dipole transitions preferred because quadrupole transitions are found to be too demanding experimentally. An inexpensive setup, utilising a dipole transition, is designed and tested. Although currently limited the setup shows potential to be an inexpensive, high fidelity method of exciting a Raman transition.

Acknowledgements

I would like to thank my supervisor, Dr. Winfried Hensinger, first for the opportunity to undertake this exciting DPhil, and also for his motivation throughout the project. His help, advice, and unlimited supply of energy provided me with constant opportunities to improve my skills, attitude and knowledge as a physics researcher. I also want to thank Barry Garraway, my second supervisor, for all the help he has offered.

I want to express a huge amount of gratitude to my colleagues Altaf Nizamani, James Siverns and Robin Sterling. I remember that first day when we all sat in the empty lab puzzling about where to begin building an ion trap experiment, so decided to start where all DIY starts, by putting up a set of shelves. Thanks must also go to Marcus Hughes who joined the group just in time for the hardship of trapping an ion, and then the other group members who conveniently arrived after the experiment was setup: Bjo 'Pepe' Lekitsch, Seb Weidt, and Kim Lake. Thanks also goes to the numerous undergraduate students who have helped out, in particular: Jessica Grove-Smith and Dave Scrivener. It's been great fun working with all you guys!

A big thank you must also go to the members from Wolfgang Lange's group: Peter Blythe, Anders Mortensen, Alex Wilson, Daniel Crick, as well as Matthias Keller and Wolfgang Lange. Despite being members of a different group, they were always at hand with invaluable knowledge and support throughout my DPhil.

I wish to express a deep gratitude to my family for keeping me supported and motivated throughout my DPhil. They were always there to listen to me complain - even when they didn't understand what I was complaining about. They never failed to offer support and advice when I needed it most and kept me going through the difficult periods. Without them I would never have managed it.

Finally a great thanks goes to all my friends outside of physics, especially: Adrian Clayton, Liz Harding and Ben Dudley, Andy Johnson, Katherine and Peter Stuart, Simon Turner, David Williams, Kim Wright and Ivor Annetts, and the friends I've made here in Sussex. They've offered an escape when it was needed and kept me sane through it all.

Detailed Acknowledgements

Several aspects of this thesis could not have been realised without the input and efforts of the other group members. Here I wish to acknowledge the contributions provided by each member.

Chapter 3 - Lasers

The external cavity diode lasers were based upon a design by Ted Hänsch and provided by Matthias Keller. Construction and modification of the lasers was performed by myself, with assistance from Robin Sterling, Jessica Grove Smith and David Scrivener.

Chapter 4 - Experimental Setup

The vacuum system was designed and constructed by Altaf Nizamani, with assistance from myself. The macroscopic experimental trap was designed by Robin Sterling, and constructed by myself, Marcus Hughes, Altaf Nizamani, James Siverns, and Robin Sterling. The resonator was designed and constructed by James Siverns while the filter, allowing a static offset to be applied to the RF signal, was developed by Kim Lake and Sebastian Weidt. The frequency modulated saturated absorption spectroscopy used to stabilise the 780 nm laser was implemented by Robin Sterling, and the scanning Fabry-Pérot cavities used in the transfer cavity lock were designed and produced by myself and Robin Sterling. The electronics for the transfer cavity lock were constructed by James Siverns and the LabVIEW program executing the lock was written by James Siverns and Altaf Nizamani. The imaging system was designed by James Siverns with assistance from Marcus Hughes, and the experimental layout was implemented by myself, Altaf Nizamani, James Siverns, Robin Sterling and Marcus Hughes. Initial trapping of an ion was achieved by myself, Altaf Nizamani, James Siverns, Robin Sterling, Marcus Hughes and Bjoern Lekitsch. The experiment control system was implemented by myself, while subsequent programming of experimental sequences were performed by myself and Altaf Nizamani.

Chapter 5 - Heating Rate Measurement of Linear Ion Trap

The initial theory, developed by Wesenberg et al [1], was reproduced by Bjoern Lekitsch with with help from myself. Experimental characterisation of the ion trap heating rate was conducted by all members of the group.

Chapter 6 - Ionisation, Doppler Cooling and Repump Wavelengths

Development of the fluorescence spot technique, and measurement of the 399 nm $^1S_0 \leftrightarrow$ $^1P_1$ transition wavelengths were performed by Altaf Nizamani and myself. Measurement of the Doppler cooling and repumping wavelengths were performed by all members of the group.

Chapter 7 - 369 nm "ColdLase" Doppler Cooling Laser

The novel laser system is intellectual property belonging to myself, Ben Jacques-Parr and Dr. Winfried Hensinger. The construction and testing of the prototype system was performed by myself with help from Ben Jacques-Parr.

Chapter 8 - Single Qubit Operations

Analysis of implementing Raman transitions in ^{171}Yb$^+$ was performed by myself. The experimental work towards implementing a two photon Raman transition was performed by myself with assistance from Sebastian Weidt.

Personal Contribution

My main contribution towards the experimental setup was the construction and modification of the laser systems to create and manipulate Yb$^+$ ions. I also offered secondary support towards other aspects of the setup including the construction and characterisation of the vacuum system, design and implementation of the scanning Fabry-Përot cavities, building the macroscopic ion trap, and trapping the first ion. I was involved with the proceeding experiments. I assisted with the reproduction of the theory describing the heating rate of a trapped ion, and worked with the team to measure the heating rate. I was involved with the development of the fluorescence spot technique and measurement of the atomic / ionic transition wavelengths. I headed the research project to develop ColdLase and performed most of the characterising tests of the prototype system. Finally I conducted the theoretical analysis and initial experimental investigation towards the manipulation of ^{171}Yb$^+$ with Raman transitions.

Publications, Intellectual Property, and Conference Contributions

Journal Publications

Versatile ytterbium ion trap experiment for operation of scalable ion-trap chips with motional heating and transition-frequency measurements,
James J. McLoughlin, Altaf H. Nizamani, James D. Siverns, Robin C. Sterling, Marcus D. Hughes, Bjoern Lekitsch, Björn Stein, Seb Weidt, and Winfried K. Hensinger,
Phys. Rev. A 83, 013406 (2011).

Doppler-free Yb spectroscopy with fluorescence spot technique,
Altaf H. Nizamani, James J. McLoughlin and Winfried K. Hensinger,
Phys. Rev. A 82, 043408 (2010).

Presentations

Towards laser cooling and photoionisation of ytterbium ions for scalable quantum information,
J.J. McLoughlin
University of Sussex, January 2009

Patent Applications

Variable wavelength laser,

J.J. McLoughlin, Ben Jaques-Parr, and Dr. W. K. Hensinger.

Patent application number: 1009428.2, 7 June 2010

Conference Contributions

Trapped ytterbium ions for scalable quantum technology,

J.J. McLoughlin, A.H. Nizamani, J.D. Siverns, R.C. Sterling, M.D. Hughes, B. Lekitsch, B. Stein, S. Weidt and W. K. Hensinger.

Poster at 1st European Conference on Trapped Ions (ECTI 2010), Redworth Hall, County Durham, UK, 19-24 September 2010.

An ytterbium ion trap experiment for scalable ion trap quantum information processing,

J.J. McLoughlin, A.H. Nizamani, J.D. Siverns, R.C. Sterling, and W. K. Hensinger.

Poster at Quantum Simulators conference, Physikzentrum Bad Honnef (Germany), 12-15 October 2009.

Towards ion trap array architectures with 171Yb+ ions,

James J. McLoughlin, Altaf H. Nizamani, James D. Siverns, Robin C. Sterling, Merlin Bevan-Stevenson, Nicholas Davies, Jessica Grove-Smith, Marcus Hughes, Ben Johnson, Kieran Lee, Ben S. Pruess, Rajiv Ramasawmy, David N. Scrivener, Tim Short, and Winfried K. Hensinger

Poster at Modern Applications of Trapped Ions conference, Les Houches, France, 18-23 May 2008.

Towards laser cooling and trapping of ^{171}Yb$^+$ ions: lasers, transitions, cooling cycles and the vacuum chamber,

James J. McLoughlin, Altaf Nizamani, Robin C. Sterling, James D. Siverns, Jessica Grove-Smith, Nicholas Davies, Dave Scrivener and Winfried K. Hensinger

Poster at Atomic Physics Gordon conference, Tilton School, NH, US, July 1-6, 2007.

Contents

List of Tables

List of Figures

"It is a mistake to think you can solve any major problems just with potatoes."

Douglas Adams, *Life, the Universe and Everything*

Chapter 1

Introduction

> "First we thought the PC was a calculator. Then we found out how to turn
> numbers into letters with ASCII - and we thought it was a typewriter. Then
> we discovered graphics, and we thought it was a television. With the World
> Wide Web, we've realised it's a brochure."
>
> - Douglas Adams.

The idea of programmable computing was first introduced in 1936 when Alan Turning presented a model for a machine capable of simulating any logic algorithm [2] - a machine now known as a Turing machine. Following this Turing developed a model for a machine capable of simulating any other Turing machine; the Universal Turning Machine (UTM). Shortly following this report the first electronic computers were developed, and over time have developed to the computers we all use today. While these systems are capable of executing a vast range of algorithms, they are limited and not quite UTM's. These machines use components which obey classical physics, so are only effective at simulating classical systems and solving deterministic problems. It is when they are used to simulate quantum systems that the limitations become apparent. To simulate quantum systems, which operate probabilistically, the number of possible permutations to be computed greatly surpasses the capabilities of modern electronic computers. In order to overcome this limitation, and effectively simulate quantum systems, a computer based upon components obeying quantum mechanics is therefore required.

Information processing using quantum systems was first introduced around 1980 by Benioff and Feynman. Benioff presented a quantum mechanical model consistent with the computational model of the UTM [3], while Feynman proposed how physical quantum systems, such as photons and atomic particles, can be used to represent and process classical information [4]. He showed that two distinguishable orientations of these quantum

system, such as photon polarisation or atomic spin, could be used to represent the binary states '0' and '1'. Furthermore by orientating these systems in a superposition state the corresponding information would also be in a superposition of 0 and 1. Thus for a system consisting of N quantum bits (qubits) there are 2^N possible encodable states. Unfortunately measurement of this system would collapse the superpositions into arbitrary states yielding random outputs. It was in 1985 that David Deutsch solved this issue, and showed how 'parallel quantum computing' enables large numbers of qubits to effectively process information [5]. Utilising entanglement between the qubits a function can simultaneously act upon a superposition of all 2^N input states to compute a single coherent output. Following Deutsch's discovery quantum computing algorithms were developed. Perhaps the most influential algorithm was Shor's factoring algorithm [6], which showed how quantum computing could factorise a large number on time scales exponentially faster than a classical computer. Since encryption schemes rely upon the inability of classical computers to factor large numbers this algorithm posed a serious threat to secure data transfer and so gained significant interest from intelligence agencies. Another well known algorithm is the search algorithm presented by Lov Grover [7], which is capable of reducing the average number of searches of an unsorted database from N/2 iterations to $\sqrt{N}/2$. Although this may not have had the same impact as Shor's algorithm it did present further applications for the quantum computer. Following this Shor and Steane introduced error correction protocols, which allow any arbitrarily long quantum algorithm to be realised on non-perfect quantum hardware [8, 9]. Shor then presented fault-tolerant quantum computing, which showed that calculations and simulations can still be achieved even in the presence of small errors [10]. These contributions greatly fuelled interest into the quantum computer and, in 2000, Divenczio presented the following requirements for a physical system to be used for QIP [11]

1. A scalable physical system with well defined qubits.

2. The ability to initialise the state of the qubits to a simple fiducial state, such as $|000...\rangle$.

3. Long relevant decoherence times, much longer than the gate operation time.

4. A "universal" set of quantum gates.

5. A qubit specific measurement capacity.

Several different potentially suitable physical quantum systems have been proposed and investigated including solid-state systems, optical systems, and atomic systems. Solid-state systems include quantum dots [12, 13], low-capacitance Josephson-junction arrays [14],

and the nuclear spin of donor atoms in electronic silicon devices [15]. Optical systems use orthogonal orientations of polarised light to represent the qubit states [16], while atomic systems include single atoms strongly coupled to an optical cavity [17], and of course the different energy states of trapped ions [18]. Although solid state systems have shown a lot of potential with, in principle, easily scalable fabrication the coherence lifetimes of these qubits are short lived and complex coherent manipulation is very difficult. Optical based qubits also have extremely short lifetimes which, without the use of another quantum system, makes the task of of memory storage impractical. It is the atomic based systems, with trapped ions in particular, that currently show the most promise for QIP.

There are currently two main approaches towards QIP using traped ions: ions confined in Penning traps (which use static electric and magnetic fields) or ions confined in radio frequency (rf) Paul traps (which use static and oscillating electric fields). Implementation of QIP via Penning traps has demonstrated many of the basic requirements including state initialisation, state detection and arbitrary qubit rotation [19], and also shuttling of ions between penning traps [20]. QIP using ions confined in rf Paul traps is, however, the more popular approach. It was kick started in 1995 with the publication of Cirac and Zoller's influential paper [18] which proposed how, through the entanglement of multiple ions, any arbitrary gate consisting of any number of qubits could be realised. Following this QIP using trapped ions exploded, with advancements including the realisation of gates such as Cirac and Zoller's gate [21, 22], a quantum Toffoli gate [23], Mølmer and Sørensen's gate [24], and other geometric phase gates [25]. Entanglement of up to fourteen trapped ion qubits [24–26], quantum error correction protocols [27–29], and algorithms such as the Deutsh-Joza algorithm [30] and Grover's algorithm [31]. Preliminary simulations of physical systems including quantum magnets [32] and Ising spins [33] have also been performed. Divenczio's other requirement of scalability has also been addressed with the ability to confine ions in microfabricated structures [34]. The demonstration of shuttling ions within ion trap arrays [35] highlights the ability to use multidimensional trap structures, allowing for 'memory' and 'interaction' regions. Trapped ions in rf Paul traps are thus currently a popular choice for the realisation of the quantum computer.

This thesis focuses on the use of $^{171}Yb^+$ ions confined in an rf Paul trap for QIP. First the implementation and characterisation of an ion trap setup is described, and then the current progress towards manipulation of the $^{171}Yb^+$ qubit is presented.

In chapter 2 the basic theory for trapping, cooling and manipulating ions for quantum information processing is described. The chapter includes the principles of operation of a

linear rf Paul trap, different methods used to photoionise neutral Yb and laser cooling Yb^+ ions, and methods of controlling the $^{171}Yb^+$ qubit. The laser systems used to achieve these tasks are described in chapter 3. Most of the lasers are constructed in-house in the Littrow external cavity configuration, and have been modified to provide frequency sidebands or large mode hop free tuning ranges to access the hyperfine structure of even isotope Yb^+ ions and $^{171}Yb^+$.

Chapter 4 presents the rest of the experiment setup including an ultra high vacuum system designed for testing different complex trap geometries, and a compatible two-layer macroscopic ion trap. The electronic feedback schemes used to stabilise the laser to an atomic reference are presented as well as the system used to image or measure ion fluorescence. Operation of the setup is described and successful trapping of ions is shown.

Motional heating due to electric field fluctuations causes decoherence in trapped ion experiments. Heating rates thus impose a limit on the fidelity of quantum logic operations. In chapter 5 the heating rate of the ion trap is characterised using an $^{174}Yb^+$ ion, and found to be consistent with previously reported results.

Creation of Yb^+ ions is achieved using two-photon photoionisation, with the first stage utilising the $^1S_0 \leftrightarrow \, ^1P_1$ transition. However, published wavelengths for this transition are not accurate. In chapter 6 a simple method, based upon the alignment of velocity dependent fluorescence spots, is devised to accurately determine these wavelengths. The measured wavelengths are found to differ from previously published work by 660 MHz. In experiments it is common for laser beams and atomic beams to adopt non-perpendicular angles, and therefore require Doppler shifted wavelengths. By adapting the devised setup these wavelengths are also predicted. Using trapped ions the $^2S_{1/2} \leftrightarrow \, ^2P_{1/2}$ Doppler cooling and $^2D_{3/2} \leftrightarrow \, ^3D[3/2]_{1/2}$ repumping transition are measured with greater precision than previously published.

Difficult to obtain wavelengths can require expensive laser systems. Alongside the implementation and characterisation of the ion trap experiment a new versatile laser system offering a simple inexpensive means of obtaining difficult wavelengths is developed. The design of the laser is described in chapter 7, and the laser is shown to be suitable for cooling Yb^+ ions.

Quantum information processing requires the coherent manipulation of the trapped ion qubit. In chapter 8 an investigation of controlling the $^{171}Yb^+$ qubit with two photon stimulated Raman transitions is presented. The suitability of dipole and quadrupole transitions for Raman transitions is analysed, with consideration taken for obtainable laser

sources and realistic experimental considerations. Dipole transitions are identified as the preferred option and an inexpensive scheme offering reduced off-resonant coupling rates is tested.

Chapter 2

Ion traps and the Yb$^+$ Ion

> "To catch mice, my lord. I lie on the ground with my mouth open and hope
>
> they scurry in."
>
> -Baldrick, *Blackadder*

The radio frequency (rf) ion trap was first introduced by Wolfgang Paul in the late 1950's [36, 37], for which he won a Nobel Prize. Following this in 1975 Hänsch and Schawlow [38] and Wineland and Dehmelt independently proposed the principle of laser cooling. Then, in 1978, Wineland *et al.* [39] and Neuhauser *et al.* [40] reported the first laser cooling experiments using Mg$^+$ and Ba$^+$ ions respectively. Since then laser cooled trapped atoms and ions have become common place, and are used for many experiments including frequency measurements for atomic clocks [41–44], cavity quantum electrodynamics [45, 46] and also as the building block for the quantum computer [39, 47, 48]. Several ionic species have been investigated as suitbale candidates for trapped ion quantum computing including Ba$^+$ [49], Be$^+$ [50], Ca$^+$ [51–55], Cd$^+$ [56], Mg$^+$ [57], Sr$^+$ [58, 59], and recently Yb$^+$ [60–63]. This chapter presents the underlying principles of the rf Paul trap, the ion species of interest: Yb$^+$, and schemes to cool and manipulate these ions for quantum information processing.

2.1   Ion Trap Basics

The purpose of the ion trap is to provide electric fields capable of confining ions in three dimensional free space. As stated in Earnshaw's theorem, however, a charged particle cannot be confined in three dimensions using electrostatic forces alone [64]. A result also embedded in Laplace's equation: $\nabla^2 \phi(x, y, z) = 0$, where $\phi(x, y, z)$ is a three dimensional

electric potential, which shows that local three-dimensional static maxima or minima cannot occur in free space. Therefore to enable confinement in all three dimensions a time dependent oscillating electric potential, $\phi(x, y, z, t)$, is required. The simplest geometries are quadrupole in shape and, in 3D Cartesian coordinates, can be expressed as

$$\phi = U_0 \frac{1}{2}(\alpha x^2 + \beta y^2 + \gamma z^2) + V_0 \cos(\Omega_D t)\frac{1}{2}(\alpha' x^2 + \beta' y^2 + \gamma' z^2)) \tag{2.1}$$

where U_0 and $V_0 \cos(\Omega_D)$ are static and time dependent voltages applied to trap electrodes, Ω_D is the frequency of the time dependent voltage, and α, β, γ, and α', β', γ' are multiplicative constants describing the geometry of the static and oscillating potentials. Since this general potential must also fulfil Laplace's condition, $\nabla^2 \phi = 0$, at every instant in time the following restrictions are imposed onto the overall geometry of the potential

$$\alpha + \beta + \gamma = 0 \tag{2.2}$$

$$\alpha' + \beta' + \gamma' = 0 \tag{2.3}$$

The two simplest solutions which fulfil these restrictions are

$$\alpha = \beta = \gamma = 0 \quad \text{and} \quad \alpha' + \beta' = -\gamma' \tag{2.4}$$

$$-(\alpha + \beta) = \gamma > 0 \quad \text{and} \quad \alpha' = -\beta', \gamma' = 0 \tag{2.5}$$

The first solution, equation 2.4, describes a simple potential consisting purely of oscillating components ($\alpha' + \beta' = -\gamma'$) and no static components ($\alpha = \beta = \gamma = 0$). This, however, is the simplest solution but does not describe the potential often implemented. Usually an additional static potential, with geometry $\alpha + \beta = -\gamma$, is included. The second solution, equation 2.5, describes a potential which requires both oscillating and static components. The oscillating component describes confinement in the $x - y$ plane while the static component describes confinement along the z-axis. The two geometries described by equations 2.4 and 2.5 can be realised using two different trap structures: cylindrical and linear traps respectively.

2.1.1 Trap Types

Cylindrical Traps

The general shape of a cylindrical trap is illustrated in figure 2.1. These traps ideally consist of two hyperbolic endcap electrodes and a ring electrode with a hyperbolic cross
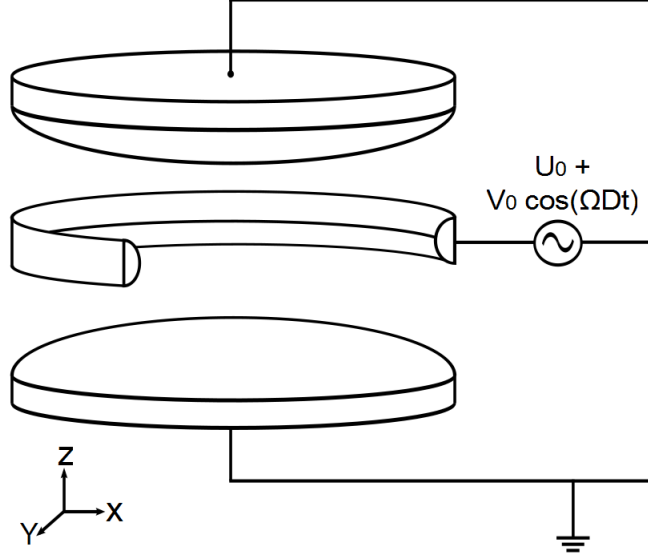
Figure 2.1: Structure of a cylindrical ion trap. The trapping potentials is achieved by applying an rf and static potential to the ring electrode while grounding the endcaps, or vice versa.

section. The three dimensional oscillating potential is generated by applying an oscillating voltage to the ring electrode while grounding the endcaps, or vice versa. The additional static potential is then generated by applying a static voltage to the same electrodes as the oscillating voltage. Considering the general quadrupole potential (equation 2.1), and geometrical restrictions, the potential at any point inside a cylindrical trap is expressed as

$$\phi = (U_0 + V_0 \cos(\Omega_{\mathrm{D}} t)) \left(\frac{x^2 + y^2 - 2z^2}{r_0^2} \right) \tag{2.6}$$

where r_0 is the distance from the ion to the trap electrodes. Due to the rotational symmetry and use of oscillating potentials in all three axes cylindrical traps provide a minimum only at the trap centre.

Linear Paul Traps

The other general trap structure, the linear Paul trap, is illustrated in figure 2.2. These traps use four long electrodes to provide confinement in the $x - y$ plane, and electrodes positioned either end of the trap to provide confinement along the z axis. Radial confinement is achieved by applying an rf voltage to a pair of diagonally opposing electrodes (the long unsegmented electrodes in Fig. 2.2) whilst grounding the other pair. The potential

at any point on the $x - y$ plane is then described by

$$\phi_{\rm V} = \frac{V_0 \cos \Omega_{\rm D} t}{2r_0^2} \left(x^2 - y^2\right) \tag{2.7}$$
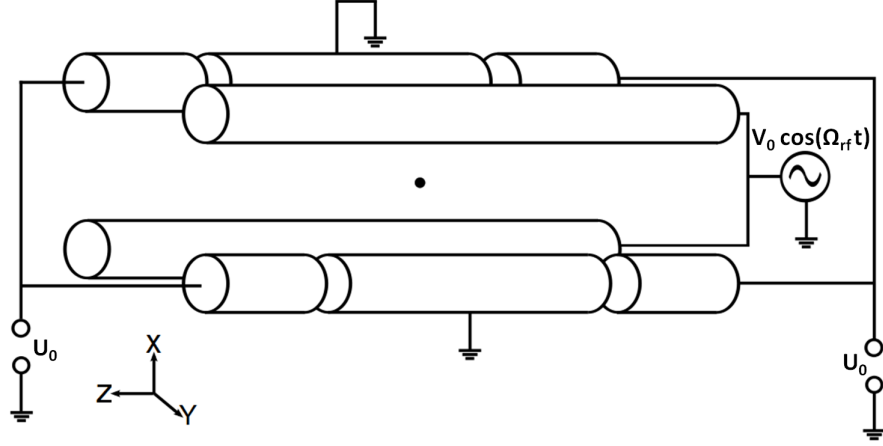
Figure 2.2: Structure of a liner ion trap. Radial confinement is achieved by applying a rf potential between a diagonally opposing pair of electrodes, while grounding the other pair. Axial confinement is achieved by applying a static potential between endcap electrodes.

Axial confinement is achieved by applying a static voltage to the endcap electrodes, with the potential along any point of the trap axis given by

$$\phi_{\rm U} = \frac{U_0}{2r_0^2} (2z^2 - (x^2 + y^2)) \tag{2.8}$$

As can be seen a static component is also present in the x and y axes. To ensure confinement in all three dimensions the rf potential must therefore overcome this static offset.

The overall trapping potential in a linear trap has a minimum running along the z-axis of the trap. This 'stretched' minimum enables several ingredients desirable for quantum computing: confining a chain of ions all in the minimum of the same harmonic potential, the scope for scalable trap geometries, and the ability to shuttle ions [35]. It is for these reasons that linear traps will be concentrated upon in this thesis. The following analysis, however, can be equally applied to cylindrical traps.

2.1.2   Ion Motion

An ion confined with a paul trap exhibits oscillatory motion as a result of the dynamic force from the oscillating quadrupole confining potential. To determine the nature of this motion the shape of the potnetial, and hence force applied to the ion is analysed.

Pseudopotential Approximation

To a first approximation the dynamic potential can time averaged over an oscillation to yield a static time-averaged potential, or 'pseudopotential'. Under this regime a time-averaged force is therefore considered and a description of the average motion during an oscillation obtained. The inhomogeneous pseudopotential within a linear Paul trap is defined as [65]

$$\Phi = \frac{e}{4m\Omega_{\mathrm{D}}^2}\left(E_0(x,y,z)\right)^2 \hat{r} \tag{2.9}$$

where m the ion mass, Ω_D the trap drive frequency, and $E_0(x,y,z)$ the spatially varying but time independent electric field. The corresponding time averaged force exerted onto the ion is

$$\bar{F} = -e\nabla\Phi\hat{r} \tag{2.10}$$

where e is the electron charge, $\hat{r}$ is a unit vector along a coordinate axis. To analyse this average force, and obtain a description of the ion motion, the time independent electric field must first be described. Given that an electric field is related to a potential via $E = -\nabla\phi$, and the quadrupole potential is described in equation 2.7, the electric field within a linear Paul trap is:

$$
\begin{aligned}
E(x,y,t) &= -\nabla\phi_{\mathrm{v}} \\
&= -\frac{V_0}{r_0^2}(x\hat{x} - y\hat{y})\cos(\Omega_{\mathrm{D}}t) \\
&= -E_0(x,y)\cos(\Omega_{\mathrm{D}}t)
\end{aligned}
\tag{2.11}
$$

Here the terms $E_0(x,y) = (V_0/r_0^2)(x\hat{x} - y\hat{y})$ and $\cos(\Omega_{\mathrm{D}}t)$ are the time independent and time dependent components respectively. Using this time independent component in equations 2.9 and 2.10 the time averaged force on the ion is:

$$
\begin{aligned}
\bar{F} &= -e\nabla\Phi\hat{r} \\
&= -e\frac{\partial}{\partial x}\left(\frac{eV_0^2 x^2}{4m\Omega_{\mathrm{D}}^2 r_0^4}\right)\hat{x} - e\frac{\partial}{\partial y}\left(\frac{eV_0^2 y^2}{4m\Omega_{\mathrm{D}}^2 r_0^4}\right)\hat{y} \\
&= -\frac{e^2 V_0^2}{2m\Omega_{\mathrm{D}}^2 r_0^4}x\hat{x} - \frac{e^2 V_0^2}{2m\Omega_{\mathrm{D}}^2 r_0^4}y\hat{y}
\end{aligned}
\tag{2.12}
$$

Considering now only the x-direction, and using the well known relation $F = m\ddot{x}$, the acceleration in the x-direction is

$$\ddot{x} = -\frac{e^2 V_0^2}{2m^2\Omega_{\mathrm{D}}^2 r_0^4}x \tag{2.13}$$

then by applying another common relation, $a(x) = -\omega^2 x$, the oscillation frequency in the x direction is

$$\omega_x = \omega_y = \frac{eV_0}{2^{1/2}m\Omega_{\mathrm{D}}r_0^2} \tag{2.14}$$

This result is the 'secular motion' of the trapped ion. The time averaged force from the oscillating electric field does not equal zero, but instead points towards the area of weaker field. Thus an ion in a rf Paul trap experiences a net force of towards the potential null inducing the harmonic motion. For a trap symmetric in the $x - y$ plane this secular (thermal) motion is the same in both the x and y axis.

Time Dependent Motion

While the previous result is a nice solution describing ion motion, it is only an approximation. To obtain a more complete solution the time dependence of the potential must be considered. The resulting motion is shown to comprise not only of secular motion, but also an additional high frequency low amplitude component. In the time dependent regime the force from the oscillating potential is

$$F = -e\nabla(\phi(x,y,z,t))\hat{r} = m\frac{d^2 r_0}{dt^2} \tag{2.15}$$

where $\hat{r}$ represents a coordinate axis. Again considering the $x - y$ plane and using the relationship, $m\, d^2 r_0/dt^2 = -e\, d\Phi/dr_0$, the equations of motion of the trapped ion are

$$\ddot{x} + \frac{e}{mx^2}(U_0 - V_0\cos\Omega t)x \;=\; 0 \tag{2.16}$$

$$\ddot{y} - \frac{e}{my^2}(U_0 - V_0\cos\Omega t)y \;=\; 0 \tag{2.17}$$

Then, by using the substitutions

$$a_x \;=\; -a_y = \frac{4eU}{mr_0^2\Omega^2} \tag{2.18}$$

$$q_x \;=\; -q_y = \frac{2eV_0}{mr_0^2\Omega^2} \tag{2.19}$$

$$\tau \;=\; \frac{\Omega t}{2} \tag{2.20}$$

equations 2.16 and 2.17 can be converted into the Mathieu differential equations

$$\frac{d^2 x}{d\tau^2} + (a + 2q\cos(2\tau))x = 0 \tag{2.21}$$

$$\frac{d^2 y}{d\tau^2} - (a + 2q\cos(2\tau))y = 0 \tag{2.22}$$

Based upon the values used for the parameters a and q these equations can have stable or unstable solutions which, in turn, describe stable or unstable confinement. The stable solutions are shown in figure 2.3, with the regions bound by dashed (solid) lines corresponding to stable confinement in the x (y) axis. The symmetry of the plot about $a = 0$ is a result of the trap symmetry in the $x - y$ plane. The regions of overlap, corresponding to stable confinement in both the x and y directions, are of key interest, and the region most commonly used is shown in figure 2.3(b). Here stable trapping is achieved with the smallest a and q parameters and, since these parameters correspond to the static and rf voltages applied to the trap electrodes, indicate the lowest static and rf voltages required for stable confinement.
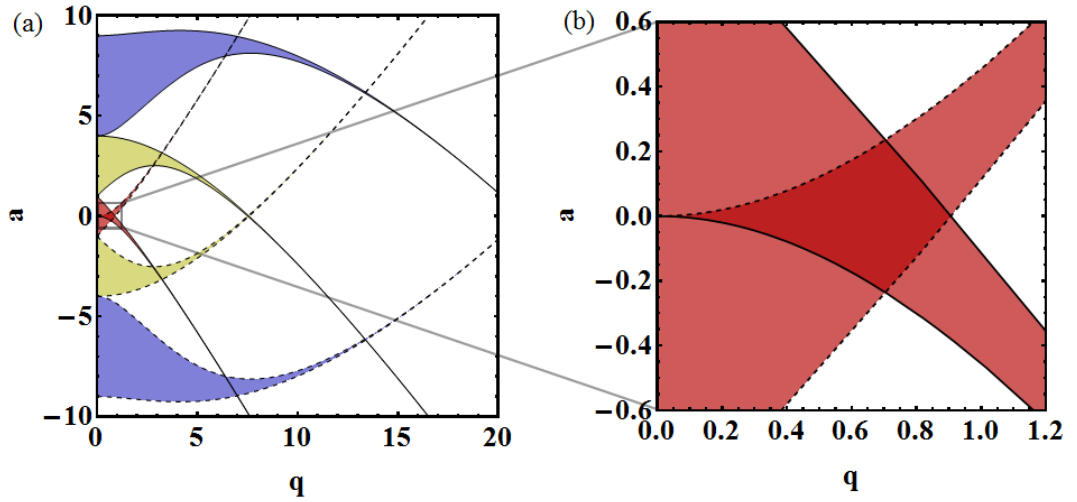
Figure 2.3: Regions for stable trapping in terms of the parameters a and q, with (a) showing multiple different stability regions and (b) showing the most commonly used stability region.

For a stable set of the parameters a and q the Mathieu equations can be solved using the Floquet theorem, as described in [63, 66–68]. The resulting ion trajectory can then be expressed as

$$x(t) = A \cos(\omega t)[1 + \frac{q}{2} \cos(\Omega_\mathrm{D} t)] \tag{2.23}$$

where A is a constant that depends upon inital conditions. It can be seen that the ion motion not only consists of secular motion at frequency ω, but has additional oscillatory motion at the drive frequency, Ω_D, known as micromotion. The amplitude of this micromotion is proportional to q which, as shown in equation 2.19, is proportional to the amplitude of the drive signal and the ion position from the trap centre.

To illustrate micromotion consider an ^{171}Yb$^+$ ion inside a trapping potential with a drive frequency of $\Omega_\mathrm{D}/(2\pi) = 21.4$ MHz and amplitude of $V_0 = 680$ V. If the ion is positioned

at $r_0 = 100$ μm from the trap null then the ion has the motion shown in figure 2.4. The blue dashed line illustrates the secular motion while the red solid line illustrates both the secular motion and micromotion. Typically the amplitude of micromotion is small, $q \ll 1$, however if the static and rf potential minima do not coincide the average position of the ion can become displaced and induce extra micromotion which can be detrimental for experiments. Using additional static fields the minimum of the static potential can be adjusted to directly coincide the rf minimum, thereby reducing micromotion [69]. It should be noted that since secular motion carries the ion back and forth across the rf minimum, micromotion cannot be eliminated, only minimised.
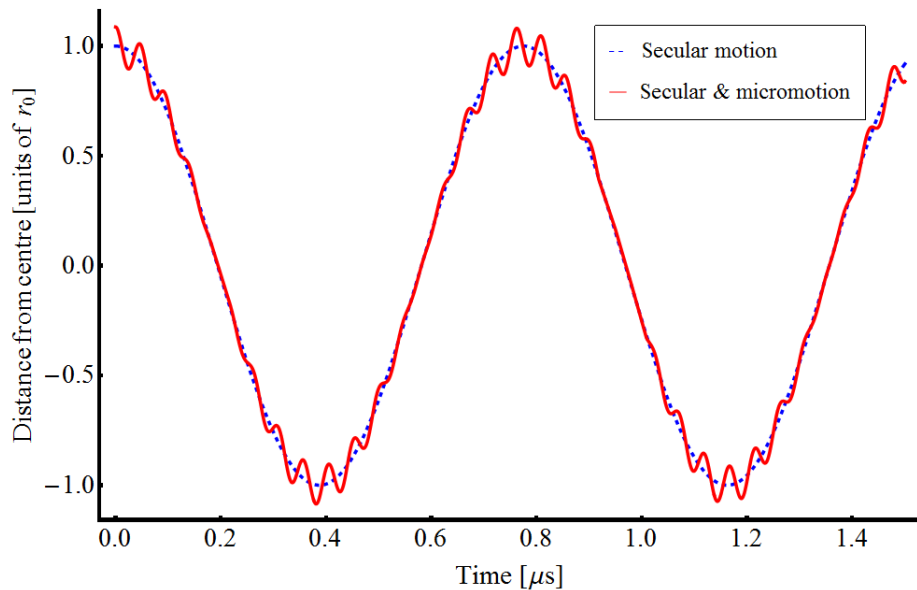
Figure 2.4: Motion of an ion within the quadrupole potential of a linear Paul trap. The blue dashed line shows the secular motion of the ion, while the solid red line shows the presence of the secular motion and micromotion.

2.2 Ytterbium

First discovered in 1878 by Jean de Marignac, and named after the Swedish village of Ytterby, ytterbium is an element that has found use in several modern day applications. Applications including metallurgy, fibre optics, and of course atomic physics experiments and quantum information processing. There are seven naturally occurring stable isotopes and are shown in table 2.1 along with their abundances and nuclear spin.

Several of these isotopes have been identified as suitable system for quantum information processing (QIP) and have have been used to demonstrated different processing mechanisms. Coupling between motional and spin states has been demonstrated us-

Isotope	Abundance	nuclear spin
^{168}Yb$^+$	0.13%	0
^{170}Yb$^+$	3.04%	0
^{171}Yb$^+$	14.28%	1/2
^{172}Yb$^+$	21.83%	0
^{173}Yb$^+$	16.13%	5/2
^{174}Yb$^+$	31.83%	0
^{176}Yb$^+$	12.76%	0

Table 2.1: Stable Yb$^+$ isotopes, with their abundance and nuclear spin.

ing ^{172}Yb$^+$ [70], photon mediated quantum gates have been achieved using ^{174}Yb$^+$ [65], and ^{171}Yb$^+$ boasts a ground state hyperfine doublet ideal for representing quantum bits (qubits) [63]. In this section methods of creating and manipulating Yb$^+$ are discussed.

2.2.1 Ionising Ytterbium

Yb$^+$ ions are created by liberating a bound electron from the outer orbital of the neutral atom, and is commonly achieved via either electron impact ionisation or photoionisation. Of these two techniques photoionisation is usually the preferred approach offering isotope selectivity, no charge build up on electrodes, and a higher ionisation rate [61].

A partial level diagram of neutral Yb, is shown in figure 2.5, indicating the possible choices of photoionisation. It can be seen that a single photon with a wavelength less than <199 nm [71] could achieve ionisation, however, this wavelength is difficult and expensive to obtain and would not be isotope selective. Instead a two-photon ionisation approach is used. Here a 398.91 nm photon excites the $^1S_0 \leftrightarrow {}^1P_1$ transition, where a consecutive photon, with wavelength λ <394 nm, advances the electron past the continuum. This is the most efficient two-photon approach as the $^1S_0 \leftrightarrow {}^1P_1$ transition is the strongest in neutral Yb [71] and, unlike 555.8 nm and 326 nm, 398.91 nm is readily available from inexpensive laser diodes. Furthermore the wavelength required to Doppler cool Yb$^+$, 369.5 nm, is used for the second stage of ionisation.

2.2.2 Gross Energy Level Structure

Singly ionised Yb$^+$ ions share the same gross energy level structure shown in figure 2.6. Although applicable to all ytterbium isotopes, it is particularly suited for the even isotopes with zero nuclear spin: ^{168}Yb$^+$, ^{170}Yb$^+$, ^{172}Yb$^+$, ^{174}Yb$^+$, and ^{176}Yb$^+$. The odd isotopes follow the general structure but exhibit a more complex hyperfine structure, such as ^{171}Yb$^+$ which is discussed in the next section.
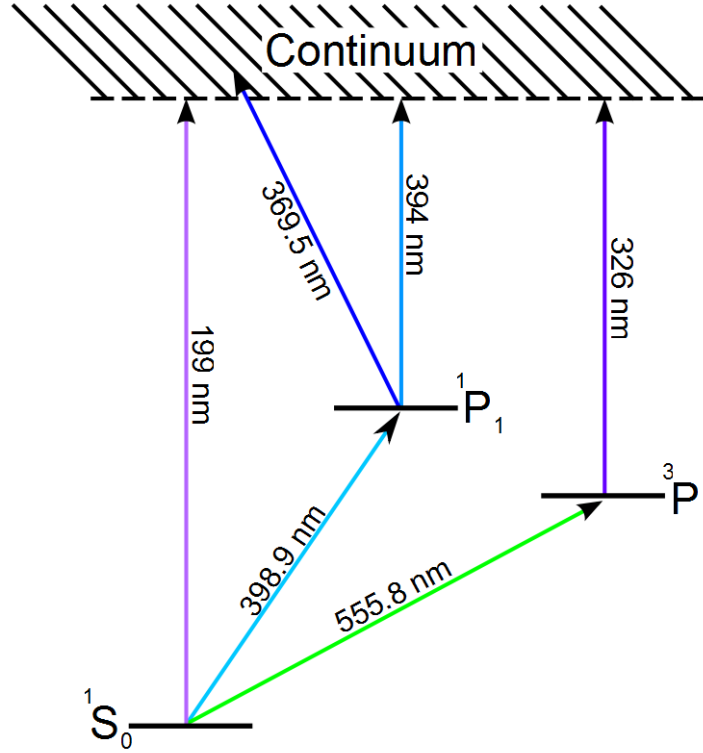
Figure 2.5: Partial level diagram of neutral ytterbium. A single photon with wavelength <199 nm can ionise a neutral atom. Similarly a photon a 398.9 nm (555.8) followed by a photon with wavelength <394 nm (<326 nm) will also result in ionisation. Ionisation via the $^1S_0 \leftrightarrow {}^1P_1$ transition is the preferred route.

The strong $^2S_{1/2} \leftrightarrow {}^2P_{1/2}$ electric dipole transition at 369 nm, natural linewidth of $\Gamma/2\pi = 19.6$ MHz [72], is used for Doppler cooling and fluorescence detection. This transition, however, is not a closed two-level system and the ion can decay from the $^2P_{1/2}$ state to the metastable $^2D_{3/2}$ state with a probability of 0.66% [63]. The long lifetime of this metastable state, $\tau = 52$ ms [43], can result in extended periods without fluorescence and also ion heating. The $^2D_{3/2}$ state is therefore depopulated using the $^2D_{3/2} \leftrightarrow {}^3D[3/2]_{1/2}$ dipole transition at 935 nm. From the $^3D[3/2]_{1/2}$ state the ion can decay via a dipole transition to the ground state and return to the cooling transition. Unfortunately, this four level system is also not completely closed. Inelastic collisions with background gas are suspected to result in population transfer from the $^2D_{3/2}$ state to the $^2D_{5/2}$ state, the rate which depends upon the quality of the vacuum surrounding the ion. By confining ions in an ultra high vacuum environment the number of collisions is reduced to only a couple per hour. The $^2D_{5/2}$ predominantly decays ($\approx$80% [73]) to the $^2F_{7/2}$ state which has a lifetime of $\approx$6 years. Depopulation of this low lying F state is therefore vital, and is achieved using the $^2F_{7/2} \leftrightarrow {}^1D[5/2]_{5/2}$ transition at 638.6 nm. From the $^1D[5/2]_{5/2}$ state the ion can return to the cooling cycle via either of the lower lying D-states.
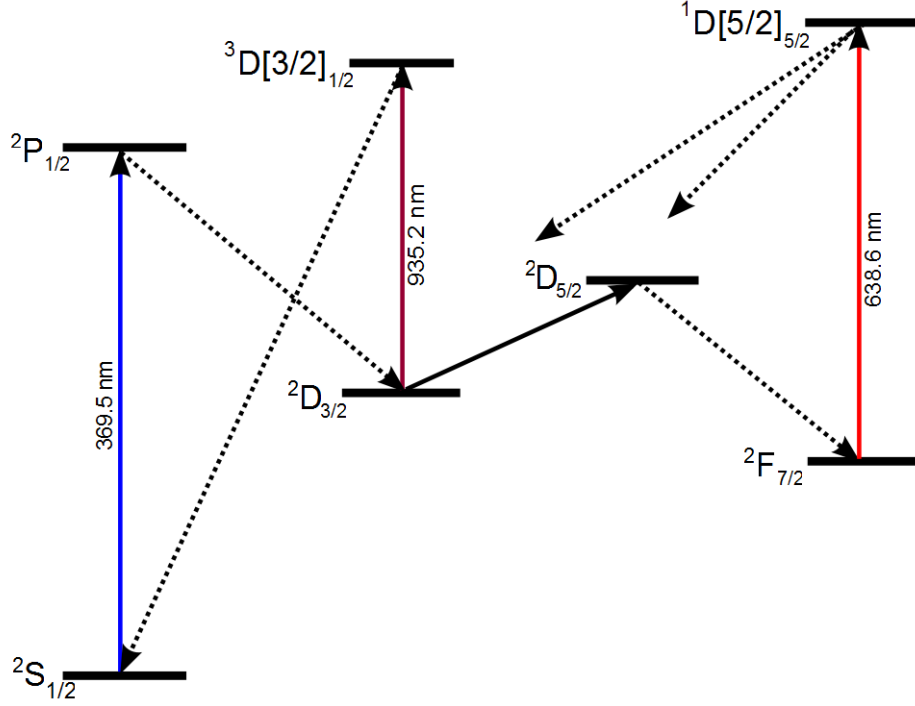
Figure 2.6: Gross energy level structure for Yb$^+$ ions. The structure is particularly applicable to the even isotopes which have no hyperfine structure. The solid lines indicates laser driven transitions, while dotted lines indicate possible decays routes.

The unusual notation of the $^3D[3/2]_{1/2}$ and $^1D[5/2]_{5/2}$ states is a result of a different coupling scheme. Unlike the usual LS-coupling, a second electron is promoted from the f-shell into the outer orbital. In the notation the value in the square brackets, K, is given by the coupling of the orbital angular momentum of the two outer electrons, L, with the core angular momentum, Jc, such that K = L + Jc. The superscript describes the coupling of the spins of the two outer electrons (using the 2S + 1 notation), which is combined with K to form the total angular momentum subscript, J. [65]

2.2.3 ^{171}Yb$^+$

With an odd number of protons and neutrons in the nucleus ^{171}Yb$^+$ possesses a one-half nuclear spin which generates the hyperfine doublet structure shown in figure 2.7, where the F states represent the total atomic angular momentum. Doppler cooling, and fluorescence detection, of this isotope is primarily achieved using the $^2S_{1/2}|F = 1\rangle \leftrightarrow {}^2P_{1/2}|F = 0\rangle$ transition. Unfortunately off-resonant coupling to the $^2P_{1/2}|F = 1\rangle$ state occurs which can result in population of the $^2S_{1/2}|F = 0\rangle$ state. Depopulation of this state can then be achieved with either microwave radiation at 12.6 GHz to excite the $^2S_{1/2}|F = 0\rangle \leftrightarrow {}^2S_{1/2}|F = 1\rangle$ transition or exciting the $^2S_{1/2}|F = 0\rangle \leftrightarrow {}^2P_{1/2}|F = 1\rangle$ transition which is 14.7 GHz detuned from the $^2S_{1/2}|F = 1\rangle \leftrightarrow {}^2P_{1/2}|F = 0\rangle$ transition. The $^2P_{1/2}$ manifold
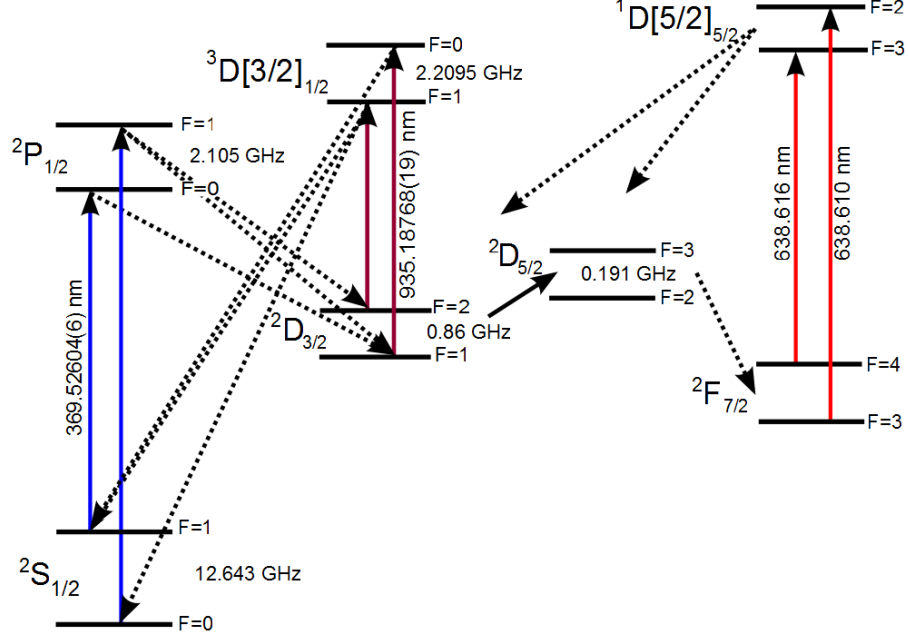
Figure 2.7: Partial level structure for ^{171}Yb$^+$, indicating the transitions required for Doppler cooling and repumping. The solid lines indicate the laser driven transitions.

can also decay to either of the $^2D_{3/2}|F = 1, 2\rangle$ states, which are subsequently depopulated by exciting the $^2D_{3/2}|F = 1\rangle \leftrightarrow \,^3D[3/2]_{1/2}|F = 0\rangle$ and $^2D_{3/2}|F = 2\rangle \leftrightarrow \,^3D[3/2]_{1/2}|F = 1\rangle$ transitions, separated by 3.07 GHz. The $^2F_{7/2} \leftrightarrow \,^1D[5/2]_{5/2}$ repump transitions occur at 638.610 nm and 638.616 nm.

To efficiently cool ^{171}Yb$^+$ the 369 nm and 935 nm beams are equipped with 14.7 GHz and 3.07 GHz frequency sidebands respectively, while the 638 nm laser is scanned between the two required wavelengths. The construction of the lasers, generation of the frequency sidebands and wavelength scanning are all detailed in chapter 3.

Dark State Destabilisation

The degeneracy of the $^2S_{1/2}|F = 1\rangle$ manifold, however, can result in the simultaneous population of the $|m_F = -1\rangle$ and $|m_F = 1\rangle$ states. The resulting transition required to liberate the ion from this superposition is $^2S_{1/2}|F = 1, m_F = -1\rangle \rightarrow \,^2P_{1/2}|F = 0, m_F = 0\rangle$ $+ \,^2S_{1/2}|F = 1, m_F = 1\rangle \rightarrow \,^2P_{1/2}|F = 0, m_F = 0\rangle$, requiring left + right circularly polarised light. Unfortunately these two polarisations superimpose to form linearly polarised light which cannot provide the required momentum change and coupling to the excited state vanishes [74]. This coherent population trapping is avoided by applying a magnetic field, known as the quantisation axis, across the ion to induce frequency shifts of the $|m_F \neq 0\rangle$ magnetic field sensitive states.

These non-degenerate m_F states are then accessed by appropriately orientating the electric field of the laser radiation relative to the quantisation axis. If linearly polarised laser radiation is aligned parallel to the quantisation axis only $\Delta m_F = 0$ (π) transitions are excited, while rotating the polarisation perpendicular to the quantisation axis excites only $\Delta m_F = \pm 1$ (σ_+/σ_-) transitions. Rotating the polarisations to an oblique angle to the quantisation axis enables π, σ_+ and σ_- transitions to all be driven simultaneously.

2.3 Laser Cooling

Laser cooling is required to reduce the ion energy to a regime where it is suitable for quantum information processing. The principle of the technique is to excite an atomic transition near resonance such that the energy gained from photon absorbtion is less that lost during photon emission, thereby reducing the ion energy. There are different techniques of laser cooling, which are used to attain different ion energies. These techniques can be grouped together into two different regimes, defined by the ratio of linewidth of the transition used, Γ, to the secular frequency, ω_{sec}. The regime where $\omega_{\text{sec}} \ll \Gamma$, commonly referred to as the weak binding regime, uses large linewidth transitions. These large linewidths allow for faster cooling rates but usually cannot reach suitably low ion energies for QIP. If instead narrower transitions are used, such that $\omega_{\text{sec}} \gg \Gamma$, or the strong binding regime, then sideband cooling techniques are possible and are used to reduce an ion to its motional ground state. Sideband cooling techniques, however, are not effective on energetic ions so cooling in the weak regime usually precedes cooling within the strong regime.

2.3.1 Doppler Cooling

The most common method of cooling in the weak binding regime is Doppler cooling, and is the initial method of cooling trapped ions. As mentioned in section 2.1.2 an ion confined within a trapping potential exhibits an oscillatory motion. Doppler cooling uses this motion to induce velocity dependent momentum transfer. The following is a semiclassical description of the technique and is similar to that present in [75,76], however more detailed quantum mechanical treatments can be obtained. A two-level ion oscillating in a potential interacting with a laser detuned from resonance by Δ has a scatter rate of

$$\frac{dN}{dt} = \frac{s_0 \Gamma / 2}{1 + s_0 + \left(\frac{2(\Delta + \Delta_D)}{\Gamma}\right)^2} \tag{2.24}$$

where Γ is the natural linewidth of the transition, $s_0 = I/I_{\text{sat}}$ is the saturation parameter with a laser intensity I and a transition saturation intensity of $I_{\text{sat}} = \pi\Gamma hc/(3\lambda^3)$, $\Delta_D = k\cdot v$ is the instantaneous Doppler shift of the transition frequency which is a function of the ion velocity v relative to the laser propagation, and k is the wavevector of the beam. When the ion moves towards the laser beam Δ_{D} becomes negative and, according to equation 2.24, scattering increases. When the ion moves away from the laser, however, Δ_{D} becomes positive and scatter is reduced. If the laser is red-detuned, such that $\Delta > \Delta_D$, photon absorption is enhanced when the ion moves towards the beam, but suppressed when it moves away.

Each absorption event imparts a momentum kick of $-\hbar k$ onto the ion, where the negative sign indicates the momentum kick is opposite to the motion of the ion. The corresponding spontaneous scatter event also gives the ion a momentum kick, but since scattering is on average considered isotropic the momentum kicks from spontaneous emission averages to zero. As photon absorption occurs from only one direction, but scattering occurs in all directions, the net result is a directionally dependent damping force reducing the ion's kinetic energy. Adjusting the propagation of the laser beam to an oblique angle to all the principle axes enables cooling in all dimensions using just a single laser beam.

The emission of each photon, however, induces a small momentum kick onto the ion, known as photon recoil, and limits the final ion energy. In appendix A the cooling and heating rates are compared and shows that when optimally cooled, detuning the laser to $\Delta = \Gamma/2$, an ion has a minimum energy of $E = \hbar\Gamma/2$. It is discussed below why this energy is still to high to be suitable for quantum information processing.

Limits of Doppler Cooling - Lamb Dicke Limit

To be suitable for QIP ion energy must be low enough such that its amplitude of oscillation is less than $\lambda/2\pi$ of the incident radiation, a limit known as the Lamb Dicke limit. Operating in this regime ensures the whole wavefunction of the ion undergoes phase coherent interaction with the applied radiation, reducing decoherence. The amplitude, however, should not be significantly less than the wavevector. When in this regime manipulations such as motional coupling, are greatly suppressed and the fidelity of subsequent QIP operations greatly severely reduces. This situation is described later in section 2.4.

The amplitude of the oscillations are first quantised by describing ion motion within the trapping potential as that of a quantised harmonic oscillator. The ion occupies only quantised states of motion, separated by ω_{sec}, which form an evenly spaced ladder of

amplitude $E = \hbar\omega_{\text{sec}}n$, where n is the motional quantum number. The Lamb Dicke limit is then given by:

$$\eta\sqrt{n+1} \ll 1 \qquad (2.25)$$

where $\eta = kx$ is the Lamb-Dicke parameter describing the ratio of the extent of the motional ground state of the ion, x, to the wavevector of the incident radiation, k, and n is the motional quantum number. k and x are expressed as

$$k = \cos(\theta)\frac{2\pi}{\lambda} \qquad x = \sqrt{\frac{\hbar}{2m\omega_{\text{sec}}}} \qquad (2.26)$$

where θ is the angle between the laser beam and axis of ion motion, and m the ion mass. If we now consider an ion cooled to the Doppler limit, it has energy $E = \hbar\Gamma/2$ and a motional quantum number of $n = \Gamma/(2\omega_{\text{sec}})$. Inserting this expected motional quantum number into the Lamb-Dicke limit (equation 2.25) it can be seen that the result is likely to be >1, indicating that Doppler cooled ions may not be within the Lamb-Dicke limit. To attain energies suitable for QIP additional techniques, capable of coupling to motion, are therefore required.

2.3.2 Cooling Below the Doppler Limit

Sub Doppler temperatures are achieved by cooling within the strong binding regime, $\omega_{\text{sec}} \gg \Gamma$. In this regime a relatively narrow atomic transition is used to resolve and couple to the motion of the ion. Mapping out this absorption profile using this narrow linewidth transition yields not only a resonance at the Doppler free resonance, ω_0, but also additional resonance peaks at $\omega_0 \pm \omega_{\text{sec}}$. These additional frequency sidebands are due to the oscillatory motion of the ion modulating the atomic transition frequency. Tuning the exciting laser to $\omega_0 - \omega_{\text{sec}}$ induces an absorbtion of a photon with energy $\hbar(\omega_0 - \omega_{\text{sec}})$. The corresponding spontaneously emitted photon then has an energy $\hbar(\omega_0 - \omega_{\text{r}})$, where $\hbar\omega_{\text{r}} = \hbar^2 k^2/2m$ is the recoil energy of the ion. If $\omega_{\text{sec}} \gg \omega_{\text{r}}$ the absorption and scatter event will reduce the ion energy by $\hbar\omega_{\text{sec}}$, reducing the ion energy by a motional quantum.

The common techniques used to achieve sub-Doppler temperatures are direct sideband cooling [55, 77, 78], Raman sideband cooling [79–81], and electro-magnetically induced transparency [82–84]. Microwave radiation has also recently been shown to resolve motional sidebands [85] and cool to the ground state, however this approach is not discussed.

Direct Sideband Cooling

This technique uses a three-level system with a ground state $|g\rangle$, metastable state $|m\rangle$ and excited state $|e\rangle$ arranged in a Ξ configuration as shown in figure 2.8. The states $|g\rangle$ and $|m\rangle$ are coupled by a narrow linewidth transition $\Gamma_{gm} \ll \omega_{sec}$ while the excited state $|e\rangle$ couples to both $|g\rangle$ and $|m\rangle$ via electric dipole transitions.
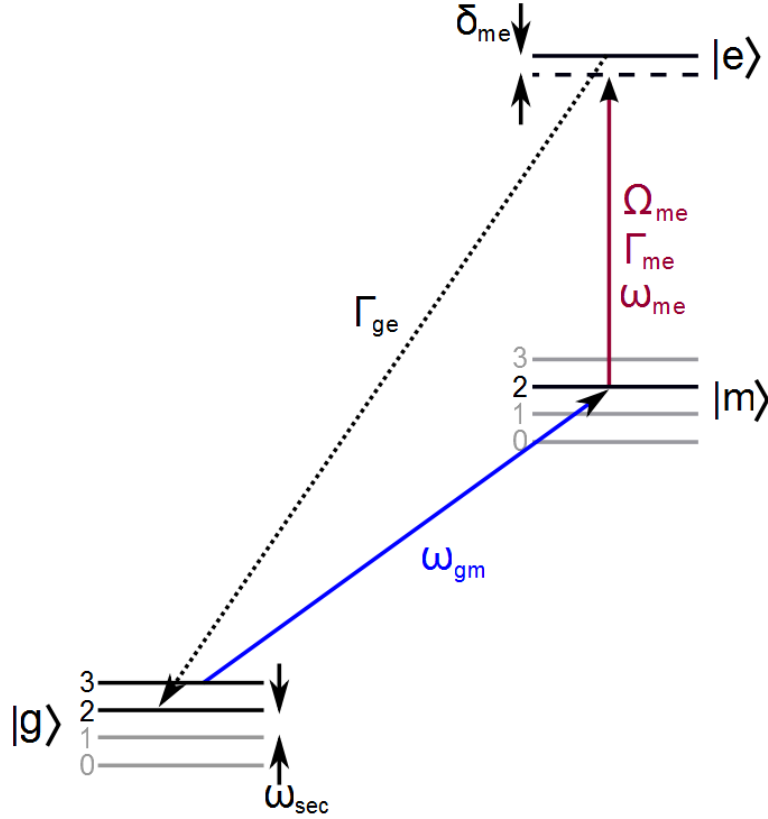
Figure 2.8: Transition configuration realising direct sideband cooling. Exciting the narrow transition $|g\rangle \leftrightarrow |m\rangle$ with a field tuned to $\omega_{gm} - \omega_{sec}$ enables coupling to a lower motional state. To increase the effective decay rate $|m\rangle$ is quenched via a dipole transition to an excited state $|e\rangle$, from which the ion can decay back to the ground state.

The transition $|g\rangle \rightarrow |m\rangle$ is excited using a field with frequency ω_{gm}. Detuning this laser frequency to $\omega_{gm} - \omega_{sec}$ enables a transition to a lower motional state, $|g,n\rangle \rightarrow |m,n-1\rangle$, to be driven. The long lifetimes of metastable states, however, result in small spontaneous decay rates, which can lead to inefficient cooling. To compensate the metastable state is 'quenched' by exciting the $|m\rangle \leftrightarrow |e\rangle$ dipole transition using a laser with frequency ω_{me}, intensity Ω_{me} and detuning δ_{me}. Since the excited state is also coupled to the ground state via dipole transition the ion can effectively decay back to the ground state faster than the decay rate of the meatastable state.

To reduce the probability of exciting to a different motional state the quenching transition is pumped below saturation, $s_{\mathrm{me}} = 2|\Omega_{\mathrm{me}}|^2/\Gamma_{\mathrm{me}}^2 \ll 1$. Excitation through $|e\rangle$ therefore only increases the decay rate, but does not change the final ion energy. The excited state can therefore be adiabatically eliminated leaving a two-level system between $|g\rangle$ and $|m\rangle$. This two-level system has then been shown to have an effective decay rate faster than the metastable's natural decay rate $\Gamma' \gg \Gamma$ [86], where

$$\Gamma' = \frac{(\Omega_{\mathrm{me}}/2)^2}{[(\Gamma_{\mathrm{ge}} + \Gamma_{\mathrm{me}})/2]^2 + \delta_{\mathrm{me}}^2}\Gamma_{\mathrm{ge}} \tag{2.27}$$

It can be seen that the decay rate of this two-level system ultimately depends upon the detuning and intensity of the quenching field and not the field exciting $|g\rangle \leftrightarrow |m\rangle$. Increasing Ω_{me} or decreasing δ_{me} will increase the effective decay rate, however this also increases the rate of off-resonant coupling to higher motional state. A compromise is therefore usually required between the cooling rate and the final ion energy.

Stimulated Raman Sideband Cooling

This technique uses a three-level system with a ground state $|g\rangle$, metastable state $|m\rangle$ and excited state $|e\rangle$ arranged in a Λ configuration, as shown in figure 2.9. The frequency separation between $|g\rangle$ and $|m\rangle$ and the excited state are ω_{ge} and ω_{me} respectively. The transitions $|g\rangle \leftrightarrow |e\rangle$ ($|m\rangle \leftrightarrow |e\rangle$) are excited using fields with intensities Ω_{ge} (Ω_{me}) and frequency $\omega_{\mathrm{ge}} + \Delta_{\mathrm{ge}}$ ($\omega_{\mathrm{me}} + \Delta_{\mathrm{me}}$) respectively, where Δ_{ge} (Δ_{me}) are the detunings of the respective fields. Both beams are detuned from resonance, $\Delta = \Delta_{\mathrm{ge}} = \Delta_{\mathrm{me}}$, to reduce the coupling to the excited state and reduce the three-level system to a two-level system between $|g\rangle \leftrightarrow |m\rangle$. Tuning the beatnote frequency to $\omega_{\mathrm{ge}} - \omega_{\mathrm{me}} = \omega_{\mathrm{gm}} - \omega_{\mathrm{sec}}$ excites the red sideband $|g,n\rangle \rightarrow |m,n\text{-}1\rangle$ transition. A third, nearly resonant, laser driving the $|m\rangle \rightarrow |e\rangle$ transition below saturation then re-initalises the ion back into $|g\rangle$. Since the recoil energy from the spontaneously emitted photon will be on the order of 10's kHz, while ion secular frequencies are usually on the order of MHz, the spontaneous decay is expected to have negligible effect on the motion state [87]. The transition rate between $|g\rangle \leftrightarrow |m\rangle$ is given by [67]

$$\Omega_{\mathrm{Ram}} = \frac{\Omega_{\mathrm{ge}}\Omega_{\mathrm{me}}}{\Delta} \tag{2.28}$$

which shows that the final transition rate scales linearly with the intensity of the laser radiation, but also inversely with the detuning from the excited state. While larger detunings reduce the rate of coupling to the excited state, reducing the rate of heating due to
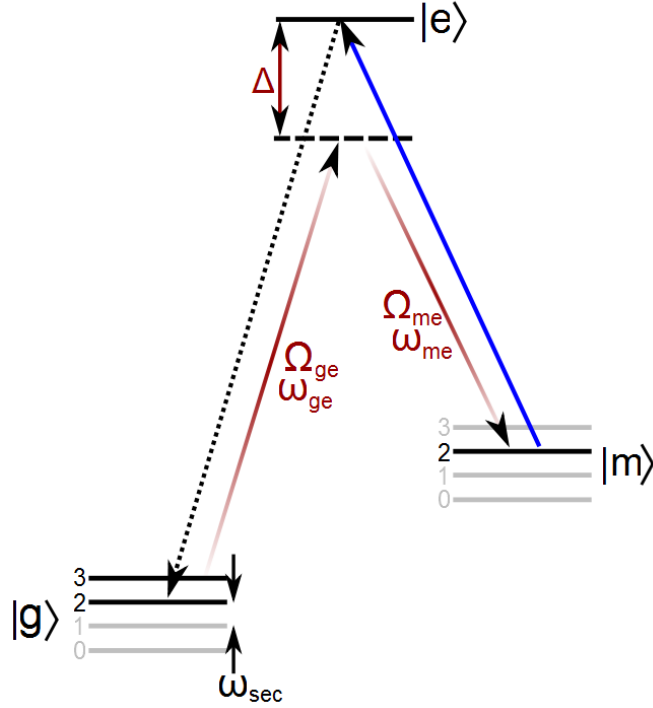
Figure 2.9: Configuration for two photon stimulated Raman transition. Fields at ω_{ge} and ω_{me}, detuned from resonance by Δ, couple the states $|0\rangle$ and $|1\rangle$ via the excited state $|e\rangle$. Tuning of the beat frequency $\omega_{ge} - \omega_{me} = \omega_{mg} - \omega_{sec}$ results in coupling to a lower motional state.

off-resonant coupling, a greater laser power is required to maintain a sufficient transition rate. A compromise is therefore usually required between the final ion temperature and the transition rate.

Electromagnetically Induced Transparency

This method exploits the quantum interference effect of electromagnetically induced transparency (EIT) to couple to motional states [83]. The scheme uses a three-level system with ground state $|g\rangle$, metastable state $|m\rangle$ and excited state $|e\rangle$ arranged in a Λ configuration, as shown in figure 2.10. State $|e\rangle$ is coupled to both $|g\rangle$ and $|m\rangle$ by dipole transitions. The $|m\rangle \leftrightarrow |e\rangle$ transition is excited by an intense 'coupling' laser field of frequency $\omega_{me} + \Delta_{me}$, where Δ_{me} is the detuning from resonance, and a Rabi frequency Ω_{me}. A second 'cooling' laser with frequency $\omega_{ge} + \Delta_{ge}$ and Rabi frequency Ω_{ge} excites the transition $|g\rangle \leftrightarrow |e\rangle$. In this scheme both the coupling and cooling beams are blue detuned from resonance. Keeping Δ_{me} constant but adjusting the detuning of Δ_{ge} produces the absorption spectrum of $|e\rangle$ shown in figure 2.10. At $\Delta_{ge} \approx 0$ the absorption profile describes the broad resonance corresponding to the large linewidth of the dipole transition. At $\Delta_{ge} = \Delta_{me}$ the absorption
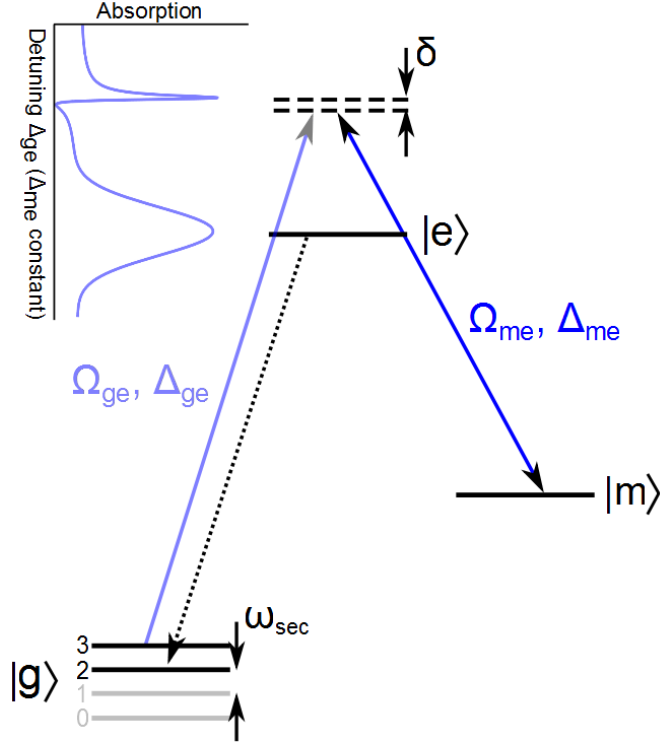
Figure 2.10: Scheme for sideband cooling using electromagnetically induced transparency (EIT). An intense 'coupling' laser couples the $|m\rangle \leftrightarrow |e\rangle$ states and a weak 'cooling' laser couples the $|g\rangle \leftrightarrow |e\rangle$ states. The coupling laser is blue detuned from resonance by Δ_{me} and adjusting the detuning of the cooling laser produces the absorption profile shown. At $\Delta_{ge} = 0$ the broad absorption profile corresponds to the large transition linewidth. At $\Delta_{ge} = \Delta_{me}$ absorption is suppressed, which is EIT, and at $\Delta_{ge} \gtrsim \Delta_{me}$ a narrow resonance occurs. The separation between the transparency and narrow resonance, δ, depends upon the intensity Ω_{me}. Adjusting it to $\delta = \omega_{sec}$ allows lower motional sidebands to be driven.

profile reduces to zero, which is the EIT. At a detuning close to the frequency of the coupling laser, $\Delta_{ge} \gtrsim \Delta_{me}$, a narrow absorption profile exists. The separation of the transparency and this narrow resonance, δ, is given by the ac Stark shift induced by the coupling laser.

$$\delta = \frac{\sqrt{\Delta_{me}^2 + \Omega_{me}^2} - |\Delta_{me}|}{2} \tag{2.29}$$

Setting $\Delta_{ge} = \Delta_{me}$ the zero of the absorption profile coincides with the $|g,n\rangle \leftrightarrow |e,n\rangle$ carrier transition. By tuning the intensity of the coupling laser the detuning of the narrow resonance can be adjusted to $\delta \approx \omega_{sec}$ to coincide with the $|g,n\rangle \leftrightarrow |e,n-1\rangle$ red sideband transition. As a result of the asymmetry of the profile, the blue sideband lies in a region of small absorption and the $|g,n\rangle \leftrightarrow |e,n+1\rangle$ transition probability is low. Once excited on the red sideband the ion decays back to the ground state at the natural linewidth Γ.

2.4 Quantum Information Processing with $^{171}\text{Yb}^+$

In trapped ion quantum computing the qubit states are assigned to different internal energy levels. This allows the system to be treated as a fictitious spin $1/2$ particle with the $|\uparrow\rangle$, $|\downarrow\rangle$ states corresponding to the lower, upper energy levels of the pseudo spin. Depending upon the ion species under study the frequency difference between the two qubit levels can range from a couple of kHz (neighboring Zeeman levels) to the optical domain where separation are on the order hundreds of THz. For $^{171}\text{Yb}^+$ the qubit states are encoded on the magnetic field insensitive ground state hyperfine levels, separated by $\omega/2\pi = 12.6$ GHz.

$$|1\rangle = |\uparrow\rangle = {}^2S_{1/2}|F = 1, m_F = 0\rangle$$
$$|0\rangle = |\downarrow\rangle = {}^2S_{1/2}|F = 0, m_F = 0\rangle$$

The model of quantum computing requires the manipulation of this qubit to include the initialisation into simple fiducial states, qubit specific measurement, and the ability to form a universal set of quantum gates. This section details the ion-field interactions used to satisfy these requirements.

2.4.1 State Preparation and Readout

State preparation and readout are achieved by exciting the transitions shown in figure 2.11. Since selection rules prohibit coupling of the ${}^2S_{1/2}|F = 0\rangle \leftrightarrow {}^2P_{1/2}|F = 0\rangle$ transition preparation into $|0\rangle$ is primarily achieved by encouraging decay from the ${}^2P_{1/2}|F = 1\rangle$ state. With the ${}^2S_{1/2}|F = 1, m_F = 1\rangle \leftrightarrow {}^2P_{1/2}|F = 1, m_F = 1\rangle$ transition also prohibited, coupling to the excited state is achieved via the ${}^2S_{1/2}|F = 1, m_F = 0\rangle \rightarrow {}^2P_{1/2}|F = 1, m_F = \pm1\rangle$ transitions, figure 2.11(a). Exciting the ${}^2D_{3/2}|F = 2\rangle \leftrightarrow {}^3D[3/2]_{1/2}|F = 1\rangle$ transition also enables population of $|0\rangle$. Once in $|0\rangle$ a coherent operation coupling both the qubit states can be used to prepare the ion into $|1\rangle$. State detection is simply performed by applying the 369 nm and 935 nm beams without any frequency sidebands, figure 2.11(b). Detection of fluorescence represents population in $|1\rangle$ while no fluorescence indicates $|0\rangle$.

To excite the ${}^2S_{1/2}|F = 1\rangle \leftrightarrow {}^2P_{1/2}|F = 1\rangle$ transition 2.1 GHz frequency sidebands are applied to the 369 nm beam, the generation of which are discussed in 3.3.5. To avoid depopulation of $|0\rangle$ the 14.7 GHz frequency sidebands are removed from the 369 nm beam.
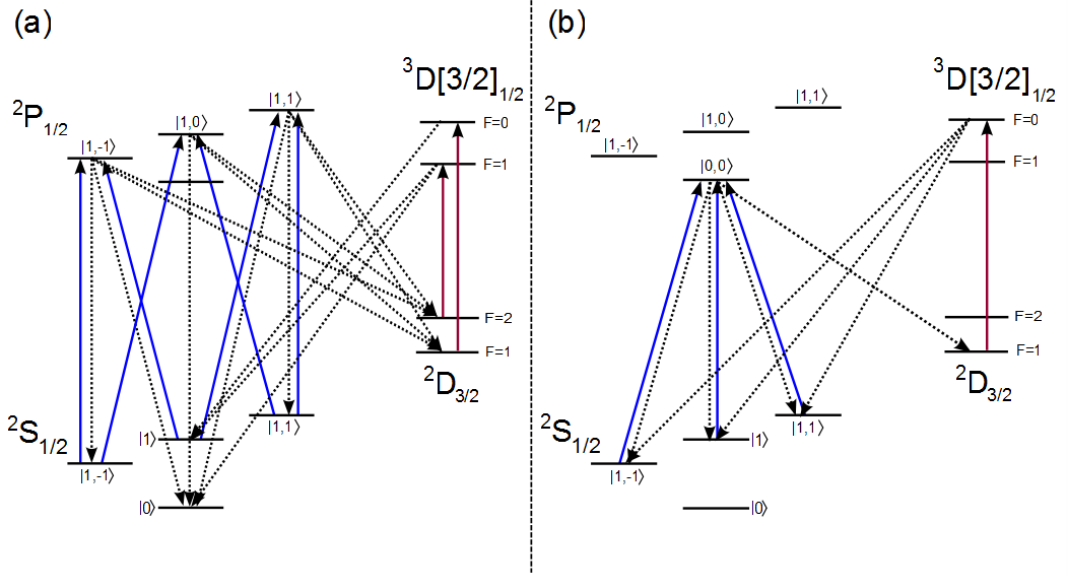
Figure 2.11: State preparation and detection of ^{171}Yb$^+$ qubit. The qubit is defined as $|1\rangle = |^2S_{1/2}, F = 1, m_F = 0\rangle$ and $|0\rangle = |^2S_{1/2}, F = 0, m_F = 0\rangle$. (a) shows the transitions used to initialise the ion into $|0\rangle$, while (b) shows the transitions used for detection. If fluorescence is detected the ion is in $|1\rangle$, otherwise the ion in $|0\rangle$.

2.4.2   Single Qubit Operations

For a trapped ion system gates are achieved through combinations of single qubit gates and multi-qubit entangling gates. Single qubit gates, such as the NOT gate, can be realised by qubit rotation, while multi-qubit gates, such as the controlled NOT or CNOT gate, are realised by entangling multiple ions. Rotating the qubit takes advantage of the quantum mechanical principle of superposition to enable preparation into any arbitrary state $\alpha|\uparrow\rangle + \beta|\downarrow\rangle$. Entangling then connects the superposition states of individual qubits to form a single coherent system. Rotations, at the simplest level, can be one photon transitions coupling the two states, while entanglement of multiple qubits requires the ability to coupling to the external motional.

The following mathematical discussion, which closely follows [67, 68, 87–89], describes the manipulation of a single ^{171}Yb$^+$ qubit. Although the qubit states are coupled by a magnetic moment, the following framework is equally applicable to other multipole couplings. In the absence of any electromagnetic fields an ion oscillating in a harmonic potential is described by the Hamiltonian

$$
\begin{aligned}
H_0 &= H_e + H_m \\
&= \frac{\hbar\omega_0}{2}\hat{\sigma}_z + \hbar\omega_i \hat{\alpha}_i \hat{\alpha}_i^\dagger
\end{aligned}
\tag{2.30}
$$

where $\hat{\sigma}_z = \begin{bmatrix} 1 & 0 \\ 0 & -1 \end{bmatrix}$ is the Pauli spin operator, ω_i is the secular frequency, and $\hat{\alpha}_i / \hat{\alpha}_i^\dagger$ are the creation / annihilation operators respectively. The state vector for this spin 1/2 system is then

$$|\Psi(t)\rangle = \sum_{n=0}^{\infty} \left(c_{\uparrow,n}(t)|\uparrow,n\rangle + c_{\downarrow,n}(t)|\downarrow,n\rangle \right) |n\rangle \tag{2.31}$$

where $|n\rangle$ are the harmonic oscillator eigenstates with energy $\hbar\omega_i$. If radiation, with a frequency resonant with the qubit separation, is now applied to the ion the Hamiltonian describing the interaction is

$$\hat{H}_i = -\hat{\mu}_B \bar{B} \tag{2.32}$$

where $\hat{\mu}_B = \mu(\hat{\sigma}_+ + \hat{\sigma}_-)$ is the magnetic dipole moment coupling the qubit states, and $\bar{B} = B_0 \cos(kr - \omega t + \phi)\hat{r}$ is the external applied time-varying magnetic field with amplitude B_0, frequency ω and propagation direction $\hat{r}$. Again a magnetic field is considered since the qubit states in ^{171}Yb$^+$ are separated by a magnetic dipole, but the framework is equally applicable to other multipole couplings. The interaction Hamiltonian can be expanded to

$$\hat{H}_i = \hbar\Omega \left(\hat{\sigma}_+ + \hat{\sigma}_- \right) \left[e^{i(kr-\omega t+\phi)} + e^{-i(kr-\omega t+\phi)} \right] \tag{2.33}$$

where $\Omega = -\mu B_0 / 2\hbar$ is the Rabi frequency for the magnetic dipole transition and the spin operators are

$$|\uparrow\rangle\langle\downarrow| = \hat{\sigma}_+ = \begin{bmatrix} 0 & 1 \\ 0 & 0 \end{bmatrix}, \qquad |\downarrow\rangle\langle\uparrow| = \hat{\sigma}_- = \begin{bmatrix} 0 & 0 \\ 1 & 0 \end{bmatrix} \tag{2.34}$$

The interaction in equation 2.33 is described in the Schrödinger picture where only the state vector has a time dependence. By transforming to the interaction picture a more realistic description of the system evolution is obtained, where both the state vector and operators obtain a time dependence. In this frame the qubit state vector becomes time varying only when the external field is applied, but is otherwise stationary. To perform the transformation the operator $\hat{U}_0 = e^{-iH_0 t/\hbar} = e^{-i(H_e + H_m)t/\hbar}$ is used

$$\hat{H}_{int} = \hat{U}_0^\dagger H_i \hat{U}_0 \tag{2.35}$$

to yield the Hamiltonian

$$\begin{aligned} \hat{H}_{int} = \quad & \hbar\Omega \left[e^{i\omega_0 t \hat{\sigma}_z/2}(\hat{\sigma}_+ + \hat{\sigma}_-)e^{-i\omega_0 t \hat{\sigma}_z/2} \right] \\ & \left[e^{i\omega_i \hat{\alpha}^\dagger \hat{\alpha}} \left(e^{i(kr-\omega t+\phi)} + e^{-i(kr-\omega t+\phi)} \right) e^{i\omega_i \hat{\alpha}^\dagger \hat{\alpha}} \right] \end{aligned} \tag{2.36}$$

The terms in the first set of square brackets describe the spin state (qubit state), while the terms in the second set of square brackets describe the motional state of the ion. The spin and creation/annihilatin operators commute allowing the two components to be treated separately. The resulting Hamiltonian, described in appendix B, is shown to take a general form of

$$\hat{H}_{int} = \hbar\Omega \left[\hat{\sigma}_+ e^{i[\eta(\hat{\alpha}e^{-i\omega_i t}+\hat{\alpha}^\dagger e^{i\omega_i t})+kr_0+\delta\omega t+\phi]} + H.c.\right] \tag{2.37}$$

where $\delta\omega = \omega - \omega_0$ is the detuning of the laser from resonance, and $\eta = k \cdot r$ is the Lamb Dicke parameter. Since it is desirable for operations to be formed within this limit, $\eta = k \cdot r \ll 1$, the interaction Hamiltonian (equation 2.37) can be expanded to the lowest order in η.

$$\hat{H}_{LD} = \hbar\Omega \left[\hat{\sigma}_+(1 + i\eta(\hat{\alpha}e^{-i\omega_i t} + \hat{\alpha}^\dagger e^{i\omega_i t}))e^{i(\phi-\delta\omega t)}\right] + H.c. \tag{2.38}$$

In this regime only coupling to neighboring motional states is applicable, and coupling to higher order sidebands is omitted. Depending upon the detuning the interaction described by equation 2.38 will either couple to the same motional state or the next higher/lower motional state. The first resonance, occurring at a detuning of $\delta\omega = 0$, describes a carrier transition, $|\uparrow, n\rangle \leftrightarrow |\downarrow, n\rangle$, which couples the two internal states but does not change the motional state of the ion. The other two resonances, occuring at $\delta\omega = \pm\omega_i$, excite transitions $|\uparrow, n\rangle \leftrightarrow |\downarrow, n \pm 1\rangle$ which couple to the external motion while rotating the qubit. The evolution and coupling strength of the three resonant transitions are determined by inserting the respective Hamiltonian and state vector, equation 2.31, into Schrödinger's equation. The resulting Hamiltonian and coupling strength for the different transitions, detailed in appendix B, are

transition	detuning	Hamiltonian	Coupling
$|\downarrow, n\rangle \leftrightarrow |\uparrow, n\rangle$	$\delta\omega = 0$	$\hat{H}_{car} = \hbar\Omega[\hat{\sigma}_+ e^{i\phi} + \hat{\sigma}_- e^{-i\phi}]$	Ω
$|\downarrow, n\rangle \leftrightarrow |\uparrow, n-1\rangle$	$\delta\omega = -\omega_i$	$\hat{H}_{rsb} = \hbar\Omega[\hat{\alpha}\hat{\sigma}_+ e^{i\phi} + \hat{\alpha}^\dagger\hat{\sigma}_- e^{-i\phi}]$	$\Omega\sqrt{n}\eta$
$|\downarrow, n\rangle \leftrightarrow |\uparrow, n+1\rangle$	$\delta\omega = +\omega_i$	$\hat{H}_{bsb} = \hbar\Omega[\hat{\alpha}^\dagger\hat{\sigma}_+ e^{i\phi} + \hat{\alpha}\hat{\sigma}_- e^{-i\phi}]$	$\Omega\sqrt{n+1}\eta$

Qubit Rotation and Motional Coupling

If we consider first the carrier transition, the state populations can be be described by

$$\dot{c}_\uparrow = i\Omega e^{-i(\phi)}\dot{c}_\downarrow \tag{2.39}$$

$$\dot{c}_\downarrow = -\Omega e^{i(\phi)}\dot{c}_\uparrow$$

The evolution of this two level system is then described by $|\Psi(t)\rangle = \hat{U}(t)|\Psi(0)\rangle$, where $U(t)$ is the time-evolution operator.

$$|\Psi(t)\rangle = \hat{U}(t) = \begin{pmatrix} \cos(\Omega t) & -ie^{i\phi}\sin(\Omega t) \\ -ie^{-i\phi}\sin(\Omega t) & \cos(\Omega t) \end{pmatrix} |\Psi(0)\rangle = R(\Omega t, \phi) \qquad (2.40)$$
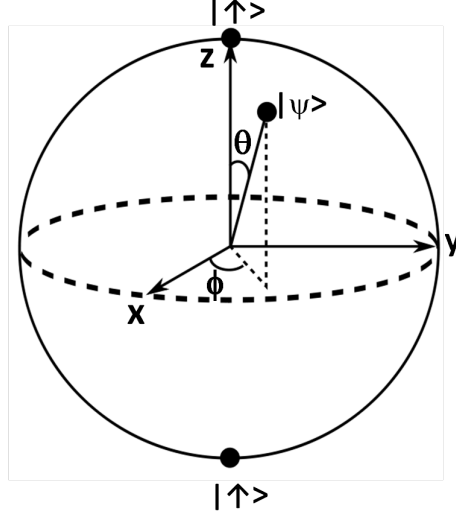
Figure 2.12: Representation of the Bloch sphere. The two poles represent the $|\uparrow\rangle$ and $|\downarrow\rangle$ states and correspond to $z = \pm 1$ respectively. Rotations by $R(\theta, \phi)$ determines how the qubit state evolves.

This matrix describes a rotation on the Bloch sphere, illustrated in figure 2.12. The position of the state vector is controlled by varying the parameters Ω, t, and ϕ. A rotation about the x-axis, described as $R_x(\theta) = R(\theta, 0)$, is achieved by instigating an interaction with Rabi frequency Ω for time t. A rotation about the y-axis, described as $R_y(\theta) = R(\theta, \phi)$, is achieved by again instigating an interaction, but with a phase difference, ϕ, of the applied radiation. Finally rotations about the z-axis can then be achieved using sequences of x and y rotations, such as $R_z(\theta) = R_x(\theta)R_y(\theta)R_x(\theta)$.

If we now consider the detunings which allow motional coupling. It can be be seen that while the carrier has a transition frequency of Ω sideband transitions are scaled by a factor of η. To maintain motional coupling a sufficiently large η is therefore required, however this presents a problem when exciting transitions separated by a magnetic dipole. With the transition requiring microwave radiation, the corresponding η results in severely reduced motional coupling stengths. To illustrate consider an $^{171}\text{Yb}^+$ ion oscillating with an axial frequency of $\omega_z/2\pi = 1$ MHz interacting with resonant microwave radiation, $\omega/2\pi = 12.6$ GHz. Even if the radiation propagates parallel to the ion motion, the maximum Lamb Dicke parameter is only $\eta = kz_0 = 3.5\text{x}10^{-6}$. Coupling to different motional states

is therefore at best a factor of 10^{-6} of the carrier transition strength. In order to couple to motional alternative methods are required.

It has been shown, by Mintert and Wunderlich [85, 90] and Johanning *et al.* [85], that applying a static magnetic field gradient across the ion allows motional sidebands to be resolved, providing a means to couple to motion and ground state cooling. This technique, however, was not realised until the end of this thesis so is not described here. Instead optical transitions which provide greater photon momentum and increased motional coupling, such as those discussed in section 2.3.2, are considered.

2.5 Suitability of Qubit Manipulation Techniques

For trapped ions to be used for QIP they must be cooled to sufficiently low temperatures, rotated to any arbitrary superposition, and also coupled to the quantised motional states. Ground state cooling of Yb^+ ions can be achieved using the three methods described in section 2.3.2. Direct sideband cooling would be implemented using the $^2S_{1/2} \leftrightarrow {}^2D_{3/2}$ quadrupole transition, with the metastable state quenched using the $^2D_{3/2} \leftrightarrow {}^3D[3/2]_{1/2}$ transition. EIT and Raman cooling would both be implemented using the $^2S_{1/2} \leftrightarrow {}^2P_{1/2}$ transition. For even isotopes the ground and metastable states can be represented with a Zeeman splitting of the ground state, while for $^{171}Yb^+$ the two qubit states can be used. While direct sideband cooling is conceptually the simplest, it is potentially the most challenging to implement. To confidently resolve motional sidebands the laser frequency must be stabilised to less than the secular frequency. Since a secular frequency of $\omega_{sec} \approx$ 1 MHz is expected, laser stability of ≤ 10 KHz is desirable, which is challenging and expensive. In contrast Raman transitions and EIT only require stability of the beat frequency between two beams, but not the absolute laser frequency. Since both beams can be derived from the same laser the relative difference can be easily maintained without such rigorous laser stability.

Qubit rotation is possible using either a two photon Raman transition or resonant microwave radiation. EIT and direct sideband cooling are unsuitable since they both rely upon spontaneous emission. While a microwave transition, in the presence of a large magnetic field gradient, has been shown to couple to motional states it was not realised until the end of this thesis. The preferred approach to cooling and manipulating the trapped ion qubit, therefore, is with two photon Raman transitions. The investigation into the implementation of this technique is discussed in greater detail in section 8.1.

Chapter 3

Lasers

" The key to this project is the giant laser, which was invented by the noted

Cambridge physicist, Dr. Parsons. So therefore, it is fitting to call it:

'The Alan Parsons Project' "

-Dr Evil, *Austin Powers 2.*

The use of coherent narrow linewidth laser radiation to efficiently excite atomic transitions has been extensively implemented. Several different types of lasers have been developed to provide such radiation, such as dye lasers and gas lasers, however it is the common semiconductor laser diode that has become the popular choice. These devices, when used in relatively simple cost effective setups, offer narrow linewidth tunable radiation over a wide range of wavelengths. Unfortunately not all wavelengths are obtainable directly from laser diodes, with wavelengths in the ultraviolet UV spectrum being particularly troublesome. Therefore experiments requiring use of UV laser radiation may require the more complex systems. This chapter describes the design and construction of the narrow linewidth semiconductor based laser systems required to create and cool Yb^+ ions including $^{171}Yb^+$.

3.1 Diode Lasers

The basic principle behind the semiconductor laser is the p-n junction. At the interface between an n-doped and p-doped material the charge carriers from the two materials (electrons and holes respectively) recombine to form the depletion region. In an equilibrium state these charge carriers have insufficient energy to overcome the depletion region. Applying a forward bias voltage across the diode, however, shifts the band structures of the doped materials allowing the carriers to cross the depletion region and spontaneously

recombine. The energy released from each recombination is in the form a photon with a wavelength related to the bandgap energy of the depletion region, $E_{\text{BG}} = hc/\lambda$, where h is Planck's constant, c the speed of light and λ the photon wavelength. These emitted photons then stimulate the decay of additional electrons in the conduction band producing more photons of the same wavelength. The difference in refractive index between the semiconductor material and external environment reflects the photons back and forth within the cavity further amplifying the effect of stimulated emission. Lasing occurs when the stimulated emission is greater than the spontaneous emission and losses within the cavity, with the resulting wavelength determined by both the bandgap energy and also the optical path length within the diode.

The emission from a laser diode, however, is not perfectly monochromatic. Spontaneous emission of random phase photons into the cavity longitudinal mode results in a finite frequency laser linewidth. The fundamental limit of laser linewidth was initially calculated by Schawlow and Townes [91], and then adapted by Sennaroglu *et al.* [92] to be

$$\Delta\nu_{\text{laser}} \quad = \quad \frac{h\nu_{\text{laser}}\theta I_{\text{tot}}T_{\text{oc}}}{4\pi T_{\text{rt}}^2 P_{\text{out}}} \tag{3.1}$$

where, h is the Planck constant, ν_{laser} the central photon frequency, T_{oc} the output coupler transmission, I_{tot} the total resonator losses, T_{rt} the resonator round-trip time, and θ the spontaneous emission factor. It can be seen the most influential factor on the linewidth is the round trip time of the photons, which is related to the coherence of the photons oscillating within the cavity. A longer cavity increases the coherence of the photons within the cavity narrowing the linewidth of the resulting laser emission [93].

A common approach of increasing cavity length is to use additional optical elements to feed a portion of the laser light back into the laser diode. Different techniques for achieving this include optical feedback from a confocal cavity [94], feedback from high contrast saturated absorption [95], and use of the Faraday effect [96]. These setups, however, can be expensive and time consuming to contruct/operate and some do not offer wavelength tunability. A cheaper, and more popular, option is to use a reflective diffraction grating to increase the cavity length and feed the narrow linewdith reflections back into laser diode. This setup is commonly known as an external cavity diode laser (ECDL) [97].

3.2 External Cavity Diode Lasers

3.2.1 Principle of Operation

In external cavity diode lasers (ECDL's) optical feedback is achieved using reflective diffraction gratings. These optical components act as dispersive elements separating any incident radiation into its different spectral components, with each wavelength propagating in a different direction. One of these narrower linewidth diffractions are directed back into the diode to stimulate emission of a similarly narrow linewidth within the diode. This narrow feedback, coupled with the internal workings of laser diode generates suitably narrow linewidth radiation.

The final wavelength emitted from an ECDL is a function of the bandgap energy and cavity length of the diode, as well as the external cavity formed by the diffraction grating and the wavelength of feedback from the grating. Figure 3.1 provides an understanding of how these mechanisms combine to reduce the emission linewidth. Figure 3.1(a) illustrates the relative intensity of the different mechanisms: the laser diode band gap energy (blue dashed trace), the laser diode internal cavity modes (solid green trace), the feedback from the grating (red dot-dashed trace), and the external cavity modes (purple dotted trace). The combination of the mechanisms are shown in figure 3.1(b) to show the summation of the mechanisms (dashed brown trace) and the resulting emission (solid purple trace).

3.2.2 ECDL Configurations

There are two main configurations for an ECDL: the Littrow and the Littman-Metcalf configurations, illustrated in figures 3.2(a) and 3.2(b) respectively. In the Littrow configuration, the grating is aligned so that the first order diffracted beam, $n = 1$, is fed back directly into the laser, while the zeroth order beam, $n = 0$, undergoes specular reflection from the grating. The advantage of this configuration is a high percentage of laser light available for the experiment, however, tuning the wavelength requires adjusting the grating angle and therefore the beam direction.

In the Littman-Metcalf configuration the diode output is aligned at grazing incidence onto the grating. Again the zeroth order beam is the experiment beam, but now the first order diffracted beam is directed towards a mirror and reflected back onto itself. The reflected beam then undergoes diffraction from the grating for a second time and the first order order beam is coupled back into the diode. By varying the angle of the mirror, to change the wavelength fed back into the laser, tuning of the laser is achieved. Since the grating
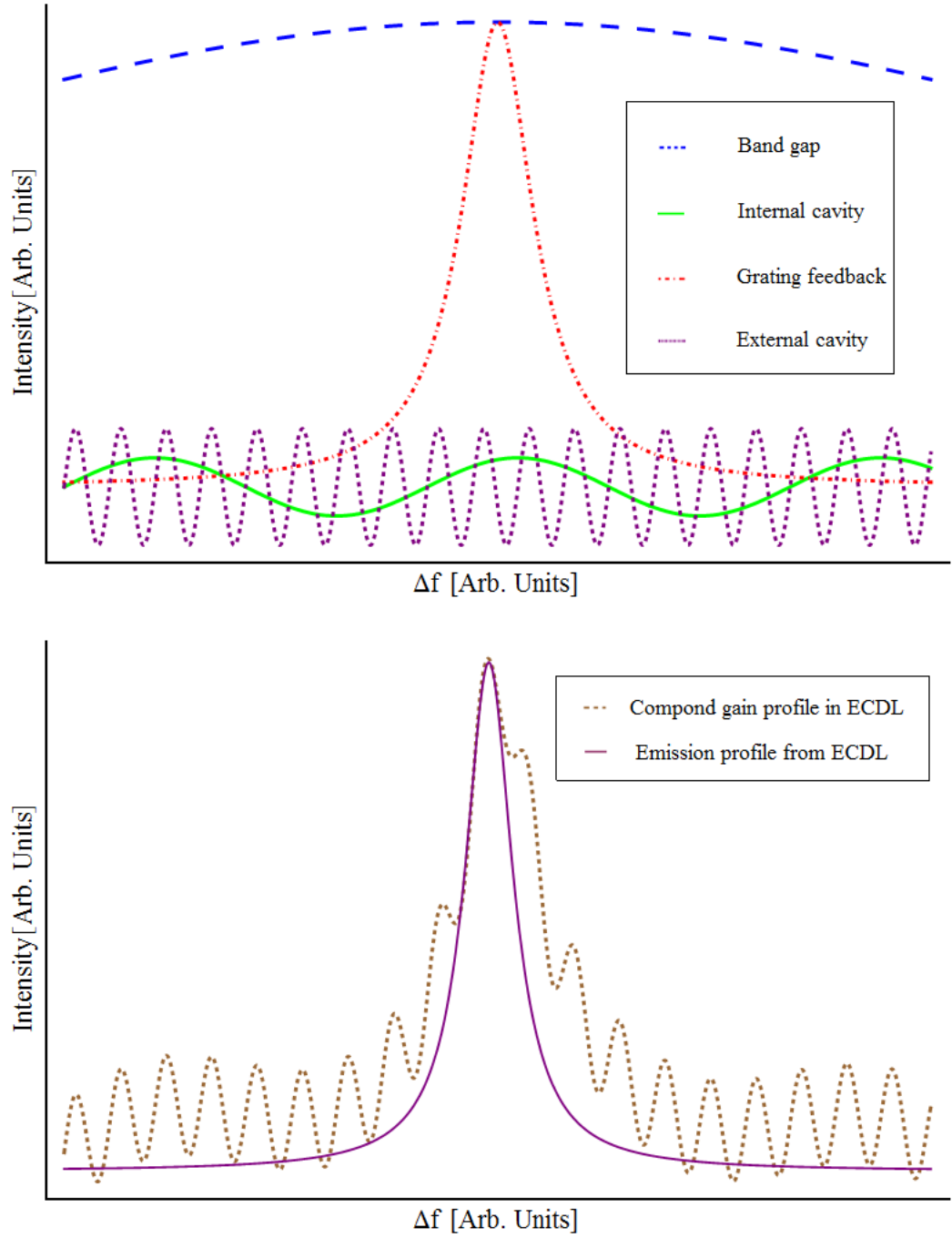
Figure 3.1: Different feedback mechanisms in an ECDL. Traces not to scale, but instead illustrate effect of each mechanism. (a) The intensity and frequency range supported by the semiconductor band gap energy, internal cavity length, feedback from the diffraction grating and external cavity length. (b) The resulting profile of all the feedback modes.
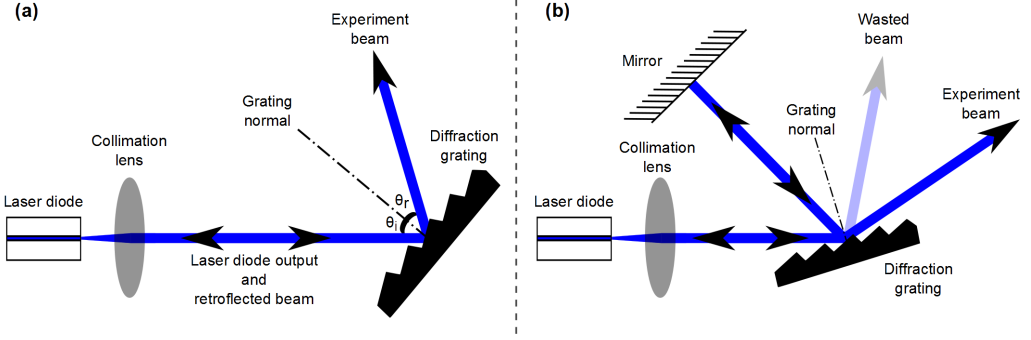
Figure 3.2: Arrangements for an external cavity diode laser in (a) the Littrow configuration. Here the grating is aligned to reflect the first order beam back into the laser diode and the zeroth order beam available for experiments. (b) The Littman-Metcalf configuration where the beam is incident upon the grating at a grazing angle. The zeroth order beam is sent to the experiment while the first order beam is sent to a mirror and reflected back onto the grating. The first order diffraction from this reflected beam is directed back into the laser diode for wavelength tuning.

does not move, the output beam angle does not change as the laser is tuned. Unfortunately the second stage of diffraction results in an additional unwanted beam, reducing the power in the experiment beam.

Out of the two options the Littrow configuration is preferable. The configuration offers a greater power in the experiment beam, and any wavelength tuning (between different isotopes) is not expected to result in a detrimental change of beam path. Given the relatively simple design of these lasers it was decided to developed them in-house. The design and choice of components are explained in the following section.

3.2.3 ECDL Components

An example of the ECDL's used in the experiment is shown in figure 3.3. The cornerstone component of the design, dubbed the 'L-piece', provides a single platform upon which all the optical components are mounted. Mounting the components on a single base reduces unwanted effects such as vibrations and temperature gradients between optical components, improving stability of the device. Laser diodes are positioned in a hole in the vertical wall of the L-piece and clamped using a brass ring. To provide flexibility and interchangeability laser diode sockets (Thorlabs: S7060R or S8060 depending upon the diode) provide electrical connection without the need to solder to the diodes directly. The beam emitted by the diode is collimated using an aspheric lens and incident upon a diffraction grating affixed to a custom grating mount. A fine pitch screw (Owis: FGS7-7.5) and piezo actuator (Piezomechanik GmbH: PSt 150/4/5 bS) inside the mount provide coarse and fine tuning of the grating angle, and horizontal alignment of the reflected first order
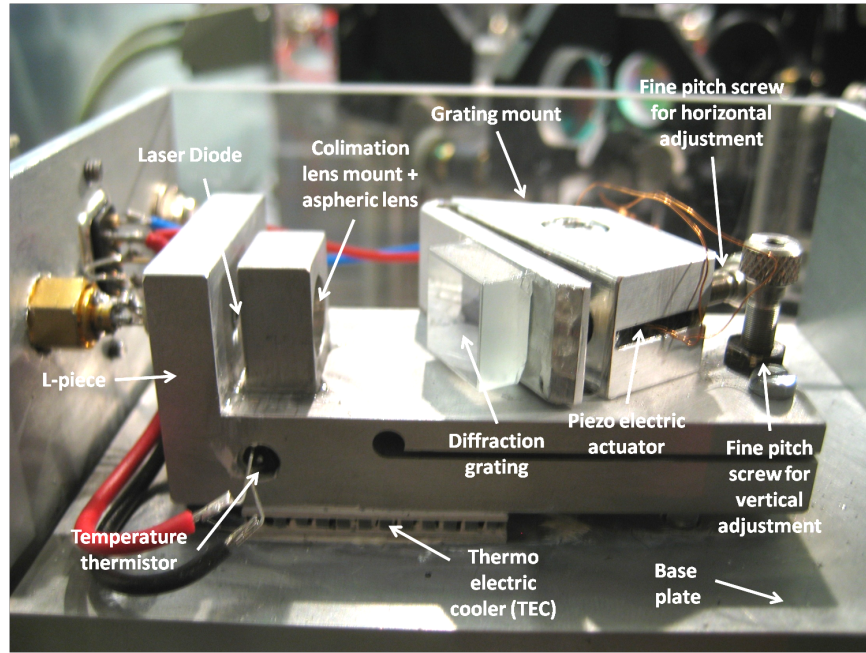
Figure 3.3: A Littrow configured ECDL used in the experiments. The laser diode, aspheric lens and grating are mounted onto the 'L-piece'. The grating is aligned using the fine pitch screws and piezo electric actuator. An AD592 temperature thermistor and thermo-electric cooler maintain the temperature of the ECDL.

beam back into the diode. An additional fine pitch screw in the L-piece allows for the vertical alignment of the first order retroflected beam. The L-piece is temperature stabilised using a thermo-electric cooler (TEC, RS: 490-1480) and AD592 temperature thermistor (Farnell: AD592ANZ). A TEC is used because it can actively regulate the temperature of the L-piece while an AD592 temperature sensor provides an actual temperature value as opposed to thermistors which provide a resistance from which temperature is inferred. Thermal grease (Farnell: 317-962) is used to improve the thermal contact between the TEC and L-piece / base, where the base provides a heat sink for the ECDL. The L-piece is secured to the base using nylon screws to maintain thermal isolation.

The whole mount is constructed from aluminium, a relatively inexpensive metal that can be thermally regulated faster than expected fluctuations of the laboratory temperature. An enclosure, formed from perspex and aluminium, shields the ECDL from unwanted external air turbulence. The aluminium parts provide electrical connection to ground, while the perspex parts allow for visual inspection of the system. Using mounting bases the heights of the lasers are increased to the height of the optics on the table. The lasers are operated using a combined laser diode current and temperature controller (Thorlabs: ITC502). Design drawings for the laser components are shown in appendix C, while the different components are described below.

Aspheric Lenses

These lenses, with a profile not a portion of a sphere, are used to reduce spherical ab-beration that occurs when collimating light from a point source, such as a laser diode. Lenses are chosen by focal length and numerical aperture. The focal length of the lens should be short enough such that the diameter of the beam is smaller than the diameter of the lens when it reaches the lens (determined using simple trigonometry). The numerical aperture (NA), which characterises the maximum angle of divergence of an incident beam the lens can accept and transmit, should be sufficient to accept the whole incident beam. Numerical aperture is defined as

$$NA = n \sin(\theta) \tag{3.2}$$

where n is the refractive index of the medium surrounding the lens, and θ the half-angle of the maximum cone of light that can enter or exit the lens. Redefining θ as the angle of divergence of the laser beam, as shown in figure 3.4, allows the minimum NA required by the lens to be determined.
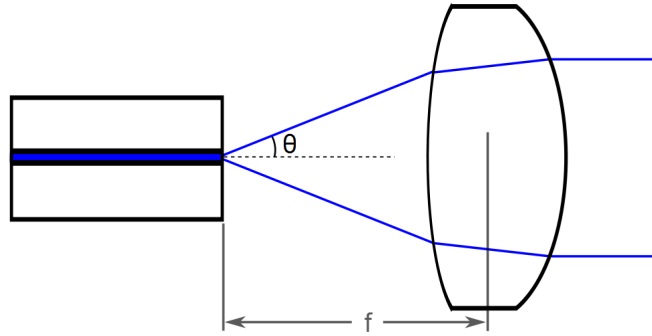
Figure 3.4: Divergence of a laser beam. The half-angle of the cone of light θ used to determine the minimum numerical aperture (NA) of the aspheric lens.

To illustrate the lens section choice consider the 399 nm diode used in the experiment ECDL (Sanyo: DL-4146-301S), which has a divergence of up to 25° from the normal. Since the lenses typically have a maximum radius of $\approx$ 2.5 mm, simple trigonometry dictates a focal length of f <5.3 mm, and to accept and collimate the whole beam NA >0.34. For this laser a lens with a numerical aperture of 0.53 and focal length of 4.6 mm is used (Thorlabs A390TM-A).

Diffraction Gratings

Selection of the diffraction grating is dictated by the groove density, d, and efficiency of the first order reflection. Groove density determines the angle at which the zeroth order beam exits the laser diode, and is better understood by analysing the grating equation [98]

$$n\lambda = d(\sin(\theta_r) - \sin(\theta_i)) \tag{3.3}$$

where n is the mode number (diffraction order), λ the wavelength, d the groove density on the grating, θ_i the angle of incidence and θ_r the angle of reflection. To align the ECDL in the Littrow configuration the grating is adjusted such that first order diffracted beam is reflected back into the laser diode. Since both beams are on the same side of the grating normal the angle of reflection is equal to the negative of the angle incidence, $\theta_r = -\theta_i$. Substituting this condition into equation 3.3 yields

$$\theta = sin^{-1}\left(\frac{\lambda}{2d}\right) \tag{3.4}$$

which describes the required angle between the incident beam and grating normal for a specific wavelength and groove density. The angle between the incident and zeroth order beam is then simply 2θ.

It is important to ensure that the grating groove density is sufficient to allow the zeroth order beam to exit the ECDL without obstruction. While this is not a big concern for near infra-red (IR) wavelengths, groove density can be an issue at ultra-violet (UV) wavelengths. To illustrate this consider the grating used for the 935 nm laser (Thorlabs: GR13-1210), which has a groove density of 1200 grooves per mm. At this wavelength the angle between the incident beam and grating normal is $\approx 34^o$, while the angle between the incident and zeroth order beam is $\approx 68^o$. If a grating with the same groove density is used in the 399 nm setup, the angle between the incident beam and grating normal becomes $\approx 14^o$ and the angle between the incident and zeroth order beam is $\approx 28^o$. At this angle the beam will be obstructed by the laser mount. To achieve an angle of $\approx 68^o$ between the incident and zeroth order beam a grating with a groove density of ≈ 2800 grooves per mm is required. The efficiency of the first order reflection describes the percentage of light in the first order beam. Efficiencies are obtained from product specification sheets, and are often specified for different orientations of the laser polarisation: 1) perpendicular, or 'S' (from the German word senkrecht meaning 'vertical' or 'normal'), or transverse magnetic (TM), and 2) parallel, or 'P', or transverse electric (TE). Perpendicular polarisation describes

orientation of the electric field perpendicular to the incident-reflection plane, while parallel polarisation describes orientation of the electric field parallel to the plane formed by the incident and reflected beams, as illustrated in figure 3.5.
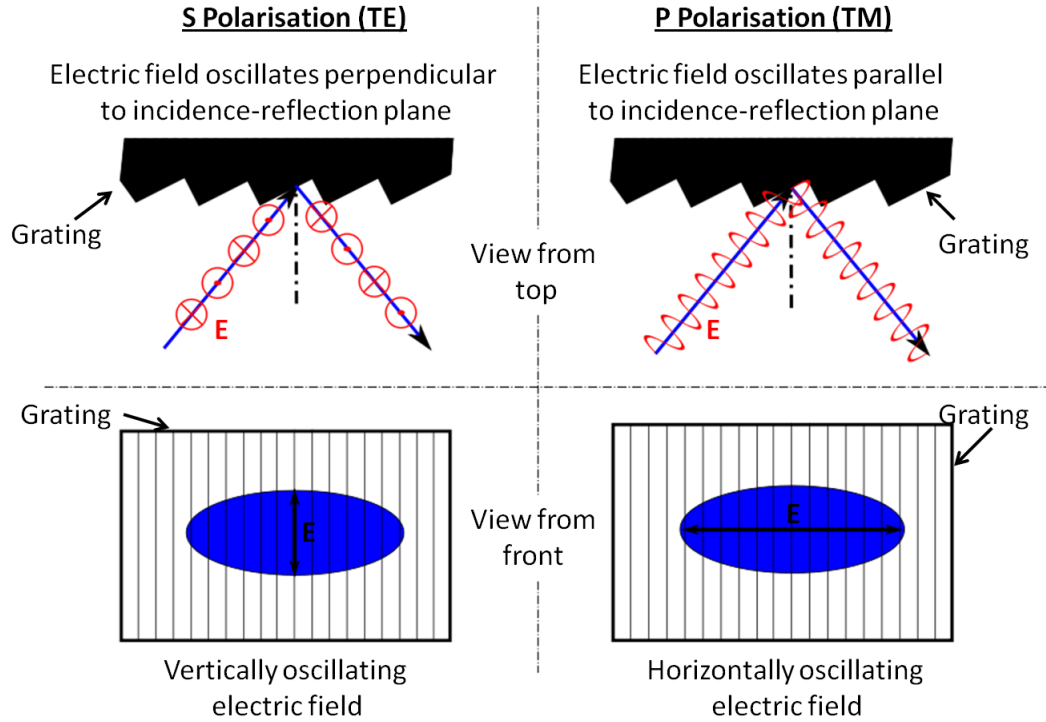
Figure 3.5: S and P polarisation. S (or transverse electric, TE), the electric field oscillates perpendicular to the plane formed by the incident and reflected beams. P (or transverse magnetic, TM), the electric field oscillations parallel to the incidence-reflection plane.

It is preferable for the beam to cover the maximum number of grooves, to improve the dispersion of the diffraction. Beams are usually elliptical in profile and normally polarised with the electric field oscillating perpendicular to the long axis. When selecting a grating the S (or TM) polarisation specification is therefore usually considered.

Thermo-Electric Coolers

Thermo-electric coolers (TEC's) consist of a two dimensional array of alternately doped semi-conductor pillars, as illustrated in figure 3.6. Applying a DC current through the pillars causes the charge carriers to move in the same direction, transferring heat with their motion. Depending upon the polarity of the applied DC current, the TEC acts as either a heating or cooling element.
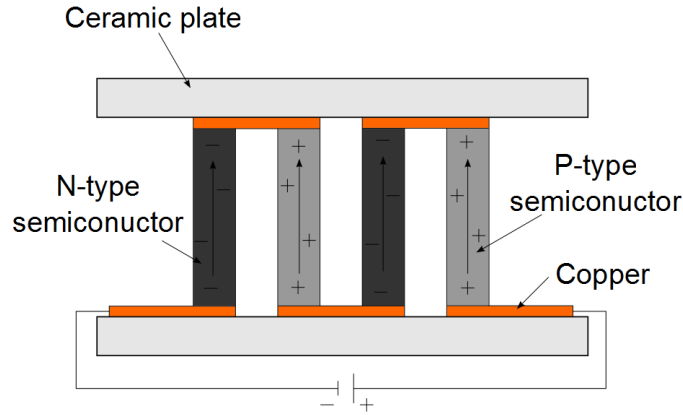
Figure 3.6: Thermo electric cooler consisting of a two dimensional array of alternately doped semiconductor pillars. Applying a current through the pillars moves charge carriers towards the same ceramic plate, transporting heat energy.

3.2.4 ECDL Alignment

Alignment and single mode operation of the ECDL at the desired wavelength is achieved using the following procedure. First the laser diode is rotated so that the long axis of beam profile is orientated horizontally. The aspheric lens is positioned, to collimate the beam, and glued in place, the grating is then aligned to reflect the first order beam back through the lens and into the diode. The laser is driven well above the current threshold, and observing the emitted beam reveals a secondary output spot close to the zeroth order beam. The grating is then coarsely adjusted so the two spots overlap, as shown in figure 3.7. The current of the laser is lowered to just below threshold and, using the two fine pitch screws, the direction of the first order retroflected beam is adjusted. When the first order feedback is improved stimulated emission within the diode is increased above the lasing threshold causing the output power, and hence brightness, of the zeroth order beam to increase. Feedback is optimised by iteratively lowering the current and adjusting the direction of the feedback. This procedure is slightly more challenging for infra-red (IR) lasers. The initial alignment is achieved using IR viewer cards (Thorlabs: IRC3), but these cards require frequent recharging and are poor indictors of spot brightness. Instead an IR CCD camera or a power meter is used for the final optimisation of beam alignment.

When feedback is optimised the driving current is set to $\approx$ 85-90% of the maximum operating specification. The diode temperature is then adjusted until the wavelength is $\lesssim$100 GHz from the desired wavelength. It is important to note that the final wavelength is fundamentally bound by the band gap energy within the laser diode so the ECDL cannot emit a wavelength that is not generated by the laser diode. Care must be taken,
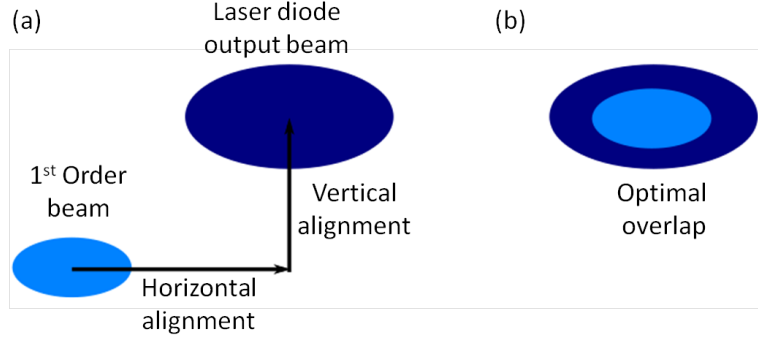
Figure 3.7: Method for aligning the grating feedback in an external cavity. Close to feedback the output resembles (a) where a second spot appears close to the zeroth order beam. (b) the two spots are overlapped.

however, to not cool the ECDL below the dew-point temperature otherwise condensation forms on optical surfaces which severely degrades ECDL performance. The grating angle is readjusted, using the horizontal fine pitch screw in the grating mount, to tune the wavelength to within a few GHz from the desired wavelength. The final wavelength is then achieved by fine tuning the grating angle with the piezo and 'tweaking' the laser diode current.

3.3   Experiment Lasers

To create and cool Yb^+ ions lasers emitting light at 369 nm, 399 nm, 638 nm and 935 nm are required. An additional laser at 780 nm is also used to frequency stabilise the other lasers, the details of which are discussed in section 4.3. The 399 nm, 935 nm, 638 nm and 780 nm lasers are all constructed in house in the Littrow configuration, while the 369 nm light is obtained by frequency doubling light at 739 nm. Presented here are the components used in each laser and the modifications made to enable efficient cooling of Yb^+ ions.

3.3.1   399 nm Photo-Ionisation Laser

Yb^+ ions are created via photoionisation, with the first stage utilising the 398.9 nm $^1S_0$ $\leftrightarrow$ $^1P_1$ transition. This ECDL consists of a 20 mW laser diode (Sanyo: DL-4146-301S), an aspheric lens with focal length f = 4.6 mm and NA = 0.53 (Thorlabs: A390TM-A), and a diffraction grating with 2400 grooves per mm and a first order efficiency of 58% (Thorlabs: GH13-24V). At the time of construction laser diodes at 399 nm were very rare. They previously existed as faulty off-cuts from 405 nm diode wafers, but as the knowledge and skill for making 405 nm diodes improved the availability of 399 nm

lasers decreased. It was possible to obtain 399 nm laser diodes that were longitudinally multimode, but fortunately the 58% grating feedback provided sufficient optical intensity to dominate the other ECDL modes and achieve single mode operation. The single mode performance had its limitations, and the ECDL was only able to produce 4 mW, $\approx 50\%$ of the expected achievable power, before unwanted longitudinal modes effected the laser diode performance.

3.3.2 935 nm Rempump Laser

The $^2D_{5/2} \leftrightarrow ^3D[3/2]_{1/2}$ repump transition is excited using light at 935.2 nm. This ECDL is constructed from a 100 mW laser diode (Roithner: RLT940-100GS), aspheric lens with focal length f = 3.1 mm and NA = 0.68 (Thorlabs: C330TM-B), and a diffraction grating with 1200 grooves per mm and 65% first order efficiency (Thorlabs: GR13-1210). Without operating the laser at maximum performance, 20 mW in the zeroth order beam was easily achievable, which is sufficient for the experiments discussed in this thesis.

3.07 GHz Sidebands

Cooling and manipulation of ^{171}Yb$^+$ however requires both the $^2D_{3/2}|F = 1\rangle \leftrightarrow ^3D[3/2]_{1/2}$ $|F = 0\rangle$ and $^2D_{3/2}|F = 2\rangle \leftrightarrow ^3D[3/2]_{1/2}|F = 1\rangle$ transitions to be driven. While a second ECDL could be used to access the second transition a cheaper alternative is to modulate the laser diode to generate frequency sidebands. The generation of sidebands is explained in detail appendix D, and shows that modulating the laser diode driving current modulates the refractive index of the path length within the cavity and also the wavelength supported within the cavity. The emitted beam then contains components at the carrier frequency, ω, and two extra frequencies at $\omega + \omega_m$ and $\omega - \omega_m$, where ω_m is the modulation frequency. Modulating the diode at 3.07 GHz allows the carrier to drive the $^2D_{3/2}|F = 1\rangle \leftrightarrow ^3D[3/2]_{1/2}|F = 0\rangle$ transition while the $+1^{st}$ order sideband can excite the $^2D_{3/2}|F = 2\rangle \leftrightarrow ^3D[3/2]_{1/2}|F = 1\rangle$ transition. Turning the sidebands on/off provides a means of state preparation and state detection.

In the experiment the modulation signal is produced by a Systron Donner 1710B-S1087 signal generator, and is combined with the DC current using a bias-t (Minicircuits: ZFBT-4R2G+). The general electrical schematic of a bias-t is shown in figure 3.8. The DC signal passes though an inductor (which blocks rf signals) and the AC signal passes though a capacitor (which blocks DC signals). The output of the bias-t is therefore the sum of the DC and AC signals. The output signal of the bias-t is transferred to the laser diode using
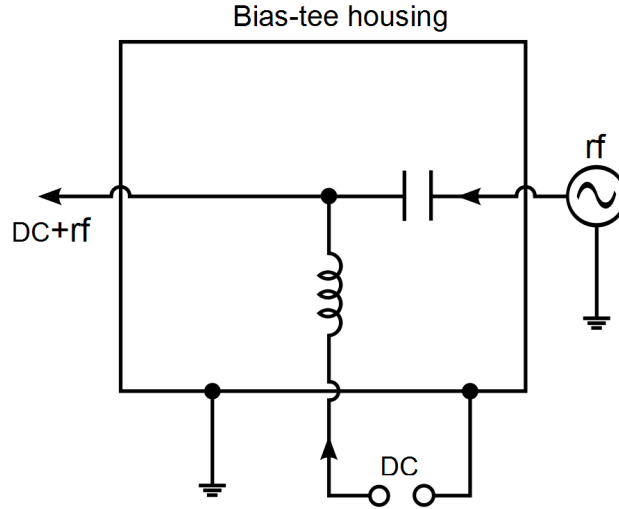
Figure 3.8: Electrical schematic of a bias-t. DC passes through an inductor while the rf input passes through a capacitor. The output consists of both the rf and DC signals.

RG58 co-axial cable to minimise impedance mismatch. While the impedance mismatch between the cable and diode is expected to be significant sufficient sideband amplitudes are obtained using small modulation signals. Sending 18 dBm to the diode (before reflections) generates the 3.07 GHz sidebands shown in figure 3.9, where the spectral components of the 935 nm laser is measured using a scanning Fabry-Pérot cavity with a free spectral range of 750(10) MHz and finesse of 134(5). The sidebands are approximately ≈5% the height of the carrier and although appear at only 70(5) MHz from the carrier correspond to carrier peaks four free spectral ranges away.

Figure 3.9: Spectrum of the 935 nm beam. The sideband peaks with an apparent frequency of 70 MHz are the 3.07 GHz sidebands corresponding to a carrier peak 4 free spectral ranges away.

It was shown by Myatt *et al.* [99] that sideband amplitudes can be enhanced if the modulation frequency is a multiple of the free spectral range of the external cavity. In this situation the modulation frequency is supported by, and resonates within, the cavity. For a littrow configured ECDL the free spectral range is considered to be FSR $\approx c/2L$, where c is the speed of light, and L is the distance between the rear facet of the laser diode and the grating. The factor 2 occurs due to light propagating the cavity length twice. For 3.07 GHz sidebands to resonate an external cavity length of $L \approx 49$ mm is required, however the laser cavity length is only $L \approx 25$ mm. Fortunately Myatt *et al.* indicate that sideband amplitude is also dependent upon modulation power. It is therefore believed that the power of the modulating signal is, to some extent, compensating for the non-resonant cavity length.

3.3.3   638 nm Repumper

The other repump ECDL, to excite the $^2F_{7/2} \leftrightarrow {}^1D[5/2]_{5/2}$ transition, operates at 638.6 nm. This ECDL comprises of a 40 mW laser diode (Sanyo: DL-6148-030), an aspheric lens (Thorlabs: A390TM-B), and a diffraction grating with 2400 groves per mm and >80% first order efficiency (Thorlabs: GH13-24V), and emits 7 mW of power.

Frequency Scanning

The 638 nm ECDL is also modified to excite the $^2F_{7/2}|F = 4\rangle \leftrightarrow {}^1D[5/2]_{5/2}|F = 3\rangle$ and $^2F_{7/2}|F = 3\rangle \leftrightarrow {}^1D[5/2]_{5/2}|F = 2\rangle$ transitions in ^{171}Yb$^+$. The two transitions occur at 638.610nm and 638.616nm, but since exact frequencies for these transitions are unknown frequency sidebands would be an unsuitable approach to accessing the transitions. Instead the laser is scanned between the two transitions, with a separation of $\approx$4 GHz. In its original state the ECDL does not have mode hop free tuning range of 4 GHz, but by scanning the laser diode current and piezo actuator (hence cavity length and grating angle) simultaneously common mode tracking (and the mode hop free tuning range) is increased. In the actual setup the ECDL wavelength is more sensitive to the driving current than the grating angle so a variable potential divider is used to regulate the amplitude of the current modulation to that of the grating modulation. Scanning of the laser between the two transition wavelengths is shown in figure 3.10, however this is not the limit of the scan and in fact a mode hop free tuning range of >20 GHz is possible. Since population of the $^2F_{7/2}$ state is expected to occur only a few times an hour so a scan rate of 0.5 Hz is deemed sufficient to depopulate the state.
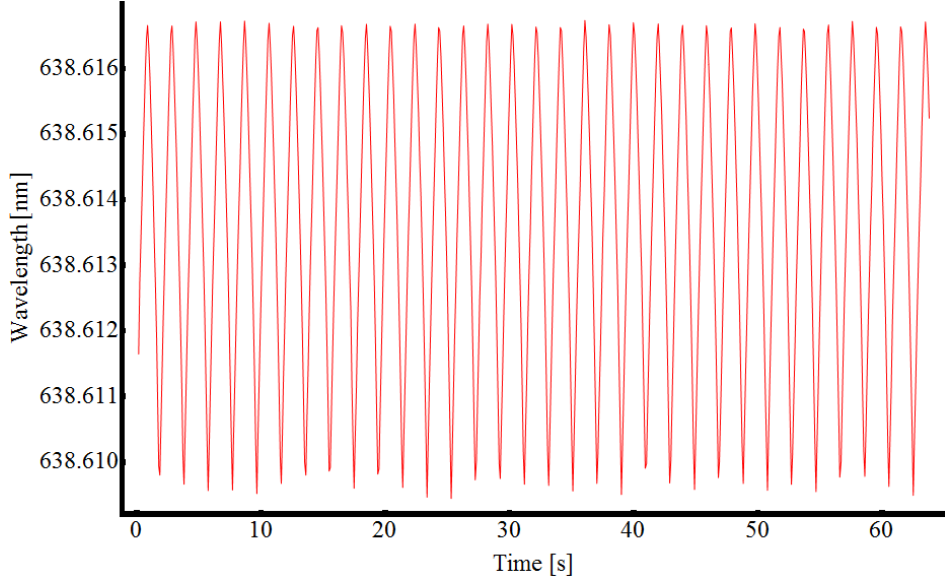
Figure 3.10: Frequency scan of the 638 nm laser. Changing the grating angle and diode current simultaneously enable the wavelength to be scanned over the range 638.610 nm and 638.616 nm, required to excite the $^2F_{7/2} \leftrightarrow {}^1D[5/2]_{5/2}$ transitions.

3.3.4 780 nm Reference Laser

The 780 nm ECDL, used for stabilising the other lasers, is constructed from a 80 mW laser diode (Thorlabs: GH0781JA2C), an aspheric lens (Thorlabs: C230TM-B), and a diffraction grating with 1800 grooves per mm and $\approx 65\%$ first order efficiency (Thorlabs: GR13-1850), and emits 30 mW.

3.3.5 369 nm Doppler Cooling Laser

The laser system used to generate the Doppler cooling light is a commercial frequency doubled system (Toptica Photonics: TA-SHG 36), converting 739 nm light to 369 nm light. In its original configuration the system is suitable for cooling only the even Yb$^+$ isotopes, but with the modifications presented the system can generate the 14.7 GHz and 2.1 GHz frequency sidebands required to cool and state prepare ^{171}Yb$^+$ respectively (discussed in section 2.2.3). A schematic of the modified laser system is illustrated in figure 3.11. The 739 nm light is generated using an external cavity diode laser configured in the Littrow configuration, which can be current modulated at 1.05 GHz (equipment not shown). After passing through an optical isolator (LINOS: FI-760-TV), the beam can be modulated at 7.37 GHz using a bulk phase electro optic modulator (EOM, New Focus: 4851). As a note the beam is only modulated at one of these frequencies, never both at the same time. The modulated beam is then amplified with a tapered amplifier (TA) and passed through another isolator (LINOS: FI-760-TV). En-route to the doubling
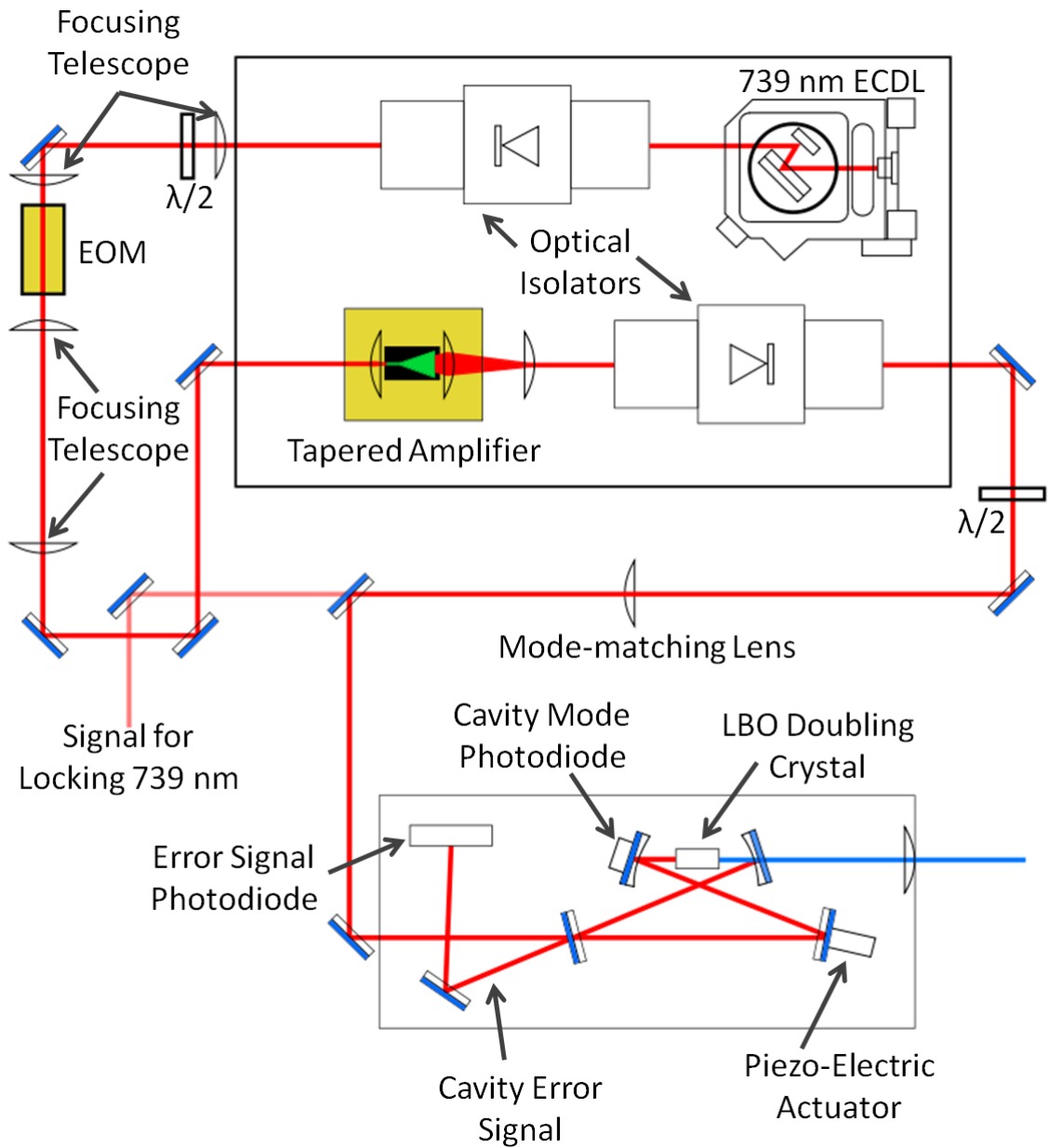
Figure 3.11: Layout of the frequency doubling system used to generate 369 nm light (Toptica Photonics TA-SHG). 739 nm light is produced by a Littrow configured external cavity diode laser, and can be current modulated at 1.05 GHz. An electro optic modulator (EOM) is used to generate 7.37 GHz sidebands on the 739 nm beam and the power of the modulated beam is increased using a tapered amplifier. Inside the cavity, with a free spectral range of 1.05 GHz, the high power modulated 739 nm beam undergoes frequency doubling to produce a 369 nm beam with $\pm$ 2.1 GHz or $\pm$ 14.7 GHz frequency sidebands.

cavity a portion of the beam is picked off for locking and wavelength control, the details of which are described in section 4.3, and the remainder of the beam coupled into the doubling cavity. The length of the doubling cavity is configured to enable all desired spectral components to resonate and undergo second harmonic generation (SHG). With a free spectral range of 1.05 GHz, a subharmonic of the carrier and sideband frequencies, the modulated 739 nm beam is converted into a 369 nm beam with either $\pm$ 14.7 GHz sidebands or $\pm$ 2.1 GHz frequency sidebands.

7.37 GHz Sideband Generation

Sideband generation using an EOM is similar in principle to current modulation and is described in appendix D. EOM's contain a crystal (in this case magnesium-oxide-doped lithium niobate, MgO:LiNbO3) with a voltage dependent refractive index. Exposing the crystal to a sinusoidally varying voltage modulates the refractive index, hence optical path length, within the crystal. The periodic change in optical path length induces a periodic phase shift of the beam passing through it, generating the extra frequency components in the beam.
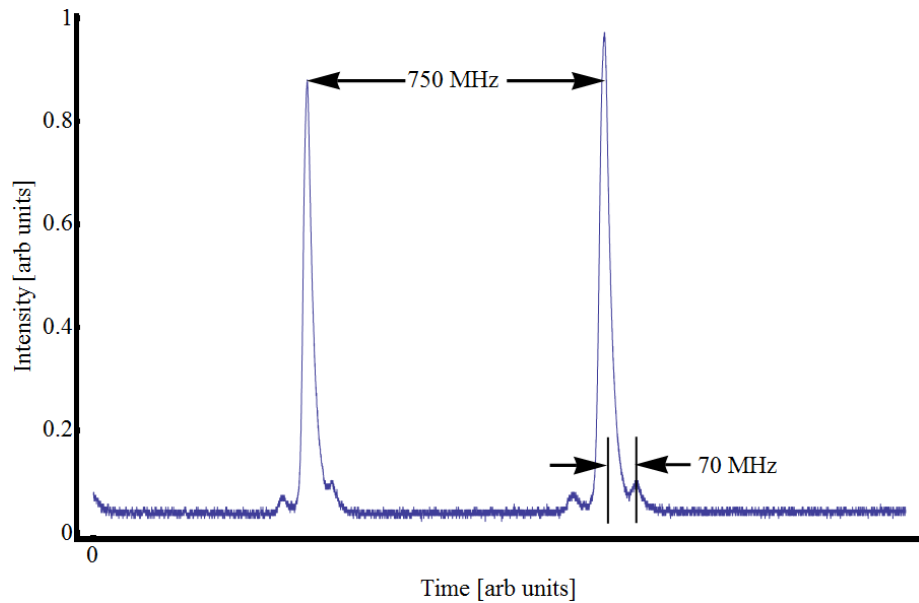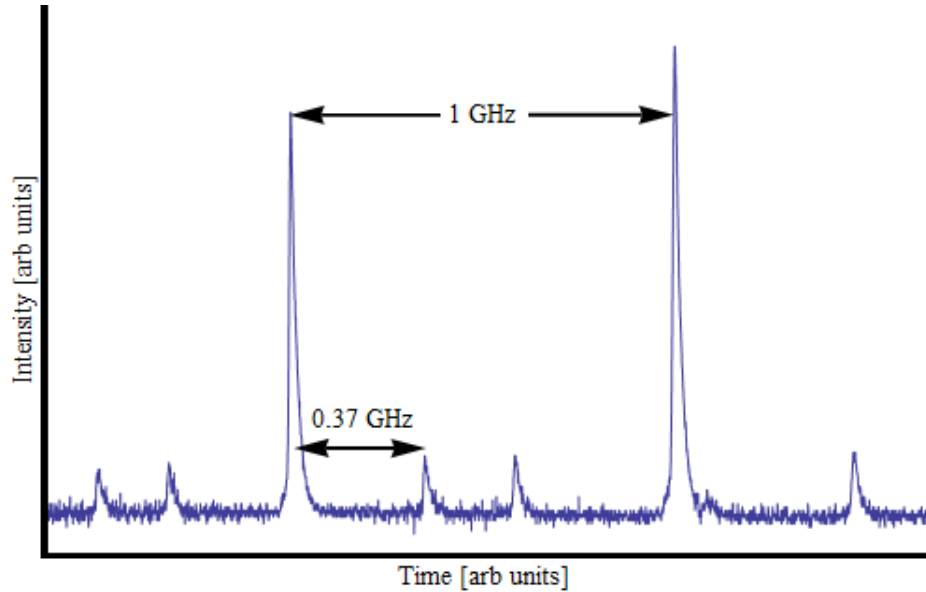

Figure 3.12: Spectrum of the modulated 739 nm beam. The sideband peaks with an apparent frequency of 370 MHz are the 7.37 GHz sidebands corresponding to a carrier peak 7 free spectral ranges away.

In the setup a HP 8684B signal generator provides the 7.37 GHz modulation signal and an amplifier (Advanced Microwave Inc: PA2503-3) increases the drive power to 31 dBm. A pair of lenses ($f_1 = 200$ mm, $f_2 = 50$ mm, with magnification of $M = 1/4$) produce a collimated beam of 0.5 mm through the EOM. Fine tuning of the beam path through the

EOM is achieved using a four tilt alignment platform (New Focus: 9071-M). A half-wave plate, positioned before the EOM, is used to align the beam polarisation parallel to the crystal's electro-optic axis. If not properly aligned the EOM will impose a polarisation rotation resulting in lower sidebands and reducing the output from the tapered amplifier. The resulting sidebands, measured using a scanning confocal fabry perot cavity with free spectral range of 1 GHz, are shown in figure 3.12. The sidebands can be seen to be 5% the height of the carrier and although appearing at 0.37 GHz actually correspond to a carrier peaks 7 free spectral ranges away.

Tapered Amplifier

Tapered amplifiers, similar to laser diodes, are semiconductor chips that provide coherent photons via electron decay across a p-n junction. The TA used in the system, illustrated in figure 3.13, has a single mode input channel which tapers to a larger output. The single mode input channel acts as a spatial mode filter, while the angle of the taper is matched to the diffraction angle of the 739 nm light to maximise the amplification of light passing through it. Both facets of the TA are anti-reflection coated to prevent the TA from acting as a cavity, avoiding optical build up within the chip and the introduction of unwanted frequencies onto the beam spectrum. Light propagating in the reverse direction will damage the chip so an isolator is positioned directly after the TA to protect against unwanted back reflections.
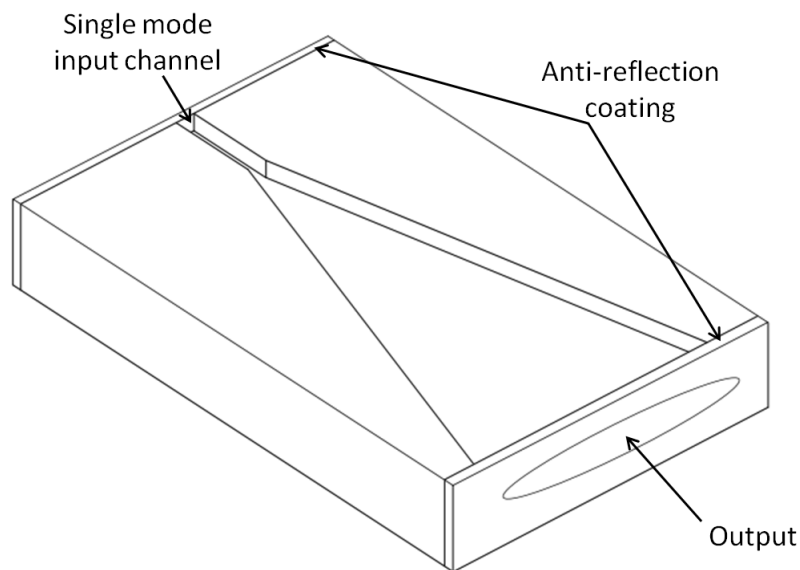
Figure 3.13: Illustration of a tapered amplifier chip, with a single mode input waveguide and and tapered output. The end facets are anti reflection coated to avoid unwanted build up in the reverse direction and generation of unwanted frequencies in the beam.

A lens positioned in front of the TA focuses the beam into the single mode channel. Maximum output power from the TA could not be achieved when using the 0.5 mm beam from the EOM so a telescope, with magnification $M = 4$, is positioned between the EOM and TA. This telescope returns the beam to its original diameter and increases the output from the TA to 420 mW (measured after the isolator). The efficiency of the amplification also depends upon the polarisation of the injected beam with respect to the polarisation of the light generated by the TA. Fortunately this polarisation is the same polarisation required by the EOM, removing the need for a second half-wave waveplate.

Frequency Doubling Cavity

Inside the doubling cavity second harmonic generation (SHG) is achieved. Here two photons with frequency ω are destroyed and, in the same quantum mechanical process, a single photon with frequency 2ω is created. Using a biaxial crystal, in this case Lithium Triborate (LBO), the modulated 739 nm beam undergoes SHG to produce 369 nm light with the desired frequency sidebands.
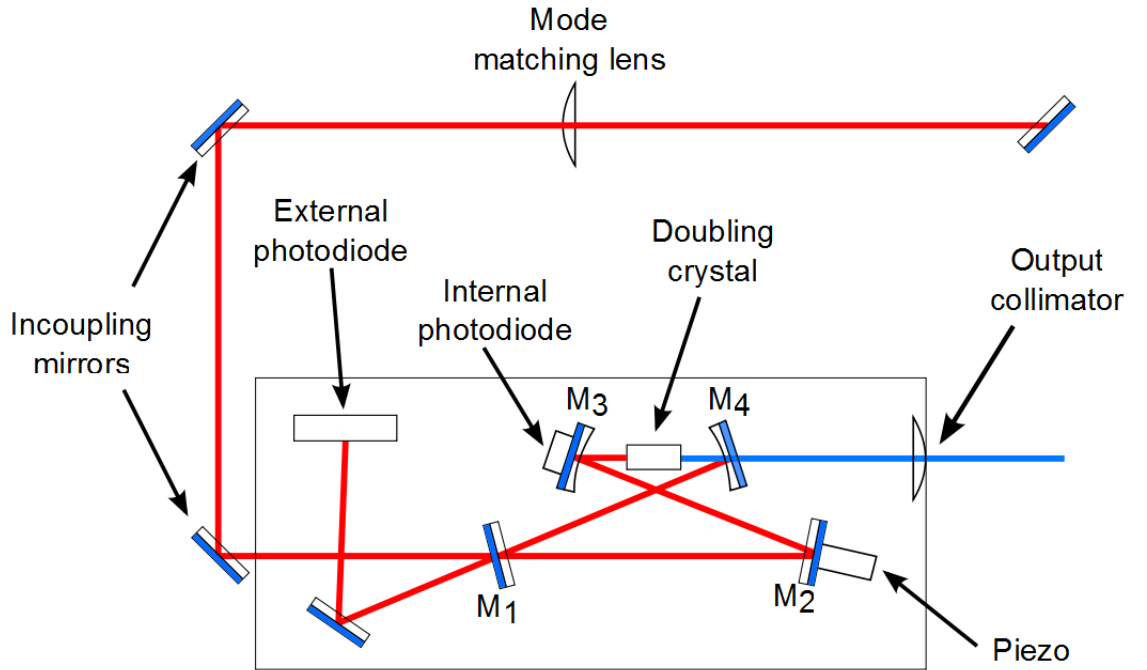
Figure 3.14: Schematic of the doubling cavity.

The crystal is positioned inside a bow-tie cavity, as shown in figure 3.14, where the cavity is used for optical build-up of the 739 nm light to increase the power of the resulting 369 nm beam. The cavity consists of two plane mirrors (M_1 and M_2) and two concave mirrors (M_3 and M_4), where the concave mirrors focus the beam through the crystal and collimate it afterwards. Mirror M_1, the in-coupling mirror, is partially transmissive. Mirror M_2 is

mounted on a piezo to provide adjustment of the cavity length. A photodiode (internal photodiode) is mounted on the rear of mirror M_3 to measure the laser power within the cavity. Finally mirror M_4, the out-coupling mirror, is coated to reflect 739 nm light and transmit 369 nm light. A lens positioned after mirror M_4 collimates the 369 nm output beam. A photodiode positioned outside of the cavity (external photodiode) measures the reflection from mirror M_1 and generates a signal used for stabilising the laser and the cavity.

To initially align the cavity the beam is directed through the entrance aperture of the unit and onto the centre of mirror M_2. Mirror M_2 is then adjusted to direct the beam onto the centre of mirror M_3, and M_3 adjusted so the beam pases through the doubling crystal and onto the centre of M_4. Mirror M_4 is adjusted to reflect the beam back to mirror M_1 and superimpose it with the input beam on the surface of mirror M_1. Mirror M_1 is then adjusted so the reflected beam overlaps the incident beam. This final step closes the cavity and if aligned properly blue light is visible after mirror M_4.

It is very unlikely at this stage, however, for the cavity to be optimally aligned. Instead of supporting just the TEM$_{00}$ fundamental mode the cavity will likely be supporting higher order spatial modes. The amplitude of these modes are determined by scanning the cavity length (by applying an oscillating voltage to the piezo behind mirror M_2) and monitoring the signal from the internal photodiode on an oscilloscope. The resulting intensity profile consists of series of narrow peaks, with each peak corresponding to a cavity mode. The regularity of the measured peaks indicates the quality of the beam alignment within the cavity. Two different situations are shown in figure 3.15, with 3.15(a) indicating an unaligned cavity, indicated by the irregular pattern of varying amplitude resonances, and 3.15(b) an aligned cavity where the TEM$_{00}$ modes are predominant, regularly spaced and of similar amplitude.

To improve alignment, hence beam path within the cavity, the mirrors M_1, M_4, or the two external incoupling mirrors are used to maximise the peaks corresponding to the fundamental mode. It is not always obvious which peaks need optimising. A useful trick is to visually observe the physical profile of the blue beam exiting the cavity (using a piece of paper) and adjust a mirror (either M_1, M_4, or the two external incoupling mirrors) until a single mode gaussian profile is visible. The peaks with the greatest amplitude then correspond to the fundamental cavity mode. By iteratively walking the beam path, first using the two in-coupling mirrors and then cavity mirrors M_4 and M_1, the fundamental cavity peaks are maximised. If, however, there are cavity modes that cannot be removed
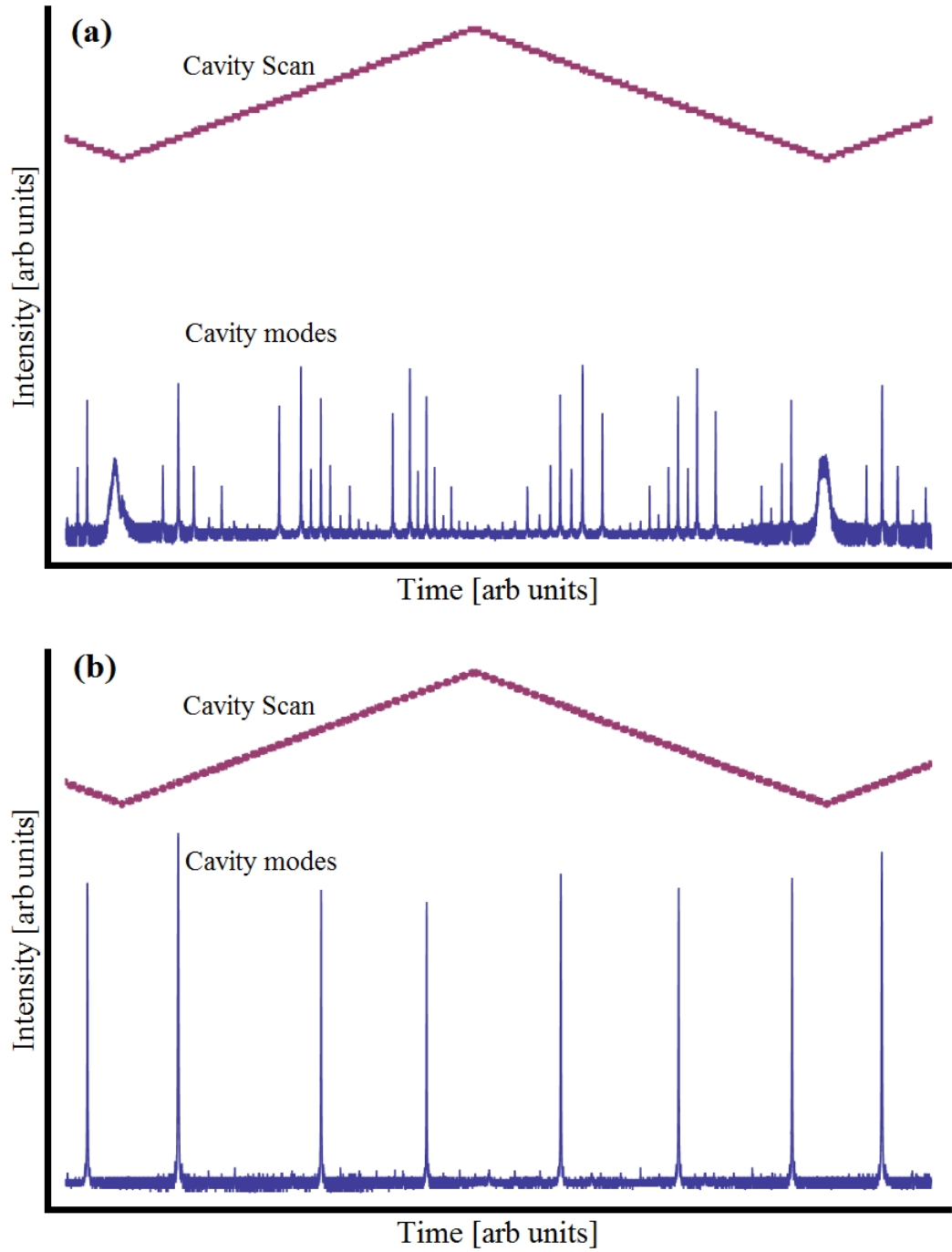
Figure 3.15: Intensity profile of the cavity modes for (a) a misaligned cavity (b) an aligned cavity.

by either horizontal or vertical adjustment then the mode-matching lens is incorrectly placed. Varying the position of the lens and repeating the alignment procedure above removes the unwanted modes.

An aligned cavity, however, does not necessarily relate to maximum 369 nm power. While cavity alignment consolidates the power of the 739 nm into a single spatial mode, the efficiency of SHG is determined by the quality of phase matching between the 739 nm and 369 nm beams. During the process of SHG the 369 nm photons created are polarised 90° with respect to the 739 nm photons. Since LBO is a biaxial crystal, and refractive index is wavelength dependent, the 369 nm and 739 nm photons experience different refractive indices. If the beam does not propagate through the crystal at the correct angle the created 369 nm photons interfere destructively. Adjusting the beam path to the correct angle enables the wavefronts of the 739 nm and 369 nm beams to propagate in phase and the 369 nm photons constructively interfere. However, this can change the alignment of the beam path within the cavity and can reduce the amplitude of the TEM_{00} mode. After adjusting the propagation direction through the crystal the cavity is realigned using the process above. Optimum alignment is achieved with the use of a third photodiode positioned outside the system to measure the the amplitude of the emitted 369 nm beam. While scanning the cavity the signal from this photodiode also consists of a series of peaks, corresponding to the TEM_{00} mode becoming resonant with the cavity length and undergoing SHG. Maximising these peaks optimises alignment of the doubling cavity. It should be noted that 739 nm light is also emitted from the cavity. Since photodiodes are more sensitive to 739 nm light than 369 nm light, measuring both wavelength can result in incorrect alignment. To avoid this a bandpass filter (Semrock; FF01-370/36-25) is used to block the 739 nm light and transmit the 369 nm light.

Stabilising the Laser System

The setup used to stabilise the laser is shown in figure 3.16. The Pound Drever device (PDD) control module provides a 100 MHz signal to current modulate the laser diode. Since current modulation at 1.05 GHz is also required for state preparation a combiner (minicircuits: ZFSC-2-5+) positioned before the bias-t enables the diode to be modulated at both frequencies. When the modulated beam reaches the doubling cavity the 1.05 GHz frequency sidebands, resonant with the cavity free spectral range, are transmitted through the cavity, while the 100 MHz sidebands are reflected away and measured on the external photodiode. The resulting photodiode signal is sent to the PDD module where
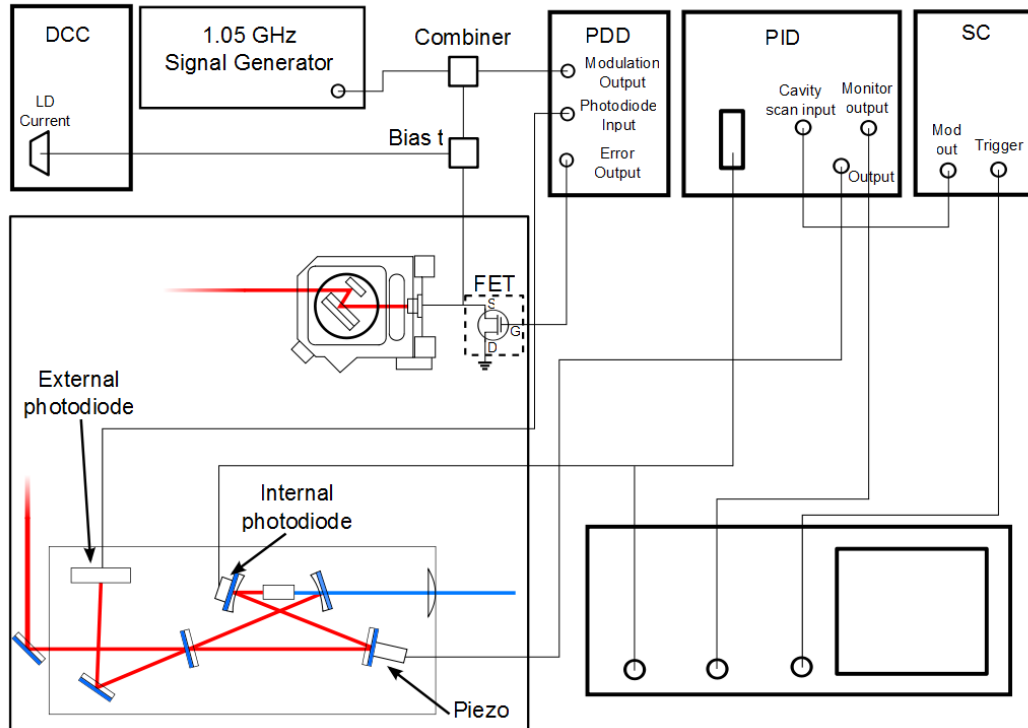
Figure 3.16: Schematic representation of the electronic setup used to stabilise the laser system.

it is mixed with the the original 100 MHz frequency. The mixed signal is then passed through a low pass filter to produce the PDH error signal (also explained in Appendix E). The error signal, retrieved from the 'Error Output' port on the PDD is shown in figure 3.17 (top curve) along with the profile of the frequency dependent intensity within the cavity (bottom curve). The Pound Drever Hall (PDH) error signal can be regarded as the derivative of the photodiode signal, with the centre of the signal (and rapid sign change) corresponding to the top of the intensity peak. Locking to this position on the error signal stabilises the cavity length supporting the maximum optical power.

The PDH error signal is then used to stabilise both the laser wavelength and the doubling cavity length. Wavelength stability is achieved using a field effect transistor (FET) connected in parallel with the laser diode. The error signal, applied to the 'Gate' port, adjusts the conductivity between the 'Source' and the 'Drain' ports, changing the current applied to the laser diode. Cavity stability is achieved by applying a feedback signal, generated from the error signal in the PID module, to the piezo behind mirror M_2. The laser feedback stabilises against fast fluctuations while the slower cavity feedback compensates for thermal fluctuations/drifts during operation.

Before the lock can be activated several conditions must be fulfilled. First the quality and offset of the error signal are analysed. The error signal should appear the same as the one
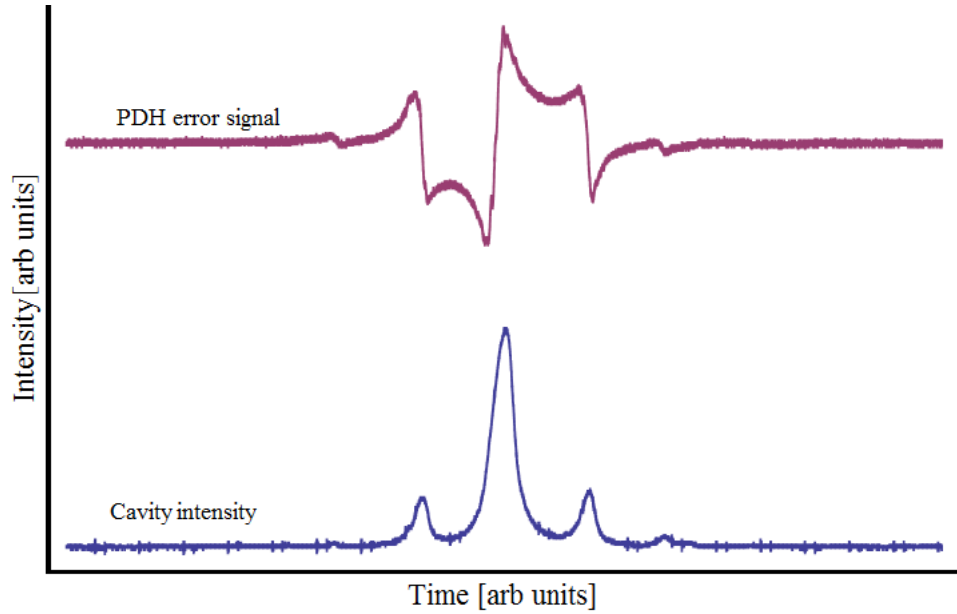
Figure 3.17: Frequency spectrum (bottom), and resulting Pound Drever Hall error signal (top), of the modulated laser diode as the cavity is scanned.

shown in figure 3.17. An incorrect error signal is a result of a phase mismatch between the signal from the external photodiode and the modulation signal. The phase between the two signals is adjusted using the 'phase' control on the PDD module. The offset of the error signal is adjusted to oscillate about ground, which corresponds to locking to the top of the peak. Second the 'minimum intensity' threshold is checked. This is a user defined threshold describing the minimum intensity required by a cavity mode to be used to for locking. This feature is designed to ensure that the cavity will only lock to the TEM_{00} fundamental mode and not higher order modes. To correctly set the minimum intensity both the cavity peaks and minimum intensity are displayed on an oscilloscope. The voltage scale of each channel are matched while the 'ground' of each channel are adjusted to the same voltage offset. When comparing the two signals only the peaks corresponding to the TEM_{00} mode should be above the minimum intensity. If not, either the cavity needs realigning or the minimum intensity threshold needs to re-adjusted.

When the checks are done the cavity scan is turned off and the PID lock engaged. The PID is set by first increasing the I component to initiate a lock and is further increased until just before the signal on the oscilloscope starts oscillating. The P and D components are then increased, again until just before the signal begins to oscillate.

Sidebands for ^{171}Yb$^+$

As explained earlier the 14.7 GHz (2.1 GHz) sidebands required to cool (state prepare) ^{171}Yb$^+$ are generated by frequency summing the 7.37 GHz (1.05 GHz) sidebands generated by the EOM (current modulation). To enable the cavity to support these multiple frequencies the free spectral range of the cavity is tuned to be a common factor of all the frequencies. For the bow-tie cavity FSR = c/L, where c is the speed of light and L the optical path length within the cavity. The carrier and modulation frequencies all have a common factor of 1.05 GHz, so adjusting the cavity length to 0.29 m (FSR = 1.05 GHz) enables all these spectral components to be supported. Since multiple frequencies are entering the cavity frequency summation actually occurs between the the different spectral components.

Using a scanning Fabry Perot cavity, with a free spectral range of 500(10) MHz, the spectrum of the modulated 369 nm is analysed. Current modulating the diode at 1.05 GHz generates the spectral profile shown in figure 3.18. It can be seen that the 369 nm beam is equipped with ±1.05 GHz and ±2.1 GHz sidebands, with the 2.1 GHz sidebands of ≈5% the height of the carrier beam.
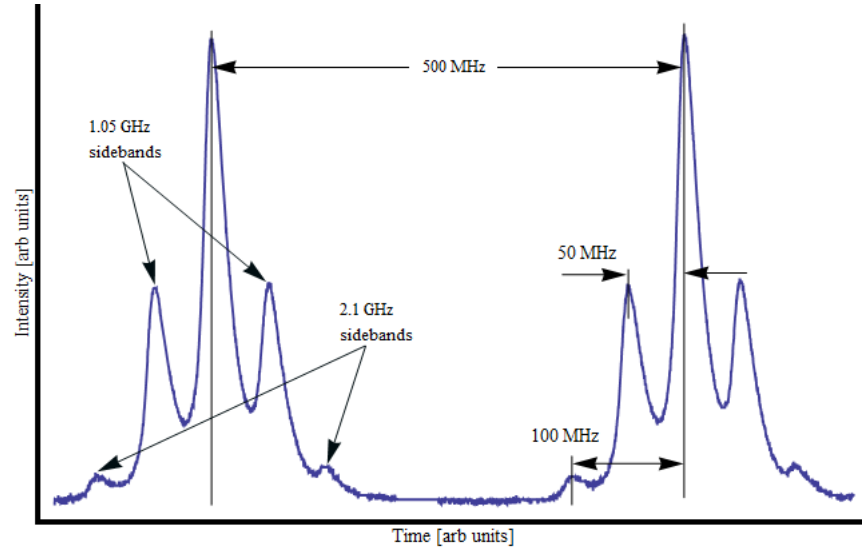
Figure 3.18: Spectrum of the 369 nm beam used to excite the ^{2}S$_{1/2}$ ↔ ^{2}P$_{1/2}$ transitions. The sideband peaks with an apparent frequency of 50 (100) MHz are actually the 1.05 (2.1) GHz sidebands corresponding to a carrier peak 2 (4) free spectral ranges away. The +2.1 GHz sidebands are used for state preparation.

Similarly when the 739 nm beam is modulated at 7.37 GHz frequency sidebands at ±7.37 GHz and ±14.7 GHz are generated on the 369 nm beam. Damaged cavity mirrors meant the ±14.7 GHz sidebands could not be measured the successful trapping and cooling of ^{171}Yb$^+$, discussed in chapter 4, demonstrates their presence.

Chapter 4

Experiment Setup

"Please excuse the crudity of this model, I didn't have time to build it to

scale or to paint it."

-Emmit Brown, *Back to the future.*

Ion trap experiments incorporate a multitude of different components: a structure to generate the confining potential, a vacuum system to isolate the ion from unwanted external influences and preserve the quantum nature of any experiments, narrow linewidth frequency stabilised laser radiation to efficiently manipulate the ion, and finally a means of measuring the state of the ion without interacting with it.

This chapter describes the design, construction and amalgamation of the these various experimental components. A versatile ultra high vacuum system and compatible macroscopic linear ion trap. The schemes implemented to stabilise the laser systems (described in chapter 3) and the system used to collect the fluorescence from trapped ions. The procedure used to trap an ion is described and finally the computer system controlling the experiment.

4.1   Vacuum System

Since interactions with other particles can destroy the quantum state of an ion, or worse expel it from the trap altogether, trapped ion experiments are required to be performed in an ultra high vacuum environment (UHV, $<10^{-9}$ mbar). Additionally a vacuum system capable of testing of complex surface and multilayer trap geometries was desired. The resulting vacuum system used in the experiments is shown in figure 4.1. The system is constructed using mostly off-the-shelf standard stainless steel ConFlat (CF) components,
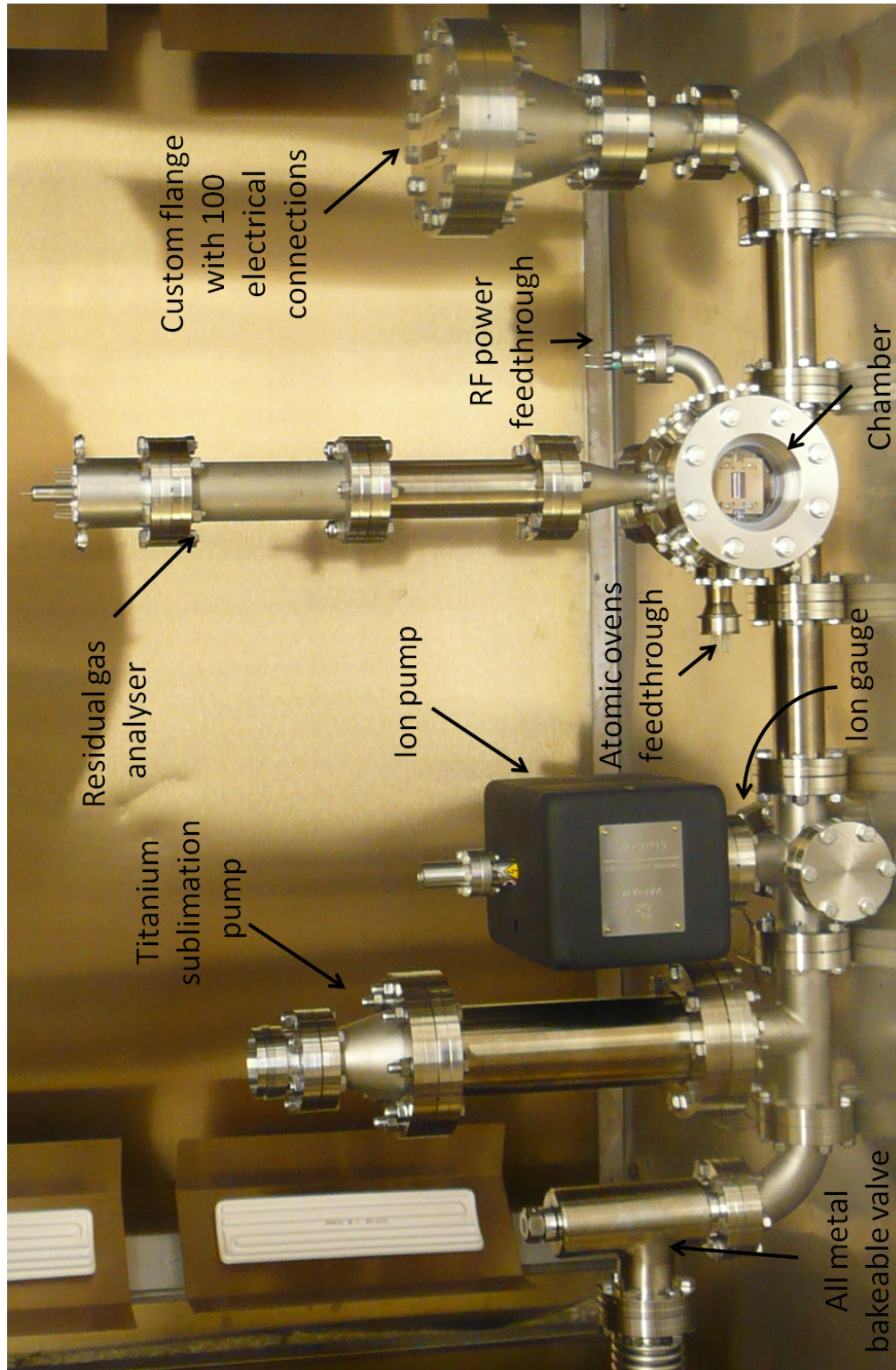
Figure 4.1: Ultra high vacuum system used in the experiment.

with copper gaskets providing the seals between components. The use of an all metal system is necessary because baking the system is required to obtain an UHV, the process of which is discussed in section 4.1.3. The chamber, described in detail the next subsection, is the testing region for the different ion traps. A power feedthrough and custom flange with two 50-pin sub-D connectors (K.J.Lesker: IFDG501056A) providing external connections to the rf and static voltage electrodes. A custom T-piece (Kurt J. Lesker: SUS090307RHLW) then positions the height of the chamber (and thus the trap centres) to the same height as the laser beams and imaging system. The system is operated at $<10^{-11}$ mbar and maintained at this pressure using an ion pump (Varian StarCell: 9191145) and titanium sublimation pump (TSP, Varian: 9160050). An UHV-24p ion gauge (Varian: 9715015), mounted on the rear flange of the 5-way cross-piece) provides measurement of the pressure within the system, while a residual gas analyser (RGA, ExTorr: XT200M) offers information on the species of any contaminants.

4.1.1 Experiment Chamber Assembly

The chamber is constructed from a hemisphere and octagon (Kimball Physics: MCF450-MH10204/8-A and MCF450-SO20008-C respectively), and is kitted out with a custom mounting bracket, atomic ovens and optical access to allow testing of multilayer and surface traps.

The mounting bracket fitted inside the chamber is shown in figure 4.2. The bracket consists of 90 gold plated receptacles (Mill-Max: 0672-1-15-15-30-27-10-0) sandwiched between two UHV compatible polyether ether ketone (PEEK) plates. The receptacles are arranged to be compatible with 101-pin CPGA chip carriers (Global Chip Material: PGA10047002) allowing for microfabricated traps, mounted onto the chip carriers, to be quickly and easily interchanged. PEEK is a polymer based plastic so prevents shorting between receptacles, and its negligible water absorption and outgassing rates make it suitable for operation in UHV. 88 of the 90 receptacles are connected to the sub-D connectors on the custom flange with Kapton insulated copper wires, enabling static voltages to be applied to respective trap electrodes. The two remaining receptacles are connected to the power feedthrough to enable the application of high rf voltages (>500 V). Kapton, however, was observed to breakdown at these voltages so 1 mm diameter copper wires insulated with ceramic beads are used instead.

The four atomic ovens are mounted inside the chamber and orientated relative to the mounting bracket as shown in figure 4.2. The two rear ovens provide atoms for multilayer
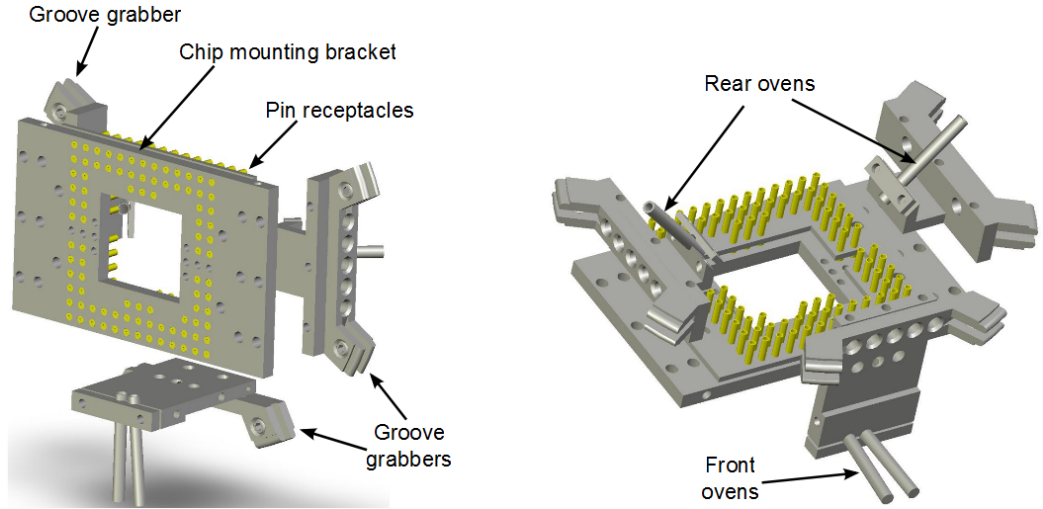
Figure 4.2: (a) Front and (b) rear view of the mounting bracket showing the 100 pin receptacles and the four atomic ovens providing natural Yb and enriched ^{171}Yb for multilayer and surface traps.

traps while the two front ovens provide ytterbium for surface traps. One of each of the front and rear ovens provides natural ytterbium (Goodfellow: 424-562-81) while the other provides enriched ^{171}Yb (Oak Ridge, Tennessee). The ovens are constructed from 20 mm stainless steel hypodermic needle tubing (Small Parts: B000FMUSNM) with an inner and outer diameter of 0.83 mm and 1.07 mm respectively, and one end crimped shut. The crimps are connected to a feedthrough using Kapton insulated wire, and passing a current through the crimps ohmically heats the tubes generating the atomic streams.
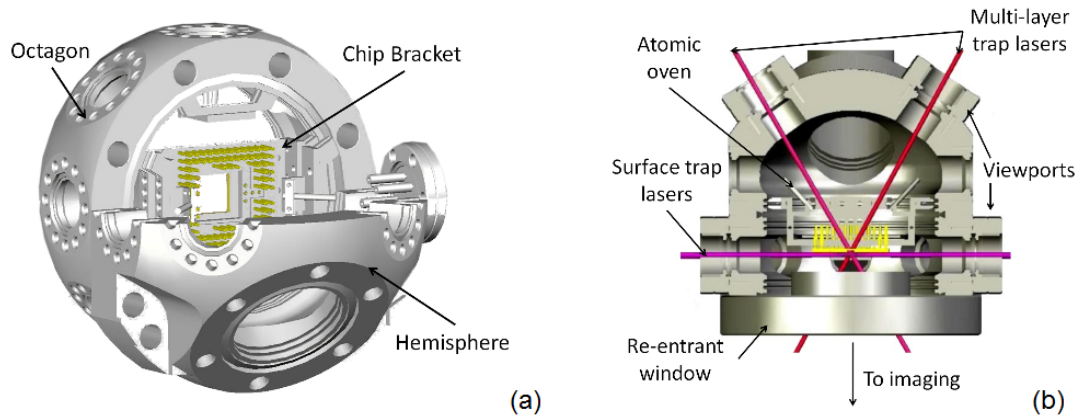
Figure 4.3: Inside view of the chamber illustrating (a) how the mounting bracket is fitted and (b) the laser access for multilayer and surface traps.

The mounting bracket and atomic ovens are attached to the chamber hemisphere using groove grabbers (Kimball Physics: MCF450-GG-CT02-A) as illustrated in figure 4.3. Also shown is the laser access to the traps via conflat mounted (CF) anti reflection coated UV-grade quartz fused silica viewports. Two 1.33" and one 2.75" viewports (Kurt J. Lesker:

VPZL-133Q and VPZL-275Q respectively) mounted on the hemisphere offer laser access to multilayer traps, while seven 1.33" viewports attached to the octagon provide optical access for surface traps. A custom re-entrant window, with recessed glass (Kurt J. Lesker: SUS300407GBR) is positioned on the chamber to enable diffraction limited imaging of ions.

4.1.2   Atomic Source Testing
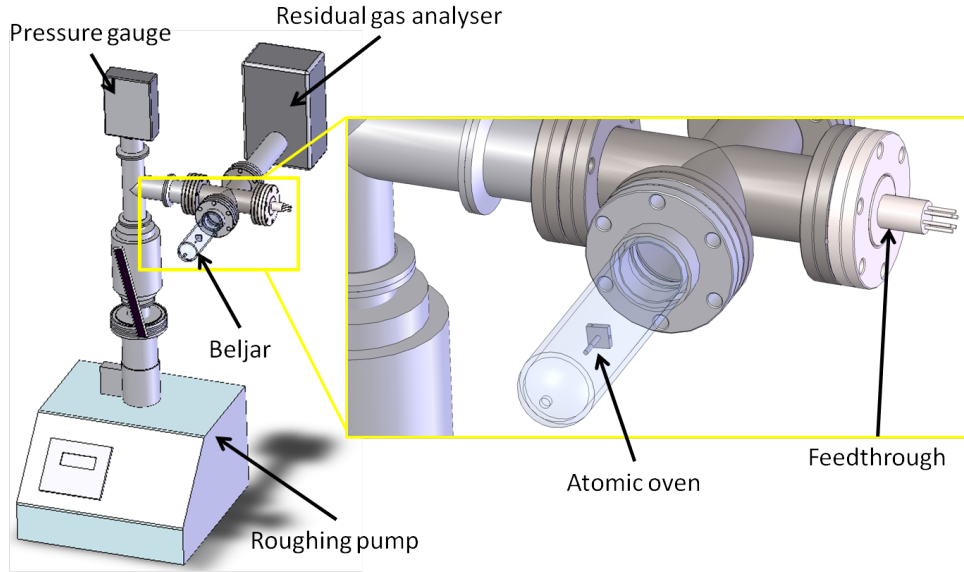
Figure 4.4: Setup used to test the atomic ovens. The magnified image shows the position and orientation of the atomic ovens.

Before operation it is vital to ensure the atomic ovens provide the necessary atomic vapour. Using the setup shown in figure 4.4 each oven is tested and characterised before being installed into the chamber. The ovens are operated under a vacuum of $\approx 10^{-7}$ mbar, achieved using a turbo molecular pump (Pfeiffer: PM S03 525), while a residual gas analyser measures the partial pressures of the vapours emitted from each oven. Since ytterbium sticks to surfaces accurate measurements are obtained by directing the open end of the ovens towards the RGA. Current is applied to the ovens using Kapton insulated wires connected to a 1.33" CF flange 6-pin power electrical feedthough (Kurt J. Lesker: EFT 0265062).

The partial pressures of the main isotopes emitted from the ovens are shown in figure 4.5. The plots on the left (right) correspond to the rear (front) ovens providing ytterbium to multilayer (surface) traps. The plots at the top (bottom) show the partial pressures of the different isotopes from the ovens containing natural (171-enriched) ytterbium. In each plot the solid, dotted, dashed and dot-dashed traces represent the partial pressures of ^{171}Yb,
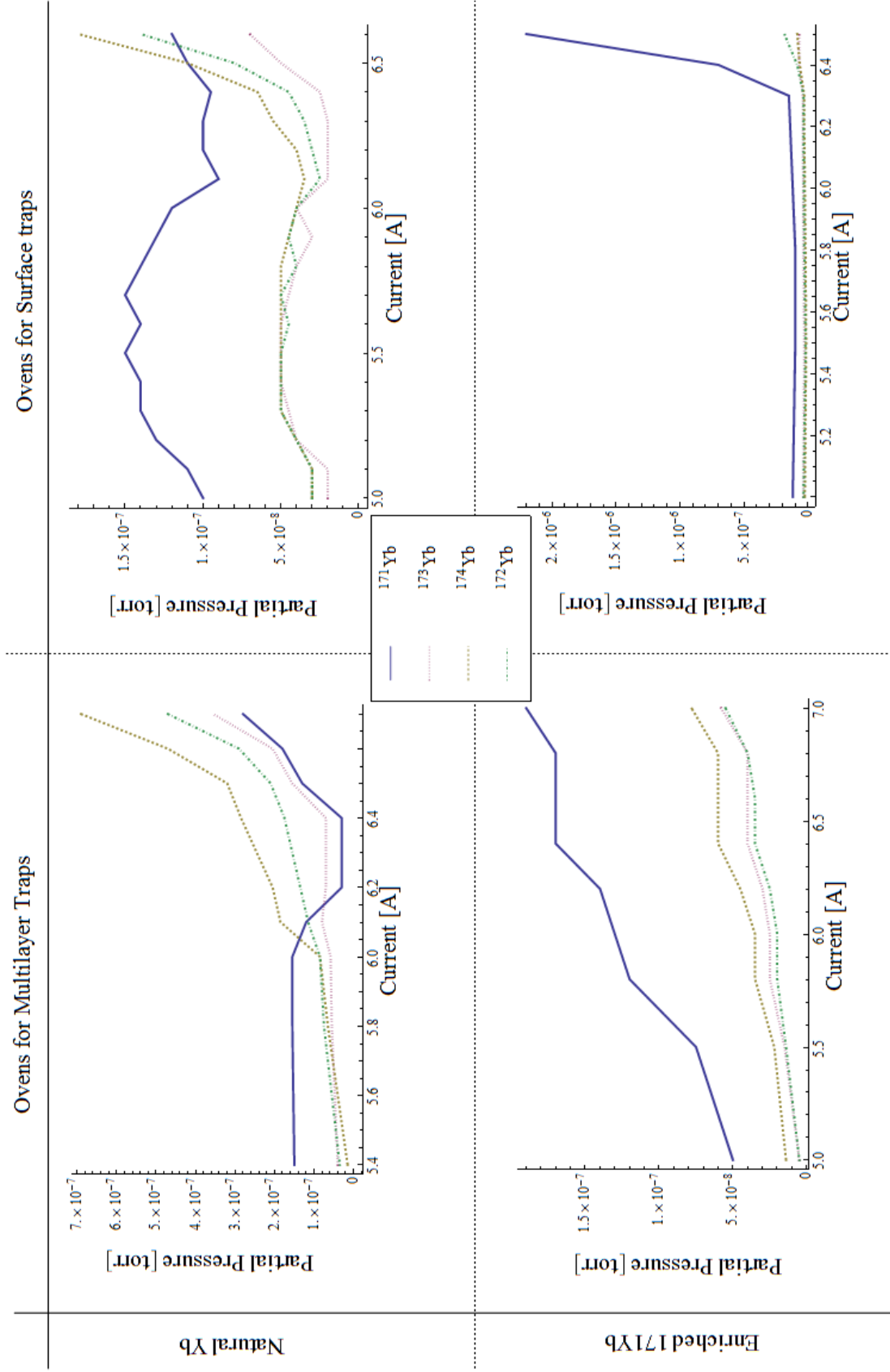
Figure 4.5: Partial pressures of the isotopes ^{171}Yb, ^{172}Yb, ^{173}Yb and ^{174}Yb present in the atomic vapour from the four atomic ovens.

^{172}Yb, ^{173}Yb and ^{174}Yb respectively. A background measurement is taken before each oven is operated, and subtracted from the partial pressure measurements to determine the actual emission from each oven. It can be seen that operating the ovens at $\approx$6.5 A produces a noticeable increase in the atomic vapour in each oven.

4.1.3 Obtaining Ultra High Vacuum

The required ultra high vacuum environment is obtained using the following procedure. First the all-metal components are cleaned with HPLC grade Acetone (Fisher Scientific) in an ultrasonic bath for at least 10 minutes. This removes any residual organic materials from component surfaces. The cleaned parts are then 'pre-baked' in a home-built oven for a week. This pre-baking is performed to create a chromium-oxide layer on the surface of the steel which reduces the rate of outgassing of hydrogen [100]. The all-steel parts are pre-baked at 300 ℃ but due to temperature limitations of seals the viewports are baked at only 200 ℃. Following the pre-bake all the components are re-cleaned in the ultrasonic bath, using the same method as before, and assembled into the vacuum system shown in figure 4.1.

The assembled system is placed inside an oven and connected to a turbo molecular pump (Pfeiffer: PM S03 525) and a 20 ls^{-1} 'external' ion pump (Varian StarCell: 9191145), positioned outside of the oven, using a one metre 2.75" CF flexible hose (Kurt J. Lesker: MH-CF-C36). Initially the vacuum system is pumped down using the turbo molecular pump. When the pressure stabilises to $\approx$1x10^{-6} mbar the electrical components inside the system are degassed. Degassing of the RGA and ion gauge is achieved using a simple in-built command, while the atomic ovens are degassed by passing a current of 5 A through them for a few minutes. The TSP filaments are degassed by running them at 37-42 Amps for 1 minute and then at 35 Amps for 1 hour and, finally, the trap is degassed by increasing the RF voltage to the electrodes. During degassing the pressure is monitored to ensure it does not drastically increase, and when degassing the trap visual inspection is performed to ensure no sparking (shorting) occurs.

After degassing, the oven temperature is ramped up to 200 ℃ at a rate of $\leq$10-15 ℃ per hour. This slow temperature gradient is used to avoid detrimental stress gradients between the viewports and steel components. After the vacuum pressure stabilises ($\approx$1x10^{-6} mbar), the external ion pump is switched on. An hour later an angle valve (Kurt J. Lesker: SA0150MCCF) is closed to isolate the roughing pump. After the pressure once again stabilises the 'internal' ion pump is turned on and a few hours later a bakeable UHV all

metal angle valve (Kurt J. Lesker: VZCR40R) is closed. Baking of the system at 200 ºC then continues until the pressure stabilises. Once stabilised the temperature is ramped down, again at a rate of ≤10-15 ºC per hour. The pressure of the system during the baking procedure is shown in figure 4.6. The solid line indicates the pressure within the system while the dashed line indicates the system temperature. At room temperature the vacuum system is removed from the oven, and the sublimation pump run for one minute every two hours until the desired pressure is reached ($\approx 4 \times 10^{-11}$ mbar).
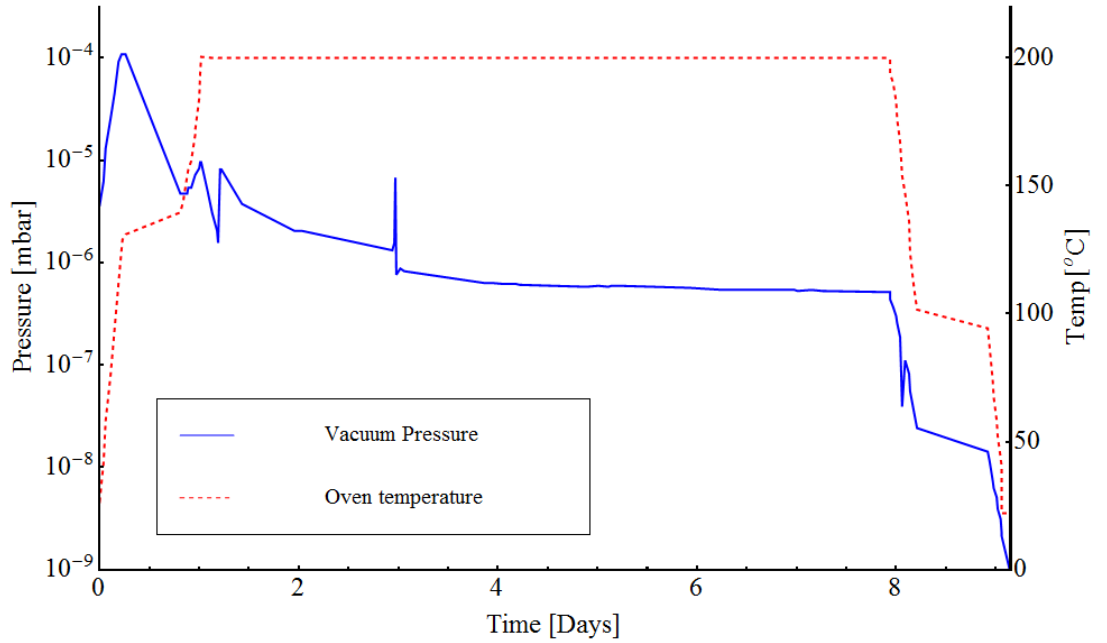
Figure 4.6: Vacuum pressure and oven temperature during bakedown.

4.2   Macroscopic Linear Ion Trap

The macroscopic linear rf-Paul used in this thesis is shown in figure 4.7. To be compatible with the vacuum system it is limited to a footprint of 3 cm × 3 cm and a height of 1 cm. The trap consists of several parts: a base made from UHV compatible PEEK, a stainless steel mount, and gold plated stainless steel electrodes. The PEEK base provides a platform upon which the trap can be mounted while removing the risk of electrical shorting between trap electrodes and to other connections in the vacuum system. Exposure to ultra violet (UV) laser radiation, however, has been shown to result in the discolouring and increased outgassing of PEEK. It is also suspected that the dielectric becomes charged and introduces unwanted fields into the trapping potential. To prevent this a stainless steel mount is used to cover the PEEK, and shield the ion from any potentially charged dielectrics.
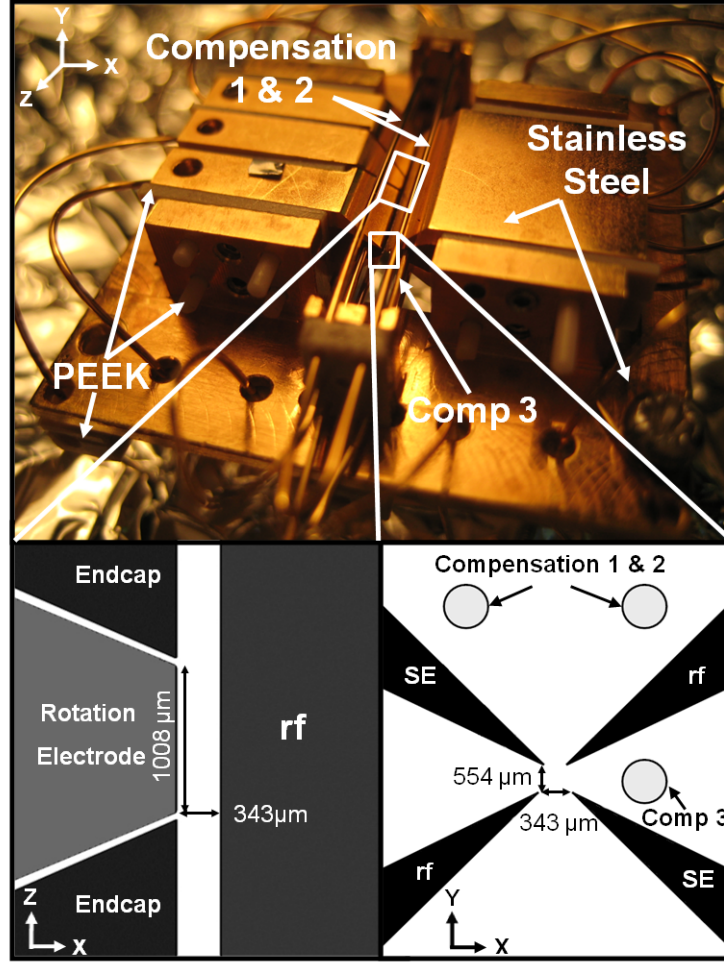
Figure 4.7: Top: Ion trap used in the experiments. Bottom right: Cross-sectional view of the radial plane of the trap, showing the spacings between the radio frequency (rf) electrodes and the static voltage electrodes (SE). Bottom left: View of the trap showing the length of the centre electrode and trapping region.

The stainless steel mount is constructed with 'walls' from which the electrodes are suspended. The electrodes are wire eroded into blades and electroplated with 5 μm of gold. The blade shapes enable smaller ion electrode separations to be achieved whilst still providing a close approximation to an ideal quadrupole trapping potential. The electrodes are separated by 343(14) μm in the x axis and 554(14) μm in the y axis, producing a trap aspect ratio of 1.6, and an ion-electrode separation is 310(10) μm. The rf electrodes span the entire axial length of the trap, while the static voltage electrodes are segmented to provide end cap potentials and rotation of the principal axes. The length of the centre electrode is 1008(14) μm. This electrode arrangement provides for a reduced residual rf ponderomotive potential along the z axis to $< 2\%$ of the radial frequency [101], and allows trapping of long ion chains without appreciable rf micromotion in the axial direction. Three parallel gold plated wires run the length of the trap to provide micromotion

compensation. Compensation electrodes 1 and 2 are electrically connected to result in a compensation along the y-axis only, while compensation electrode 3 acts in the x axis only. Gold plated wires, passing through holes in the mount, connect the trap electrodes to pin receptacles in the mounting bracket.

4.2.1 Application of High RF voltages

To generate the potential required for successful trapping a narrow bandwidth rf voltage is required. Narrow bandwidth ensures the trapping potential does not oscillate at multiple frequencies, causing unwanted complex motion, while high voltages provide suitably deep trapping potentials and secular frequencies on the order of MHz. Impedance mismatch between the voltage source and trap however can result in potentially damaging signal reflections, and also reduce voltage at trap electrodes. To enable signal filtering, as well as impedance match the voltage source and the ion trap, an inductively coupled helical quarter wave resonator is used.

In its most basic form an inductively coupled resonator consists of a single conducting wire inside a conducting can, and an antenna coil positioned at one end of the can. Applying an rf voltage to the antenna coil generates an oscillating magnetic field which in turn induces an rf voltage into the conducting wire. The wavelength at which maximum coupling between the antenna and conducting wire occurs is determined by the length of the wire as $L = \lambda_{\mathrm{res}}/4$, i.e. a quarter of the wavelength. Wavelengths not resonant with the wire length are reflected away, thereby providing signal filtering. The bandwidth of transmitted radiation is expressed as its quality factor 'Q'. The voltage output from a resonator is then expressed as

$$V = \kappa\sqrt{PQ} \tag{4.1}$$

where P is the input RF power, and κ is a geometrical efficiency factor.

Typical frequencies used in ion trap experiments are on the order of 10's MHz, so require impractical wire lengths of several metres. To reduce these to more manageable sizes the wire is wound into a helix, forming a helical quarter wave resonator. The helix geometry, however, introduces additional capacitances and inductances which further affects the resonant frequency. The final resonant frequency (of an unloaded resonator) is therefore determined by the exact dimensions of the coil and the shielding can, the relationship of which are described in detail by Macalpiner [102] and Siverns [103]. When the trap is attached to the resonator however, the additional resistances and capacitances from the connecting cables and trap electrodes again cause the resonant frequency to change.
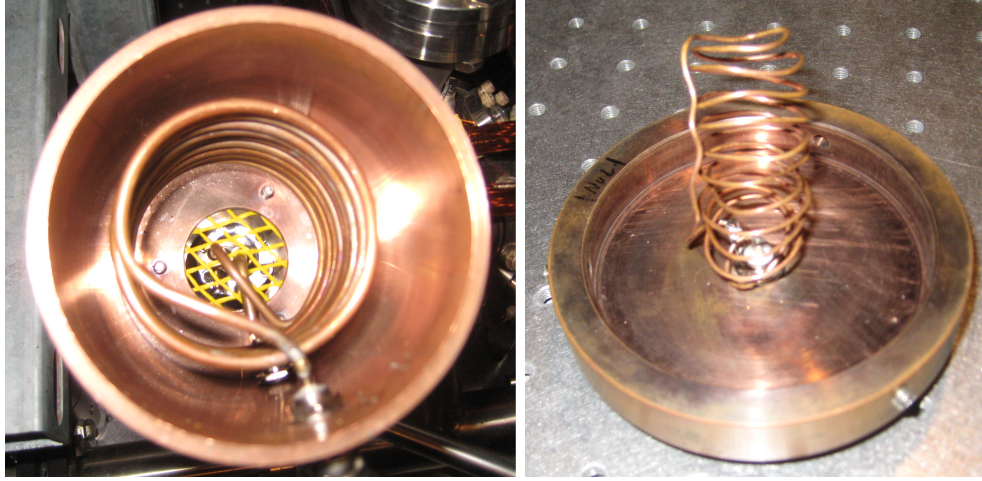
Figure 4.8: Quarter wave helical resonator used in the experiments. The left image shows the helix inside the conducting can, while the right image shows the antenna coil.

The resonator used in the experiments is shown in figure 4.8, and has dimensions detailed in table 4.1. When loaded with the trap it has a quality factor, $Q = 200(20)$, a geometric factor $\kappa = 24(8)$ [103], and a resonant frequency of ≈ 25 MHz. Impedance matching is achieved by adjusting the position of the antenna relative to the coil position. A directional power-meter (Rhode and Schwarz, part number: NAUS 3) is used to measure the power applied to, and reflected from, the resonator. By minimising reflection coupling is maintained at $\geq 95\%$.

Shield Diameter, D [mm]	76(1)
Shield length, B [mm]	103(1)
Coil Diameter, d [mm]	52(3)
Coil Length, b [mm]	63(5)
Coil diameter, d_0 [mm]	3.14(3)
Winding pitch, τ [mm]	6(2)
Number of turns, N	9.50(25)
Resonant frequency with trap load, f_0 [MHz]	21.5(1)
Q with trap load	200(20)

Table 4.1: Resonator design specifications.

Some experiments require a static offset to be applied to the rf signal. For these experiments the filter illustrated in fig 4.9 is attached to the coil. The red dashed section acts as an rf ground preventing the high rf signal from reaching the static voltage supply. The blue dotted section is used to remove an unwanted 10 Hz signal occurring on the offset voltage.
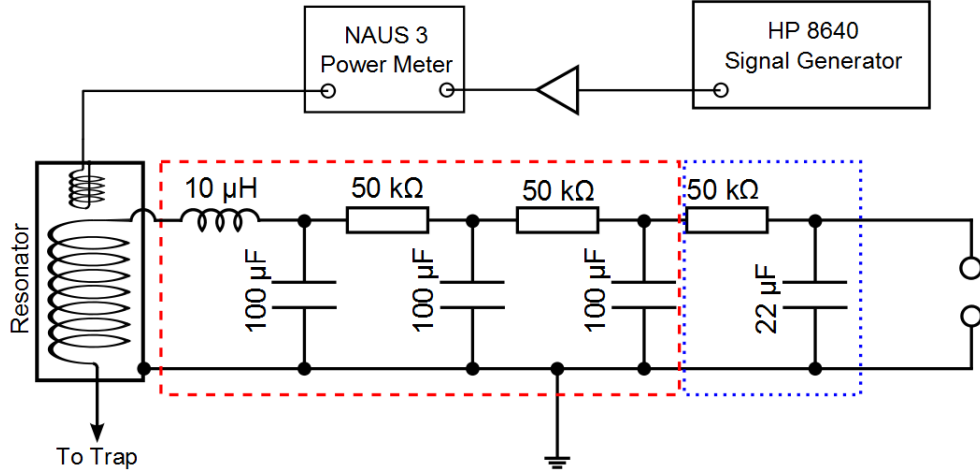
Figure 4.9: Circuit used to apply a static bias to the radio frequency signal. The red (dashed) section prevents rf from reaching the static voltage supply while the blue (dotted) section removes an unwanted 10 Hz signal present on the static voltage.

4.3 Laser Stabilisation

Efficient laser cooling requires narrow linewidth frequency stabilised laser radiation. Narrow linewidth radiation is achieved using Littrow configured external cavity diode lasers (ECDL's), described in detail in section 3.2, however these systems are prone to current fluctuations, vibrations, and temperature drifts. To compensate for these unwanted effects the lasers are actively stabilised to the stable D_2 atomic line in ^{87}Rb using a series of locking schemes. First an ECDL at 780 nm is stabilised to the Rb atomic transition using feedback from frequency modulated (fm) saturated absorption spectroscopy. The stability of the 780 nm laser is then transferred to the 739 nm and 935 nm lasers using a transfer cavity locking scheme [104]. Due to experimental constraints, however, the 399nm and 638 nm lasers are instead stabilised using feedback based upon absolute wavelength measurement with a commercial wavemeter (High Finesse: WS7).

4.3.1 Stabilisation of the 780nm Laser

The fm saturated absorption spectroscopy setup is shown in figure 4.10. Here the 780 nm laser is separated into three beams: a 'reference beam', 'pump beam' and 'probe beam'. The pump and probe beams counter propagate and overlap through an in-house built Rb vapour cell, while the reference beam propagates through the vapour cell without interacting with either the pump or probe beams. The intensity of the probe and reference beams transmitted through the vapour are measured using photodiodes, and monitored as the laser wavelength is scanned.
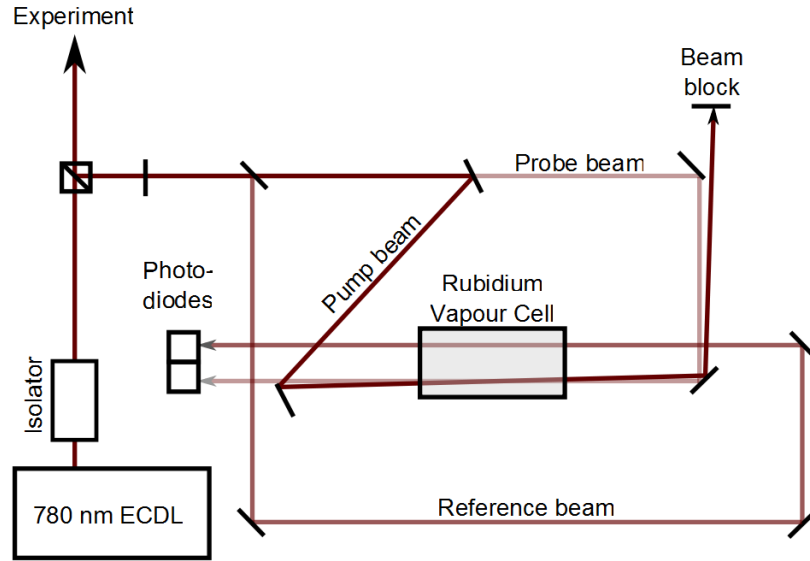
Figure 4.10: Saturated absorption spectroscopy of ^{87}Rb. The laser beam is split into the 'pump', 'probe', and 'reference' beams, which propagate through an inexpensive Rb vapour cell built by the university glass blowing facility. Photodiodes measure the intensity of the probe and reference beams transmitted through the vapour.

The resulting intensity profiles during a scan represent the absorption profile of the atomic vapour as a function of wavelength. Since the velocities of the atoms in the vapor are distributed in all directions this absorption profile becomes Doppler broadened. When the laser is resonant with a Doppler free transition frequency, however, all the beams interact with atoms with the same relative velocity group, i.e. zero velocity. At this frequency the greater intensity of the pump beam 'saturates' the atomic transition and absorption of the probe beam by the vapour is reduced. The beam intensity detected by the probe photodiode increases and produces narrow peaks in the Doppler broadened absorption profile, corresponding to the narrow hyperfine transitions. Since the reference beam does not interact with either of the other beams the corresponding frequency-varying intensity profile describes only the Doppler broadened absorption profile. Subtracting this reference signal from the hyperfine rich probe signal produces a Doppler free saturated absorption signal consisting of only the narrow hyperfine transition peaks.

The 780 nm laser is stabilised to these peaks using the setup shown in figure 4.11. The laser diode is current modulated at 160 kHz such the signals from the photodiodes also contain an oscillating component. A differential amplifier then subtracts the reference signal from the probe signal. The resulting modulated Doppler free signal is passed into a lock-in amplifier where it is mixed with a reference signal with a frequency equal to that of the modulation frequency. As described appendix E this mixing generates a signal comprising
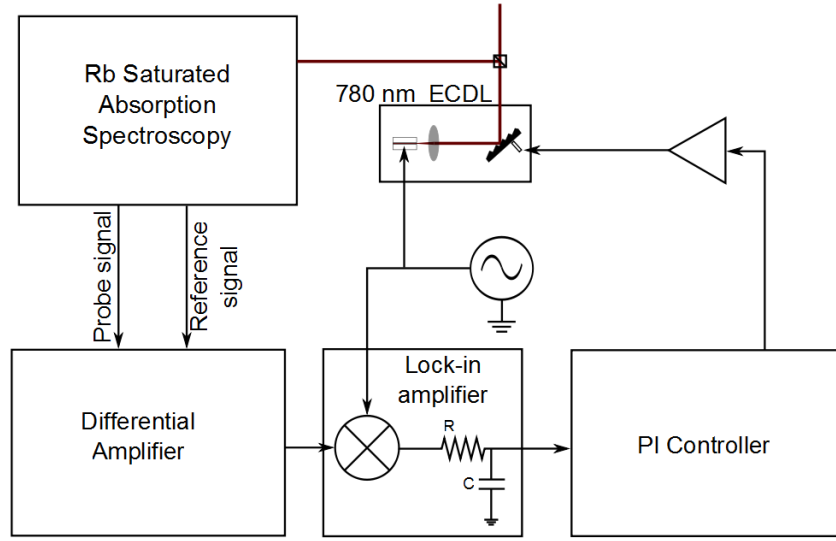
Figure 4.11: Setup used to stabilise the 780 nm laser to the Rb spectroscopy signal. The modulated 780 nm laser results in modulated photodiode signals. The probe and reference beam are subtracted using a differential amplifier and the Doppler free absorption signal is sent into a lock-in amplifier, where the error signal is generated. The error signal is passed through a PI controller to produce the error signal which is sent back to the laser.

several frequency components and a slowly time-varying DC component. Passing this mixed signal thorough a low pass filter extracts the DC component, which is the error signal.

An example of an error signal, in relation to a Doppler free saturated absorption signal, is shown in figure 4.12. The lower (black) trace shows the Doppler free signal corresponding to the different hyperfine transition in ^{87}Rb, with each peak corresponding to different hyperfine transition between $5^2S_{1/2}|F = 2\rangle$ and $5^2P_{3/2}|F' = x\rangle$. The upper (red) trace shows the error signal produced from each hyperfine transition. To a first approximation this error signal is the derivative of the Doppler free trace and by locking to the mid-point of the cross over on the error signal the laser is stabilised to the top of a transition peak. The error signal is passed through a proportional-integral (PI) controller to generate a feedback voltage, the amplitude of which is determined by the duration and magnitude of the error signal. The feedback signal then adjusts the grating angle in the external cavity diode laser, changing the laser wavelength. Using the error signal derived from the peak corresponding to the $5^2S_{1/2}|F = 2\rangle \leftrightarrow 5^2P_{3/2}|F = 2 \times 3\rangle$ crossover resonance the 780 nm laser is stabilised to <1 MHz for over an hour.
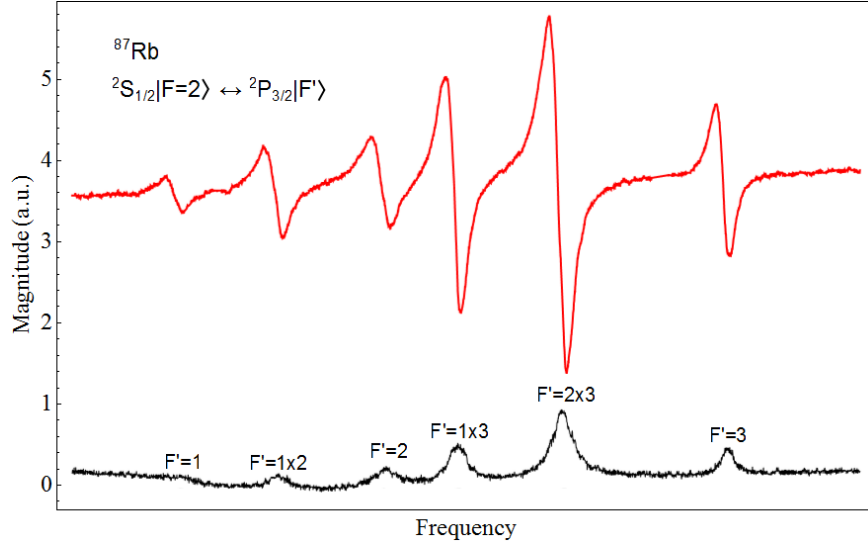
Figure 4.12: The lower trace shows the fm doppler free saturation spectroscopy signal. The different peaks correspond to different hyperfine transitions, with crossover transitions indicated by ×. The upper trace shows the error signal derived from the doppler free signal. The data was taken by Robin Sterling.

4.3.2   Stabilisation of External Cavity Diode Lasers

The stability of the 780 nm laser is transferred to the 739 nm and 935 nm lasers using the transfer cavity locking scheme [104]. Here the wavelengths of the 739 nm and 935 nm beams are compared to that of the stabilised 780 nm laser using scanning confocal Fabry-Pérot cavities, with the resulting fringe patterns identifying the relative wavelengths of the different lasers. With computer controlled feedback the fringe separations are held constant, stabilising the 739 nm and 935 nm lasers to the 780 nm laser.

Transfer Cavities

Confocal Fabry-Pérot cavities use two highly reflective concave mirrors separated by a distance equal to the radius of curvature of the mirrors, $L = R_1 = R_2$. This separation determines the characteristic feature known as free spectral range (FSR) which describes the frequency separation between successive resonances of the same wavelength. For a confocal Fabry-Pérot cavity FSR $= c/4L$, where c is the speed of light, and the factor 4 arises as a result of the beam propagation inside the cavity as shown in figure 4.13. The cavities used are shown in figure 4.14 and consist of a brass 'male' part, an aluminium 'female' part, and custom mirror mount. A fine pitch thread on the male and female parts allow for fine tuning of the cavity length, with different materials used to avoid mechanical 'jamming' when length tuning. Technical drawings for the cavities and custom adaptor piece shown in appendix F. The 780 nm / 739 nm cavity uses mirrors with a
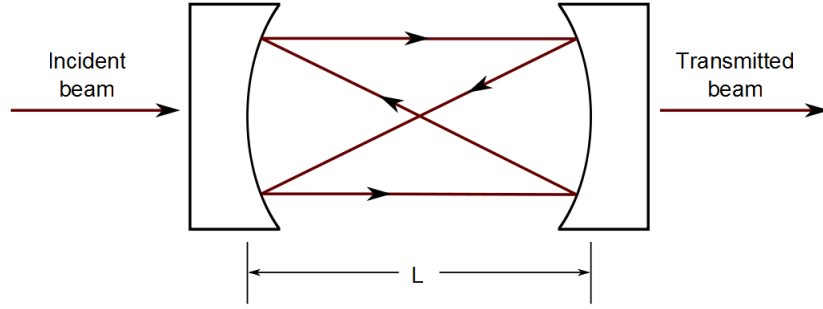
Figure 4.13: Beam path through a confocal optical cavity.

reflectivity of >99% at both wavelengths, and a radius of curvature of $R_{1,2} = 75$ mm (CVI: TLM2-750-0-0537-0.075CC) yielding a FSR = 1 GHz. The 780 nm / 935 nm cavity mirrors have a reflectivity of >99.3% and a radius of curvature of $R_{1,2} = 100$ mm (CVI: TLM1-369/399/780/935-0-0537-UV-0.010CC), resulting in a FSR = 750 MHz. To enable scanning one mirror from each cavity is mounted to a ring piezo with a thread adaptor (Piezomechanik: HPSt 150/14-10/12 HAg) using the custom adaptor.
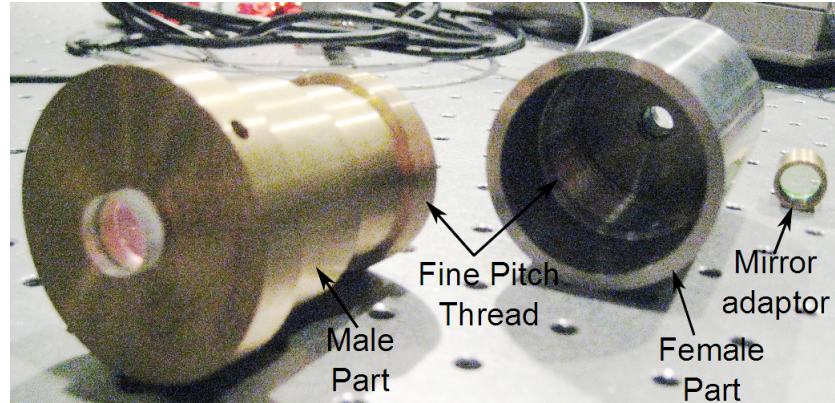
Figure 4.14: The different components used to make the scanning confocal cavities.

Transfer Cavity Lock Setup

The transfer cavity locking scheme is implemented using the setup shown in fig 4.15. The 739 nm and 935 nm beams are each combined with the 780 nm beam using polarising beam splitters and directed into separate cavities. The transmitted beams are separated, again with polarising beam splitters, and detected using photodiodes (Hamamatsu: S5972). Since the measured beams have different powers and the photodiodes have different spectral sensitivities the signals from the photodiodes have significantly different amplitudes. To equalise the photodiode signals inverting amplifiers with different gains are used after each photodiode.
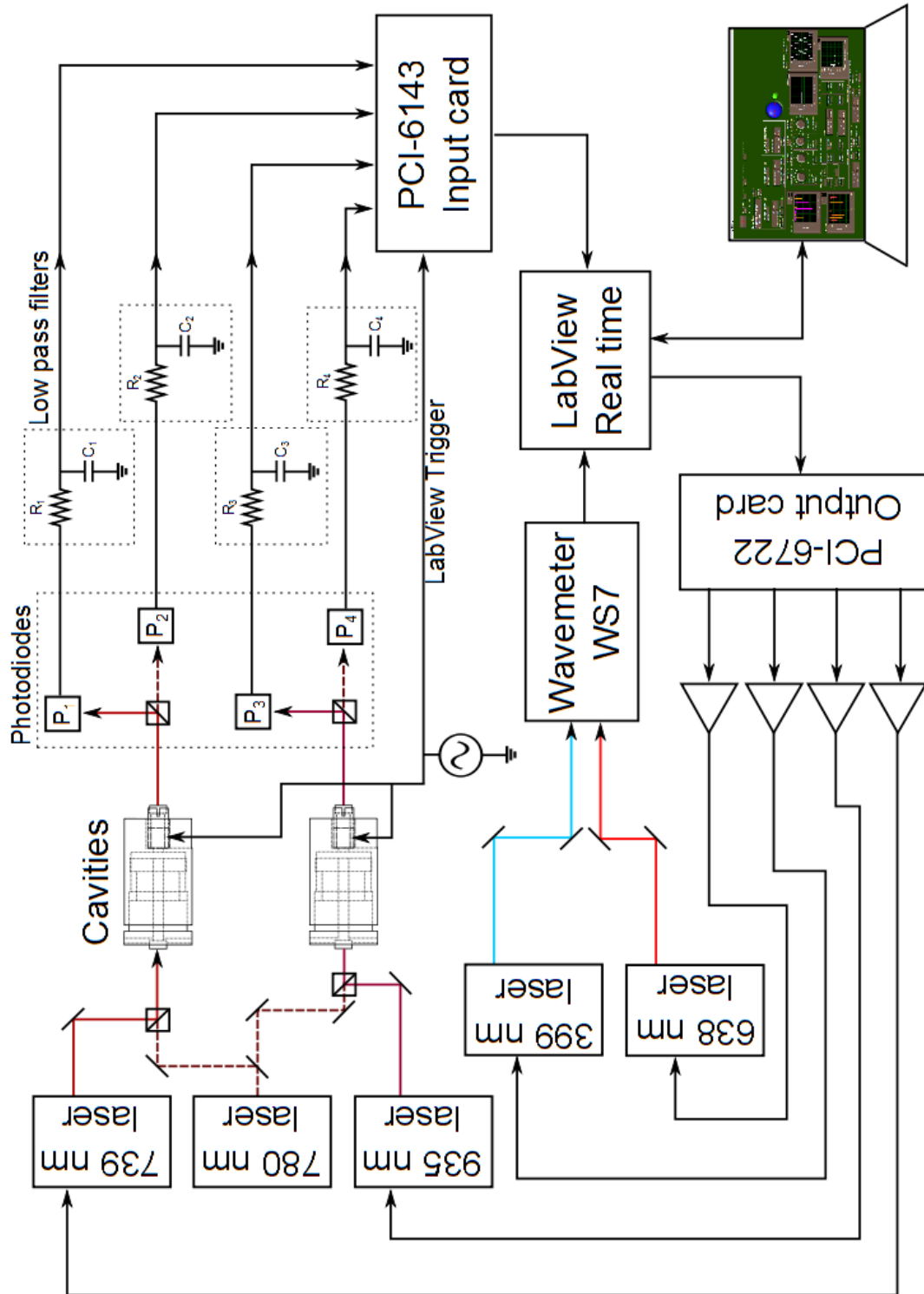
Figure 4.15: Schematic of the system used to stabilise the laser via the transfer cavity lock.

Following the amplifiers low pass filters with a cut off frequency of $f_c = 10$ kHz (consisting of $R_f = 100\ \Omega$ and $C_f = 16$ nF) remove noise from each signal. An example of the cleaned resonance fringes obtained from a cavity scan are shown in figure 4.16. The blue (solid) trace is the signal from the 739 nm photodiode, while the red (dashed) trace is the signal from the 780 nm photodiode. The small peaks in the centre of the 739 nm signal correspond to the 7.37 GHz sidebands. The peaks on the 739 nm trace occurring at the same position as the 780 nm peaks correspond to 780 nm light leaked onto the 739 nm photodiode.
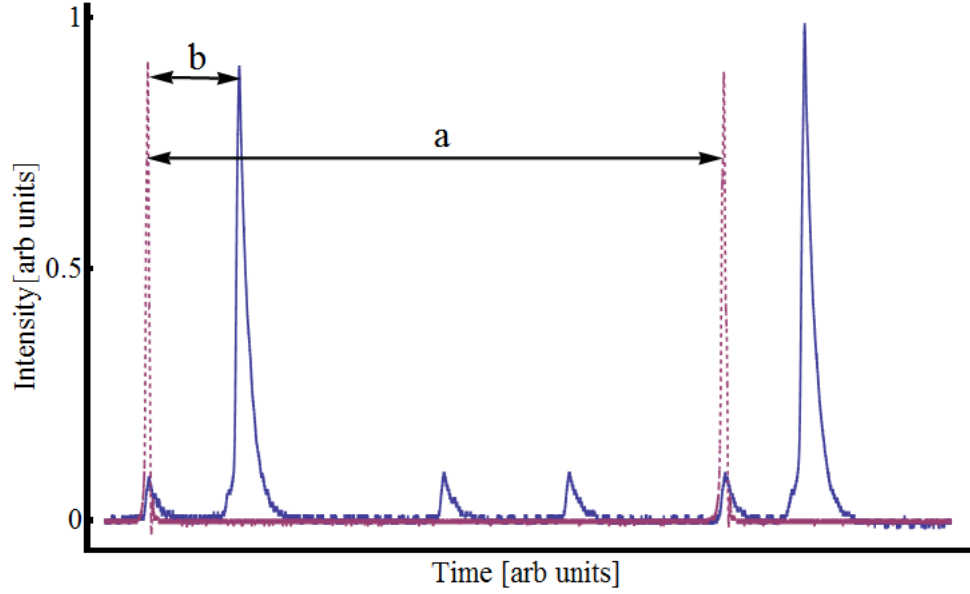
Figure 4.16: Combined signal from two photodiodes. The free spectral range of the 780 nm reference laser, a, is measured as well as the separation between the first 780 nm peak and the first 739 nm peak, b.

The signals are read into a 'target' computer, operating on LabVIEW Real Time, via an analog input card (National Instruments PCI-6143). A custom LabVIEW program compares the separation of two 780 nm resonance peaks, a, to the separation of the first 780 nm peak and 739 nm (935 nm) peak, b, to generate the ratio b/a. A change in this ratio corresponds to the wavelength drift of the 739 nm (935 nm) lasers. A virtual PI control in the program generates a feedback signal corresponding to the duration and magnitude of this deviation. The feedback signal is sent to the lasers via an analogue output card (NI PCI-6722) and amplifiers (Piezomechanik Gmbh: SVR 150/3).

This techniques stabilises the lasers and also allows for remote frequency tuning. By changing the ratio the wavelength of either the 739 nm (hence 369 nm) or 935 nm beams can be tuned. An issue that arose from current modulation is a shift in the carrier emission wavelength, caused by the extra power applied to the diode, but the stabilisation of the

resonance peak separation compensates for this. Additionally, monitoring the spectral components in real time provides up-to-date status of frequency sidebands and single mode performance.

Stabilisation via Absolute Wavelength Measurement

The 399 nm and 638 nm lasers are stabilised using feedback based upon the wavelengths measured by the wavemeter (High Finesse: WS7). The low transmission of ultra violet light through the Fabry-Pérot cavities and poor response of photodiodes at these wavelengths meant stabilising the 399 nm laser via the transfer cavity technique is impractical. Since the exact wavelengths for the $^2F_{7/2} \leftrightarrow {}^1D[5/2]_{5/2}$ transitions are also unknown stabilising the 638 nm laser using the transfer cavity technique is deemed unnecessary. Laser stability is achieved by transmitting the measured wavelengths into the target computer using a COM port. The locking program compares the recorded wavelength to a desired set point wavelength and generates a feedback signal relating to the magnitude and duration of the wavelength difference. The error signals are then sent back to the respective lasers via the analogue output card (NI PCI-6722) and amplifiers (Piezomechanik Gmbh: SVR 150/3).

Laser Stabilisation Program

The front end of the LabVIEW program used to achieve this is shown in figure 4.17 and described below

1 The plots show the cavity resonances measured by the photodiodes, similar to those shown in figure 4.16. The top plot shows the 739 nm and 780 nm fringes while the lower plot shows the 935 nm and 780 nm fringes. The signals are inverted purely as a result of the inverting amplifiers after the photodiodes. The 7.37 GHz sidebands can be seen on the 739 nm trace.

2 These controls ensure that undesired peaks, such as those relating to frequency sidebands or a wrong wavelength detected by a photodiode, are not considered. These unwanted peaks are neglected using the fields labelled 'Peak Threshold' which dictate the minimum amplitude required for a peak to be used for locking. To account for fluctuations in signal amplitude, and unwanted peaks rising above the amplitude threshold, an additional dial indicating a minimum width required for a peak to be considered is used. With both of
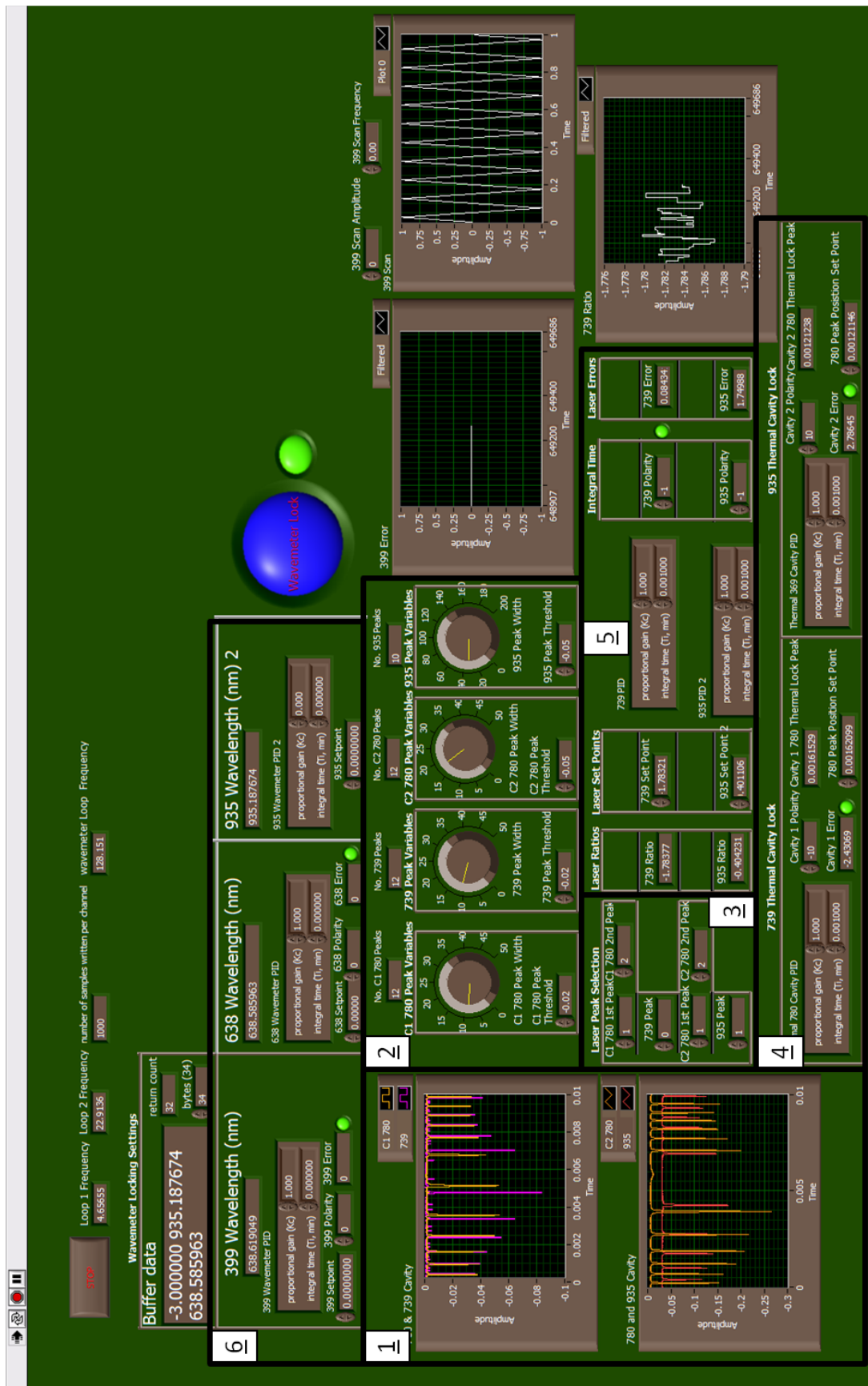
Figure 4.17: Front end of the program used to stabilise the lasers.

these controls only the desired resonance peaks are recognised and the number of usable peaks are shown in the 'Peak Variables' controls.

3 These fields choose the specific resonance peaks to be used to generate the ratio b/a. The labels above each field refer to the peak used for each laser, and 'C1' corresponds to the 739 nm / 780 nm while 'C2' corresponds to the 935 nm / 780 nm cavity.

4 These controls hold the positions of the 780 nm peaks constant with respect to the cavity scan, to ensure the parameter a is kept constant. The 'Peak Position Set Point' field describes the position of the 780 nm peak on the x-axis of the graphs shown in box **1**. The 'Polarity', 'Proportional gain' and 'Integral time' fields are input controls for a virtual PID used to maintain the position of the 780 nm peaks.

5 The measured ratio b/a is shown in the 'Laser Ratio' fields, while the desired ratio is indicated in the 'Set Point' fields. The 'Polarity', 'Proportional gain' and 'Integral time' fields are again input controls to a virtual PID to maintain the current ratio at the desired ratio.

6 These controls are used to stabilise the 399 nm, 638 nm, and 935 nm lasers using the the wavemeter measurements. The fields at the top of each section show the measured wavelength, the 'Setpoint' fields show the desired wavelengths, and the 'Polarity', 'Proportional gain' and 'Integral time' fields control another virtual PI controlling the feedback.

4.4   Table Setup

Figure 4.18 shows a unifying picture of the different aspects of an ion trap experiment so far discussed: the lasers, the rubidium spectroscopy setup and transfer cavities used for laser stabilisation, the wavemeter couplers used for wavelength measurement, and the vacuum chamber with ion trap. Between the lasers and vacuum system optical isolators are used to protect the lasers from unwanted feedback, optical fibres are used to maintain beam quality and pointing stability, and an AOM to enable fast switching of the 369 nm beam. The beams are then combined and focused through the centre of the trap.
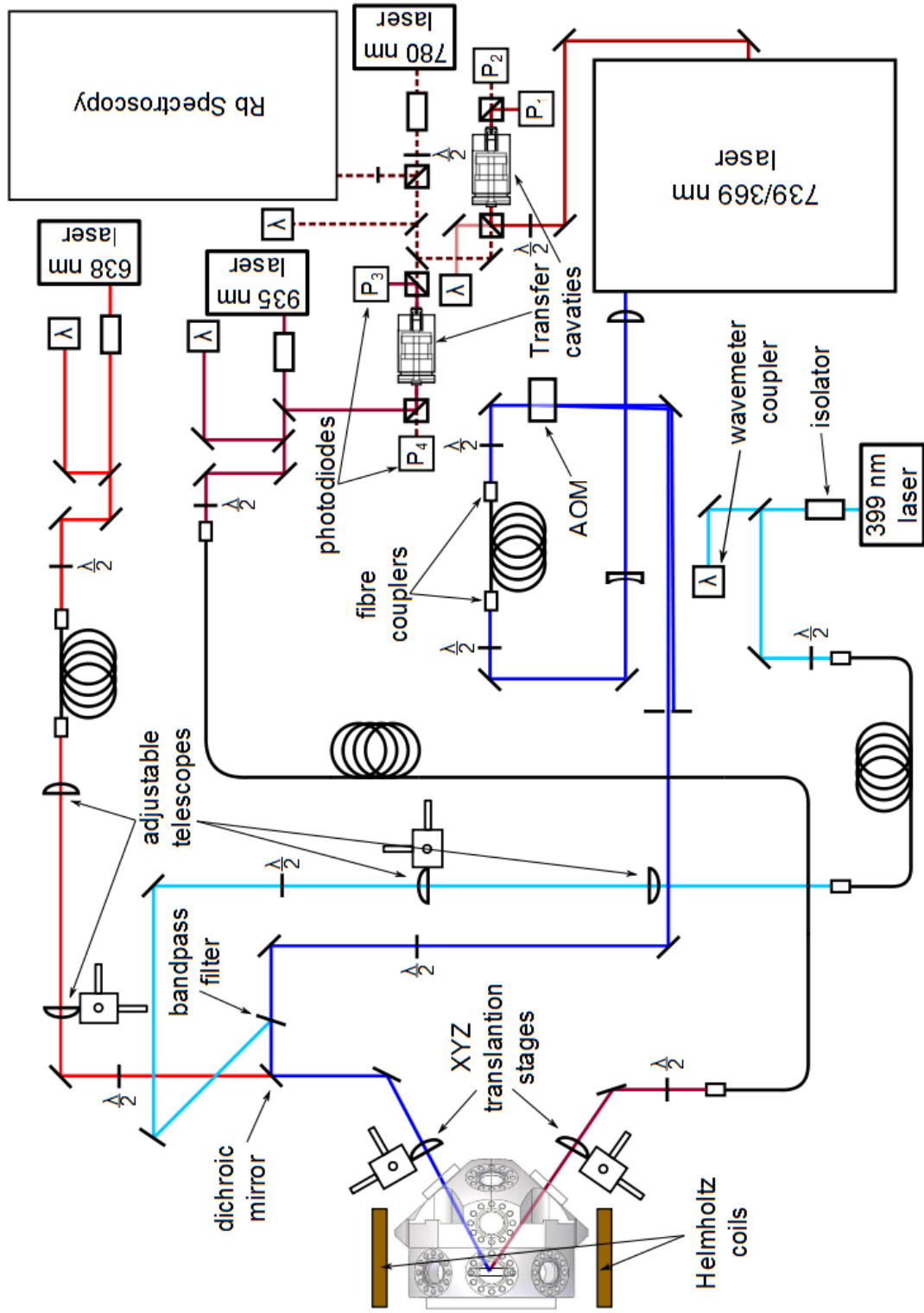
Figure 4.18: Setup of the optical table, showing the positions of the lasers and the optics used to direct and overlap the beams through the centre of the trap.

Isolators

Unwanted feedback can effect the wavelength of the light emitted by the external cavity diode lasers (ECDL's), or worse can permanently damage the semiconductor diodes. Each ECDL is therefore protected using an optical isolator, the design of which is illustrated in figure 4.19.
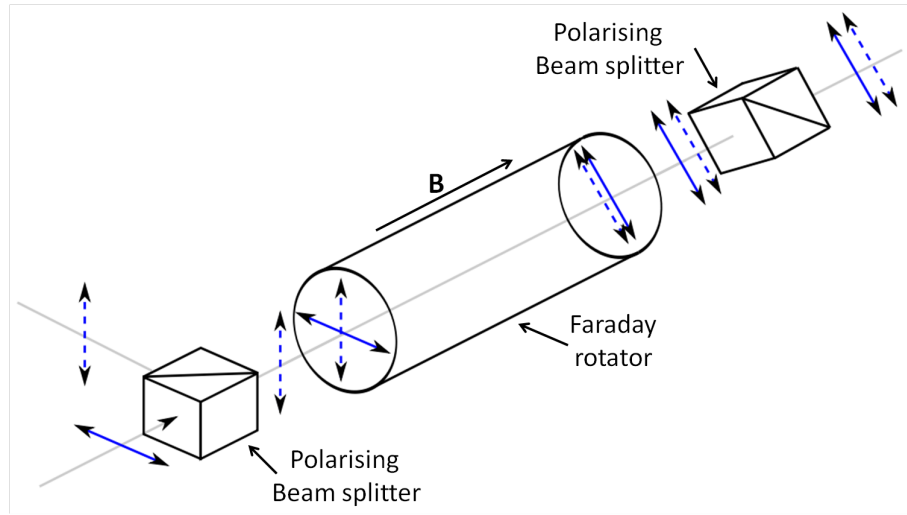
Figure 4.19: Optical isolator, comprising of two polarising beam splitter cubes and a faraday rotator. Light emitted from the ECDL (solid) is transmitted through the isolator, while light reflected back towards the ECDL (dashed) is reflected away.

Isolators consist of three components: an input polarising beam splitter, a Faraday rotator, and an output polarising beam splitter. The input polariser filters light from the ECDL (solid lines) to allow only linearly polarised light into the Faraday rotator. The Faraday rotator consists of a material which, when exposed to a magnetic field, rotates the polarisation of light transmitting through it. The rotator rotates the polarisation by 45°, and the output polariser is orientated to allow light to be transmitted out of the isolator. Reflections back into the isolator (dashed lines) are first filtered by the output polariser, and any light transmitted into the Faraday rotator undergoes a further rotation of 45°. Fortunately, the direction of rotation is independent of the direction of propagation. At the input polariser the reflected beam is polarised 90° with respect to the beam from the ECDL so is reflected away by the polarising beam splitter. Isolator performance is characterised in terms of the percentage of light transmitted in the forward direction and the proportion of unwanted reflected transmitted back through the isolator, measured in dB. The isolators used for the 399 nm, 638 nm, 780 nm, and 935 nm lasers, along with performance specifications, are shown in table 4.2.

ECDL	Isolator	Transmission [%]	Attenuation [dB]
399 nm	OFR: IO-5-399-LP	92	-33.6
638 nm	OFR: IO-5-638-PBS	93.2	-39.5
780 nm	OFR: IO-5D-780-VLP	87.9	-42.9
935 nm	OFR: IO-5D-935-VLP	92.7	-43.1

Table 4.2: Specifications of the isolators used for each external cavity diode laser.

Fibres

Following the isolators the beams used for ionisation, cooling and repumping pass through single mode polarisation maintaining fibres. Since the lasers often need readjusting the path of each beam is expected to change. Coupling each beam immediately through a fibre eliminates the need for realignment through any subsequent optical components. The fibres are single mode to ensure only TEM_{00} beam profiles reach the ion, and polarisation maintaining to ensure only linearly polarised light is transmitted. Light transmitted from non-polarisation maintaining fibres consists of all polarisation types: linear, circular, elliptical, etc, regardless of the input polarisation. The fibres used, and lenses coupling light into and out of the fibres, are identified in the table 4.3.

Wavelength	Fibre [Thorlabs]	Lenses [Thorlabs]
369 nm	PM-S350-HP-CUSTOM	A390TMA
399 nm	PM-S350-HP-CUSTOM	A390TMA
638 nm	P3-630PM-FC-2	C220TME-B
935 nm	P3-780PM-FC-2	C220TME-B

Table 4.3: The optical fibres and input/output coupling lenses used for the ionising, cooling and repumping beams.

It was found that elliptical beam profiles resulted in lower coupling than circular beam profiles. While this is considered unimportant for the 638 nm and 935 nm beams, due to the high powers, it is considered important for the 369 nm beam. Using two cylindrical lenses, first a plano-concave lens (Thorlabs: LK1936L1-A) with a focal length of -100 mm and then a second plano-convex lens (Thorlabs: LJ1144L2-A) with a focal length of 500 mm a circular beam profile is produced. Using this circular profile power transmitted through the fibre is increased from 25% to 40%.

Acousto Optic Modulator

Blocking of the 369 nm beam is often required in experiments. As timescales for experiments can be as short as a few microseconds switching of the beam must occur on sub-microsecond timescales. Mechanical components with maximum switching rates on

the order of kHz are too slow. Instead an acousto-optic modulator (AOM, Isomet: 1212-2-949) which can divert a beam path on timescales of 100-nanosecond is used.
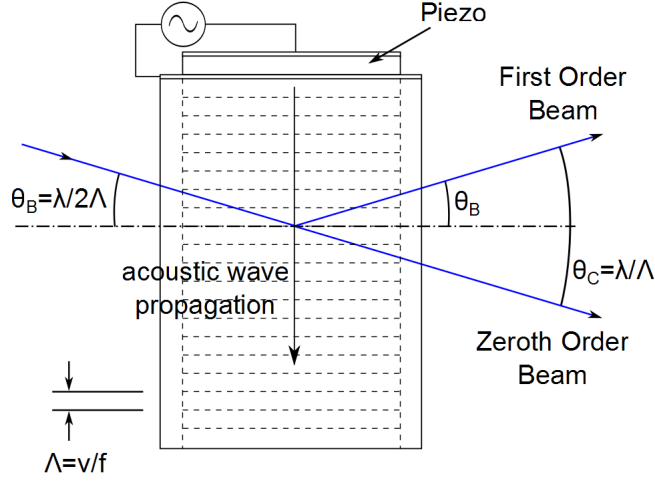
Figure 4.20: Internal working of an acousto optic modulator (AOM). The piezo induces periodic density changes within the crystal. Light incident into the AOM is diffracted in a fashion similar to Bragg diffraction.

As the name suggests AOM's are devices which mediate an interaction between acoustic and optical waves. The internal design of an AOM, illustrated in figure 4.20, consists of an optically isotropic medium with a piezoelectric transducer attached to one end. Applying an oscillating voltage to the piezo causes an acoustic wave to propagate through the crystal, resulting in a periodic change in the crystal density with the period equal to the acoustic wavelength Λ. Since the speed of sound is approximately six orders of magnitude slower than the speed of light any light propagating in the medium views this periodic density profile as stationary. Light is then diffracted from the density planes in a fashion similar to Bragg diffraction. Bragg diffraction is expressed as $n\lambda = 2d\sin(\theta)$, where λ is the wavelength of the light, d the atomic spacing, n an integer, and θ the angle of incidence with respect to the atomic planes. Similarly diffraction in an AOM is expressed as

$$n\lambda = 2\eta\Lambda\sin(\theta_{\mathrm{B}}) = \frac{2\eta v}{f}\sin(\theta_{\mathrm{B}}) \tag{4.2}$$

where n is an integer corresponding the order of the diffracted beam, λ the wavelength of the light, Λ the acoustic wavelength, f the acoustic frequency applied to the AOM, η the refractive index of the crystal medium, v the acoustic velocity in the medium, and θ_{B} the angle formed between the incident beam and the acoustic wavefronts. The diffracted beams are separated from the zeroth order beam by angles of $2\theta_{\mathrm{B}}$ and acquire a frequency shift of $\pm nf$, where the sign of this frequency shift is determined by the relative

propagation of the optical and acoustic waves. Since the optical wave is incident at an angle of θ_B to the wavefronts of the acoustic wave, there is a component of propagation parallel/antiparallel to the acoustic wave. If this component is parallel to the direction of the acoustic wave the diffracted beam is reduced in frequency, while propagation opposite to the acoustic frequency increases the frequency of the diffracted beam. The resonance frequency, magnitude of the frequency shift and separation between diffracted beams are ultimately determined by the the crystal used.

Several experiments require tuning of the optical frequency, which can be achieved by tuning the modulation frequency. As can be seen from equation 4.2 however, frequency tuning changes the direction of the diffracted beam. By redirecting the diffracted beam back through the AOM any path change occurring from the first pass is compensated for on the second pass. This double pass technique can be configured in two ways, with the preferred method dependent upon the diffraction efficiency at different polarisations. If performance is similar at both horizontal and vertical polarisations a suitable double pass configuration uses a concave mirror, quarter wave-plate and polarising beam splitter [105, 106]. The mirror reflects the beam back through the AOM while the quarter waveplate, positioned between the AOM and mirror, rotates the polarisation of beam between the first and second passes. A polarising beam splitter before the AOM separates the incident and second pass beams. Unfortunately the diffraction efficiency of the AOM used in the experiments drops to 25% with non-optimal polarisation. Instead the double pass would be implemented by laterally translating the beam, using a lens and right angled prism, before directing it back through the AOM [107].

Since frequency tuning is possible using the locking control described in section 4.3 only a single pass configuration is required. To align the AOM in a single pass the beam is first directed through the centre of the crystal. The AOM is then coarsely rotated until the different order diffracted beams are visible. Turning the AOM off shows only the zeroth order beam, then turning the AOM back on again the $\pm 1^{\text{st}}$ order beams correspond to the spots neighbouring the zeroth order beam. The AOM is rotated using a four-axis tilt aligner (New Focus: 9071M) enabling θ_{B} to be adjusted to improve the power in the diffracted beam. Rotating the beam polarisation with a half wave plate further optimises the diffraction efficiency. Once aligned the power driving the AOM is adjusted to obtain maximum diffraction efficiency. The separation between the first and zeroth order diffracted beams is ≈ 5 mrad, requiring a beam path >1 m to resolve and isolate the first order diffracted beam.

Coupling Beams Through The Trap
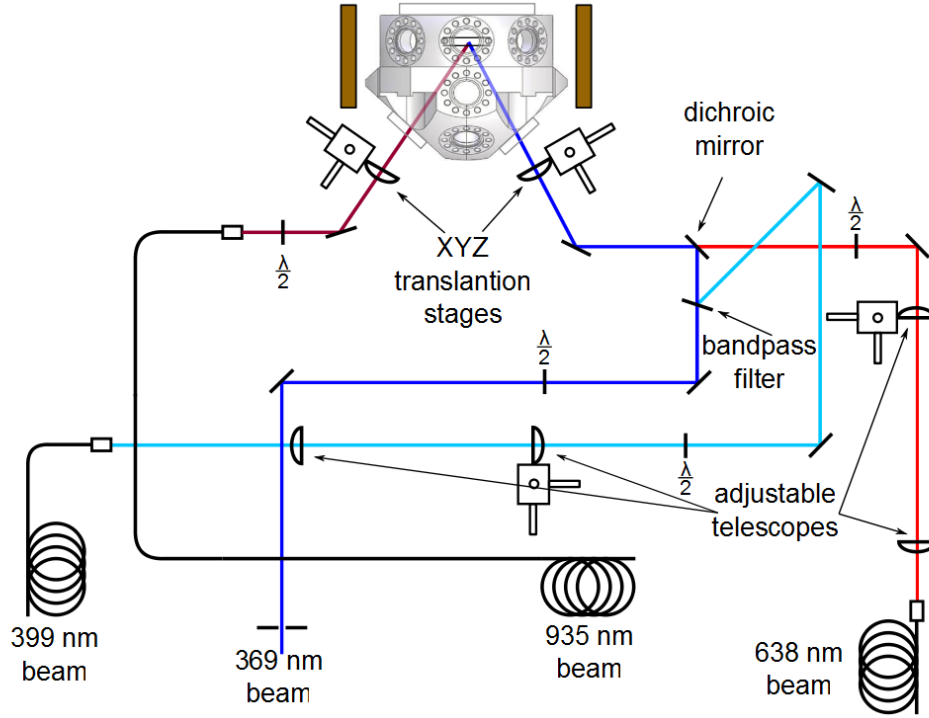
Figure 4.21: Coupling beams through the trap. The 369 nm and 935 nm beams are combined using a bandpass filter (Semrock: FF01-370/36-25), and then combined with the 638 nm beam using a cold mirror (CVI: HT-1.00). The beams are focused through the trap using lenses mounted on XYZ translation stages, while adjustable telescopes positioned in 399 nm and 638 nm beams account for chromatic abberation.

Following the fibres and AOM the beams are combined and focused through the centre of the trap using the arrangement shown in figure 4.21. The 369 nm and 399 nm beams are combined using a bandpass filter (Semrock: FF01-370/36-25) which transmits light between 347 nm and 393 nm, but reflects light >393 nm. These two blue beams are then combined with the 638 nm beam using a cold mirror (CVI: HT-1.00) which reflects (transmits) light below (above) 550nm. The multi-chromatic beam, and the 935 nm beam are focused through the trap using the XYZ translation stage mounted lenses positioned directly in front of the chamber's right and left viewports respectively. Chromatic abberation, however, causes the 369 nm, 399 nm, and 638 nm beams to each focus at different distances from the lens, resulting in only one beam being focused at the trap centre. Adjustable telescopes (with magnification of M=1) are therefore positioned in the 399 nm and 638 nm beam paths, before the combing optics, to compensate for this. The 369 nm beam is focused in the trap using the lens in front of the chamber, while the 399 nm and 638 nm beams are positioned using the adjustable telescopes.

Helmholtz Coils

As discussed in section 2.2.3 a magnetic field is required to avoid coherent population trapping in ^{171}Yb$^+$. The magnetic field is applied using Helmholtz coils positioned around the vacuum chamber, as indicated in figure 4.22. The coils each have 80 turns, a diameter of 170 mm, are separated by 120 mm, and passing a current of 2 A through them generates a magnetic field of 0.5 mT over the ion. Depending upon the experiment the direction of the required magnetic field may vary so three pairs of coils are used to enable the quantisation axis to be orientated in any direction.
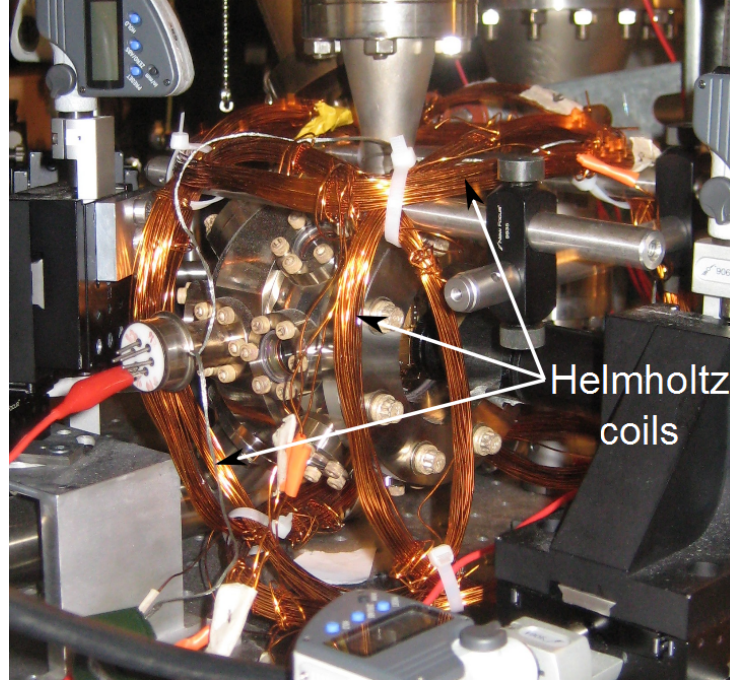
Figure 4.22: Helmholtz coils providing the quantisation axis and removing degeneracy in ^{171}Yb$^+$. Three pairs of coils enable the quantisation axis to be orientated in any direction.

4.5 Ion Detection

Ions are detected by collecting the fluorescence from the $^2S_{1/2} \leftrightarrow {}^2P_{1/2}$ 369 nm cooling transition using the system illustrated in figure 4.23. The emitted photons are collected using a triplet lens (Special Optics: 54-17-29-369, coated for 369 nm), which reduces abberation, especially spherical aberration, and provides a magnified ion image. The magnification of the triplet lens is $M_{\mathrm{T}} = -17.5$, where the negative sign indicates the image position is behind the lens. Positioning the lens 23.5 mm from the ion generates a magnified image 549.7 mm behind it. Mounting an aperture at this same position removes unwanted photon scatter without interfering with the ion image. After the aperture a doublet lens,

comprising of two plano-convex lenses with the flat surfaces facing the outside, further magnifies the ion image. The overall magnification of the doublet is determined by the focal lengths of the two lenses, and also the ratio of the object to image distance.
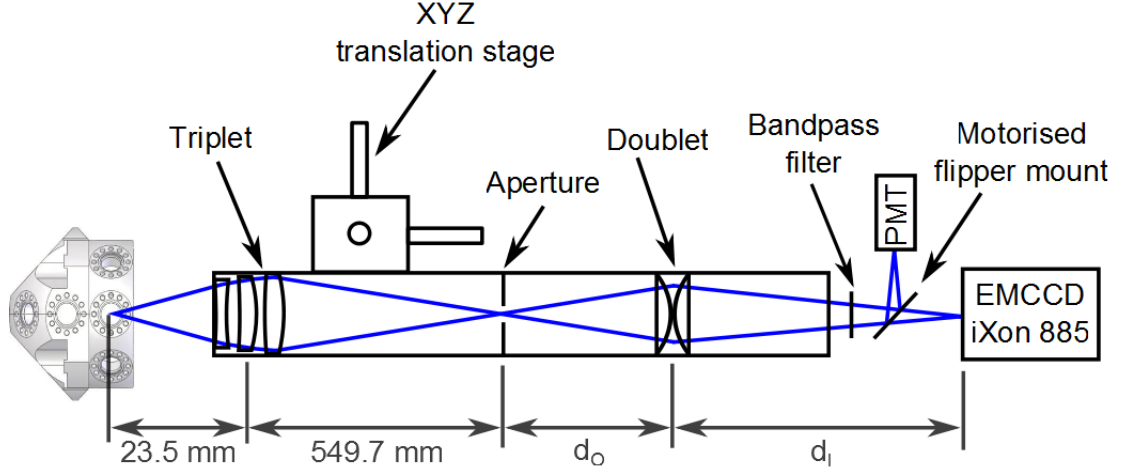
Figure 4.23: Optical setup used to detect and image trapped ions. Photons are collected and magnified by the triplet lens. An aperture is used to remove unwanted scatter before the image is magnified a second time using a doublet lens. The collected photons are measured using either a PMT or EMCCD.

In terms of object and image distance the magnification is expressed as

$$M_{\mathrm{D}} = \frac{d_{\mathrm{i}}}{-d_{\mathrm{o}}} \tag{4.3}$$

where d_{o} is the object distance (distance between the doublet and iris) and $-d_{\mathrm{i}}$ is the image distance (distance between the doublet and the detector). Again the image distance is negative since it is behind the lens. The object and image distances are related to the focal lengths of the two lenses via

$$\frac{1}{f_1} + \frac{1}{f_2} = \frac{1}{d_{\mathrm{o}}} - \frac{1}{-d_{\mathrm{i}}} \tag{4.4}$$

where f_1 and f_2 are the focal lengths of the two individual lenses. Thus choosing specific lenses as well as the object and image distances the magnification of the doublet can be designed. In the experiment the doublet is formed using lenses with focal lengths of $f_1 = 200$ mm and $f_2 = 300$ mm to yield a doublet focal length of $f_{\mathrm{D}} = 120$ mm. Positioning the doublet and detectors at $d_{\mathrm{o}} = 180$ mm and $d_{\mathrm{i}} = 360$ mm produces a magnification of $M_{\mathrm{D}} = -2$, yielding a total magnification of the imaging system of $M_{\mathrm{Tot}} = M_{\mathrm{T}}M_{\mathrm{D}} = 35$. With the detector area of the EMCCD being 8 x 8 mm an area of 230 x 230 μm is imaged, an area just smaller than the ion-electrode separation.

The triplet, iris and doublet are mounted in lens tube mounts and extensions. The tube in turn is mounted on an XYZ translation stage to allow different positions of the trap to be imaged. A bandpass filter (Semrock: FF01-370136, with a transmission of 94% between 347 nm and 393 nm and ≤0.008% for all other wavelengths) is positioned between the doublet and detectors to filter away any light not at 369 nm. A motorised flipper mirror mount (NewFocus: 8892-M) allows the collected photons to be measured on either an electron multiplied CCD array (EMCCD, Andor: iXon885) or photomultiplier tube (PMT, Hamamatsu: H8259-01), where the device chosen depends upon the experiment being performed.

4.6   Trapping an Ion

To successfully create, trap, cool and image ions several experimental parameters must be correctly adjusted: the voltages applied to the trap electrodes must result in a stable three dimensional trapping potential, the beams must pass through the null of the trapping potential, each laser must be lasing at the correct wavelength, and finally the imaging system must be positioned to image the desired region.

The first step is to map out the electrode geometry. This enables suitable electrode voltages and the position of the trapping null to be determined. The electrodes are identified by intentionally scattering 369 nm light from them and imaging the scatter with the EMCCD. The resulting electrode structure for the experiment trap is shown in figure 4.24. As can be seen the electrodes are not perfect, the null of the trapping potential is therefore unlikely to occur at the geometrical centre of the trap. Using analysis techniques, as described by Hucul *et al.* [108], the voltages to apply to electrodes to provide stable confinement and position of the corresponding potential null are calculated. The set of electrode voltages used in the experiment are shown in table 4.4, along with an rf drive signal of $\Omega/2\pi = 21.48$ MHz. Due to the imperfect electrodes the calculated displacement of the null from the geometric centre is 10, 18 and 24 μm in the x, y and z-axes respectively.

Using the translation stages the beams are readjusted to focus through this newly described potential null, with the width of the beam adjusted to compromise the uncertainty of beam position against the uncertainty of wavelength. Quite simply wider beams reduce the uncertainty of beam overlap in the trapping null. Smaller beam waists, however, increase the laser intensity and power broadening of the transition, reducing the accuracy required for each wavelength. When first trying to trap the 399 nm and 369 nm beams, with powers of ≈500 μW and ≈1 mW respectively, are focused to beam waists of 30(5)

Front electrodes
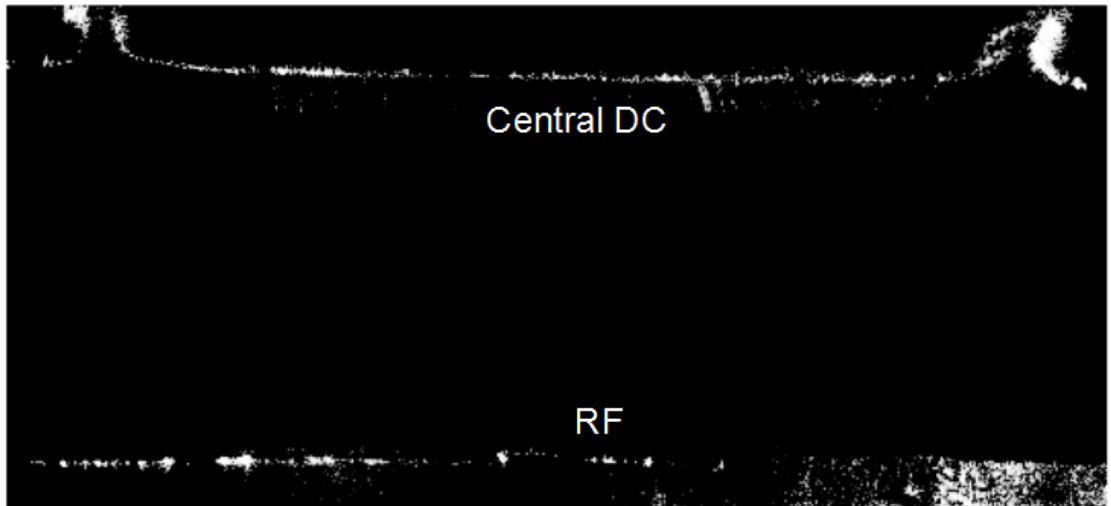
Rear electrodes
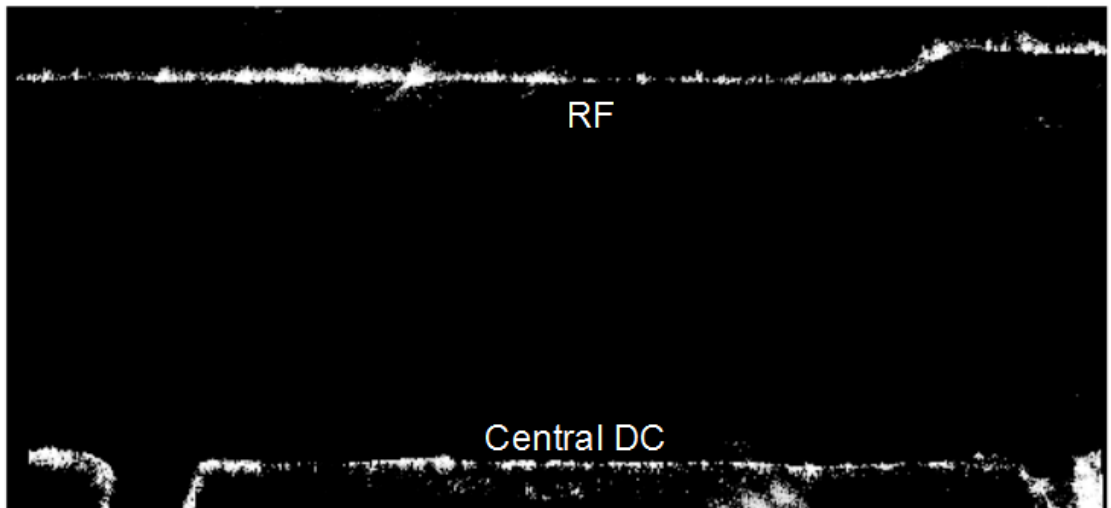
Figure 4.24: Image of the trap electrodes taken with the EMCCD camera. Images taken by illuminating the electrodes with 369 nm light.
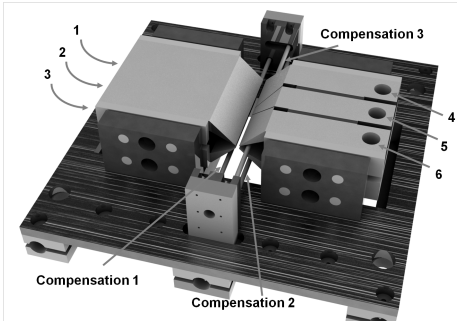
Electrode	Voltage [V]
1	148.88 (1)
2	7.36 (1)
3	25.03 (1)
4	0.00 (1)
5	0.00 (1)
6	167.76 (1)
compensation 1	169.22 (1)
compensation 2	169.22 (1)
compensation 3	-2.70 (1)
RF	680 (10)

Table 4.4: Voltages applied to the trap electrodes.

μm. The 638 nm and 935 nm beams with power of $\approx$7 mW each allow for wider radii of 60(5) μm while maintaining sufficiently high beam intensities. The polarisation of all the beams are rotated at 45^o to the quantisation axis to excite the σ_+, σ_- and π transitions required for ^{171}Yb$^+$.

The wavelengths of the 399 nm $^1S_0 \leftrightarrow {}^1P_1$ dipole transition, required for ionisation, are determined using a newly developed spot technique, discussed in detail in chapter 6. Approximate 369 nm, 935 nm and 638 nm transition wavelengths are obtained from previously published results. These values were reported to only several GHz, so the final wavelengths were determined through trial and error. More accurate wavelengths for these transitions for most of the stable isotopes are also presented in chapter 6.

Using these parameters the isotopes: ^{170}Yb$^+$, ^{171}Yb$^+$, ^{172}Yb$^+$, ^{174}Yb$^+$ and ^{176}Yb$^+$ are trapped and cooled. Figure 4.25 (a) shows a 3-ion crystal, while figure 4.25(b) shows a multi-isotope crystal, highlighting the potential for many isotope experiments such as sympathetic cooling, figure 4.25(c) shows a zigzag crystal, and figure 4.25(d) shows an ion cloud.

The secular frequencies of the trapped ions are determined by applying an ac 'tickle' voltage to one of the end-cap electrodes. When the ac voltage equals a secular frequency the ion is resonantly heated resulting in visible de-crystallisation. The electrode voltages shown in table 4.4 result in secular frequencies of $(\omega_x, \omega_y, \omega_z)/2\pi = (2.069, 2.110, 1.030)$ $\pm$ 0.001 MHz. Using these secular frequencies in electric field simulations the depth of the trapping potential is estimated to be 4.9(2) eV.
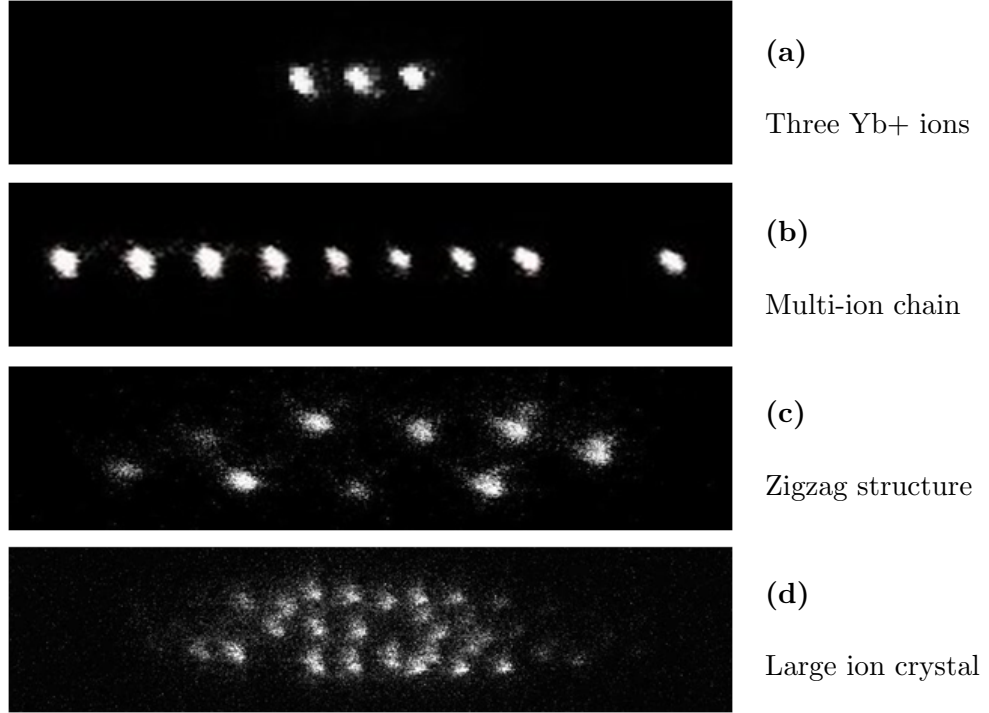
Figure 4.25: Crystal of (a) three Yb+ ions, (b) a multi-ion chain of mixed species, (c) a zigzag structure of nine Yb+ ions, and (d) a large ion crystal.

4.7   Experimental Control

Computer control of the experiment is achieved using a field programmable gate array (FPGA: National Instruments: NI-PXI-7842R), and a custom built 'host' computer. The FPGA is used to synchronise the operation of the different components and receive data from the PMT, while the computer is used to receive data from the EMCCD camera directly. To avoid potential interrupts associated with common operating systems the FPGA is mounted in an external chassis (National Instruments: NI-RIO PXI-1033) and connected to the host computer using a PCIe x1 card. Control sequences and data are transferred between the computer and FPGA at pre determined periods to ensure minimum intrusion upon experiment times.

The FPGA has 96 digital input/output channels offering and receiving TTL pulses, as well as 8 analogue input and 8 analogue output channels. In the present setup only the digital channels are used. The channels are connected, via a connector block (National Instruments: SCB-68), to switches positioned between signal generators and EOM/AOM/lasers and also the PMT. A switch (American Microwave Corporation: SWN-218-2DT) is used to turn the 7.37 GHz sidebands on/off, while additional switches (Minicircuits: ZFSWA2-63DR+) turn the 1.05 GHz and 3.07 GHz on/off. The 'off' ports of these switches are grounded using 50 Ω terminators to minimise any reflections back to the signal generators.

Switching of the AOM is achieved by adjusting the gain of the amplifier attached to the AOM. Changing the gain between zero and maximum effectively turns the AOM off/on. The TTL signals sent to the PMT and EMCCD are used to start and stop data collection. Data from the PMT is sent to the FPGA while data from the camera is sent to the host computer.

The PMT is specified to produce a single TTL pulse for every photon collected, where the pulses have 30 ns duration followed by a dead time of 5 ns. When choosing the FPGA it was important to ensure the sample rate of the FPGA was sufficient to cope with the output rate of the PMT. If the PMT released pulses at its maximum rate the FPGA would require a sample rate of at least 1 GHz (1 ns) to ensure an accurate photon count and the 40 MHz sample rate of the FPGA would be unsuitable. Fortunately this is not the case. Since the Doppler cooling transition has a maximum scatter rate of $\approx$10 MHz and the imaging system has an estimated detection efficiency of 0.06%, a count rate from the PMT of only $\approx$12 kHz is expected. In this situation the dead time between pulses from the PMT increases to $\approx$83 μs, and the 40 MHz (25 ns) sample rate of the FPGA is more than sufficient to distinguish single pulses. To ensure a pulse is only counted once, the FPGA is programmed to acknowledge only a positive change in the received signal. Measuring '0' then '1' results in a photon count, whereas measuring '1' then '1' produces no change in count rate.

The host computer is created to handle the more demanding data transmission from the EMCCD camera. The host computer contains a motherboard (Asus E3303) with a PCI-2.2 slot for the EMCCD camera and a PCIe x1 slot for the external chassis, a Nvidia GeForce 7300LE graphics card, an Intel core 2 quad processor (2.6 GHz), 4 GB of RAM, and Windows XP. A redundant array of independent disks (RAID) configuration, required to cope with increased data transmission when the camera is operated in its 'kinetic mode', is created with two hard disk drives (Western digital RE3 250GB SATA 2).

With this control system it is possible to remotely operate the different aspects of the experiment as well as enable the rapid repetition of trapped ion experiments. Indeed this system was used to control the experiments performed in the following chapters. The large number of unused channels on the FPGA also allow numerous features to be controlled including, for example, electrode voltages for automatic micromotion minimisation or shuttling.

Chapter 5

Heating Rate Measurement of Linear Ion trap

> "The Elders tell of a young ball much like you. He bounced three metres in the air. Then he bounced 1.8 metres in the air. Then he bounced four metres in the air. Do I make myself clear?"
>
> - Brain Ball, *Futurama*

To be suitable for quantum information processing ion's must have sufficiently low energies otherwise incoherent laser-ion interactions occur, resulting in reduced fidelities of quantum logic operations. Ion energy and heating rates are therefore important when considering trapped ion quantum manipulations for reliable information processing. Heating is induced by noise such as electric field fluctuations (from thermal electric Johnson-Nyquist noise) and fluctuating patch potentials (patch noise) on trap electrodes [109–112]. Conventional approaches of determining heating rates include the detection of motional sidebands [77–79, 81, 112], however these techniques can be quite demanding. As an alternative Wesenberg *et al.* [1] presents a simpler method of determining heating rates, based upon the measurement of ion fluorescence during Doppler cooling. This method was subsequently implemented by Epstein *et al.* [113] and shown to be in reasonable agreement with the more sophisticated methods. In this chapter the model developed by Wesenberg *et al.* [1] to determine ion energy is explained and then the procedure is implemented to determine the heating rate of the ion trap.

5.1 Model

The model used by Wesenberg *et al.* [1] describes a weakly bound ion oscillating in a one-dimensional harmonic potential, such that $\omega_{\text{sec}} \ll \Gamma$ where ω_{sec} the ion secular frequency and Γ is the excited state decay rate. The ion is Doppler cooled using a laser detuned from resonance by $\Delta = \nu_{\text{laser}} - \nu_{\text{trans}}$, where ν_{laser} is the laser frequency and ν_{trans} is the resonant transition frequency. The oscillatory motion of the ion, however, creates additional instantaneous Doppler shifts, $\Delta_{\text{D}} = -k_{\text{z}}v_{\text{z}}$, where v_{z} is the ion velocity in the z axis and k_{z} the laser beam wave vector in the z-axis. The negative sign indicates that photon absorption only occurs when the ion is travelling opposite to the propagation of the laser beam. During an oscillation the effective instantaneous laser detuning, experienced by an ion, is $\Delta_{\text{eff}} = \Delta + \Delta_{\text{D}}$. As the ion is weakly bound the excited state population, ρ_{ee}, can be approximated to be in a steady state with respect to the effective instantaneous detuning. Under this regime the excited state population is expressed as

$$\rho_{\text{ee}}(v_{\text{z}}) = \frac{s/2}{1 + s + (\frac{2\Delta_{\text{eff}}}{\Gamma})^2} \tag{5.1}$$

where s is the saturation intensity parameter. The instantaneous photon scatter rate dN/dt is then

$$\frac{dN}{dt} = \Gamma \rho_{\text{ee}}(v_{\text{z}}) = \frac{\Gamma s/2}{1 + s + (\frac{2\Delta_{\text{eff}}}{\Gamma})^2} \tag{5.2}$$

The resultant velocity dependent force imposed onto the ion from photon absorption is then

$$F_{\text{z}}(v_{\text{z}}) = p\frac{dN}{dt} \tag{5.3}$$

where $p = \hbar k_{\text{z}}$ is the momentum kick from the ion from each photon absorption. If the relative change in energy over an oscillation is small the effect of $F_{\text{z}}(v_{\text{z}})$ can be averaged over the oscillatory motion. The evolution of the ion energy can then be expressed as

$$\left\langle \frac{dE}{dt} \right\rangle = \langle v_{\text{z}} F_{\text{z}}(v_{\text{z}}) \rangle = \left\langle p v_{\text{z}} \frac{dN}{dt} \right\rangle \tag{5.4}$$

Similarly, the average energy evolution per oscillation can be expressed as

$$\left\langle \frac{dE}{dt} \right\rangle = \left\langle \frac{dE}{dN} \frac{dN}{dt} \right\rangle \tag{5.5}$$

where $dE/dN = -\hbar k_{\text{z}} v_{\text{z}} = -\hbar \Delta_{\text{D}}$ is the average energy lost per scattered photon over an oscillation, with the negative sign indicating a loss of energy from each absorption/scatter

event. If now the time during cooling is considered the evolution of the ion energy during the cooling process can be determined.

5.2 Time Dependent Energy Evolution

The following description for the change of ion energy during Doppler cooling follows the work presented by Wesenberg *et al.* [1]. The scatter rate is dependent upon the effective instantaneous laser detuning experienced by the ion and therefore the instantaneous Doppler shift, as indicated in equation 5.2. For an ion undergoing harmonic motion inside the trapping potential the distribution of the instantaneous shifts Δ_D during an oscillation is described using the probability density function

$$P_D = \int_0^{2\pi} \delta_{\text{Dirac}}[\Delta_D - \Delta_{\max}\sin(\phi)]\frac{d\phi}{2\pi} \tag{5.6}$$

where $\Delta_{\max}$ is the maximum instantaneous Doppler shift for an oscillation, ϕ is the angular position of the ion during an oscillation, and δ_{Dirac} is the Dirac delta function. This equation compares all possible instantaneous Doppler shifts against the maximum Doppler shift over all angular positions during an oscillation. The solutions to the density function have been shown to be [1]

$$P_D = \begin{cases} \frac{N}{2\pi\sqrt{\Delta_{\max}^2 - \Delta_D^2}} & \text{for} |\Delta_D| < \Delta_{\max} \\ 0 & \text{for} |\Delta_D| \geq \Delta_{\max} \end{cases} \tag{5.7}$$

The average scatter rate during an oscillation, $\langle dN/dt \rangle$, is then defined as the instantaneous scatter rate, dN/dt, weighted by the probability density of experienced Doppler shift integrated over all possible Doppler shifts.

$$\left\langle \frac{dN}{dt} \right\rangle = \int \frac{dN}{dt} P_D d\Delta_D = \int \Gamma\rho_{\text{ee}} P_D d\Delta_D \tag{5.8}$$

As shown in equation 5.4, the average energy removed per scatter event is $\Delta E = -\hbar\Delta_D$. The average energy change per oscillation $\langle dE/dt \rangle$ can therefore be expressed as

$$\left\langle \frac{dE}{dt} \right\rangle = \int \hbar\Delta_D \frac{dN}{dt} P_D d\Delta_D = \int \hbar\Delta_D \Gamma\rho_{\text{ee}} P_D d\Delta_D \tag{5.9}$$

The average scatter rate and average energy removed during an oscillation depend upon the relationship between instantaneous scatter rate dN/dt, or transition linewidth L, and the
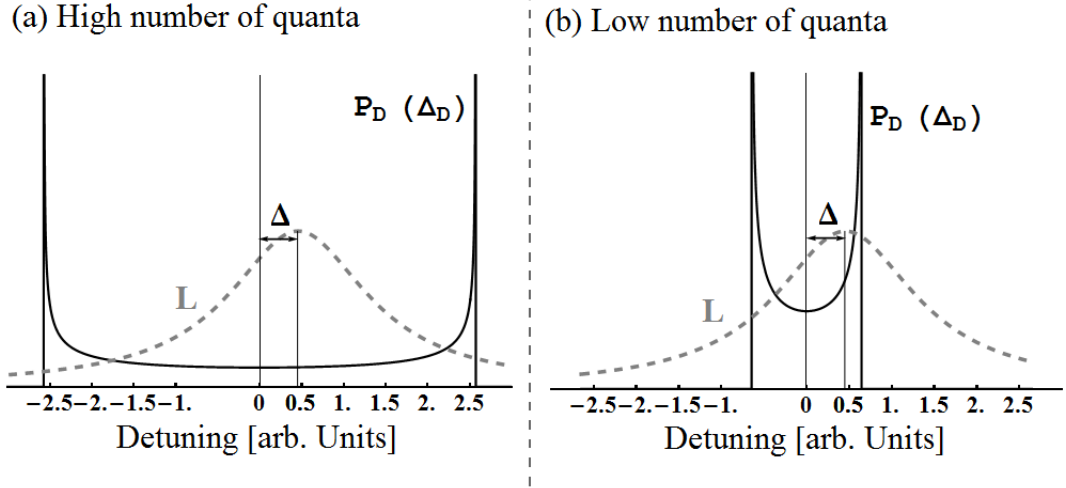
Figure 5.1: Comparison between the probability density of Doppler shift, P_D (solid line) with the transition linewidth L (dashed line). (a) Diagram showing the case for a hot ion, with a maximum Doppler shift greater than the broadened transition linewidth and laser detuning, $\Delta_{\max} \gg |\Gamma\sqrt{1+s}/2| + |\Delta|$. The overlap of both functions is low, leading to a low scatter rate. (b) Diagram showing the case for a cold ion with less energy. The peaks of P_D move closer together, resulting in a stronger overlap and an increase in scatter rate.

expected Doppler shift experienced by the ion during an oscillation P_D. The relationship is illustrated in figure 5.1, where 5.1(a) shows the situation for a 'hot ion' with $\Delta_{\max} \gg |L| + |\Delta|$, where Δ is the laser detuning from resonance. Here the Doppler shift probability density and transition linewidth poorly overlap, resulting in a low absorption/scatter rate. Figure 5.1(b) shows the effects of a cold ion, where the probability density overlaps well with the transition linewidth producing an increased scatter rate. In the hot ion regime the scatter rate can be considered constant over the transition linewidth allowing further simplification of the energy evolution and average scatter rates.

A more detailed evaluation of this relationship can be found in appendix G, and shows that after applying the hot ion approximation equations 5.8 and 5.9 can be simplified to

$$\left\langle \frac{dN}{dt} \right\rangle = \frac{s\Gamma^2}{4\Delta_{\max}\sqrt{1+s}} \tag{5.10}$$

$$\left\langle \frac{dE}{dt} \right\rangle = \frac{s\Gamma^2\hbar\Delta}{4\Delta_{\max}\sqrt{1+s}} \tag{5.11}$$

The energy associated with a maximum Doppler shift is $\Delta_{\max} = k_z\sqrt{2E/m}$. Using this

equations 5.10 and 5.11 become

$$\left\langle \frac{dN}{dt} \right\rangle = \frac{s\Gamma^2}{4\sqrt{1+s}\sqrt{\frac{2E}{m}}k_{\mathrm{z}}} \tag{5.12}$$

$$\left\langle \frac{dE}{dt} \right\rangle = \frac{s\Gamma^2\hbar\Delta}{4\sqrt{1+s}\sqrt{\frac{2E}{m}}k_{\mathrm{z}}} \tag{5.13}$$

which show the average scatter rate and energy evolution during cooling to be dependent upon the ion's energy at that instant. The ion energy at time t is therefore determined by integrating equation 5.13 over t to give [1]

$$E(E_0,t) = \left[E_0^{3/2} + \frac{3s\Gamma^2\hbar\Delta}{8\sqrt{1+s}\sqrt{\frac{2}{m}}k_{\mathrm{z}}}t \right]^{2/3} \tag{5.14}$$

where E_0 is the ion energy at the start of cooling. The average scatter rate as a function of ion energy is then determined by substituting equation 5.14 into equation 5.12, which yields

$$\left\langle \frac{dN}{dt}(E(E_0,t)) \right\rangle = \frac{s\Gamma^2}{4\sqrt{1+s}\sqrt{E(E_0,t)}\sqrt{\frac{2}{m}}k_{\mathrm{z}}} \tag{5.15}$$

Due to the stochastic nature of heating the initial energy of the ion, E_0, is also stochastically distributed. The initial ion energy is therefore described with a 1D-Maxwell-Boltzmann distribution

$$P_{\mathrm{B}}(E_0) = \frac{E_0}{\bar{E}}e^{-(E_0/\bar{E})} \tag{5.16}$$

where $\bar{E}$ is the mean energy gained after a certain heating time. The average scatter rate dN/dt, with an average start energy E_0, is therefore the average energy dependent scatter rate $dN/dt(E(E_0,t))$ weighted by the distribution describing the average start energy $P_{\mathrm{B}}(E_0)$

$$\left\langle \frac{dN}{dt} \right\rangle_{E_0} = \int_0^\infty P_{\mathrm{B}}(E_0)\frac{dN}{dt}(E(E_0,t))dE_0 \tag{5.17}$$

This equation describes the fluorescence rate as a function of the ion energy at the start of recooling, E_0, and the energy of the ion during recooling E.

5.3   Experiment Procedure

The heating rate is determined using the experiment performed by Epstein *et al.* [113]. The Doppler cooling laser is blocked allowing the ion to heat for a known delay period,

then reapplied and the fluorescence measured during the recooling process. The model is then used to determine the ion energy after the heating period, then repeating at different heating periods enables a heating rate to be obtained.

The heating measurement is performed on an ^{174}Yb$^+$ ion, and the trap voltages are set to comply with the restrictions dictated by the model. An effective one-dimensional harmonic oscillator is created by adjusting the trap voltages to produce secular frequencies of $(\omega_x, \omega_y, \omega_z)/2\pi = (2.069, 2.110, 0.178) \pm 0.001$ MHz. Since heating is assumed to have a $1/\omega^2$ dependence [112], these secular frequencies allow dominant heating to occur along the z-axis. Use of the 369 nm $^2S_{1/2} \leftrightarrow {}^2P_{1/2}$ Doppler cooling transition ensures the weak binding regime $\omega_z \ll \Gamma$ and so the steady state approximation for the excited state. The ion is cooled using a 369 nm laser with saturation parameter of 1.0(2), and detuning of $\Delta = 6(2)$ MHz. The angle of incidence of the laser with respect to the quantisation axis results in the z component of the laser beam wave vector to be $k_z = 0.45k$.

Before each measurement ion micromotion is minimised. First the amplitude of the rf drive signal is increased to generate a steep trapping potential. The corresponding ion position, imaged using the electron multiplied ccd array (EMCCD), indicates the location of the potential null. The amplitude of the rf signal is then reduced and the ion position monitored. A movement of the ion indicates that the nulls of the static and rf potentials do not overlap, which will induce excess micromotion. To compensate the voltages on the static electrodes (endcaps, rotation and compensation electrodes) are adjusted to reposition the ion at it's original location, corresponding to an improved overlap between the static and rf potentials. This is repeated until ion movement cannot be detected. The $^2S_{1/2} \leftrightarrow {}^2P_{1/2}$ transition linewidth is then determined by measuring the ion fluorescence as the laser is scanned over resonance. The resulting fluorescence profile indicates half of the atomic linewidth since photon absorption is significantly reduced when the laser is blue-detuned past resonance. The minimum linewidths obtained are $L = 40(5)$ MHz, with this wide transition expected to be a result of power broadening and residual micromotion.

Measurement

The experiment is performed using the control sequence shown in figure 5.2. The ion is first Doppler cooled for one second to ensure consistency between measurements. The beam is blocked using an acousto optic modulator (AOM: Isomet:1212-2-949) for delay periods ranging from 1-7 seconds. 1 ms before the end of the heating period, the PMT is turned on to provide a suitable background count and also eliminate any lag that may

exist between the signals controlling the PMT and AOM. The laser is then reapplied and
the ion fluorescence measured in 50 μs bins for 4 ms. The AOM has a response time of
100 ns, so is not expected to effect photon counts.
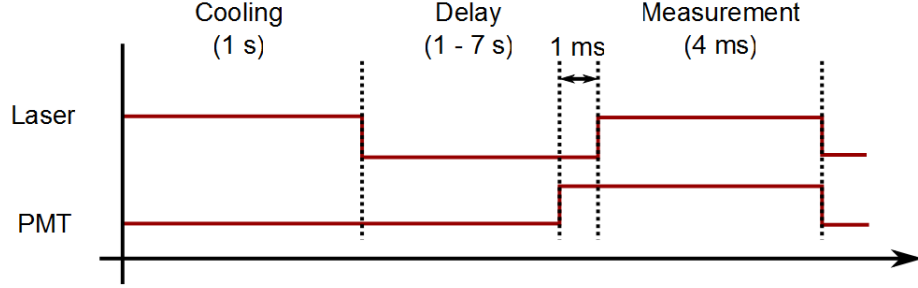
Figure 5.2: Experimental sequence to determine heating rate.

To account for the thermal averaging of E_0 the experimental control sequence is repeated
500 times for each delay period. The fluorescence from each measurement bin is then
averaged and the average fluoresce rate for the whole cooling period normalised. An
example of the change in fluorescence during cooling is shown in figure 5.3, for which
$\omega_z = 178$ kHz and the delay period is 3 seconds. The red curve shows the fit provided by
equation 5.17, and is adjusted by altering the ion energy before recooling E_0. Since each
measurement is ultimately related to the spontaneous decay from the excited state the
overall uncertainty of these measurements is stochastic in nature. The standard deviation
the fluorescence measurements thus corresponds to the error of each bin, and the standard
deviation of the range of acceptable fits determines the error on E_0.
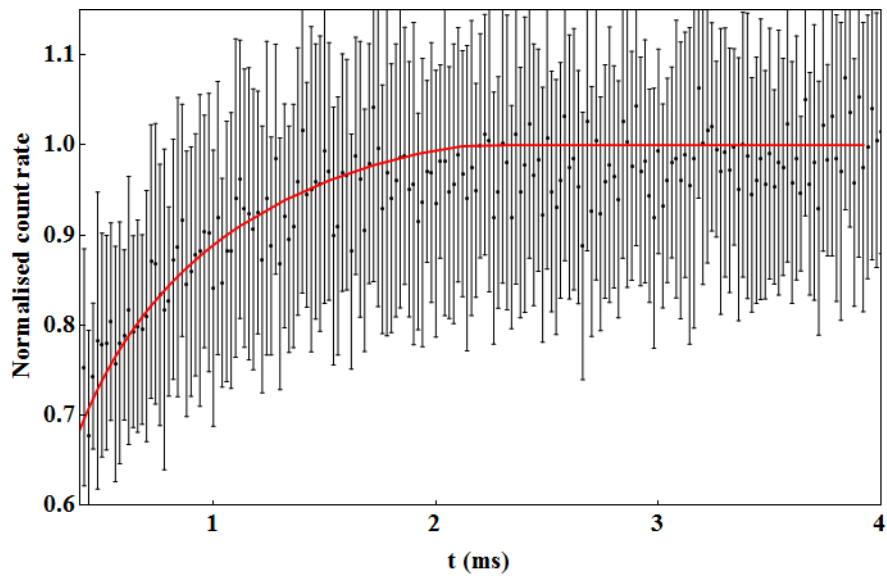
Figure 5.3: Ion fluorescence during first 4 ms of cooling after a delay period of 3 seconds,
$\omega_z = 178$ kHz. Each point corresponds to a 50 μs bin averaged over 500 runs.

This energy is converted in to motional quanta, using $\langle n \rangle = E_0/\hbar\omega_z$. The motional quanta measured after heating periods of 1, 3, 5, and 7 seconds are shown in fig. 5.4, and the error bars correspond to the standard deviation of E_0.
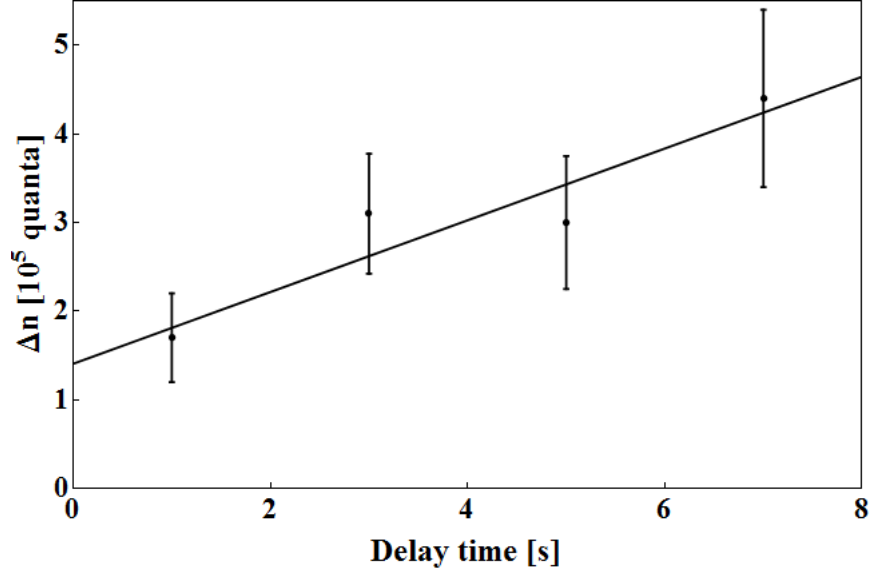
Figure 5.4: Change of motional quanta after different heating periods of 1, 3, 5, and 7 seconds.

To determine the electric field noise density $S_E(\omega_z)$, and also ensure the validity of the $\dot{n} \propto 1/\omega^2$ assumption, the heating rate measurement was repeated at different axial secular frequencies. By adjusting the endcap voltages and the voltage applied to the rf electrodes three secular frequencies of $\omega_z/2\pi = (178, 287, 355) \pm 1$ kHz, were used. The results are shown in figure 5.5, with the uncertainty of each measurement determined as the uncertainty of the gradient of each heating rate measurement. The straight line fit on a log-log plot justifies the earlier assumption that $\dot{n} \propto 1/\omega^2$ and also the creation of a one-dimensional system by setting $\omega_z \ll \omega_{x,y}$. The offset of the gradient is expected to an effect of the residual micromotion on the ion, and also radiation pressure exerted by the laser. The laser used to Doppler cool the ion is expected to apply a pressure onto the ion causing it to rest at a position off the potential null. When the laser is turned off the ion has an initial unwanted motional quanta, introducing an offset on the measurements. With a constant intensity used throughout the experiment this is expected to cause a systematic offset only, and not significantly effect the heating rate measurement.

These frequency dependent heating rates enable the electric field noise density to be determined. Electric field noise density $S_E(\omega_z)$ is a more useful measure of heating as it is independent of ion mass. $S_E(\omega_z)$ is related to the change in motional quanta, $\langle \dot{n} \rangle$ [111,112]
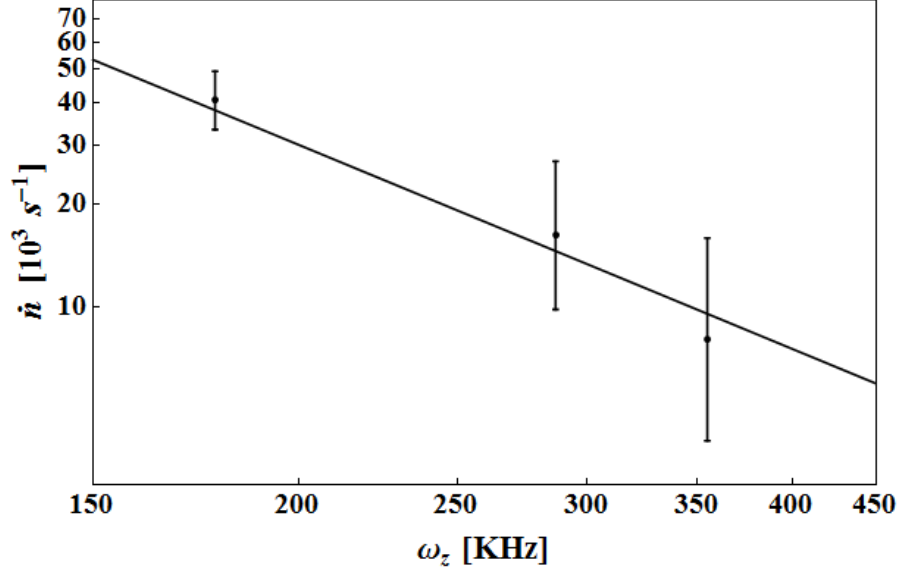
Figure 5.5: Heating rate as a function of secular frequency. Heating measurements at secular frequencies of $\omega_z/2\pi = (178, 287, 355) \pm 1$ kHz, are consistent with a $1/\omega^2$ dependence of the trap heating rate.

$$\langle \dot{n} \rangle = \frac{q^2}{4m\hbar\omega_z} S_E(\omega_z) \tag{5.18}$$

where q is the ion charge, m the ion mass. Extrapolating our data to $\omega_{sec} = 1$ MHz a prediction of $S_E(1\text{MHz}) = 3.6(9) \times 10^{-11}$ $V^2 m^{-2} Hz^{-1}$ is obtained.

Our measured value for S_E is compared to other previously measured values in figure 5.6. Each label shows ion species and electrode material used, with out result indicated by the royal purple triangle: Yb^+ - Au. It can be seen that the heating rate for our trap, with an ion electrode distance of 310(10) μm, is consistent with other traps of similar dimension and with different ion species. This heating measurement, the first for a ytterbium ion in such a small ion trap structure, has mitigated a concern that electrodes coated with small amounts of ytterbium may lead to abnormally high heating rates. It is an encouraging result for the use of Yb^+ ions in quantum information processing.
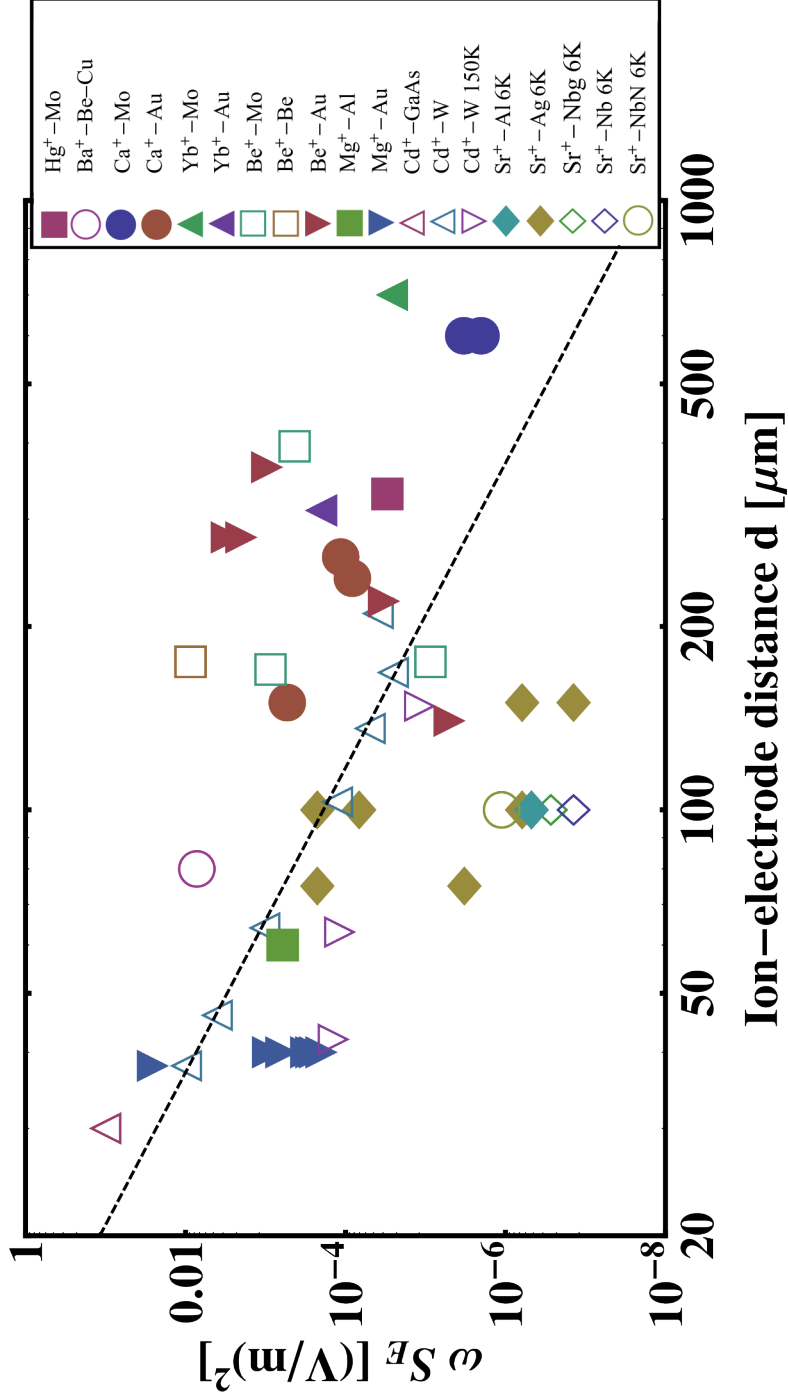
Figure 5.6: Plot taken from [114] showing previously published electric field noise densities S_E, scaled by secular frequency ω, as a function of ion to electrode distance d. Each label shows ion species and electrode material used, with out result indicated by the royal purple triangle: Yb^+ - Au. Measurements performed below room temperature the temperature is also noted. The trend indicates the expected $1/d^4$ trend.

Chapter 6

Ionisation, Doppler Cooling and Repump Wavelengths

> "First of all we measured the speed of light. Jeff got a torch. When you
> shout 'go' switch on the torch and I will time how long it takes to see the
> light, OK. Oh hold on... I'll hear that after I see the light. Say go slightly
> earlier so I can hear that and time how long...'
>
> Eddie Izzard, *Definite Article*

Ytterbium is an element widely used in atomic physics experiments including frequency standards [73,115–117], atomic clocks [118–121], quantum optics [122], trapping of neutral atoms and ions [43,123–133], and of course quantum computing [61,79]. The $^1S_0 \leftrightarrow {}^1P_1$ transition line, and isotope shifts, in neutral Yb have gained particular importance since they are used for laser cooling and isotope selective photoionisation. The $^2S_{1/2} \leftrightarrow {}^2P_{1/2}$ and $^2D_{3/2} \leftrightarrow {}^3D[3/2]_{1/2}$ transitions in singly ionised ytterbium are also important as they are used for Doppler cooling and repumping.

Published frequencies for these transitions, however, are either inconclusive or lack the accuracy required for atomic physics experiments. While various spectroscopy methods have been employed to investigate the neutral transition [134–138] few report absolute transition frequencies and state only isotope shifts instead. The absolute transitions that have been published also do not agree with each other other. Published results of the ionic transitions are also limited, with transition frequencies for the Doppler cooling and repump transitions reported to a precision of only several GHz [139]. This chapter describes experiments used to obtain more accurate wavelengths for these transitions [140,141].

6.1 $^1S_0 \leftrightarrow ^1P_1$ Wavelength Study

6.1.1 Fluorescence Spot Technique

The neutral $^1S_0 \leftrightarrow ^1P_1$ transition wavelengths are measured using a simple technique based upon the observation of fluorescence spots resulting from directionally dependent laser-atom interactions. The principle of the technique is illustrated in figure 6.1. Two pairs of non-overlapping counter propagating laser beams are aligned through an un-collimated atomic beam. The atom-laser interactions result in four resolvable fluorescence spots which, depending upon the laser wavelength relative the transition frequency, adopt one of the three configurations shown. When the laser is resonant with the Doppler free transition wavelength each beam interacts with atoms of the same velocity group (i.e. the zero velocity group) and the four spots align perpendicular to the beam propagation, as seen in 6.1(b). When the wavelength is detuned from resonance the beams become resonant with the Doppler shifted transition frequencies of atom moving non-perpendicularly to the beams. The four spots adopt a zigzag formation, as shown in figs. 6.1(a) and 6.1(c), with the orientation dependent upon the sign of the detuning. It should also be noted that this technique requires the atoms to propagate in a known direction. If a vapour cell was used, for example, the random direction of the atoms would generate fluorescence across the entire laser beam arm. Fluorescence would not be localised and the effects of wavelength tuning could not be observed.
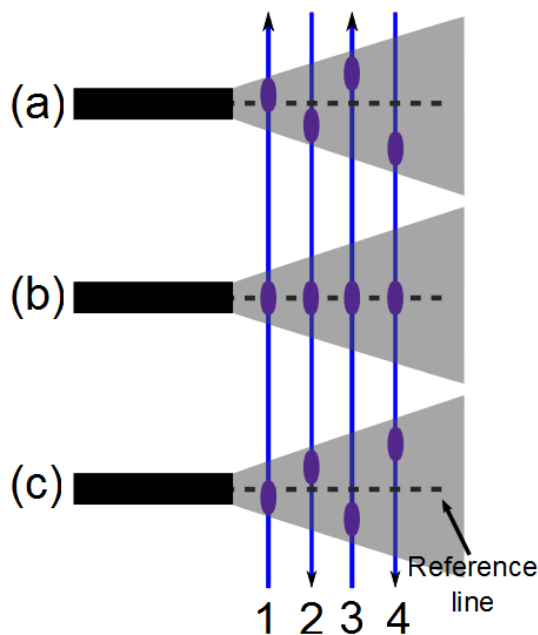
Figure 6.1: Fluorescence spot orientations when the laser frequency is (a) red-detuned from resonance, (b) at resonance, and (c) blue detuned from resonance.

Experiment Setup

The setup for this technique is illustrated in figure 6.2. The $^1S_0 \leftrightarrow {}^1P_1$ 399 nm dipole transition is excited using an in-house built external cavity diode laser (ECDL), the construction of which is described in section 3.2. The output from the laser is split into four beams, each with an intensity of 4.5 mWcm^{-2}, and aligned through the atomic beam. The Yb atomic beam is generated using a resistively heated stainless steel oven tube with an inner diameter of 0.83 mm, and a wall thickness of 0.24 mm. A small piece of natural Yb (Goodfellow: GO0196) is placed inside the oven and running an electric current of 5 - 6 A through the oven produces the atomic beam. The oven is similar in construction to those used in the main vacuum chamber (described in section 4.1.1) to simulate future experimental conditions. To avoid interactions with the external lab environment, the atomic oven is positioned inside a beljar, and the beljar evacuated to 10^{-8} torr. The fluorescence spots are imaged using an inexpensive CCD camera, which is positioned orthogonal to both the atomic beam and laser beams. A lens positioned between the beljar and CCD camera aids in fluorescence collection.

To obtain initial estimates of the $^1S_0 \leftrightarrow {}^1P_1$ resonances the laser wavelength is coarsely scanned, by varying the voltage to the piezo, and the appearance/disappearance of the fluorescence spots monitored. After narrowing down a frequency range for each resonance ($\approx$ 80 MHz), the laser frequency is fine tuned using LabVIEW operated feedback. The LabVIEW program (discussed in detail in section 4.3) compares the wavelength measured by a commercial wavemeter (High Finesse: WS-7) to that of a desired wavelength. To correct for any wavelength deviation the program generates a feedback signal proportional to the wavelength difference, which is then sent to the ECDL piezo via a multifunction data acquisition card (National Instruments: NI-6143). Adjusting this set point wavelength enables wavelength tuning.

The resulting spot configurations when the laser is tuned over resonance are shown in figure 6.3. In figure 6.3(c) the laser is resonant with the Doppler free transition wavelength and the four spots align perpendicular to the laser beams. In figures 6.3(b)/(d) the laser frequency is detuned by -20 MHz/+20 MHz from resonance respectively, while in figures 6.3(a)/(e) the laser frequency is detuned by -40 MHz/+40 MHz respectively. With a detuning of only 20 MHz resulting in a visually observable zig zag formation, the potential resolution of the technique can be estimated at <20 MHz. Furthermore the relative intensity of the spots provides a qualitative indication of the relative abundance of the isotope under study.
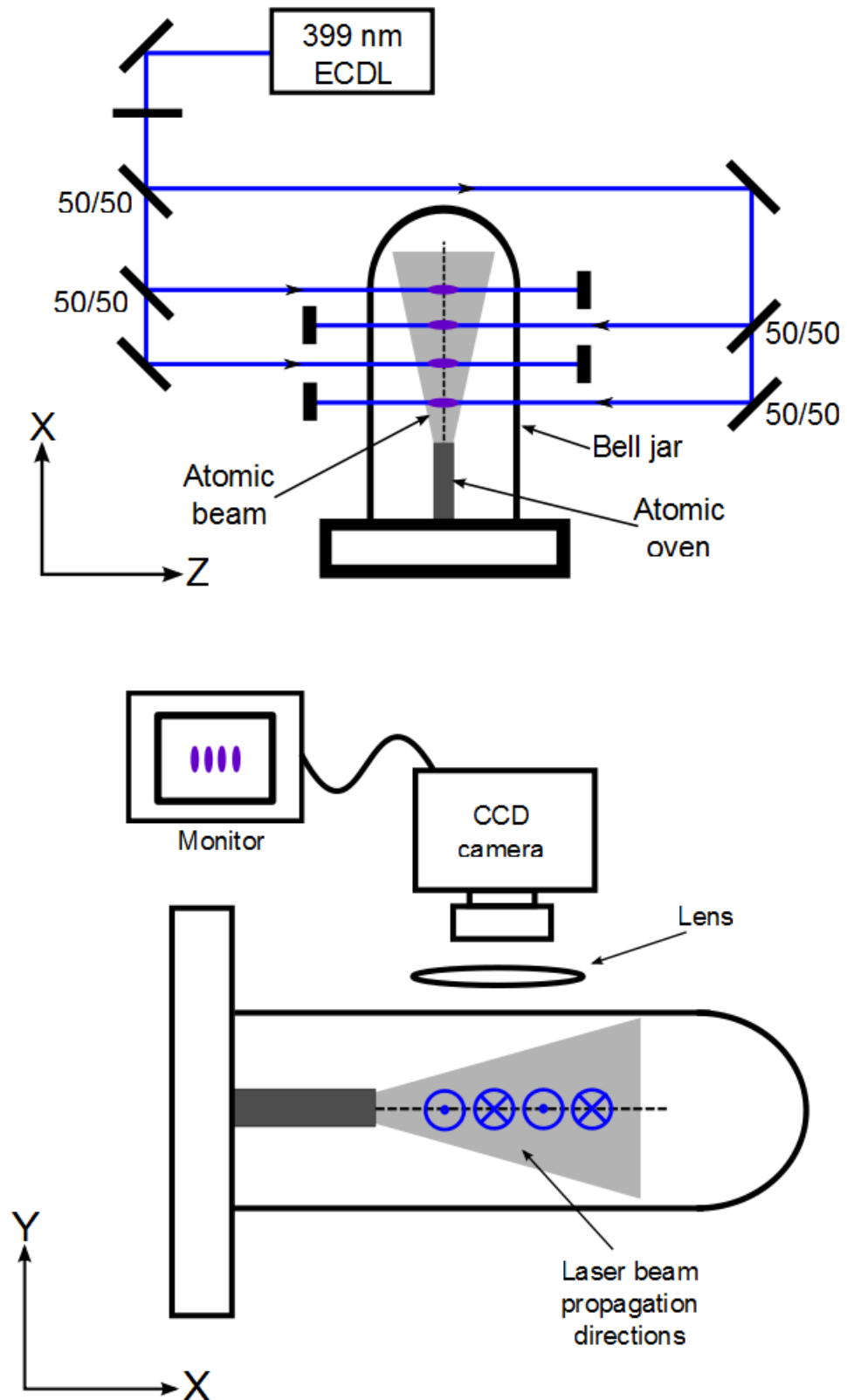
Figure 6.2: Schematic diagram (a) shows the counter propagating laser beams crossing the atomic beam and (b) shows the direction of laser beams and ccd-camera setup.
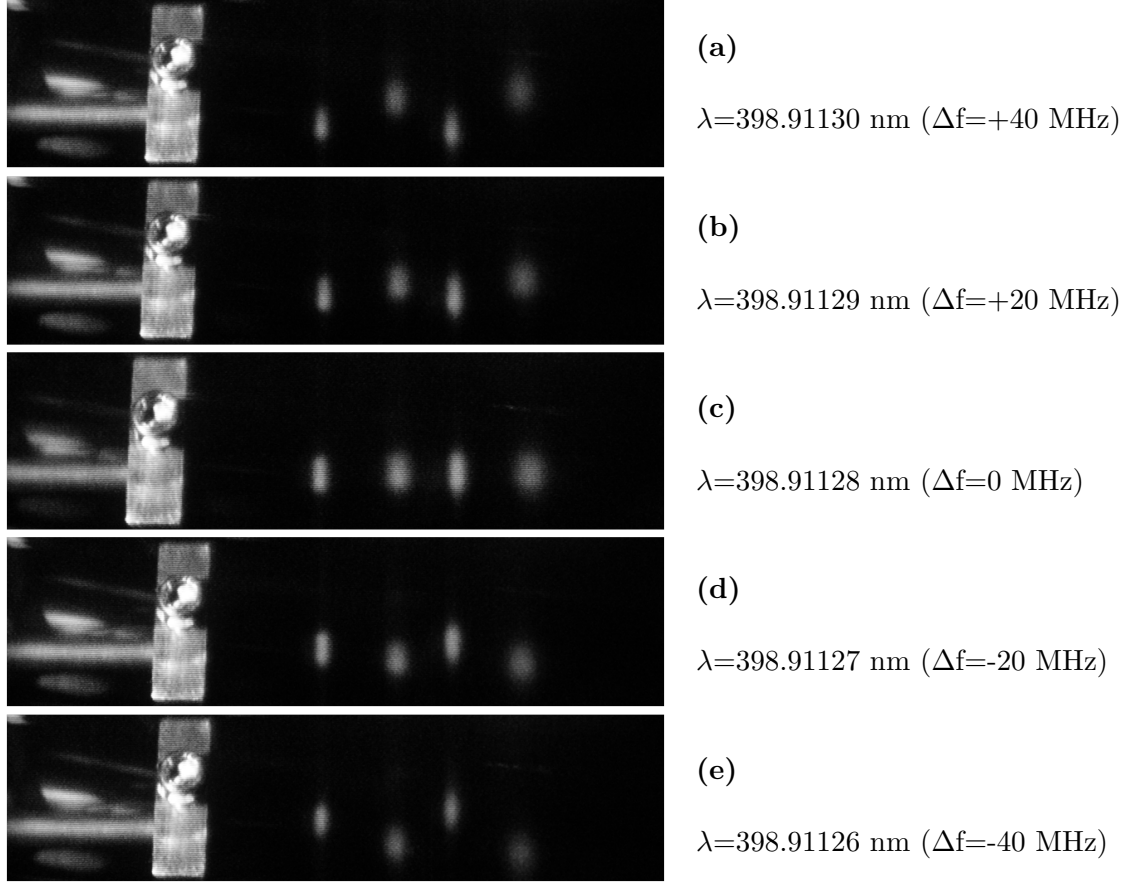
Figure 6.3: Images of the fluorescence spot technique. Pictures show the atomic ovens and fluorescence spots where the laser beams intersect the atomic beam taken at (a) +40MHz detuning, (b) +20MHz detuning, (c) on resonance, (d) -20MHz detuning, and (e) +40MHz detuning.

$^1S_0 \leftrightarrow {}^1P_1$ Wavelength Measurements

The $^1S_0 \leftrightarrow {}^1P_1$ transition wavelengths measured using the fluorescence spot technique are shown in table 6.1, with the corresponding frequency for ^{174}Yb being 751.52665 THz ±60 MHz. This frequency, however, disagrees with a previously published value of 751.525987761 THz ±60 kHz by Das *et al.* [135], by ≈660 MHz. This discrepancy is expected to be a result of Das *et al.* basing their measurements on a home-built wavemeter. The authors stated the accuracy of their wavemeter to be 20 MHz, but it is speculated that the actual uncertainty was larger than they claimed. Our measurement also differs from the NIST Atomic Spectra Database [142] by 260 MHz, which lists the energy of the Yb $^1P_1$ level at 25068.222 cm^{-1} (751.52639 THz). Closer examination of this discrepancy shows the database lists Meggers *et al.* [134] as the most recent source of their data. Meg-

gers *et al.*, however, list the energy of the level at 25068.227 cm^{-1} (751.52654 THz) which is only 110 MHz away from our measurement. This points to a possible typographical error on the NIST Atomic Spectra Database. Considering that Meggers *et al.* [134] used a natural mixture of Yb isotopes, their result is consistent with our measurement, but shows a 550 MHz discrepancy with Das *et al.* [135]. A recent independent measurement of the atomic transition by Schauer *et al.* [143] further supports the measurements obtained via the spot technique.

Isotope	Doppler Free Wavelength [nm] ± 60 MHz
^{168}Yb	398.91028
^{170}Yb, ^{171}Yb (1/2)	398.91067
^{171}Yb (3/2)	398.91084
^{172}Yb, ^{173}Yb (3/2, 7/2)	398.91099
^{174}Yb	398.91128
^{173}Yb (5/2)	398.91142
^{176}Yb	398.91155

Table 6.1: Doppler free resonant transition wavelengths for the $^1S_0 \leftrightarrow {}^1P_1$ in stable isotopes Yb isotopes.

Using the measured wavelengths the isotope shifts of the $^1S_0 \leftrightarrow {}^1P_1$ transition, relative to ^{174}Yb, are calculated. Figure 6.4 illustrates the isotope shifts [135] while table 6.2 shows the shifts obtained with the spot method and other recently published results. It can be seen that the isotope shifts determined using the spot technique are in very good agreement with previously published work [135–137, 144]. The precision of the technique, however, is limited by the linewidth of the transition, with any transitions separated by less than this linewidth resulting in overlapping and unresolvable fluorescence spots. In this situation it is only possible to observe a broadened absorption peak comprising of the narrower lines. Given that the frequency shifts between the ^{172}Yb $^1S_0 \leftrightarrow {}^1P_1$ and ^{173}Yb $^1S_0|F = 1/2\rangle \leftrightarrow {}^1P_1|F = 3/2\rangle$ / ^{173}Yb $^1S_0|F = 1/2\rangle \leftrightarrow {}^1P_1|F = 7/2\rangle$ transitions are 18 / 55 MHz respectively [135] the wavelength measured using this technique represents an average of these three lines. Similarly since the ^{170}Yb $^1S_0 \leftrightarrow {}^1P_1$ and ^{171}Yb $^1S_0|F = 1/2\rangle \leftrightarrow {}^1P_1|F = 1/2\rangle$ transitions are separated by 38 MHz [135], the measured wavelength also describes the broadened absorption peak.

Isotope	Transition	Shift from ^{174}Yb (MHz)				
		This work	Ref. [135]	Ref. [136]	Ref. [144]	Ref. [137]
^{168}Yb	$^1S_0 \leftrightarrow {}^1P_1$	1883 ±30	1887.400 ±0.05			1870.2 ±5.2
^{170}Yb*	$^1S_0 \leftrightarrow {}^1P_1$		1192.393 ±0.066	1175.7 ±8.1		1172.5 ±5.7
^{171}Yb*	$^1S_0(F=1/2) \leftrightarrow {}^1P_1(F=1/2)$	1149 ±60	1153.696 ±0.061	1151.4 ±5.6	1104±69	1136.2 ±5.8
^{171}Yb	$^1S_0(F=1/2) \leftrightarrow {}^1P_1(F=3/2)$	829 ±30	832.436 ±0.05	832.5 ±5.6	822 ±51	834.4 ±4.0
^{172}Yb*	$^1S_0 \leftrightarrow {}^1P_1$		533.309 ±0.053	527.8 ±2.8	534±33	
^{173}Yb*	$^1S_0(F=1/2) \leftrightarrow {}^1P_1(F=3/2)$	546 ±60	515.972 ±0.2			
^{173}Yb*	$^1S_0(F=1/2) \leftrightarrow {}^1P_1(F=7/2)$		587.986 ±0.056	578.1 ±5.8		
^{173}Yb	$^1S_0(F=1/2) \leftrightarrow {}^1P_1(F=5/2)$	-264 ±30	-253.418 ±0.05		-262 ±16	
^{176}Yb	$^1S_0 \leftrightarrow {}^1P_1$	-509 ±30	-509.310 ±0.05	-507.2 ±2.5	-554 ±35	

Table 6.2: The frequency shifts for the various isotopes of Yb from the ^{174}Yb $^1S_0 \leftrightarrow {}^1P_1$ transition line. The values are obtained from the fluorescence spot technique and compared with the previous published work.

* can not be resolved with the spot method
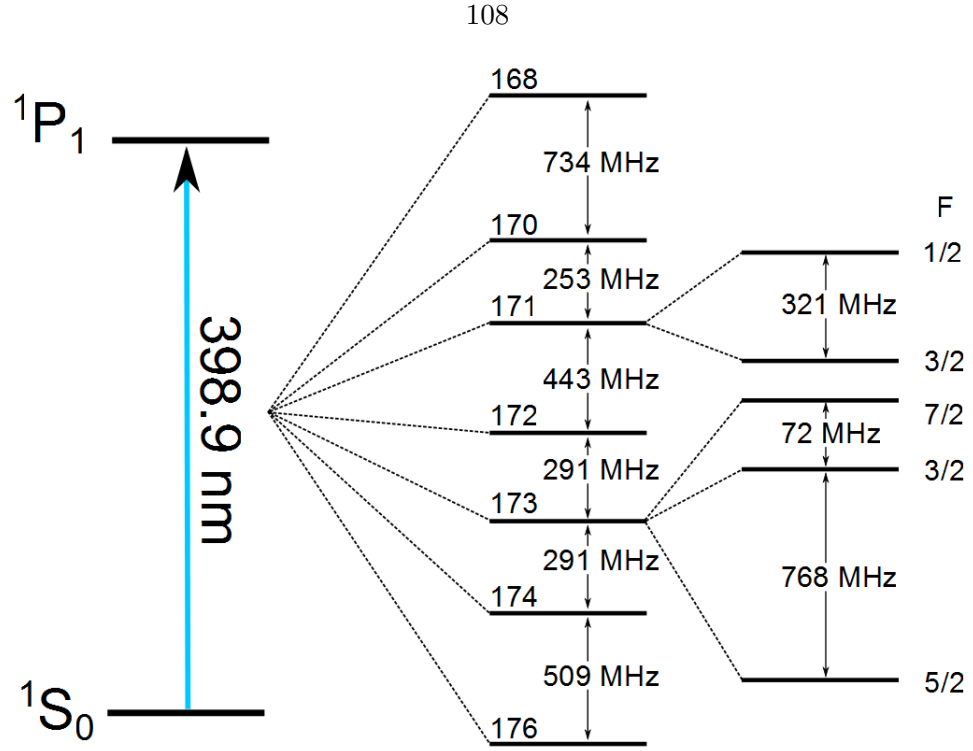
Figure 6.4: Diagram showing the frequency shifts between different isotopes, as measured by Das *et al.* [135].

Error Analysis

The resonant frequencies, and isotope shifts, are measured using a commercial wavemeter (High Finesse: WS7). The wavemeter is calibrated using a 780 nm laser, locked to <1 MHz of the ^{87}Rb D$_2$ line, and a He-Ne laser (SIOS SL02/1 calibrated to 1 MHz) is used to provide confirmation of the calibration. Using the frequency doubling system a further two point check is performed to ensure calibration in the ultra-violet frequency range. The laser system converts 739 nm light into 369 nm and by measuring the two wavelengths simultaneously the wavemeter is confirmed to operate within specifications. The wavemeter is calibrated before and after measurements and no change in calibration measurements are observed. The accuracy of the wavemeter is specified to 60 MHz for absolute frequency measurements between 370 nm and 1200 nm. For relative frequency measurements of closely spaced transitions (i.e. the isotope shifts) the accuracy improves to the display resolution. At 399 nm the relative accuracy (display resolution) is 20 MHz, which relates to an uncertainty on the isotope shift of 28 MHz. The isotope shifts involving the overlapping transition lines, however, could not be resolved better than 60 MHz. Other sources of error include non-parallel alignment of the laser beams where misalignment by 1° would result in a 15 MHz error on the measured wavelength. Since the technique can resolve <20 MHz detuning misalignment of a single beam would result

in a visible deviation of the corresponding spot with respect to the other aligned spots. The beams can therefore be aligned to better than 1 degree and the uncertainty caused by beam misalignment can be neglected. The relative beam intensities (4.5 ± 0.9 mWcm^{-2}) compared to the transition saturation intensity (60 mWcm^{-2}) result in power broadening of the transition by 3 MHz. Combining these errors results in an uncertainty of 60 MHz for absolute wavelength measurements and 30 MHz for isotope shifts.

6.1.2 Saturation Absorption Spectroscopy

To provide a comparison for the results obtained using the fluorescence spot technique, a typical saturation absorption spectroscopy experiment was performed (the details of which are described in section 4.3.1). The experimental setup used is shown in figure 6.5. A picker (Thorlabs: PSF10-A1) splits the 399 nm beam into a 'pump' and 'probe' beam with intensities of 127 mWcm^{-2} and 2 mWcm^{-2} respectively. The photodiode used to measure the intensity of the probe beam (Hamamatsu: S5972) has poor sensitivity at ultraviolet wavelengths so an amplifier, with a gain of 1x10^6, is used to increase the signal. A low-pass filter, with a cut off frequency of 100 Hz, is used after the amplifier to remove noise.
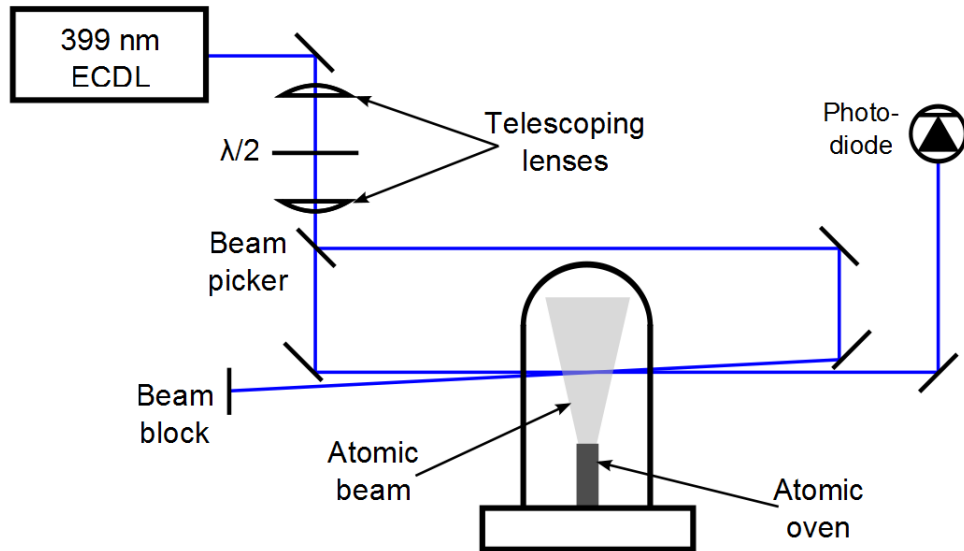
Figure 6.5: Schematic of the experimental setup for saturated absorption spectroscopy of neutral ytterbium.

Based upon the calculated isotope shifts (section 6.1) the frequency separation between all the isotopes spans $\approx$2.5 GHz. The 399 nm laser is therefore required to scan over a range of $\approx$3 GHz. Wavelength tuning by adjusting the grating angle alone, however, only provides a mode hop free tuning range of only 800 MHz. To increase the mode hop free tuning range the signal used to adjust the piezo voltage is simultaneously used to adjust the laser

diode current. This resulting 'frequency tracking' between the feedback frequency from the grating angle and preferred emission wavelength from the diode increases the mode hop free tuning range to >5.5 GHz.
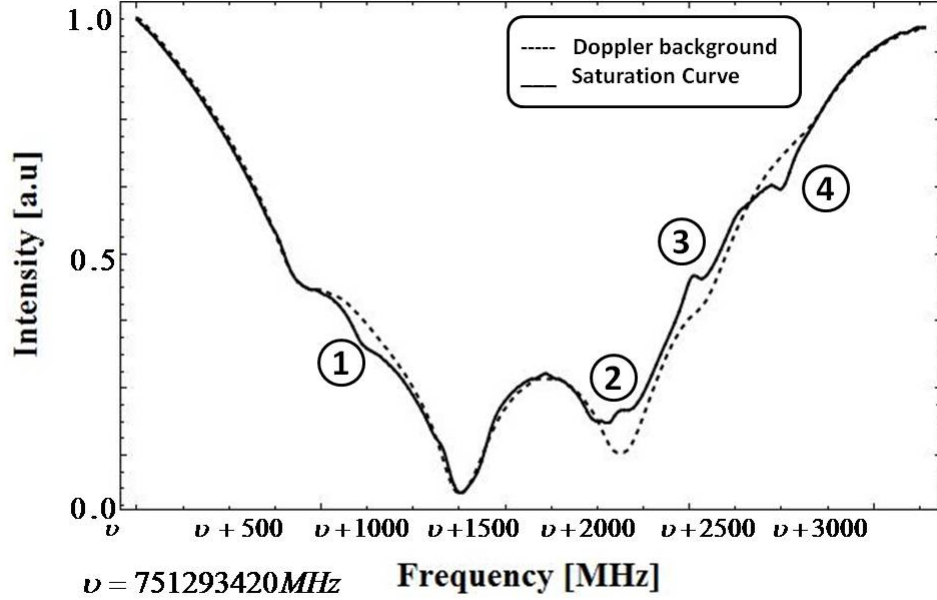
Figure 6.6: $^1S_0 \leftrightarrow {}^1P_1$ transition peaks for different isotopes of Yb obtained with saturation absorption spectroscopy. The transitions corresponding to labels 1 to 4 are shown in Table 6.3. The dashed line represents the Doppler background.

Scanning the wavelength at 10 Hz produces the saturation profile shown in figure 6.6. The dashed trace represents the Doppler background, obtained by blocking the pump beam, while the solid trace shows the resulting resonance peaks when the the pump beam is included. The saturation peaks for different isotopes can be seen by labels 1, 2, 3 and 4 on the profile, and the corresponding frequencies are listed in table 6.3. Also shown in table 6.3 are the results obtained with the spot method, and it can be seen that the wavelengths obtained from both methods are in good agreement. However, it can be seen that the signal-to-noise ratio using the saturation spectroscopy setup is poor compared to that of the spot method. Furthermore, saturation spectroscopy can only be used to determine Doppler free transition frequencies. The spot technique, on the other hand, can be adapted to measure Doppler shifted transition frequencies, thereby providing interaction wavelengths when the laser-atomic beam configuration is not perpendicular. Measurement of these Doppler shifted transition frequencies are presented below.

Peak	Isotope	Transition	Transition Frequency Frequency [THz] (Saturation)	Transition Frequency Frequency [THz] (Spot Method)
1	^{176}Yb	$^1S_0 \leftrightarrow {}^1P_1$	751.52615(6)	751.52615(6)
	^{172}Yb(*)	$^1S_0 \leftrightarrow {}^1P_1$	751.52714(12)	751.52720(12)
2	^{173}Yb(*)	$^1S_0(F=1/2) \leftrightarrow {}^1P_1(F=3/2)$	751.52714(12)	751.52720(12)
	^{173}Yb(*)	$^1S_0(F=1/2) \leftrightarrow {}^1P_1(F=7/2)$	751.52714(12)	751.52720(12)
3	^{171}Yb	$^1S_0(F=1/2) \leftrightarrow {}^1P_1(F=3/2)$	751.52760(6)	751.52749(6)
	^{170}Yb(*)	$^1S_0 \leftrightarrow {}^1P_1$	751.52779(12)	751.52780(12)
4	^{171}Yb(*)	$^1S_0(F=1/2) \leftrightarrow {}^1P_1(F=1/2)$	751.52779(12)	751.52780(12)

not resolved

Table 6.3: The absolute frequencies for $^1S_0 \leftrightarrow {}^1P_1$ transition line of Yb isotopes obtained by saturation spectroscopy and the spot technique.

6.1.3   Doppler Shifted Fluorescence Spot Technique

In many experiments the atomic motion is not necessarily perpendicular to the laser beams. In this situation a component of the atoms velocity is parallel (or antiparallel) to the laser beam and the frequency of the resonance line becomes Doppler shifted. The resulting frequency shift, Δf, can therefore be expressed as [75]

$$\Delta f = \frac{f}{c} v \cos(\theta) \tag{6.1}$$

where f is the Doppler free transition frequency, c is the speed of light, v is the mean velocity of the atoms along the direction of reference axis and θ is the angle between the atom motion and laser beam. The $v \cos(\theta)$ term represents the mean velocity component of the atoms parallel to the laser beam.

With a slight modification to the setup used in section 6.1 these Doppler shifted wavelengths can be measured. The change to the setup is illustrated in figure 6.7, with the modification being the rotation of atomic oven. The motivation behind the rotation is to increase the atomic flux along the desired direction, and also to use the cylindrical axis of the atomic oven as reference axis. It should be noted that the rotation is motivated purely for convenience and does not affect the final wavelength measurement. With these
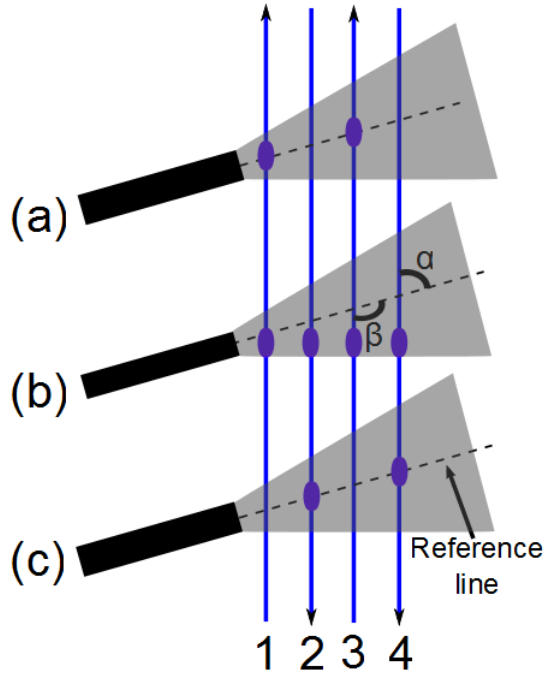
Figure 6.7: Illustration of the modified setup used to determine the Doppler shifted transition wavelengths. Laser beams 2 and 4 make an acute angle α while beams 1 and 3 make an obtuse angle β with the reference axis. In (a) the laser is red detuned from resonance, (b) the laser is on resonance and (c) the laser is blue detuned.

non-perpendicular geometries the direction of propagation of the laser beams is now an important factor. One pair of the laser beams (2 and 4) forms an acute angle, α, while the other pair of lasers (beam 1 and 3) form an obtuse angle β with reference axis. In both cases the magnitude of the angular difference from 90° (and hence the frequency shift) is the same, but the sign is different. To align a pair of spots to the reference axis the laser is detuned from resonance. Blue detuning aligns the spots corresponding to lasers 2 and 4 to the reference axis, while red detuning aligns the fluorescence spots corresponding to lasers 1 and 3 to the reference axis.

Demonstration of the Doppler shifted fluorescence spot technique is shown in figure 6.8. Here the laser is (a) red detuned to align the spots to the reference axis for an angle of $\alpha = 70^o$ and (c) blue detuned to align the spots for an angle of $\beta = 110^o$. When the laser is tuned to the Doppler free resonance measured in section 6.1, (b), the spots align perpendicular to the laser beams. This confirms the measured wavelengths are independent of the angle between the laser beam and atomic oven.

(a)

λ=398.91116 nm (angle = 110°)

(b)

λ=398.91128 nm (angle = 0°)

(c)

λ=398.91140 nm (angle = 70°)
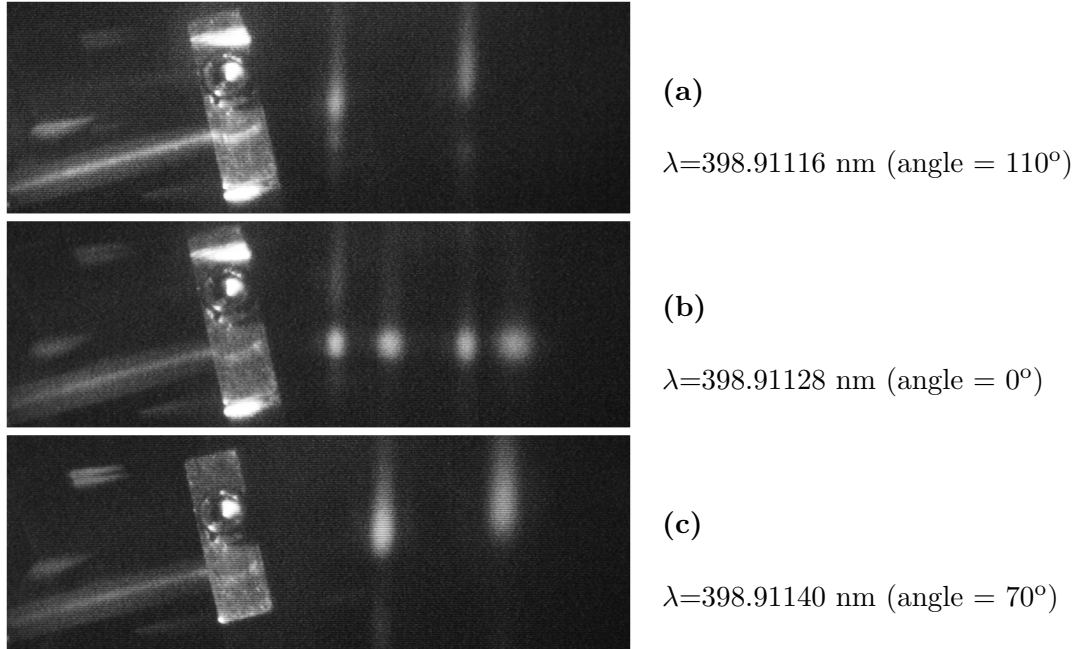
Figure 6.8: Images of the modified fluorescence spot technique. Pictures show the atomic ovens and fluorescence spots where the laser beams intersect the atomic beam taken at angles of (a) 110°, (b) 0°, and (c) 70°.

The reference axis is then rotated to angles of $\alpha = 63^o$, 70°, 75° and 80° with one pair of lasers, and hence $\beta = 117^o$, 110°, 105° and 100° with the other pair of lasers respectively. The measured Doppler shifted frequencies of ^{174}Yb atoms at each of these angles is shown in figure 6.9. The measured data is in good agreement with the theoretical fit provided by equation 6.1. To provide confirmation of these measured Doppler shifted wavelengths,

they are used in the final experimental setup, where laser and atomic beam form an angle of 63 $^\circ$. Using these wavelengths and a laser at 369 nm selective ionisation and trapping of the different ytterbium isotopes was successful [141].
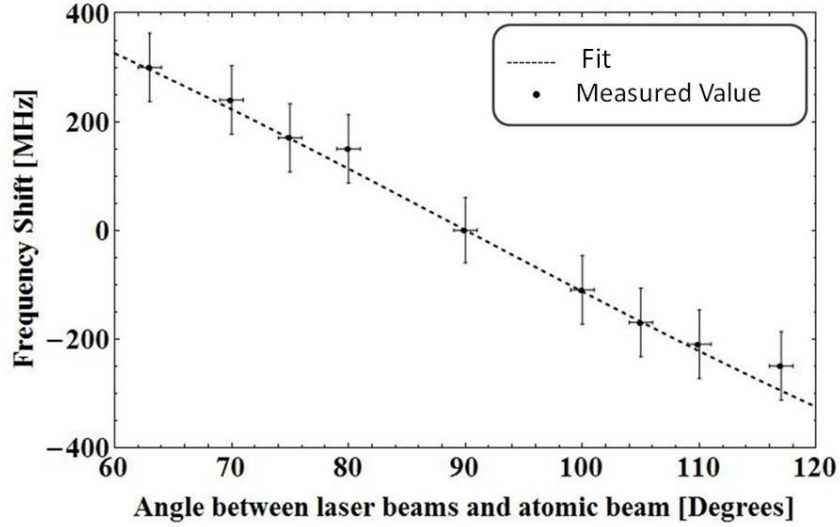
Figure 6.9: Doppler frequency shift in $^1S_0 \leftrightarrow ^1P_1$ transition of ^{174}Yb as a function of angle between the laser beams and atomic beam.

6.2   Yb$^+$ Doppler Cooling and Repump Wavelengths

The resonant wavelengths of the $^2S_{1/2} \leftrightarrow ^2P_{1/2}$ Doppler cooling and the $^2D_{3/2} \leftrightarrow ^3D[3/2]_{1/2}$ repump transitions are measured by scanning the respective laser, monitoring the frequency dependent fluorescence, then measuring the wavelength on a wavemeter (High Finesse; WS7). The wavelengths the $^2S_{1/2} \leftrightarrow ^2P_{1/2}$ transition wavelengths are determined as the wavelengths just before the fluorescence rapidly drops to background level, which corresponds to heating of the ion. The $^2D_{3/2} \leftrightarrow ^3D[3/2]_{1/2}$ transition wavelengths are determined as the wavelengths at which maximum fluorescence is obtained. For the experiment the intensity of the 369.5 nm and 935.2 nm beams are reduced to 0.4 Wcm^{-2} and 0.02 Wcm^{-2} respectively to reduce the effects of power broadening and ac Stark shifts. The measured cooling and repumping wavelengths (in vacuum) for the different Yb isotopes are shown in table 6.4. For ^{171}Yb$^+$ an external static magnetic field of 0.5 mT was applied to the ion to remove degeneracy within the hyperfine states, but keep the Zeeman shifts at a manageable level. The even isotopes however have no hyperfine states so the magnetic field was removed.

Isotope	$^2S_{1/2} \leftrightarrow {}^2P_{1/2}$ transition wavelength [nm]	$^2D_{3/2} \leftrightarrow {}^3D[3/2]_{1/2}$ transition wavelength [nm]
^{170}Yb$^+$	369.52364(6)	935.19751(19)
^{171}Yb$^+$	369.52604(6)	935.18768(19)
^{172}Yb$^+$	369.52435(6)	935.18736(19)
^{174}Yb$^+$	369.52494(6)	935.17976(19)
^{176}Yb$^+$	369.52550(6)	935.17252(19)

Table 6.4: Wavelengths (vacuum) for the $^2S_{1/2}|F = 1\rangle \leftrightarrow {}^2P_{1/2}|F = 0\rangle$ and $^2D_{3/2}|F = 1\rangle \leftrightarrow {}^3D[3/2]_{1/2}|F = 0\rangle$ transitions in Yb$^+$.

The measured 369.5 nm cooling wavelengths are in good agreement with those previously published by E. W. Streed *et al.* [139] who, using an Yb$^+$ hollow cathode lamp, observed a Doppler absorption line centred about 369.525nm. As a hollow cathode lamp was used, however, the observed line contained overlapping lines from the multiple ytterbium isotopes and was broadened to $\approx$3 GHz. While both measurements are consistent the results presented here are more precise. Due to infrequent population, precise transition wavelengths for the 638 nm $^2F_{7/2} \leftrightarrow {}^1D[5/2]_{5/2}$ transition are difficult to obtain. During experiments 120 Wcm^{-2} of 638 nm light is applied to the ion. Setting the laser wavelength to 638.618 nm for the even isotopes, and scanning between 638.610 nm and 638.616 nm for ^{171}Yb$^+$, no obvious fluorescence interrupts were observed, indicating these values are reasonably close to the exact transition wavelengths.

6.2.1 Error Analysis

The main sources of uncertainties of the measurements are from the absolute accuracy of the wavemeter, power broadening of the transition linewidths, ac Stark shifts, and Zeeman shifts. Each of these source are analysed below.

Wavemeter Uncertainty

This source of error is the most significant of those listed. The absolute accuracy of the wavemeter is specified to 60 MHz between 370 nm - 1100 nm and to 200 MHz below 370 nm. The 369.5 nm wavelengths are therefore inferred by halving the measured 739.05 nm wavelengths. This results in an uncertainty of 120 MHz compared to 200 MHz if the 369.5 nm wavelengths are measured directly. To eliminate systematic offsets the wavemeter is calibrated with a 780 nm laser, stabilised to 1 MHz, and a He-Ne laser, calibrated to <1 MHz. The wavemeter is also calibrated before and after each measurement and no change in calibration measurement were observed.

Power Broadening

Power broadening of a transition is expressed as $\Gamma' = \Gamma\sqrt{1 + s_0}$, where Γ is the transition natural linewidth, and $s_0 = I/I_{\text{sat}}$ is the laser-ion saturation parameter relating the laser intensity, I, to the saturation intensity of the transition, I_{sat} [75]. The 369.5 nm beam, with an intensity of 0.4 Wcm^{-2}, broadens the $^2S_{1/2} \leftrightarrow {}^2P_{1/2}$ transition by 40 MHz while the 935 nm beam, with an intensity of 0.02 Wcm^{-2}, broadens the $^2D_{3/2} \leftrightarrow {}^3D[3/2]_{1/2}$ transition by 32 MHz. Since the $^2S_{1/2} \leftrightarrow {}^2P_{1/2}$ Doppler cooling transition frequency is determined by the immediate drop in fluorescence, which occurs when the laser is blue-detuned from resonance, it is insensitive to power broadening. The widened transition linewidth therefore is expected to be a negligible source of measurement uncertainty.

AC Stark Shift

The first order AC stark shift is given by [75]

$$E_{\text{e,g}} = -\frac{\hbar}{2}\left(\Delta \pm \sqrt{\Delta^2 + |\Omega|^2}\right) \tag{6.2}$$

where $\hbar$ is the reduced Plank constant, Δ the laser detuning and $\Omega = \sqrt{(\Gamma^2 I)/(2I_{\text{sat}})}$ the transition Rabi frequency. As the wavelengths are measured on resonance $\Delta = 0$ the 369.5 nm beam, with an intensity of 0.4 Wcm^{-2}, shifts the $^2S_{1/2} \leftrightarrow {}^2P_{1/2}$ transition by 38 MHz while the 935.2 nm beam, with an intensity of 0.02 Wcm^{-2}, shifts the $^2D_{3/2} \leftrightarrow {}^3D[3/2]_{1/2}$ transition by 17 MHz.

Zeeman Shift

The frequency shift of atomic magnetic hyperfine states due to a magnetic Δf are expressed using the Breit-Rabi formula [145]

$$\Delta E = \frac{E_{\text{hf}}}{2(2I+1)} - g_{\text{I}}\mu_{\text{B}}m_F B \pm \frac{1}{2}\sqrt{E_{\text{hf}}^2 + \frac{4m_F}{2I+1}(g_{\text{J}} - g_{\text{I}})\mu_{\text{B}}BE_{\text{hf}} + (g_{\text{J}} - g_{\text{I}})^2\mu_{\text{B}}^2 B^2} \tag{6.3}$$

where E_{hf} is the energy splitting of the hyperfine states when no magnetic field applied, B the applied magnetic field, μ_{B} is the Bhor magnetron, h is the Plank constant, m_{F} the magnetic hyperfine state, and g_{I} and g_{J} are the nuclear and electronic g-factors respectively. g_{I} is several orders of magnitude lower than g_{J} so can be neglected, and g_{J} is expressed as [76]

$$g_{\mathrm{J}} = \frac{3}{2} + \frac{S(S+1) - L(L+1)}{2J(J+1)} \tag{6.4}$$

where J, L and S are the total, orbital and spin angular momenta of the electron respectively. A 0.5 mT external magnetic field applied when measuring $^{171}\mathrm{Yb}^+$ is estimated to change the $\Delta\mathrm{m}_F = \pm1$ transitions by $\approx \pm7$ MHz, while transition wavelengths between the magnetic field insensitive $m_F = 0$ state are not expected to change. Reducing the magnetic field to 0.25 mT reduces the $\Delta\mathrm{m}_F = \pm1$ transitions to $\approx \pm3.5$ MHz, but due to the relatively large uncertainty associated with the wavemeter, no observable change in the resonance wavelengths were measured. The magnetic field is removed for measurements of the even isotopes, leaving the ions exposed to low magnetic fields such as that from the Earth, which are estimated to induce a shift of only ≈1 MHz.

By combining all above errors, the overall uncertainty associated for the $^2S_{1/2} \leftrightarrow {}^2P_{1/2}$ transition is ±126 MHz, while for the $^2D_{3/2} \leftrightarrow {}^3D[3/2]_{1/2}$ transition is ±63 MHz.

Chapter 7

369 nm "ColdLase" Doppler Cooling Laser

"A common mistake that people make when trying to design something completely foolproof is to underestimate the ingenuity of complete fools."

-Douglas Adams, *Mostly Harmless*

At the start of the experiment light at 369 nm was achieved using expensive complex laser systems, such as dye lasers or frequency doubling systems. During the course of the experiment, however, laser diodes at 371 nm became available which, if cooled, could emit light at 369 nm. Operating these cold diodes in a standard external cavity arrangement would greatly reduce the expense and maintenance associated with obtaining this wavelength. Systems capable of cooling an external cavity diode laser to sub-zero temperatures have been constructed (Fletcher and Close [146], Kielspinski *et al* [62] and Nguyen *et. al.* [147]), however these systems have limitations. The Fletcher and Close system is not air-tight, which presents the risk of condensation on optical components. The Kielpinski system has no diode modulation capabilities so without external modulation it is restricted to cooling even isotope ions. The Nguyen system is housed inside a vacuum system, requiring the need for a vacuum pump and offering limited access once the system is in operation. The ColdLase system presented in this chapter is designed to improve upon the previous systems - to produce a cost effective, easy to maintain laser that can provide stable, single mode 369 nm light, which can also be modulated to enable cooling of ^{171}Yb$^+$.

7.1 Design Criteria

The first obvious criterion is to cool and stably maintain the diode at sub zero temperatures. It was advised by the manufacturer [148] that a temperature of -10 °C is required to obtain 369 nm from a 371 nm laser diode. To provide a comfortable error margin stable cooling down to at least -20 °C is therefore desired. The easiest and cheapest way to control the temperature is using a thermoelectric cooler (TEC). TEC's transfer heat through controlled electron movement so do not introduce the risks of vibrations or leaks associated with mechanical parts or cooling fluids. They are also relatively inexpensive to operate. Exposing the diode to the laboratory environment, however, can make cooling extremely difficult if not impossible. Hermetic isolation of the diode from this damp, hot and uncontrollable environment is therefore required. A second criterion is adjustability during operation. To achieve this only the diode and lens are mounted inside the enclosure, and the grating positioned outside. The enclosure must therefore have suitable feedthrough connections for the electrical components housed within it, as well an optical port that allows the beam to exit but minimises unwanted feedback into the diode. A means to reduce/remove the moisture from the air in the chamber is also required to avoid condensation on any of the optical surfaces. The system must be capable of passive heat dissipation to avoid unwanted vibrations onto the system. Finally a means to create frequency sidebands to access the hyperfine states in ^{171}Yb$^+$ would be advantageous.

7.2 ColdLase Design

The laser is based upon a Littrow configured external cavity diode laser (explained in detail in section 3.2). The design for the system is shown in figure 7.1. The whole ECDL is mounted on a single base which acts as the heatsink (1). The laser diode and aspheric lens are mounted inside the enclosure (2), and the diffraction grating (3) is positioned outside.

Inside the chamber the laser diode (10, Nichia: NDU1113E) and aspheric lens (13, Thorlabs: A390TM-A) are mounted in a collimation module (9) using a brass clamp ring (12) and a locking nut (not shown) respectively. The module is in contact with the cold side of a two stage thermoelectric cooler (15, TE Tech: te-2-(127-127)-1.3), while a thermistor recess (14) accepts a thermistor (Farnell: AD592ANZ) providing constant measurement of the module temperature. The hot side of the TEC is in contact with a podium (8), which acts as a thermal conduit to the bulk of the heat sink as well as positioning the beam at

1) Heat Sink
2) Airtight chamber
3) Adjustable grating mount
4) Anti reflection coated window
5) Electrical feedthrough
6) Vacuum connection port
7) Desiccant holder
8) Podium
9) Laser diode module
10) Laser diode
11) Laser diode socket
12) Laser diode clamping ring
13) Aspheric lens
14) Temperature sensor recess
15) Thermo electric cooler
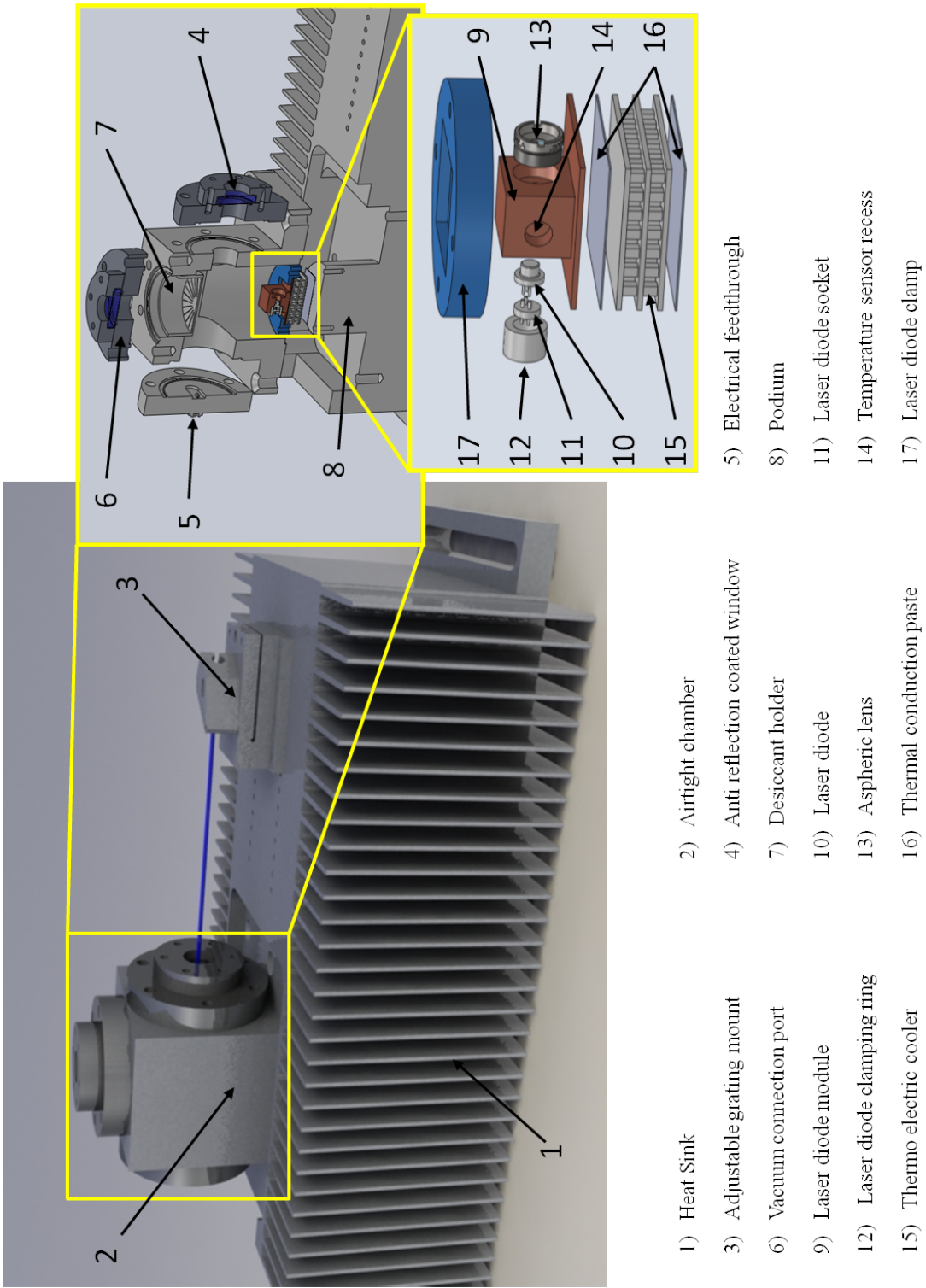16) Thermal conduction paste
17) Laser diode clamp

Figure 7.1: Overview of the laser system showing the external arrangement, an exploded view of the isolating chamber and an exploded view of the laser diode module.

the optical height of the table. Thermal grease (16) is used to improve the thermal contact at the module/TEC and TEC/podium interfaces. A clamp (17), constructed from teflon to minimise unwanted thermal conduction, secures the module to the podium.

The chamber is fitted with an anti-reflection coated window (4, Thorlabs: WL41050-C6) to allow the beam to exit while minimising reflections. The window is also mounted at an oblique angle to prevent any reflections being directed back into the diode. A second port on the chamber (5) is fitted with a sub-D9 connector, providing connections to the TEC and thermistor, and an SMA feedthrough allowing for a modulated signal to reach the laser diode. A third port (6) is designed to either accept a cup of desiccant (7) or to be fitted with a vacuum pump to reduce the moisture within the chamber. The desiccant used is 'Molecular Sieve' (Baltimore Innovations: BIL-10127-WSG), which can absorb up to 20% of its own weight in moisture. The volume (and therefore weight) of desiccant that can be held by the cup is enough to remove all moisture from within the chamber. The chamber is in thermal contact with the heatsink to ensure it has a temperature above the dew-point and that no condensation will occur on either side of the anti-reflection coated window.

An additional feature to this laser, which is not included in other designs, is the ability to change the diode grating distance. Changing this distance (and hence the free spectral range of the external cavity) changes the frequencies which resonate within the cavity, enabling the carrier frequency and any frequency sidebands to resonate simultaneously [99].

7.3 Thermal Considerations

Normally laser diodes are not cooled below $\approx$15 °C, and issues such as diode heating rates, cooling rates and energy dissipation can be treated as negligible. When cooling a diode to -20 °C, however, these considerations become more prominent, and can in fact limit the system's performance. To determine if a diode can be stably maintained at these sub-zero temperatures an in depth heat flow analysis of the systems is required.

For the ColdLase system the different aspects of the thermal system are shown in figure 7.2 and, as a result of the system design, are interconnected. The enclosure causes heating of the diode via black body radiation which is removed using the TEC and deposited onto the heat sink, along with the energy required to operate the TEC. The heat sink, however, is not a perfect emitter and will increase in temperature. The chamber temperature will subsequently increase and so will heating of the diode. To maintain the diode at the same temperature the TEC now has to remove energy from the diode faster while maintaining

an increased temperature gradient. This deposits more energy onto the heat sink again adjusting this interconnected thermal system. The system is expected to equilibrate, but the diode temperatures that can be maintained at equilibrium depends upon the efficiency the TEC and heat sink. To determine if the system can maintain a diode at -20 °C the different diode heating mechanisms are considered and compared against the performance of the TEC and heat sink.
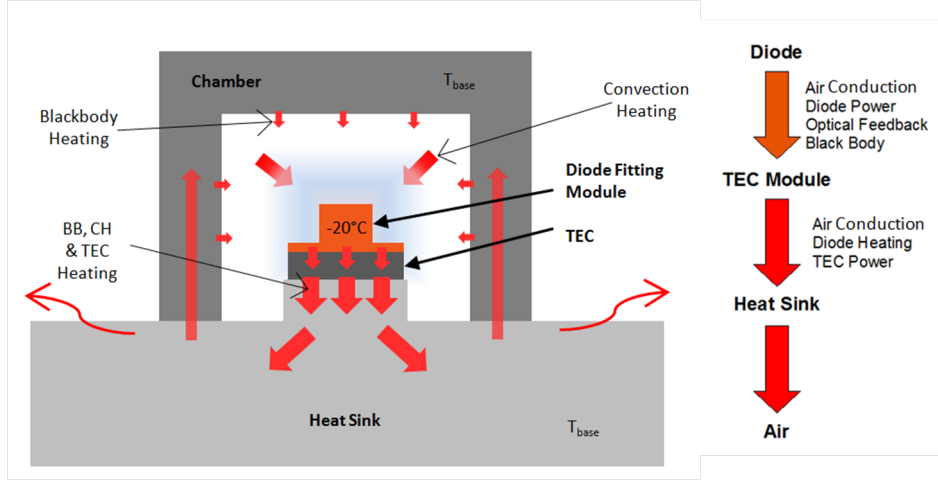
Figure 7.2: Heat flow through the system including heat sources onto and out of the diode.

Diode Operation

Laser diodes are not 100% efficient. A proportion of the electrical energy used to drive the lasers is converted into phonon modes that can heat the diode. For the analysis, any drive power not converted into light is assumed to be converted into phonon modes, and heating of the diode. Thus

$$P_\mathrm{p} = I_\mathrm{d}V_\mathrm{d} - P_\mathrm{opt} \tag{7.1}$$

where P_p is the phonon heating per unit time, I_d is the diode drive current, V_d is the diode drive voltage, and P_opt is the optical power emitted from the laser diode. The diode is specified to generate 20 mW at a maximum drive current and voltage of 85 mA and 5 V respectively. The worst case would therefore result in the diode at room temperature generating up to 405 mW of phonon heating per second. Diode efficiency is expected to increase as it is cooled, thereby decreasing phonon related heating. The change of this heating with temperature, however, is difficult to predict and assuming it as constant allows for the worst case scenario.

Optical Feedback

In the Littrow configuration the external diffraction grating reflects light back into the diode, with the magnitude of reflected light dependent upon the grating efficiency. Assuming this optical power is completely converted to heat within the diode, the power increase due to optical feedback is

$$P_{\text{fb}} = P_{\text{opt}} G_{\text{eff}} \tag{7.2}$$

where P_{fb} is the power of the reflected first order beam, and G_{eff} the first order diffraction efficiency of the grating. The grating used has an efficiency of 52% which, when considering 20 mW is emitted from the diode, results in an extra 10.4 mW of power within the diode.

Blackbody Radiation

All surfaces with temperatures above absolute zero naturally emit radiation, and the power radiated is given by the back body equation [149]

$$P = \epsilon \sigma A T^4 \tag{7.3}$$

where ϵ is the emissivity of the radiating material (unitless), σ the Stephen-Boltzmann constant ($5.67\text{x}10^{-8}$W m-2 K^{-4}), A the surface area, and T the surface temperature. It is assumed that all the radiation emitted by the chamber walls is absorbed by the module, and in turn all the radiation emitted by the module is absorbed by the chamber. The resulting heat flow onto the diode is described as

$$P_{\text{bb}} = \epsilon_c \sigma A_c T_c^4 - \epsilon_m \sigma A_m T_m^4 \tag{7.4}$$

where the subscripts c and m refer to the chamber and module respectively. The surface area and emissivity of the chamber are $(7.44 \pm 1)\text{x}10^{-3}$m^2 and 0.057 respectively, while the surface area and emissivity of the module are $(1.58 \pm 1)\text{x}10^{-3}$m^2 and 0.023 respectively.

Thermal Conduction

For two separated objects at different temperatures, heat will flow from the the hot object to the cold object. The rate of heat flow is expressed as [149]

$$P_c = A k \frac{\Delta T}{x} \tag{7.5}$$

where k is the thermal conductivity of the insulating material between the objects, A is the surface area of the 'hot' object, $\Delta T = T_c - T_m$ is the temperature gradient between the objects, and x the distance between the objects. In the model the two objects are the chamber and module. They have a minimum separation of 6 ± 1 mm and air ($k = 0.0245 \mathrm{Wm}^{-1}\mathrm{K}^{-1}$) is the medium between them. If a vacuum pump is used to evacuate the chamber then conduction heating can be reduced to almost zero. Since it is preferred for the system to operate without a vacuum pump this heating source is considered in the calculations.

Thermo-Electric Cooler

The module and laser diode are cooled using a thermo-electric cooler (TEC). The current and voltage needed to operate the TEC depend upon the required rate of energy transfer across the TEC and the temperature gradient between the cold side (laser diode) and hot side (heat sink), and are obtained from the device's performance plots. The TEC chosen for the system (TE Tech: te-2-(127-127)-1.3) is a two stage TEC, and has the performance plots shown in figure 7.3. The top plot indicates the current required to achieve a desired energy flow through the TEC at a given temperature gradient. The lower plot indicates the corresponding voltage required. The Qcold=0 curve (ticks) indicates the voltage required when no heat load is considered and only a temperature gradient is required. The DT=0 curve (squares) indicates the voltage required when only a heat load needs to be removed, but no temperature gradient is present. Since a heat load is removed across a temperature gradient the system operates at an intermediate gradient. As this curve is unknown the upper curve, which results in the highest heating power, is used.

Heat Sink

Heat sink performance, referred to as thermal resistance, is defined as the power required to increase the temperature of the heat sink by 1 °C. A heat sink with a low thermal resistance can dissipate heat quickly and will experience a lower temperature rise. The temperature rise can therefore be expressed as

$$T_{hs} = P_{hs}R_{th} \tag{7.6}$$

where P_{hs} is the power load deposited into the heat sink and R_{th} is the thermal resistance. Since the heat sink temperature affects the chamber temperature, which in turn affects the heating of the diode and subsequently P_{hs}, reducing the thermal resistance is of great
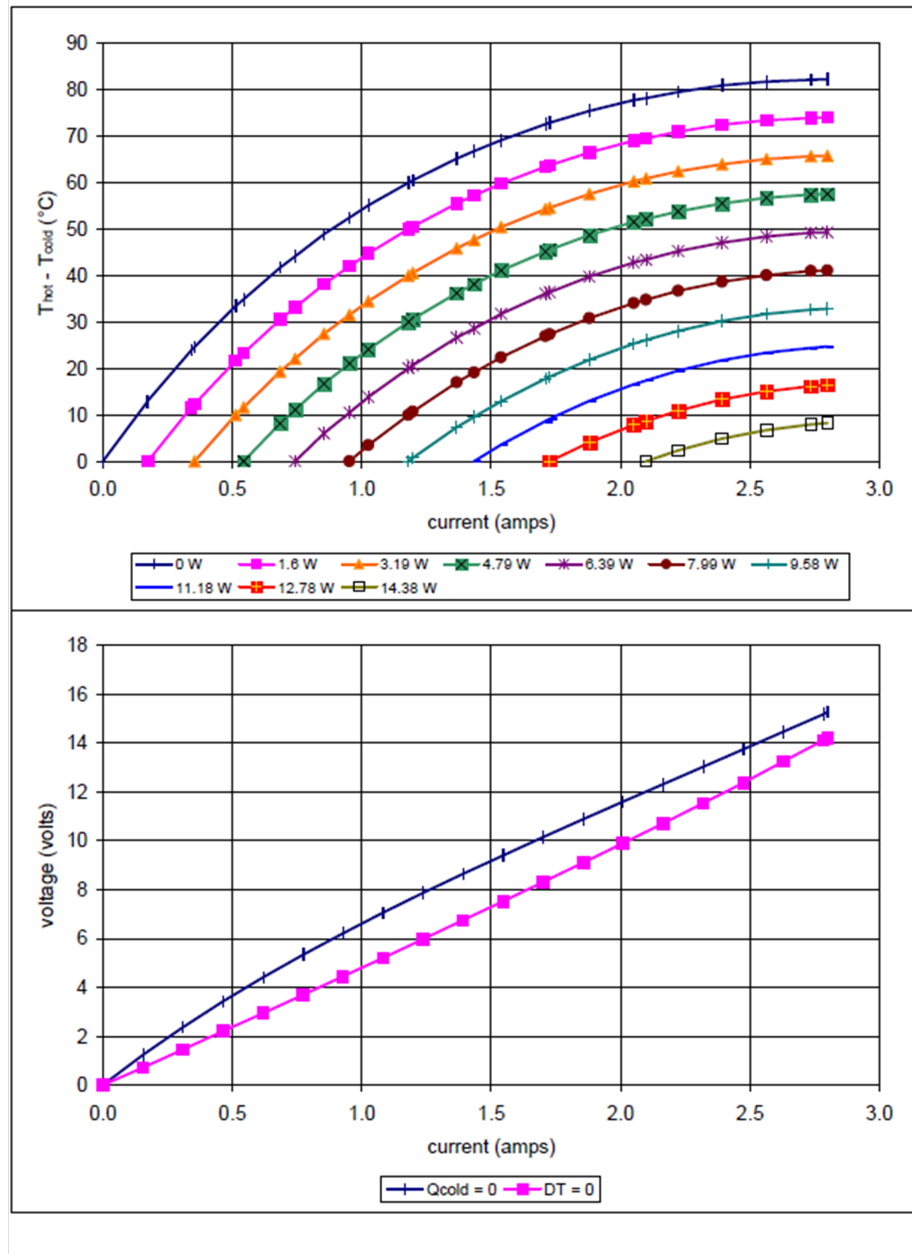
Figure 7.3: Electrical performance plots for the TEC (TE Tech: te-2-(127-127)-1.3). The top plot indicates the current required to achieve a desired energy flow at a given temperature gradient, while the lower graph indicates the voltage required.

importance. Given that heat is required to be dissipated passively (via radiation and conduction only) the thermal resistance is ultimately dependent upon the emissivity of the material used, and the surface area of the heat sink. It was decided to construct the heat sink using aluminium. Aluminium offers an emissivity of 0.057, and while other materials boast superior emissivities they are considerably more expensive. The expected reduction in thermal resistance from these materials is not justified by the price. The surface area is increased by machining fins into the side of the heat sink. The fin design is based upon a heat sink from Ficher Elektronik (sk101), however the fins on ColdLase

are slightly longer and also two sets of fins are used (one on each side). Based upon the efficiency of the Ficher Elektronik design the thermal resistance for the ColdLase heat sink is estimated to be 0.5 KW^{-1}. Oxidising the aluminium can further increase emissivity, but based upon the calculations shown in the next section this is not required.

7.3.1 Heat Flow Analysis

The diode heating mechanisms, TEC performance, heat sink efficiency, and the interconnected effects between these elements are now considered. The first stage of the thermal analysis is to determine the heating rate of the diode, and is estimated by adding the different heating influences

$$P_{\mathrm{m}} = P_{\mathrm{p}} + P_{\mathrm{fb}} + P_{\mathrm{bb}} + P_{\mathrm{c}} \tag{7.7}$$

where P_{m} is the heating rate of the module. To maintain a diode temperature the rate of cooling must equal the rate of heating. The power to be extracted by the TEC must therefore equal P_{m}. The electrical requirements of the TEC to maintain this power flow and also the temperature gradient are measured from the performance plots. The TEC drive power, P_{TEC} is then combined with the power removed from the diode to yield a total power deposited onto the heat sink of

$$P_{\mathrm{tot}} = P_{\mathrm{m}} + P_{\mathrm{TEC}} \tag{7.8}$$

Using this total power and the thermal efficiency estimate the increase in the heat sink temperature is determined. As mentioned before this increase in heat sink temperature increases the chamber temperature which increases diode heating from black body radiation and thermal conduction. The greater heat sink temperature also increases the temperature gradient across the TEC. Both of these influences increase the drive power of the TEC, which further increases the heat sink temperature. The heat flow analysis just described is therefore reiterated, but using the new heat sink and chamber temperature. Monitoring the heating rates, TEC drive power and heat sink temperature after each iteration determines whether or not the system will stabilise. Converging parameters indicate that the thermal flow within the system will equilibrate and the diode can be maintained at the desired temperature. Diverging parameters, however, indicate an unstable system and the diode temperature cannot be maintained. The thermal analysis for the ColdLase system is as follows.

1st Iteration

Initially the module temperature is set to -20 °C and the chamber is assumed to be at room temperature (25 °C), creating a temperature gradient of 45 °C across the TEC. The power onto the module from black body radiation and thermal conduction, at room temperature, are estimated to be $P_{bb} = 0.18$ W and $P_c = 1.47$ W respectively. When combined with the heating from phonons and optical feedback the heating rate of the module is $P_m = 2.05$ W. The TEC is therefore required to transfer 2.05 W across a temperature gradient of 45 °C and is achieved using an operating current of 1.1 A and voltage of 7 V (as shown by the solid line in figure 7.4). The total power deposited onto the heat sink is therefore $P_{tot} = 9.75$ W, and will cause the temperature of the heat sink and chamber to increase by 4.88 °C to 29.88 °C.

2nd Iteration

Using the new external temperature of 29.88 °C diode heating due to black body radiation and conduction increase to $P_{bb} = 0.21$ W and $P_c = 1.61$ W respectively. The temperature gradient across the TEC increases to 49.88 °C, and the operating current and voltage for the TEC increase to 1.3 A and 8.1 V respectively (dashed line). The total power deposited onto the heat sink is now $P_{tot} = 12.75$ W and the heat sink temperature increases to 31.38 °C. It can be seen that the temperature rise between the first and second iterations (1.74 °C) is less than the temperature rise between initial conditions and the first iteration (4.88 °C). These converging parameters suggest stability.

3rd Iteration

With a base temperature of 31.38 °C, heating from black body radiation and thermal conduction become $P_{bb} = 0.215$ W and $P_c = 1.67$ W respectively and the temperature gradient across the TEC increases to 51.38 °C. The TEC now requires $P_{TEC} = 11.9$ W of electrical power (dotted line) resulting in a power of $P_{tot} = 14.21$ W deposited into the heat sink. The heat sink temperature raises to 32.11 °C, which is only an increase of 0.59 °C from the last iteration. Since this increase is also within the error associated with reading the TEC performance plot, the system can be said to stably maintain the diode at -20 °C.
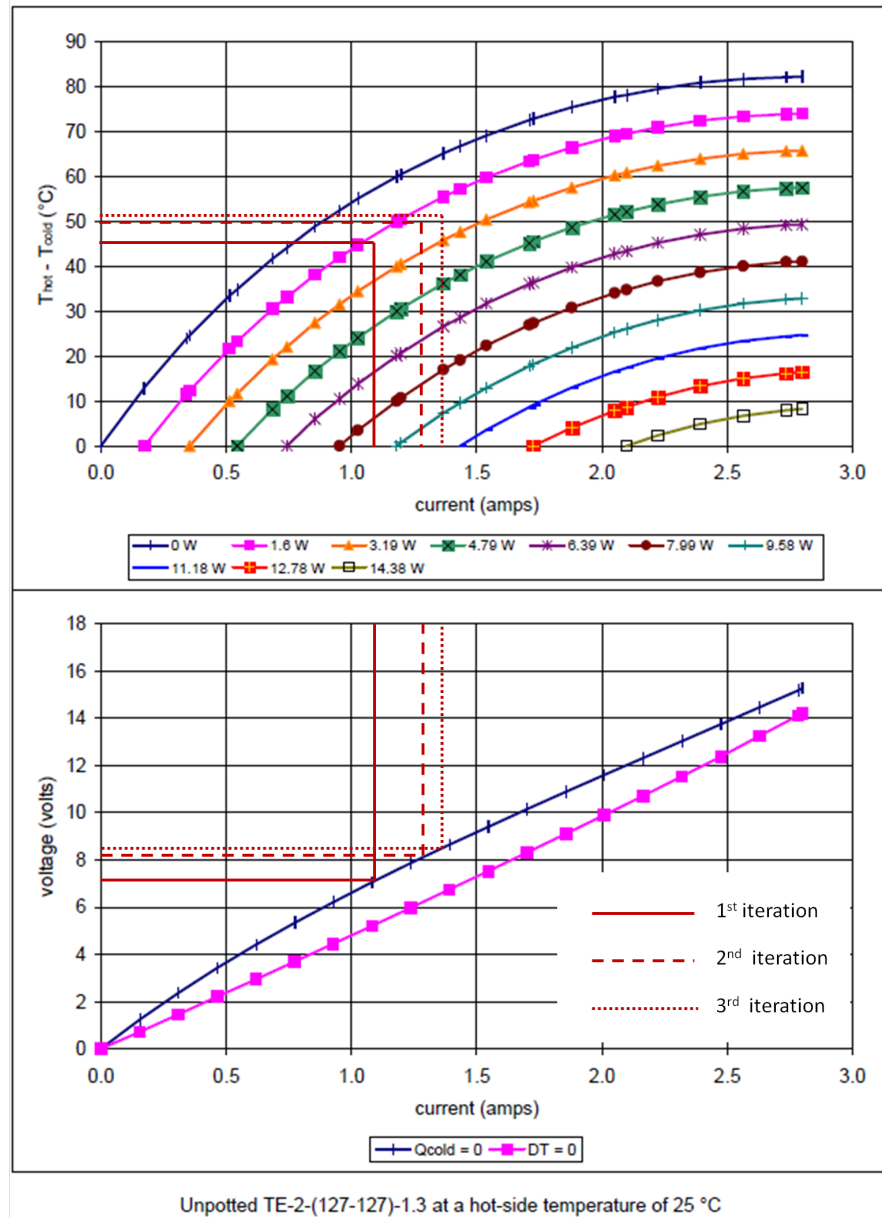
Figure 7.4: Electrical performance plots for the TEC (TE Tech: te-2-(127-127)-1.3), indicating the specific values used in the heat flow calculations.

7.4 ColdLase Performance

The laser is first operated with a diode at 800 nm, (Thorlabs: L808P010), and the ability to drag the wavelength with temperature is tested. For this test the grating is not included as it can also change the final emission wavelength of the laser. Instead the collimated beam from the diode is measured directly using a commercial wavemeter (High Finesse: WS7). The diode wavelength at different temperatures is shown in figure 7.5. It can be seen that the system can in fact stably cool the diode down to -35 °C and at 800 nm the wavelength changes at ≈ 0.2 nm°C^{-1}.

The 800 nm diode is replaced with the 371 nm Nichia laser diode and the system cooled
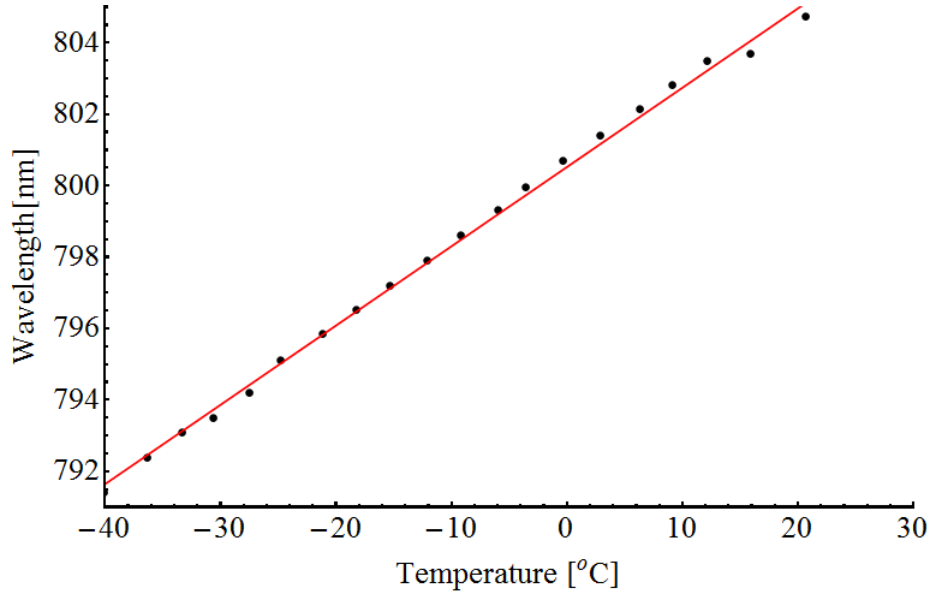
Figure 7.5: Wavelength vs temperature plot for the 800 nm laser diode.

again. The emission wavelength as a function of temperature is shown in figure 7.6. It can be seen that at 371 nm the wavelength changes at a rate of $\approx$0.05 nm^{o}C^{-1}, and in order to obtain 369.5 nm the diode only has to be cooled to $\approx$-4 ^{o}C, instead of the expected -20 ^{o}C.
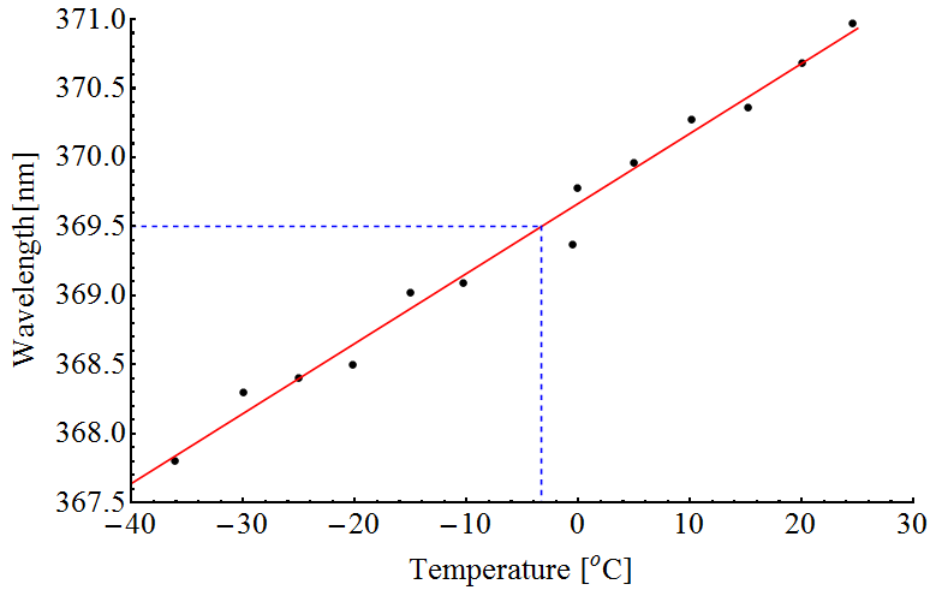
Figure 7.6: Wavelength vs temperature plot for the 371 nm laser diode.

The grating is then included to form the external cavity. Single mode performance at 369.05 nm was achieved by operating the diode at a temperature of -3.9 ^{o}C and driving it with a current of 42.7 mA. Unfortunately the diode also exhibits multimode behaviour and a maximum power of 2.8 mW is obtained from the ECDL, as opposed to the expected

maximum power of ≈10 mW. A bias tee (Pulsar Microwave: BT-29-400S) is connected to the SMA feedthrough adaptor and a 5 dBm 2.1 GHz signal, generated from a HP 8673C signal generator, is sent to the laser diode. The resulting 2.1 GHz sidebands, observed using a scanning transfer cavity with a free spectral range of 500(10) MHz, are shown in figure 7.7. The frequency sidebands are measured to be 116(10) MHz and have an amplitude of 13(2)% that of the carrier. The poor resolution in this figure is a result of the poor transmission through the cavity and only a small beam power measured by the photodiode. Although this lower resolution does increase the uncertainty of the frequency and amplitude of the sidebands, figure 7.7 has demonstrated that 2.1 GHz sidebands can be applied to the cold laser.
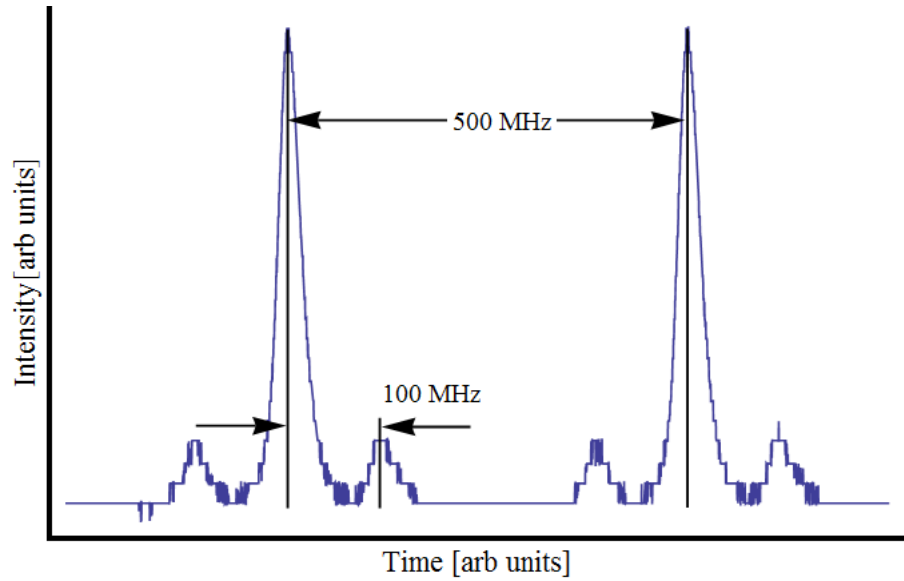
Figure 7.7: Spectrum of the 369 nm ColdLase beam when current modulated at 2.1 GHz. The apparent sideband peaks occurring at 100 MHz are 2.1 GHz sidebands corresponding to a carrier peak 4 free spectral ranges away. The +2.1 GHz sidebands are used for state preparation.

Unfortunately it was not possible to obtain 14.7 GHz sidebands using current modulation. This is not too surprising since the response of the laser diode is expected to be significantly slower than this. A means of obtaining these sidebands would be to position a 7.37 GHz bulk phase electro-optic modulator in the beam and use the second order sidebands. Alternatively applying 12.6 GHz microwave radiation to the ion will couple the $^2S_{1/2}|F = 0\rangle \leftrightarrow ^2S_{1/2}|F = 1\rangle$ states, thereby providing access to the $^2S_{1/2}|F = 0\rangle$ states. At the time of writing the system has been used to successfully cool the even Yb$^+$ isotopes. A lack of 14.7 GHz optical sidebands or a 12.6 GHz microwave source meant trapping of ^{171}Yb$^+$ with this system could not be shown.

Chapter 8

Qubit Manipulation

-I'm a genius again!... Ask me a question. Any question, and I'll answer it.

-Any question...How to break the speed of light?... How to marry quantum

mechanics and classical physics?... anything? OK, would you like some toast?

-Holly and Talkie Toaster, *Red Dwarf*

Trapped ions are regarded as an extremely suitable system for realising the quantum information processor. The basic tools for reliable information processing are the rotation of the qubit and the ability to couple to the external motion. Rotating the qubit takes advantage of the quantum mechanical principle of superposition enabling arbitrary states of $\alpha|\uparrow\rangle + \beta|\downarrow\rangle$ to be created. Motional coupling enables ions to become entangled, allowing for the exchange of information between qubits and the formation of complex gates.

It is also preferable for the ion to be cooled to the motional ground state. Decoherence of a superposition or entangled state is a limiting factor of the fidelity of any corresponding operation. While many factors contribute to decoherence high ion energies provide a significant limitation. Cooling to the motional ground state increases the coherence, and fidelities, of any logic operations.

Qubit rotation is achieved through transitions that couple both of the qubit states. Entanglement and ground state cooling, however, also require the ability to couple to motion. In chapter 2 different techniques of qubit manipulation are discussed and it is the two photon stimulated Raman transitions, capable of driving all the required manoeuvres, that is the preferred approach. In this chapter different approaches of implementing a Raman transition in $^{171}\text{Yb}^+$ are discussed and a novel setup to exciting a Raman transition tested.

8.1 Stimulated Raman Transitions

Two-photon Raman transitions involve three states: the two qubit states ($|\downarrow\rangle$ and $|\uparrow\rangle$) and an excited state $|e\rangle$, arranged in a Λ configuration as shown in figure 8.1. The frequency span between the qubit states, $|\uparrow\rangle$ and $|\downarrow\rangle$, and the excited state are $\omega_{\uparrow,e}$ and $\omega_{\downarrow,e} = \omega_{\uparrow,e} + \omega_0$ respectively, and are coupled using optical fields, $\bar{E}_l(r) = E_l(r)\cos(\bar{k}_l \cdot \bar{r} - \omega t - \phi_l)\epsilon_l$, where $l = \alpha, \beta$ respectively. Both fields are detuned from the excited state by Δ and have a frequency difference of $\omega_\alpha - \omega_\beta = \omega_0 + \delta\omega$.
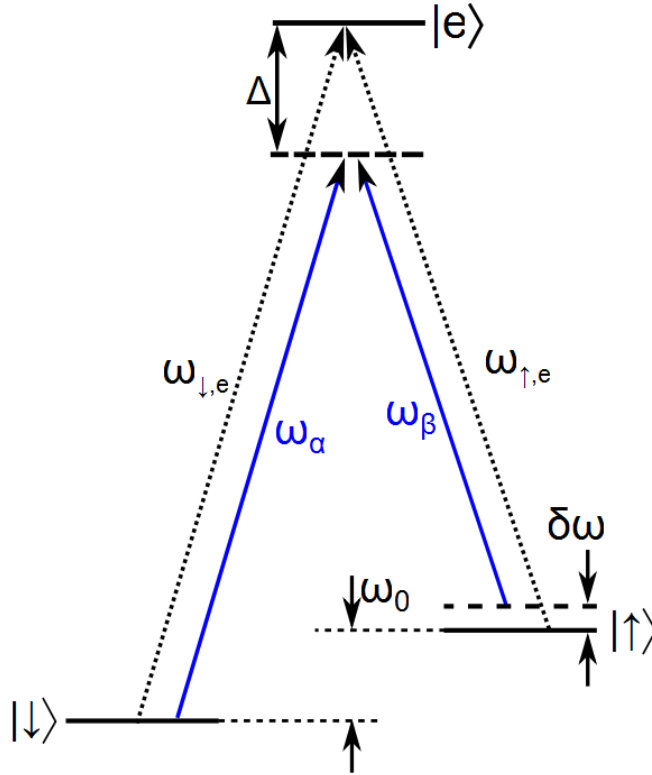
Figure 8.1: Two photon stimulated Raman transition. Fields at ω_α and ω_β, detuned from resonance by Δ, couple the qubit states $|\uparrow\rangle$ and $|\downarrow\rangle$ via the excited state $|e\rangle$.

To understand the process of a Raman transition first consider the Hamiltonian describing the interaction: $\hat{H}_i = -\hat{\mu} \cdot (\bar{E}_\alpha + \bar{E}_\beta)$, where $\hat{\mu}$ is the electric dipole transition and the subscripts indicate the different optical fields. Inserting the expressions for the electric fields into the interaction Hamiltonian then yields

$$\hat{H}_i = -\hbar \left[g_\alpha e^{i(\bar{k}_\alpha \cdot \bar{r} - \omega_\alpha t + \phi_\alpha)} + g_\beta e^{i(\bar{k}_\beta \cdot \bar{r} - \omega_\beta t + \phi_\beta)} + h.c. \right] \tag{8.1}$$

where $g_l = -\hat{\mu} \cdot E_l \epsilon_l(r)/(2\hbar)$ is the coupling strength between the qubit states and the excited state. This Hamiltonian, however, describes transitions within a three-level sys-

tem. To be suitable for coherent population transfer between the two qubit states direct interaction with the excited state must be removed, reducing the configuration to a two level system.

Adiabatic Elimination of Excited State

In the situations where the Raman beams are far-detuned from the excited state $|e\rangle$, such that $\Delta_R \gg \gamma, |g_l^2|$, population of the excited state can neglected. Several derivations showing adiabatic elimination can be found [67,89] with perhaps the more intuitive derivations provided by Deslauriers [87] and King [68], who present the elimination using state populations. Following Deslauriers and King the state population of the three level system is first obtained:

$$
\begin{aligned}
\dot{c}_{e,m} &= i\frac{g_\alpha}{2} \sum_{m=0}^{\infty} e^{it[\omega_x(n-m)+\Delta+\delta\omega]} \langle m|e^{ik_\alpha \cdot x}|n\rangle c_{\uparrow,n} \\
&\quad + i\frac{g_\beta}{2} \sum_{m=0}^{\infty} e^{it[\omega_x(n-m)+\Delta]} \langle m|e^{ik_\beta \cdot x}|n\rangle c_{\downarrow,n} \tag{8.2}
\end{aligned}
$$

$$
\dot{c}_{\uparrow,m} = i\frac{g_\alpha^*}{2} \sum_{m=0}^{\infty} e^{it[\omega_x(n-m)-\Delta-\delta\omega]} \langle m|e^{-ik_\alpha \cdot x}|n\rangle c_{e,n} \tag{8.3}
$$

$$
\dot{c}_{\downarrow,m} = i\frac{g_\beta^*}{2} \sum_{m=0}^{\infty} e^{it[\omega_x(n-m)-\Delta]} \langle m|e^{-ik_\beta \cdot x}|n\rangle c_{e,n} \tag{8.4}
$$

These state populations are then transformed to a rotating frame given by $c_{e,n} \to c_{e,n}' e^{i\Delta t}$, yielding

$$
\begin{aligned}
\dot{c}_{e,m}' &= \frac{g_\alpha}{2} \sum_{m=0}^{\infty} e^{i[\omega_x(n-m)+\delta\omega]t} \langle m|e^{ik_\alpha \cdot x}|n\rangle c_{\uparrow,n} \\
&\quad + \frac{g_\beta}{2} \sum_{m=0}^{\infty} e^{i[\omega_x(n-m)]t} \langle m|e^{ik_\beta \cdot x}|n\rangle c_{\downarrow,n} - i\Delta c_{e,n}' \tag{8.5}
\end{aligned}
$$

$$
\dot{c}_{\uparrow,m} = \frac{g_\alpha^*}{2} \sum_{m=0}^{\infty} e^{i[\omega_x(n-m)-\delta\omega]t} \langle m|e^{-ik_\alpha \cdot x}|n\rangle c_{e,n}' \tag{8.6}
$$

$$
\dot{c}_{\downarrow,m} = \frac{g_\beta^*}{2} \sum_{m=0}^{\infty} e^{i[\omega_x(n-m)]t} \langle m|e^{-ik_\beta \cdot x}|n\rangle c_{e,n}' \tag{8.7}
$$

The term $\dot{c}_{e,m}'$ from equation 8.5 is now neglected using the assumption $\dot{c}_{e,m}' \ll i\Delta c_{e,m}'$. This assumption implies that changes in the excited state population do not affect the long term populations of the resulting two level system. Under this assumption the average excited state population, $c_{e,m}'$, can therefore be described using the dynamics of the two

qubit levels as

$$
\begin{aligned}
c'_{e,m} &= i\frac{g_\alpha}{2\Delta}\sum_{m=0}^{\infty} e^{i[\omega_x(n-m)+\delta\omega]t}\langle m|e^{ik_\alpha\cdot x}|n\rangle c_{\uparrow,n} \\
&+ \frac{g_\beta}{2}\sum_{m=0}^{\infty} e^{i[\omega_x(n-m)]t}\langle m|e^{ik_\beta\cdot x}|n\rangle c_{\downarrow,m}
\end{aligned}
\tag{8.8}
$$

Plugging this into equations 8.6 and 8.7, yields the dynamics of the two-level system

$$
\dot{c}_{\uparrow,n} = \frac{|g_\alpha|^2}{2\Delta}c_{\uparrow,n} + i\frac{g_\alpha g_\beta^*}{2\Delta}\sum_{m=0}^{\infty} e^{i[\omega_x(m-n)-\delta\omega]t}\langle n|e^{i\Delta kx}|m\rangle c'_{\downarrow,m}
\tag{8.9}
$$

$$
\dot{c}_{\downarrow,n} = \frac{|g_\beta|^2}{2\Delta}c_{\downarrow,n} + i\frac{g_\alpha^* g_\beta}{2\Delta}\sum_{m=0}^{\infty} e^{i[\omega_x(n-m)+\delta\omega]t}\langle n|e^{-i\Delta kx}|m\rangle c'_{\uparrow,m}
\tag{8.10}
$$

The first terms in these equations, $\frac{|g_\alpha|^2}{2\Delta}$ and $\frac{|g_\beta|^2}{2\Delta}$, are the ac Stark shifts experienced by $|\uparrow\rangle$ and $|\downarrow\rangle$ respectively. To simplify the derivation these contributions can be removed by either redefining the energies of $|\uparrow\rangle$ and $|\downarrow\rangle$ to include the shifts or by transforming to a rotating frame of the ac Stark shifted resonance.

The remainder of equations 8.9 and 8.10 describe the system dynamics, and how qubit and motional states can undergo a population transfer. These expressions can be seen to be similar to the single photon coupling described earlier, but with k replaced by $\Delta\bar{k}$, where $\Delta\bar{k} = \bar{k}_2 - \bar{k}_1$ is the wavevector difference between the two beams. While the increased wavevector of the optical radiation enables stronger motional coupling, the final coupling strength in a Raman transition is determined by the wavevector difference, $\Delta\bar{k}$, from the beam orientation. The optimum geometry uses two counter propagating beams aligned along a trap axis, yielding $\Delta\bar{k} = 2k$. For co-propagating beams, however, $\Delta\bar{k} = 0$ which cannot induce motional coupling. Similarly if the resultant wavevector is $\Delta\bar{k}\cdot z = 0$ motional coupling is not possible.

Provided $\Delta\bar{k}$ offers sufficient coupling strength, the motional states that can be coupled are determined by the detuning of the beat-note frequency, $\delta\omega$. As illustrated in figure 8.2, using a detuning of $\delta\omega = 0$ results in coupling to the same motional state, $|m\rangle = |n\rangle$, while a detuning of $\delta\omega = \pm\omega_i$ couples motional states $|m\rangle = |n\pm 1\rangle$.

If we now consider the system to be in the rotating frame of the Stark shifted resonance and the beatnote tuned near a motional resonance, $\delta\omega \approx (n-m)\omega_i$, applying a rotating wave approximation results in a single stationary term in each equation. The equations
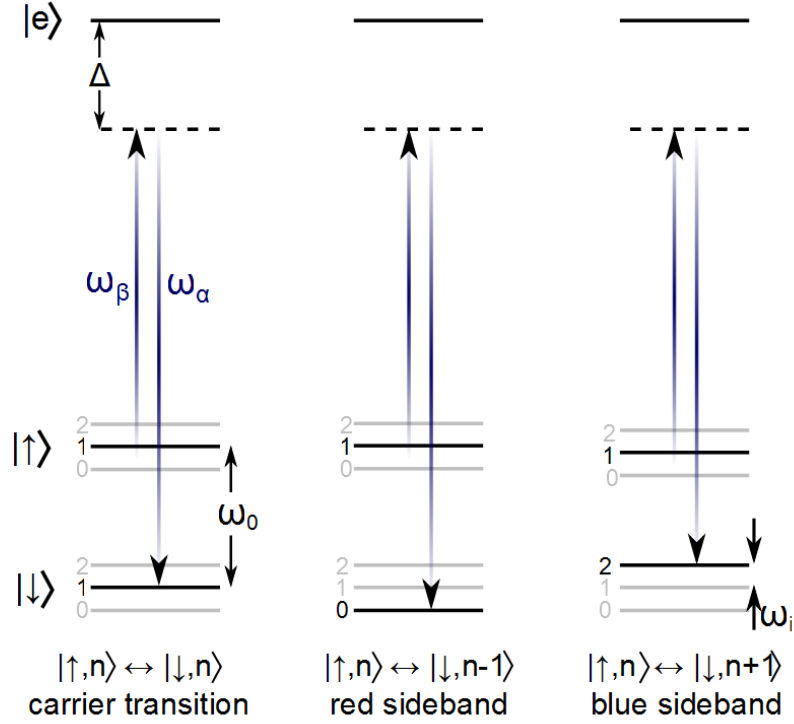
Figure 8.2: Coupling between different motional states using a stimulated Raman transition. Detuning the beat frequency $\delta\omega = 0$ results in a carrier transition, $\delta\omega = +\omega_i$ couples to a lower motional state, and $\delta\omega = -\omega_i$ couples to a higher motional state.

of motion then become

$$\dot{c}_{\uparrow,n} = -i\Omega_{n,m}e^{-i\delta\omega t}c_{\downarrow,m} \tag{8.11}$$

$$\dot{c}_{\downarrow,n} = -i\Omega_{n,m}^{*}e^{i\delta\omega t}c_{\uparrow,m} \tag{8.12}$$

where $\Omega_{n,m} = \Omega_{m,n}$ is the generalised Rabi frequency between the qubit states and motional states, and is expressed as

$$\Omega_{n,m} = \frac{g_\alpha g_\beta^*}{2\Delta}\langle m|e^{\,i\Delta k_z z}|n\rangle \tag{8.13}$$

where $g_\alpha^* g_\beta/2\Delta$ is the base Raman transition frequency. It can be seen that the resultant transition frequency of a two-photon Raman transition has a quadratic dependence upon the electric field strength.

Off Resonant Scattering

Unfortunately coupling to the excited state is an unavoidable source of decoherence. Although the lasers are detuned from the excited state off resonant coupling is only reduced, not eliminated. The rate of spontaneous coupling depends upon the laser intensity and

detuning and can be estimated by considering the general expression for scatter rate [75].

$$\gamma_p = \frac{\gamma s/2}{1 + s + (\frac{2\Delta}{\gamma})^2} \qquad (8.14)$$

where Δ is the detuning, γ the natural linewidth and s the saturation parameter. When exciting a Raman transition the lasers are detuned from resonance such that $(2\Delta/\gamma)^2 \gg (1+s)$, the spontaneous emission rate can then be approximated to

$$\gamma_p \approx \frac{s\gamma^3}{8\Delta^2} \qquad (8.15)$$

It is more informative to show the probability of a spontaneous scatter event occurring during a stimulated Raman transition. This is achieved by comparing the off-resonant coupling rate to the Raman transition rate. The probability is then

$$P = \frac{\gamma_p}{\Omega_{\text{Ram}}} = \frac{\gamma}{8\Delta} \qquad (8.16)$$

where $\Omega_{\text{Ram}} = s\gamma^2/\Delta$. It can be seen that the probability of off resonant coupling scales as $1/\Delta$, however the Raman transition rate, as shown in equation 8.13, also scales as $1/\Delta$. By increasing the detuning to reduce off resonant scattering a greater laser intensity is required to maintain a sufficiently high transition frequency. A compromise must be made between achievable laser power and off resonant scattering is usually required.

It has been shown by Ozeri *et al.* [150] that for detunings beyond the fine structure splitting $\Delta \gg \omega_f$ coherence can be preserved even during spontaneous scattering. Spontaneous scattering is the sum of spontaneous Rayleigh (elastic) scattering and spontaneous Raman (inelastic) scattering. Rayleigh scattering returns the ion to the same internal state while Raman scattering transfers the ion to a different internal state. A Rayleigh scattered photon therefore preserves the quantum nature of the system, however, Raman scattering carries information relating to a hyperfine state and effectively measuring the atomic state, destroying any coherence. In the regime defined by $\Delta > \omega_f$ total scattering scales as $1/\Delta^2$ while Raman scattering scales as $1/\Delta^4$, suppressing the decohering scattering. In this regime however, Raman, transition frequencies also scale as $1/\Delta^2$ so requires significant laser intensities to maintain transition rates. If sufficient laser power can be achieved then this is the preferred regime as the probability of an unwanted scatter event during a Raman transition scales as $1/\Delta^2$, (as opposed to $1/\Delta$ in the $\Delta < \omega_f$ regime).

8.2   Raman Transitions in ^{171}Yb$^+$

Previous implementations of Raman transitions use an $S \leftrightarrow P$ dipole transition, which would suggest the $^2S_{1/2} \leftrightarrow {}^2P_J$ in ^{171}Yb$^+$ should be used. However, the light required to access the ^{2}P$_{1/2}$ and ^{2}P$_{3/2}$ manifolds is at 369 nm and 329 nm respectively, which would require an additional expensive laser source. A study of the energy level structure of ^{171}Yb$^+$ presents possible alternatives: the quadrupole transitions to the low lying ^{2}D$_J$ manifolds. At first glance this might seem ridiculous since Raman transition rates depend upon transition linewidths, but the wavelengths of the two manifolds are at 411 nm and 435 nm. These wavelengths can be obtained from inexpensive laser diodes which, if they can supply sufficient optical power, could make a quadrupole transition a suitable alternative. To analyse both approaches the Raman transition rate, equation 8.13, is first re-expressed into a more general form using a derivation presented by D.F.V. James [151]. The derivation, found in Appendix H, shows that Raman transitions via dipole and quadrupole transitions can be expressed as

$$\Omega_{Ram} = \frac{e^2 \Gamma}{4\hbar^2 c \alpha k^3} \frac{P}{\pi r \varepsilon_0 c} \sum_J \sum_{F=|I-J|}^{I+J} \sum_{m=-F}^{F} \left(\frac{\sigma_i^{(s)} \chi_i^{\Delta m} \sigma_j^{(s)} \chi_j^{\Delta m}}{\Delta_J} \right) \qquad (8.17)$$

where e is the electron charge, Γ the spontaneous decay rate of the excited state, $\hbar$ the reduced Plank constant, c the speed of light, α the fine structure constant, k the wavevector of the light used, P the total power incident upon the ion from both beams, r the beam waist, and ε_0 the permittivity of free space. The $\sigma^{(s)}$ terms are the Clebsch-Gordan coupling coefficients between specific m_F states with $s = 1, 2$ representing a dipole and quadrupole transition respectively, and i, j correspond to the transitions $|\downarrow\rangle \leftrightarrow |e\rangle$ and $|\uparrow\rangle \leftrightarrow |e\rangle$ respectively. Δ_J is the detuning of the radiation from the specific J manifold, and the $\chi^{\Delta m}$ term describes the relative direction and radiative patterns of the radiation and quantisation axis. The sums indicate that all available channels for exciting a transition are considered. For excitation via the P-manifold $J = 1/2$ and $3/2$, while for the D-manifold $J = 3/2$ and $5/2$.

The coupling coefficients between different $m_{\rm F}$ states, and available channels between the qubits states and excited states, are shown in appendix I. To excite a Raman transition both qubit states must couple to the same excited state. As illustrated in the appendix, only the $|^2P_{1/2,3/2}, F = 1, m_F = \pm 1\rangle$ states or the $|^2D_{3/2,5/2}, F = 2, m_F = \pm 1, 2\rangle$ states can be used. Due to geometrical restrictions however, the available states in the D manifolds are reduced to $|^2D_{3/2,5/2}, F = 2, m_F = \pm 1\rangle$, which is discussed next.

8.2.1 Geometrical Considerations

The expected experimental setup is shown in figure 8.3, indicating the relative beam paths, and the direction of the quantisation axis. Since a multilayer trap is used the beams are restricted to propagate at an angle of 45° to the trap axis and 90° with respect to each other. The required beam polarisations are then dictated by the transition to be excited and also the coupling coefficients.
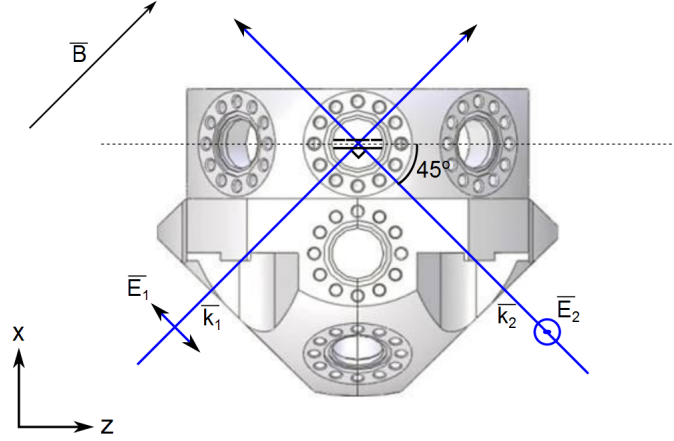

Figure 8.3: Non co-propagating Raman beam setup. The beams propagate 45° to the trap axis and 90° with respect to each other. The resulting wavevector difference $\Delta \bar{k}$ is along the z-axis. The beam polarisations and orientation relative to the quantisation axis result in optimal coupling for the $^2\mathrm{S}_{1/2} \leftrightarrow {}^2\mathrm{P}_\mathrm{J}$ manifolds.

When coupling via the $|^2P_J F = 1, m_F = \pm 1\rangle$ states the optimum Raman transition rate is achieved using the polarisation arrangement shown in figure 8.3 [89]. Since only $\Delta m_F = \pm 1$ transitions can be used both beams should be polarised perpendicular to the quantisation axis. The product of the coefficients describing coupling via the $|^2P_{1/2,3/2}, = 1, m_F = -1\rangle$ states $(-1/\sqrt{3} \times -1/\sqrt{3}, \sqrt{2/3} \times -1/\sqrt{6})$ has equal amplitude, but opposite sign compared to coupling via the $|^2P_{1/2,3/2}, F = 1, m_F = -1\rangle$ states $(1/\sqrt{3} \times -1/\sqrt{3}, \sqrt{2/3} \times 1/\sqrt{6})$. To account for this '$\pi$'-phase shift the product of the field components driving a transition via the $m_F = -1$ states, $E_{-,\alpha} E^*_{-,\beta}$, must have a π phase shift relative to the fields exciting a transition via the $m_F = +1$ states, $E_{+,\alpha} E^*_{+,\beta}$ [89]. This phase shift is created using the configuration illustrated in figure 8.3. The σ_+ and σ_- components of the beam travelling parallel to the quantisation axis have the same phase. However the beam travelling perpendicular to the quantisation axis is polarised in the y-axis and the circular components have a π phase shift. The resulting product of the fields $E_{-,\alpha} E^*_{-,\beta} = -E_{+,\alpha} E^*_{+,\beta}$ has the phase shift required for the transition amplitudes to constructively interfere.

To excite via the D manifolds the required polarisations are inferred from the results presented by Roos [152] and Kirchmair [153]. According to Kirchmair $m_F \leftrightarrow m'_F$ quadrupole transitions can be treated as $m_j \leftrightarrow m'_j$ transitions, and both Roos and Kirchmair have identified polarisations that enable $\Delta m_F = \pm 1, 2$ transitions. To optimally excite a $\Delta m_F = \pm 2$ transition the quantisation axis, laser propagation, and laser polarisation must be mutually orthogonal. However, the coefficients describing coupling via the $m_F = \pm 2$ excited states also have the π-phase shift. The resulting configuration to excite a Raman transition would therefore require both beams to be polarised mutually orthogonal to each other and to the quantisation axis. As it is impossible to achieve this configuration, exciting a Raman transition via the $\Delta m_F = \pm 2$ states is impossible. Kirchmair and Roos have shown that to excite a $\Delta m_F = \pm 1$ transition circularly polarised light can be used. This however will only couple to either the $m_F = 1$ or $m_F = -1$ state, but not both.

Assuming the above configurations the geometric factor when coupling via either m_F state in the $|^2 P_J\rangle$ manifolds is $\chi^{\pm 1} = 1/\sqrt{2}$. When coupling via either of the m_F states in $|^2 D_J\rangle$ manifolds, each beam results in a different geometric factor. For the beam perpendicular to the quantisation axis $\chi^{\pm 1} = 1/(2\sqrt{3})$, while for the beam parallel to the quantisation axis $\chi^{\pm 1} = 1/\sqrt{3}$ [153].

8.2.2 Comparison

The ability to excite a Raman transition via the $^2 S_{1/2}|F = 1, m_F = 0\rangle$ and the $|^2 D_J, F = 2, m_F = 1/-1\rangle$ states is now assessed. Due to the narrow linewidths of quadrupole transitions the detunings from either the $^2 D_{3/2}$ or $^2 D_{5/2}$ manifolds are expected to be significantly less that the separation of the D states. Thus the contribution from one manifold is expected to be negligible when coupling to the alternative manifold. The two manifolds can therefore be considered as two different states. The larger linewidths of the dipole transitions, however, demand larger detunings and if detuning is on the order of the fine structure splitting coupling to both of the manifolds must be considered.

Previous experiments have achieved rates of $\Omega_{\text{Ram}}/2\pi = 100$ kHz [81]. Thus a transition of at least $\Omega_{\text{Ram}}/2\pi = 50$ kHz should be achieved. Based upon the available light sources at 411 nm and 435 nm, it is expected to achieve a Raman beam pair providing a total intensity of 500 Wm^{-2} at the ion. This corresponds to two beams each of 0.5 mW focused to waists of $r = 50\mu$m. Although the the 369 nm beams are expected to provide a greater intensity an intensity of 500 Wm^{-2} is assumed for the comparison. The spontaneous decay rates of the excited states are $\Gamma_{D_{3/2}}/2\pi = 3$ Hz [154], $\Gamma_{D_{5/2}}/2\pi = 22$ Hz [73], and $\Gamma_{P_{1/2}}/2\pi = 19.6$

MHz [72] and the Clebsch-Gordan coefficients and geometric factors have been described in appendix I. For the analysis the ion is assumed to be oscillating along the z-axis with with a secular frequency of $\omega_z/2\pi = 1$ MHz. The resulting Raman transition rates as a function of detuning are shown in figure 8.4. The dashed line indicates a Raman transition rate of $\Omega_{\text{Ram}}2\pi = 50$ kHz. The first curve corresponds to coupling via the $^2D_{3/2}$ manifold, the second curve represents coupling via the $^2D_{5/2}$ manifold, and the last curve represents coupling via the $^2P_{1/2}$ manifold. The detuning from this P manifold is small considered to the fine structure splitting, so is considered independent of the $^2P_{3/2}$ manifold. Each curve corresponds to red or blue detuning from the respective excited state.
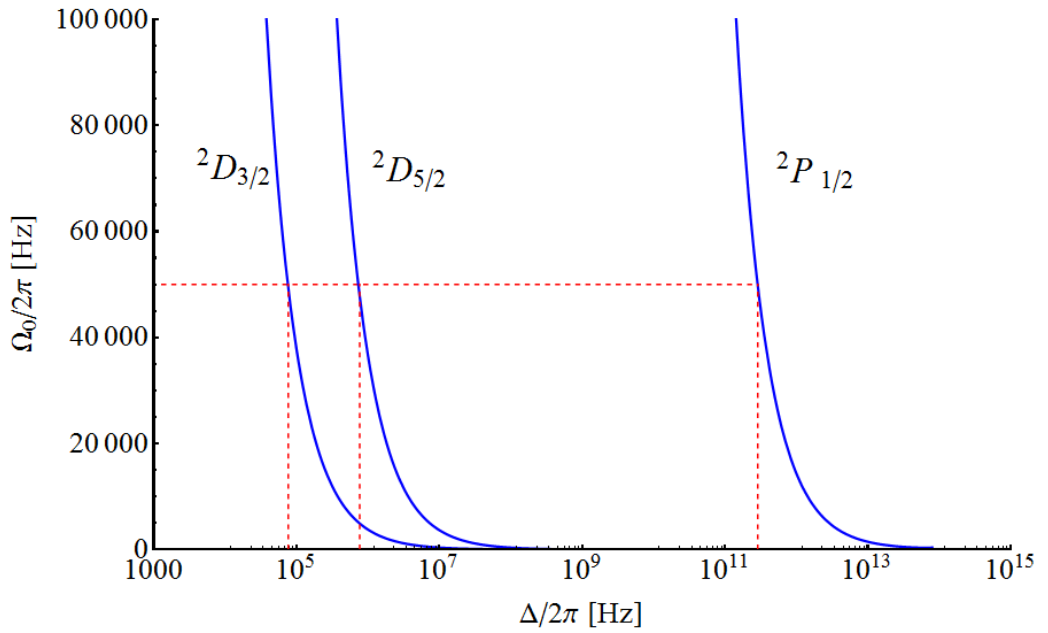
Figure 8.4: Raman transition rate as a function of detuning for two beams with intensities of 500 mW^{-2}. The three curves represent required detunings when exciting via the $^2S_{1/2}$ $\leftrightarrow$ $^2D_{3/2}$, $^2S_{1/2} \leftrightarrow$ $^2D_{5/2}$ and $^2S_{1/2} \leftrightarrow$ $^2P_{1/2}$ manifolds.

When coupling via the $^2D_{3/2}$ manifold a detuning of $\Delta/2\pi \approx 75$ kHz is required, while coupling via the $^2D_{3/2}$ requires a detuning of $\Delta/2\pi \approx 750$ kHz, and coupling via the ^2P_J manifold requires a detuning of $\Delta/2\pi \approx 280$ GHz. When considering a transition via the $^2D_{3/2}$ state maintaining a detuning of ≈ 50 kHz causes concern. To ensure reliable performance the detuning should vary by no more than 1%, which dictates that laser stability on the order of 500 Hz is required. While this has previously been achieved [155] stability of this magnitude requires expensive components, such as ultra low expansion glass, and sophisticated control electronics. For the purpose of the experiments for this thesis and for future experiments this is an impractical option. Exciting via the $^2D_{3/2}$ manifold is slightly more forgiving as requiring a detuning ≈ 500 kHz, but this still requires

laser stability of ≈ 1 kHz, which is again challenging.

Increasing the detuning would ease the laser stability requirements when exciting via the D manifolds. A fluctuation in the detuning of 2% would be acceptable which, assuming a laser stability of 100 kHz, corresponds to a minimum detuning of $\Delta/2\pi = 50$ MHz. The expected Raman transition frequencies as a function of power at the ion at this detuning are shown in figure 8.5. It can be seen that to achieve $\Omega_{Ram}/2\pi = 50$ kHz at $\Delta/2\pi = 50$ MHz the power at the ion is required to be ≈ 210 mW and ≈ 18 mW when coupling via the $^2D_{3/2}$, and $^2D_{5/2}$ states respectively. Obtaining 210 mW from any laser source is extremely demanding so coupling via the $^2D_{3/2}$ seems completely unsuitable. Coupling via the $^2D_{5/2}$ requires a comparatively lower 18 mW (9 mW per beam). At the time of writing there was no simple/ cost effective method of achieving this power at 411 nm. For now coupling via the ^2P_J manifold is the preferred option however should the technology improve then coupling via the $^2D_{5/2}$ manifold may become a viable option.
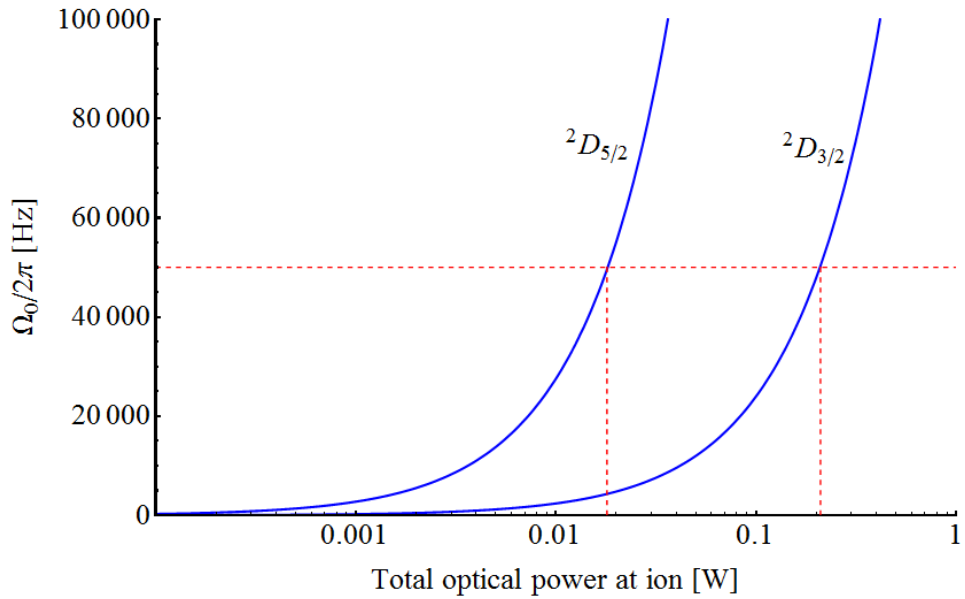
Figure 8.5: Raman transition rate as a function of beam power for a detuning of $\Delta/2\pi = 100$ MHz. The two curves represent the powers required when exciting via the $^2S_{1/2} \leftrightarrow {}^2D_{3/2}$ and $^2S_{1/2} \leftrightarrow {}^2D_{5/2}$ manifolds.

8.3   Implementing Raman Transitions

To excite a Raman transition via the ^2P_J manifolds several laser options are considered. An obvious candidate would be another frequency doubling system generating light near 369 nm (similar to the system used for Doppler cooling described in section 3.3.5). These systems however, are costly and can be temperamental so a more cost effective, robust

system is investigated. The most promising option in fact came in the form of laser diodes at 405nm boasting up to 120 mW of power (Egismos: AS-D6-7-405-120). At 405 nm the relative detuning from the ^{2}P$_{1/2}$ state is $\Delta \approx$80 THz. The power of the diodes is sufficient to compensate for this detuning and the off resonant scatter rate per Raman transition would be on the order of 10^{-7}. Furthermore the diodes could be operated in home-built external cavity diode lasers (ECDL) greatly reducing expense and maintenance issues.

To achieve a transition rate of $\Omega_{Ram} = 50$ kHz at this detuning requires two beams each with a power of 60 mW at a radius of r=50 μm. Obtaining two beams, each of 60 mW and separated by 12.6 GHz, from just one diode is clearly impossible. Fortunately Shahriar *et al.*, who demonstrated injection locking of laser diodes using the frequency sidebands from a modulated laser beam, provided a solution [156].
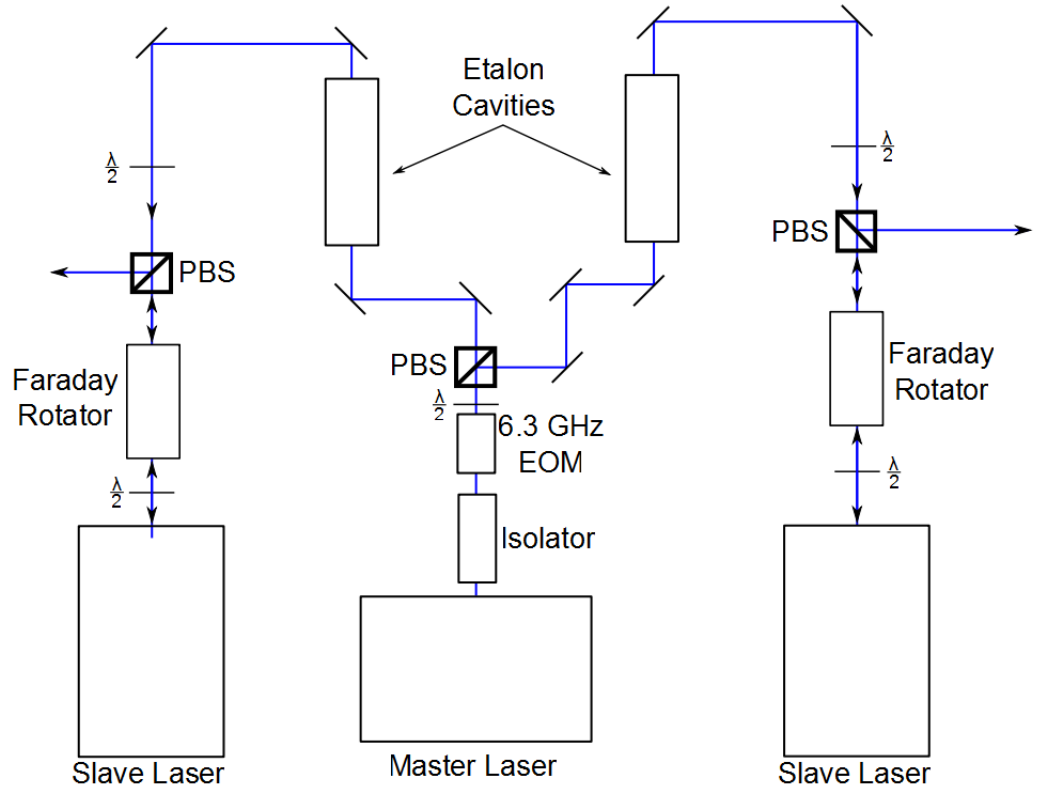
Figure 8.6: Proposed setup to generate two beams at 405 nm capable of driving Raman transitions. The beam from the master ECDL is immediately modulated at 6.3 GHz. The modulated beam is split using a 50/50 beam splitter, and two etalon cavities isolate the desired spectral components. The remaining beams injection lock two slave lasers. The emission for the slave lasers are extracted using faraday rotators, half-waveplates and polarising beam splitters.

The proposed setup is illustrated in figure 8.6. A master laser, in the littrow configuration, generates a beam of 405nm which is immediately modulated to generate $\pm$6.3 GHz frequency sidebands. The modulated beam is split, using a 50/50 beam splitter, and each

beam is then passed through a different etalon cavity which isolates different frequency sidebands. The resulting monochromatic beams are then used to injection lock slave lasers to produce two beams separated by 12.6 GHz each offering 120 mW. The beams emitted from the slave lasers are then separated from the seed beams using faraday rotators, half-waveplates and polarising beam splitters. Using this arrangement simple tuning of the modulation frequency by $\omega_{\text{sec}}/2$ enables coupling between different motional states.

External Cavity Diode Laser

The ECDL is constructed in the littrow configuration, similar to those described in chapter 3.2, and consists of the Egismos diode (AS-D6-7-405-120), a diffraction grating (Thorlabs: GH13-24V) and an aspheric lens (Thorlabs: A390TM-A). Under standard operating condition the ECDL generates 70 mW of single mode light.

Sideband Generation

Two options are available for generating the frequency sidebands: current modulation, or with an electro optic modulator. Current modulation is tested by applying a 6.3 GHz modulation signal to the laser diode. The signal is generated using a HP 8673C signal generator, amplified to 15 dBm (minicircuits: ZX60-V82-S+) and combined with the DC drive signal using a bias t (minicircuits: ZX05-153LH-S+). To minimise losses associated with cable attenuation the diode is soldered directly to the SMA connector on the bias tee. Using this approach a sideband amplitude of only $\approx 2\%$ the amplitude of the carrier peak could be achieved and, at this modulation frequency, the single mode performance of the diode became very sensitive to current and temperature fluctuations. Thus generating the 6.3 GHz sidebands via current modulation was deemed an unsuitable approach.

Sideband generation was then tested with the 7.37 GHz EOM (New Focus: 4851) used in the frequency doubling system (section 3.3.5). Although this particular modulator operates at a different frequency this model EOM can be tuned to 6.3 GHz. Testing sideband modulation with this particular EOM is therefore deemed a suitable indication of performance. Using a drive signal, provided by a HP 8684B signal generator and amplified to 31 dBm (Advanced Microwave Inc: A2503-3) sidebands $\approx 10\%$ the height of the carrier are obtained, and are stable. Sideband generation with an EOM is therefore the preferred option.

Injection Locking

To test the injection locking, a simplified setup similar to figure 8.6 is used. The test setup uses just two lasers: the master ECDL, and a slave laser consisting of a laser diode (Egismos: AS-D6-7-405-120) and aspheric lens (Thorlabs: A390TM-A). The aspheric lens is mounted on an XYZ translation stage to allow fine adjustment of the focused beam into the slave diode. A beam picker (Thorlabs: PSF10-A1) is used to separate the beam emitted by the slave laser from the seed beam. The picker however can result in unwanted feedback into the master laser, resulting in an uncontrollable mutual injection-locking between the two lasers. To prevent this an optical isolator (Lambda Photometrics: IO-5-36-HP) is used to protect the master laser from any feedback from the slave laser that might result in mutual injection locking. The power of the unwanted feedback reaching the master laser is only 7 μW, which when compared to the 50 mW feedback from the grating is expected to have a negligible effect. The emission wavelengths from both lasers are measured on a commercial wavemeter (High finesse: WS7).

It has been reported, by P. Kohns and W. Süptiz [157], that a single frequency can be obtained from a slave laser even when seeded with a modulated beam, provided the sidebands frequency is outside the 'locking' range of the carrier peak. If the 6.3 GHz frequency sidebands are outside this locking range then the need for etalon cavities can be removed, simplifying the setup. Unfortunately when the slave laser is seeded with 2 mW (corresponding to the expected power in each sideband after losses) injection locking was possible at detunings >10 GHz from the master laser. The greater power of the carrier wavelength would definitely dominate any wavelength generation in the slave lasers, therefore demanding the need for frequency sideband isolation.

It is assumed an additional 30% loss would be incurred from the etalon cavities. The power of the seeding beam is then reduced to 1.4 mW to simulate the power expected in each sideband after the cavities. The injection locking obtained under these conditions is shown in figure 8.7. The solid red and dashed blue curves in the upper plot show the wavelength of the master and slave laser respectively and the difference between the two lasers is shown in the lower plot. A distinct correlation can be seen between the two wavelengths. The magnitude of the frequency difference can be seen to be typically $\approx$ 5 MHz, with a maximum fluctuation of 12 MHz. When compared against the 20 MHz relative uncertainty of wavemeter at 405 nm, and considering that both wavelength are not measured exactly simultaneously but in 2 ms intervals, the result suggests injection locking was, to a first approximation, successful. To accurately determine the stability

of the beat-note both beams would have to be mixed and the resultant beat frequency monitored.
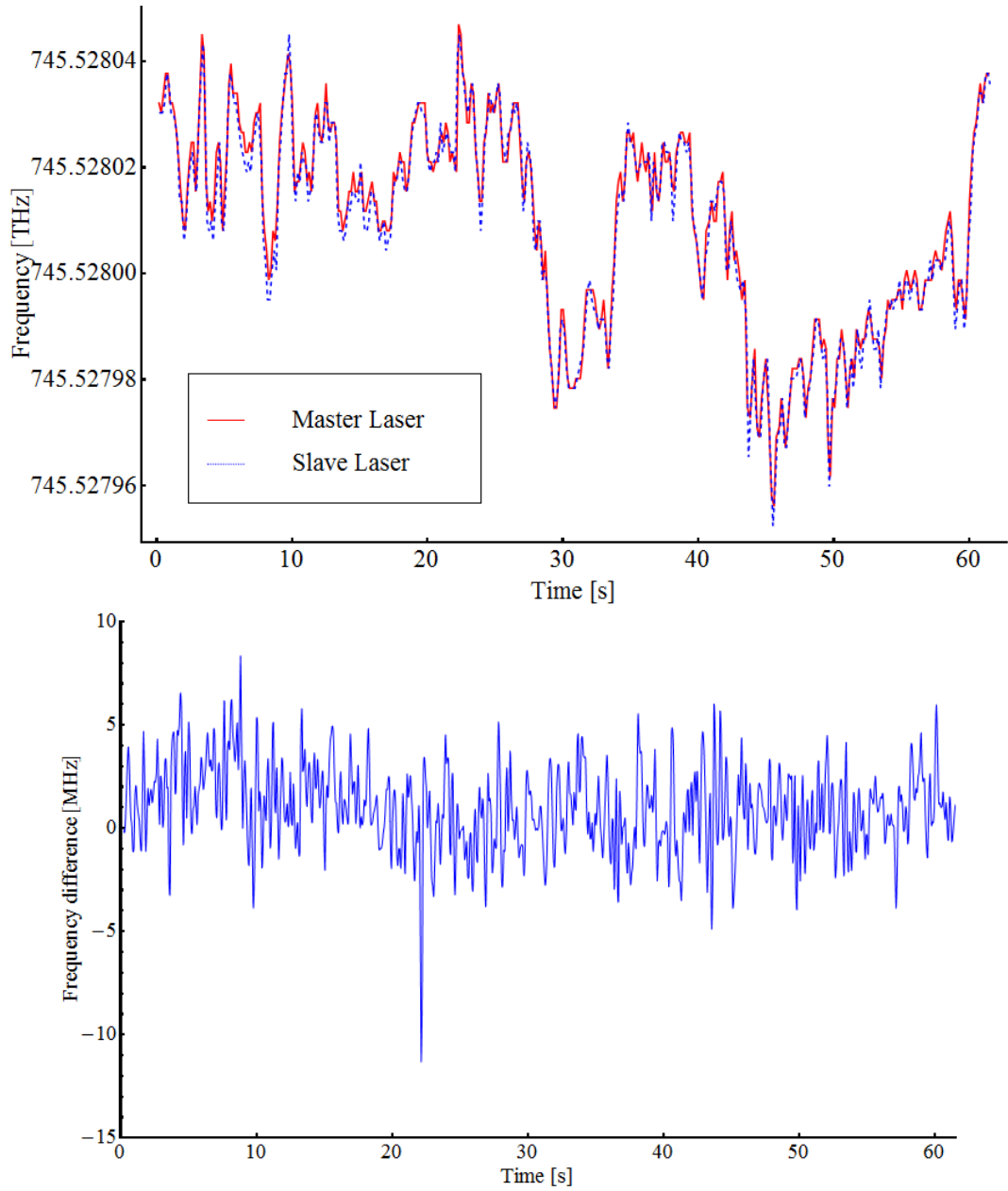
Figure 8.7: Top plot shows the wavelengths of the master (solid red) and slave (blue dashed) lasers during injection locking. Bottom plot shows the frequency difference between the two wavelengths.

Unfortunately beat frequency stability is not the limiting issue. The downfall of the scheme arises from the multimode behaviour of the diodes. Single mode performance from the slave laser is only possible when operating at a low driving current. When the slave laser is operated at high currents the relatively low power of the seed beam is insufficient to generate a dominant single mode. With a seed beam power of 1.4 mW the output power of the slave laser, inferred by measuring the beam after the picker, is only 13 mW. Assuming

power losses of $\approx 50\%$ the resulting power on the ion is only ≈ 7 mW and the Raman transition rate is only ≈ 6 kHz. The flexibility of the setup can be expanded to include a second stage of injection locking. Indeed it is found that injecting the slave laser with 8 mW (simulating the power of the second seed beams) produced a single mode beam with a power 120 mW. Unfortunately, introducing this second stage of injection locking increased the cost, setup time, and concerns relating to possible instabilities to a level that deemed this approach unsuitable.

Based upon the experimental work performed, generation of Raman beams via injection locking blue/ultraviolet laser diodes is perhaps too complex and time consuming when compared to alternative approaches. Should the single mode performance of these diodes improve then only a single stage of injection locking may be possible, or injection locking may not even be required at all. This approach could provide an inexpensive effective method of motional coupling. Currently, however, an alternative approach is required.

8.4 Alternative Schemes

An alternative option utilises the laser systems already described in this thesis. The ColdLase system, in conjunction with a 12.6 GHz microwave horn, could be be used for trapping, Doppler cool and state preparation. The frequency doubled system could then be used to generate a suitable Raman beam pair, as demonstrated by Deslauriers [87]. Here the fundamental 739 nm beam would be modulated at $\omega_0/2 = 6.3$ GHz. Since the doubling cavity is already tuned to have a free spectral range a subharmonic of the modulation frequency (FSR = 1.05 GHz) the different spectral components would resonate and undergo frequency summation. The resulting UV beam would consist of a comb of frequencies centred around 369 nm separated by $\omega_0/2 = 6.3$ GHz. The beam would then be split, using a series of two AOM's, and recombined at the ion. The pairs of spectral components separated by ω_0 can then stimulate Raman transitions. With this setup forming a Mach-Zehender interferometer the relative phases of the spectral components of the beams can be controlled, and total destructive interference of the beatnotes removed. By adjusting the frequency of the two AOM's the beatnote frequency of the Raman beam pair can be adjusted to access the various resonances.

The output power of the frequency doubling system is ≈ 50 mW. The EOM, as tested earlier, is expected to generate frequency sidebands $\approx 10\%$ of the carrier. While the amplitude of these sidebands is expected to increase as a result of summation between 739 nm carrier ± 6.3 GHz sidebands 10% assumes a worst case. At 10% the sidebands will have

a power of ≈ 4 mW. Selecting 40% from the first AOM and 66% from the second AOM generates two Raman beams each of 1.6 mW. Assuming additional losses of 50% from other optical components resulting in beam powers of 800 μW. As shown earlier in the comparison section of this chapter two beams each of 500 μW at a detuning of $\Delta/2\pi \approx 280$ GHz can achieve a transition rate of $\Omega_{\text{Ram}}/2\pi = 50$ kHz. This approach should therefore provide a suitable Raman transition rate.

Towards the end of this thesis Hayes *et al.* [158] and Campbell *et al.* [159] demonstrated qubit rotations, motional coupling, ground state cooling and entanglement using an ultrafast pulsed laser. Similarly Wunderlich's group has shown motional coupling using microwaves and magnetic field gradients [85]. These can also be suitable approaches for controlling the qubit.

Chapter 9

Conclusion

"A learning experience is one of those things that says: 'You know that thing

you just did? Don't do that' "

-Douglas Adams, *The Salmon of Doubt*

In this thesis an experimental setup to trap and manipulate Yb$^+$ ions for quantum information processing has been described. The construction and implementation of the lasers used to cool and prepare the ions is described in detail. The experiment as a whole is presented, operation of the setup and successful trapping of Yb$^+$ including ^{171}Yb$^+$ is shown, and then characterised. Using a trapped ^{174}Yb$^+$ ions the heating rate of the ion trap was measured and found to be consistent with previously reported rates of other ion species in different ion traps using established scaling laws. This result removes previous concerns regarding ytterbium having a higher heating rate, and further solidifies the suitability of the Yb$^+$ ion for quantum information processing.

New wavelengths required for ionising neutral Yb and cooling Yb$^+$ ions were also measured. A simple technique was devised to measure the $^1S_0 \leftrightarrow {}^1P_1$ transition wavelengths in neutral Yb, with the results obtained differing from previously published work by 660 MHz. The devised method has additional ability to predict Doppler shifted transition frequencies which are required when the laser and atomic beam are non-perpendicular. The $^2S_{1/2} \leftrightarrow {}^2P_{1/2}$ Doppler cooling and $^2D_{3/2} \leftrightarrow {}^3D[3/2]_{1/2}$ repump transitions have been measured to a greater precision than previously published. These measurements are particularly useful for groups setting up an ytterbium ion trap experiment, as the availability of more precise frequency measurements significantly simplifies initial trapping.

Alongside the implementation and characterisation of the ion trap setup a new laser system was developed. The motivation for the laser was to provide a simple inexpensive

alternative to obtaining wavelengths that are otherwise achieved using complex expensive lasers systems. The system, based upon a Littrow configured external cavity setup, operates with any Fabry-Pérot laser diode so can be used with a wide range of atoms and ions. The inclusion of current modulation capabilities further enables control of ions with hyperfine structures. The first incarnation of the system, although not perfected, is demonstrated to be suitable for use with Yb^+ ions including $^{171}Yb^+$. Future revisions to the models should provide a cheap alternative to complex expensive lasers.

Lastly the foundations for implementing a Raman transition using the $^{171}Yb^+$ trapped ion qubit were investigated. Raman transitions are a powerful tool that can be used to induce arbitrary qubit rotations as well as couple the qubit states to the external motion. Previously reported implementation of these transitions have all utilised dipole transitions, however the internal energy level structure of $^{171}Yb^+$ presented the possibility of using a quadruple transition. Analysis of the two options showed that use of quadrupole transitions may, at present, not be the most optimum option and the use of dipole transitions is preferable. However, with the increase of power from blue laser diodes or ease of achieving increased levels of laser stability quadrupole transitions could become a viable alternative. A setup to implement a Raman transition via a dipole transition using injection locked laser diodes was tested. The setup was also unfortunately limited by the unexpected performance of blue laser diodes. However, with the improvement of these diodes the scheme may offer a cost effective, and high fidelity, alternative to other available laser systems.

9.1 Outlook

Looking to the future the next step is the implementation of a scheme capable of qubit manipulations. The different approaches include utilising the ColdLase and frequency doubling system, described at the end of chapter 8, the use a picosecond pulsed laser [158,159], or microwave radiation and a large magnetic field gradient [85]. The pulsed laser approach does offer incredibly fast, sub microsecond, gates however it is expensive and has very sensitive experimental parameters, such as the pulse repetition rate and the phase between pulses. Small differences in these parameters can be extremely detrimental to qubit operations. At present the level of accuracy required for these parameters cannot be provided by manufacturers, making pulsed lasers an expensive and risky approach to take. The microwave option, although resulting in slower gate speeds, is significantly cheaper, more rugged, and offers simple scalability. With future gates involving large numbers of ions, and given that additional research projects within the group are developing multidimen-

sional trap arrays, simple scalability is a powerful tool. The simpler optical technique (utilising ColdLase and the frequency doubled system) is also being considered since most of the equipment is already in the laboratory and therefore requires little additional overhead to implement. With both optical and microwave schemes the suitability of different gates can be compared.

The implementation of either scheme requires an upgrade of the setup described in this thesis. The scanning cavity lock used to stabilise the lasers is being replaces with a dual resonance cavity lock, and the implementation of phase stability of between experimental components is also underway. A microwave horn has been included into the setup and initial results are being obtained for qubit state detection fidelities and basic one photon rotation of the qubit. Once mastered motional coupling is the next tool to demonstrate, followed then by the realisation of the Mølmer Sørensen gate. From there more complex gates involving multiple ions could be achieved which, depending upon the progression of trap development, could be in multiple dimensions. The realisation of large scale entanglement is an exciting prospect, and the work in this thesis has laid the first stepping stones for our research group, and contributed towards the large scale effort of making the quantum computer a reality.

Bibliography

[1] J. H. Wesenberg, R. J. Epstein, D. Leibfried, R. B. Blakestad, J. Britton, J. P. Home, W. M. Itano, J. D. Jost, E. Knill, C. Langer, R. Ozeri, S. Seidelin, and D. J. Wineland. Fluorescence during doppler cooling of a single trapped atom. *Phys. Rev. A*, 76:053416, 2007. Cited on viii, 91, 92, 93, 95, 195, 196

[2] A. M. Turing. On computable numbers, with an application to the entscheidund-problem. *Pro. Lond. Math. Soc. 2*, 42:230, 1936. Cited on 2

[3] Paul Benioff. The computer as a physical system: A microscopic quantum mechanical hamiltonian model of computers as represented by Turing machines. *Journ. Satat. Phys.*, 22(5):563, 1980. Cited on 2

[4] Rischard P. Feynman. Simulating physics with computers. *Int. Jour. Theor. Phys.*, 21(6/7):467, 1982. Cited on 2

[5] D. Deutsch. Quantum theory, the Church-Turning priciple and the universal quantum computer. *Pro. R. Soc. Lond. A*, 400:97–117, 1985. Cited on 3

[6] P. W. Shor. Algorithms for quantum computation: Discrete logarithms and factoring. *Proceedings of the 35th Annual Symposium on the Foundations of Computer Science*, page 124, 1994. Cited on 3

[7] L. K. Grover. A fast quantum mechanical algorithm for database search. *Proceedings, 28th Annual ACM Symposium on the Theory of Computing (STOC)*, pages 212–219, 1996. Cited on 3

[8] Peter W. Shor. Scheme for reducing decoherence in quantum computer memory. *Phys. Rev. A*, 52(4):R2493, 1995. Cited on 3

[9] A. M. Steane. Error correcting codes in quantum theory. *Phys. Rev. Lett.*, 77(5):793, 1996. Cited on 3

[10] Peter W. Shor. Fault-tolerant quantum computation. *arXiv:quant-ph/9605011v2*, 1997. Cited on 3

[11] David P. DiVincenzo. The physical implementation of quantum computation. *Fortschr. Phys.*, 48:771, 2000. Cited on 3

[12] Daniel Loss and David P. DiVincenzo. Quantum computation with quantum dots. *Phys. Rev. A*, 57(1):120, 1998. Cited on 3

[13] Mark S. Sherwin, Atac Imamoglu, and Thomas Montroy. Quantum computation with quantum dots and terahertz cavity quantum electrodynamics. *Phys. Rev. A*, 60(5):3508, 1999. Cited on 3

[14] Alexander Shnirman, Gerd Schön, and Ziv Hermon. Quantum manipulations of small Josephson junctions. *Phys. Rev. Lett.*, 79(12):2371, 1997. Cited on 3

[15] B. E. Kane. A silicon-based nuclear spin quantum computer. *Nature*, 393:133, 1998. Cited on 4

[16] E. Knill, R. Laflamme, and G. J. Milburn. A scheme for efficient quantum computation with linear optics. *Nature*, 409:46, 2001. Cited on 4

[17] Q. A. Turchette, C. J. Hood, W. Lange, H. Mabuchi, and H. J. Kimble. Measurement of conditional phase shifts for quantum logic. *Phys. Rev. Lett.*, 75(25):4710, 1995. Cited on 4

[18] J. I. Cirac and P. Zoller. Quantum computations with cold trapped ions. *Physical Review Letters*, 74(20):4091–4094, 1994. Cited on 4

[19] Michael J. Bieruck, Hermann Uys, Aaron P. Vandevender, Nobuyashu Shiga, Wayne M. Itano, and John J. Bollinger. High fidelity quantum control using ion crystals in a Penning trap. *Quant. Inf. Comput.*, 9(11 & 12):0920, 2009. Cited on 4

[20] D. R. Crick, S. Donnellan, S. Ananthamurthy, R. C. Thompson, and D. Segal. Fast shuttling of ions in a scalable Penning trap array. *Review of Scientific Instruments*, 81:013111, 2010. Cited on 4

[21] C. Monroe, D. M. Meekhof, B. E. King, W. M. Itano, and D. J. Wineland. Demonstration of a fundamental qunatum logic gate. *Phys. Rev. Lett.*, 75(25):4714, 1995. Cited on 4

[22] Ferdinand Schmidt-Kaler, Hartmut Häffner, Mark Riebe, Stephan Gulde, Gavin P. T. Lancaster, Thomas Deuschle, Christoph Becher, Christian F. Roos, Jürgen Eschner, and Rainer Blatt. Realization of the Cirac–Zoller controlled-not quantum gate. *Nature*, 422:408, 2003. Cited on 4

[23] T. Monz, K. Kim, W. Hänsel, M. Riebe, A. S. Villar, P. Schindler, M. Chwalla, M. Hennrich, and R. Blatt. Realization of the quantum Toffoli gate with trapped ions. *Phys. Rev. Lett.*, 102(040501), 2009. Cited on 4

[24] C. A. Sackett, D. Kielpinski, B. E. King, C. Langer, V. Meyer, C. J. Myatt, M. Rowe, Q. A. Turchette, W. M. Itano, D. J. Wineland, and C. Monroe. Experimental entanglement of four particles. *Nature*, 404:256, 2000. Cited on 4

[25] D. Leibfried, B. DeMarco, V. Meyer, D. Lucas, M. Barrett, J. Britton, W. M. Itano, B. Jelenkovic, C. Langer, T. Rosenband, and D. J. Wineland. Experimental demonstaration of a robust, high-fidelity geometric two ion-qubit phase gate. *Nature*, 422(412), 2003. Cited on 4

[26] Thomas Monz, Philipp Schindler, Julio T. Barreiro, Michael Chwalla, Daniel Nigg, William A. Coish, Maximilian Harlander, Wolfgang Hänsel, Markus Hennrich, and Rainer Blatt. 14-qubit entanglement: Creation and coherence. *Phys. Rev. Lett.*, 106(130506), 2011. Cited on 4

[27] N. Timoney, V. Elman, S. Glaser, C. Weiss, M. Johanning, W. Neuhauser, and Chr. Wunderlich. Error-resistant single-qubit gates with trapped ions. *Phys. Rev. A*, 77(052334), 2008. Cited on 4

[28] J. Chiaverini, D. Leibfried, T. Schaetz, M. D. Barrett, R. B. Blakestad, J. Britton, W. M. Itano, J. D. Jost, E. Knill, C. Langer, R. Ozeri, and D. J. Wineland. Realisation of quantum error correction. *Nature*, 432(602), 2004. Cited on 4

[29] Marisa Pons, Veronica Ahufinger, Christof Wunderlich, Anna Sanpera, Sibylle Braungardt, Aditi Sen(De), Ujjwal Sen, and Maciej Lewenstein. Trapped ion chain as a neural network: Error resistant quantum computation. *Phys. Rev. Lett.*, 98:023003, 2007. Cited on 4

[30] S. Gulde, M. Riebe, G. P. T. Lancaster, C. Becher, J. Eschner, H. Häffner, F. Schmidt-Kaler, I. L. Chuang, and R. Blatt. Implementation of the Deutsch-Jozsa algorithm on an ion-trap quantum computer. *Nature*, 421:48, 2003. Cited on 4

[31] K.-A. Brickman, P. C. Haljan, P.J. Lee, M. Acton, L. Deslauriers, and C. Monroe. Implementation of Grover's quantum search algorithm in a scalable system. *Physical Review A*, 72(050306(R)), 2005. Cited on 4

[32] A. Friedenauer, H. Schmitz, J. T. Glueckert, D. Porras, and T. Schaetz. Simulating a quantum magnet with trapped ions. *Nature Physics*, 4:757, 2008. Cited on 4

[33] K. Kim, M.-S. Chang, S. Korenblit, R. Islam, E. E. Edwards, J. K. Freericks, G.-D. Lin, L.-M. Duan, and C. Monroe. Quantum simulation of frustrated Ising spins with trapped ions. *Nature*, 465:590, 2010. Cited on 4

[34] J. Britton, D. Leibfried, J. Beall, R. B. Blakestad, J. J. Bollinger, J. Chiaverini, R. J. Epstein, J. D. Jost, D. Kielpinski, C. Langer, R. Ozeri, R. Reichle, S. Seidelin, N. Shiga, J. H. Wesenberg, and D. J. Wineland. A microfabricated surface-electrode ion trap in silicon. *arXiv:quant-ph/0605170*, 2006. Cited on 4

[35] W. K. Hensinger, S. Olmschenk, D. Stick, D. Hucul, M. Yeo, M. Acton, L. Deslauriers, J. Rabchuk, and C. Monroe. T-junction ion trap array for two-dimensional ion shuttling, storage, and manipulation. *Appl. Phys. Lett.*, 88(034101), 2006. Cited on 4, 10

[36] Wolfgang Paul. Electromagnetic traps for charged and neutral particles. *Rev. Mod. Phys.*, 62:531, 1990. Cited on 7

[37] R. F. Wuerker, H. Shelton, and R. V. Langmuir. Electromagnetic traps for charged and neutral particles. *J. Appl. Phys.*, 30:342, 1958. Cited on 7

[38] T.W. Hänsch and A.L. Schawlow. Cooling of gases by laser radiation. *Optics Communications*, 13(1):68–69, 1975. Cited on 7

[39] D. J. Wineland, R. E. Drullinger, and F. L. Walls. Radiation-pressure cooling of bound resonant absorbers. *Phy. Rev. Lett.*, 40(25):1639, 1978. Cited on 7

[40] W. Neuhauser, M. Hohenstatt, P. Toschek, and H. Dehmelt. Optical sideband cooling of visible atom cloud confined in parabolic well. *Phy. Rev. Lett.*, 41(4):233, 1978. Cited on 7

[41] Th. Udem, S. A. Diddams, K. R. Vogel, C. W. Oates, E. A. Curtis, W. D. Lee, W. M. Itano, R. E. Drullinger, J. C. Bergquist, and L. Hollberg. Absolute frequency measurements of the Hg^+ and Ca optical clock transitions with a femtosecond laser. *Phys. Rev. Lett.*, 86:4996–4999, 2001. Cited on 7

[42] S. A. Webster, P. Taylor, M. Roberts, G. P. Barwood, and P. Gill. Kilohertz-resolution spectroscopy of the $^2S_{1/2}$-$^2F_{7/2}$ electric octupole transition in a single ^{171}Yb$^+$ ion. *Phys. Rev. A*, 65:052501, 2002. Cited on 7

[43] Chr. Tamm, S. Weyers, B. Lipphardt, and E. Peik. Stray-field-induced quadrupole shift and absolute frequency of the 688-THz ^{171}Yb$^+$ single-ion optical frequency standard. *Phys. Rev. A*, 80:043403, 2009. Cited on 7, 16, 101

[44] M. Chwalla, J. Benhelm, K. Kim, G. Kirchmair, T. Monz, M. Riebe, P. Schindler, A. S. Villar, W. Hänsel, C. F. Roos, R. Blatt, M. Abgrall, G. Santarelli, G. D. Rovera, and Ph. Laurent. Absolute frequency measurement of the ^{40}Ca$^+$ $4s^2S_{1/2}$-$3d^2D_{5/2}$ clock transition. *Phys. Rev. Lett.*, 102:023002, 2009. Cited on 7

[45] M. Keller, B. Lange, K. Hayasaka, W. Lange, and H. Walther. Deterministic cavity quantum electrodynamics with trapped ions. *J. Phys. B: At. Mol. Opt. Phys*, 36(3):2099–2105, 2003. Cited on 7

[46] M. Keller, B. Lange, K. Hayasaka, W. Lange, and H. Walther. Continuous generation of single photons with controlled waveform in an ion-trap cavity system. *nature*, 431:1075–1078, 2004. Cited on 7

[47] J. I. Cirac and P. Zoller. A scalable quantum computer with ions in an array of microtraps. *Nature*, 404:579–581, 2000. Cited on 7

[48] H. Häffner, C. F. Roos, and R. Blatt. Quantum computing with trapped ions. *Physical Reports*, 469:155–203, 2008. Cited on 7

[49] M. R. Dietrich, A. Avril, R. Bowler, N. Kurz, J. S. Salacka, G. Shu, and B. B. Blinov. Barium ions for quantum computation. *arXiv:0905.2701*, 2009. Cited on 7

[50] D.J. Wineland, C. Monroe, W.M. Itano, B.E. King, D. Leibfried, D.M. Meekhof, C. Myatt, and C. Wood. Experimental primer on the trapped ion quantum computer. *Fortschr. Phys.*, 46(4-5):363–390, 1998. Cited on 7

[51] H.C. Nägerl, W. Bechter, J. Eschner, F. Schmidt-Kaler, and R. Blatt. Ion strings for quantum gates. *Appl. Phys. B*, 66:603–608, 1998. Cited on 7

[52] D. M. Lucas, C. J. S. Donald, J. P. Home, M. J. McDonnell, A. Ramos, D. N. Stacey, J.-P. Stacey, A. M. Steane, and S. C. Webster. Oxford ion-trap quantum computing project. *Phil. Trans. R. Soc. A*, 66:603–608, 1998. Cited on 7

[53] R. J. Hughes, D. F. V. James, J. J. Gomez, M. S. Gulley, M. H. Holzscheiter, P. G. Kwiat, S. K. Lamoreaux, C. G. Peterson, V. D. Sandberg, M. M. Schauer, C. M. Simmons, C. E. Thorburn, D. Tupa, P. Z. Wang, and A. G. White. The Los Alamos trapped ion quantum computer experiment. *Fortschr. Phys.*, 46:329–361, 1998. Cited on 7

[54] K. Koo, J. Sudbery, D. M. Segal, and R. C. Thompson. Doppler cooling of Ca$^+$ ions in a Penning trap. *Phys. Rev. A*, 69:043402, 2004. Cited on 7

[55] Stephan A. Schulz, Ulrich Poschinger, Frank Ziesel, and Ferdinand Schmidt-Kaler. Sideband cooling and coherent dynamics in a microchip multi-segmented ion trap. *New J. Phys.*, 73:045007, 2008. Cited on 7, 21

[56] B. B. Blinov, L. Deslauriers, P. Lee, M. J. Madsen, R. Miller, and C. Monroe. Sympathetic cooling of trapped Cd$^+$ isotopes. *Phys. Rev. A*, 65:040304(R), 2002. Cited on 7

[57] M. D. Barrett, B. DeMarco, T. Schaetz, V. Meyer, D. Leibfried, J. Britton, J. Chiaverini, W. M. Itano, B. Jelenković, J. D. Jost, C. Langer, T. Rosenband, and D. J. Wineland. Sympathetic cooling of ^{9}Be$^+$ and ^{24}Mg$^+$ for quantum logic. *Phys. Rev. A*, 68:042302, 2003. Cited on 7

[58] C. E. Pearson, D. R. Leibrandt, W. S. Bakr, W. J. Mallard, K. R. Brown, and I. L. Chuang. Experimental investigation of planar ion traps. *Phys. Rev. A*, 73:032307, 2006. Cited on 7

[59] V. Letchumanan, G. Wilpers, M. Brownnutt, P. Gill, and A. G. Sinclair. Zero-point cooling and heating-rate measurements of a single ^{88}Sr$^+$ ion. *Phys. Rev. A*, 75:063425, 2007. Cited on 7

[60] A. S. Bell, P. Gill, H. A. Klein, A. P. Levick, Chr. Tamm, and D. Schnier. Laser cooling of trapped ytterbium ions using a four level optical-excitation scheme. *Phys. Rev. A*, 44(1):20–23, 1991. Cited on 7

[61] Chr. Balzer, A. Braun, T. Hannemann, Chr. Paape, M. Ettler, W. Neuhauser, and Chr. Wunderlich. Electrodynamically trapped Yb$^+$ ions for quantum information processing. *Phys. Rev. A*, 73:041407(R), 2006. Cited on 7, 15, 101

[62] D. Kielpinski, M. Cetina, J. A. Cox, and F. X. Kärtner. Laser cooling of trapped ytterbium ions with an ultraviolet diode laser. *Opt. Lett.*, 31(6):757, 2006. Cited on 7, 118

[63] S. Olmschenk, K. C. Younge, D. L. Moehring, D. N. Matsukevich, P. Maunz, and C. Monroe. Manipulation and detection of a trapped Yb^+ hyperfine qubit. *Phys. Rev. A*, 76:052314, 2007. Cited on 7, 13, 15, 16

[64] S. Earnshaw. On the nature of the molecular forces which regulate the constitution of the luminiferous ether. *Trans. Camb. Phil. Soc.*, 7:91–112, 1842. Cited on 7

[65] Steven Matthew Olmschenk. Quantum teleportation between distant matter qubits. *PhD thesis, University of Michigan*, 2009. Cited on 11, 15, 17

[66] Pradip K. Ghosh. *Ion Traps*. Clarendon Press, Oxford, 1995. Cited on 13

[67] D. J. Wineland, C. Monroe, W. M. Itano, D. Leibfried, B. E. King, and D. M. Meekhof. Experimental issues in coherent quantum-state manipulation of trapped atomic ions. *J. Res. Natl. Inst. Stand. Technol.*, 103(3):259, 1998. Cited on 13, 23, 27, 133

[68] Brian E. King. Quantum state engineering and information processing with trapped ions. *PhD thesis, University of Colorado*, 1999. Cited on 13, 27, 133, 171

[69] D. J. Berkeland, J. D. Miller, J. C. Bergquist, W. M. Itano, and D. J. Wineland. Minimization of ion micromotion in a paul trap. *Jour. Appl. Phys*, 83(10):5025–5033, 1998. Cited on 14

[70] Michael Johanning, Andrés F. Varón, and Christof Wunderlich. Quantum simulations with cold trapped ions. *J. Phys. B*, 42(15):154009, 2009. Cited on 15

[71] Yu. Ralchenko, A. E. Kramida, J. Reader, and NIST ASD Team (2008). *NIST Atomic Spectra Database (Version 3.1.5), [http://physics.nist.gov/asd3]*, 2010, October 16. Cited on 15

[72] S. Olmschenk, D. Hayes, D. N. Matsukevich, P. Maunz, D. L. Moehring, K. C. Younge, and C. Monroe. Measurement of the lifetime of the $6p^2P^o_{1/2}$ level of Yb^+. *Phys. Rev. A*, 80:022502, 2009. Cited on 16, 140

[73] M. Roberts, P. Taylor, S. V. Gateva-Kostova, R. B. M. Clarke, W. R. C. Rowley, and P. Gill. Measurement of $^1S_{1/2}$-$^2D_{5/2}$ clock transition in a single $^{171}Yb^+$ ion. *Phys. Rev. A*, 60(4):2867, October 1999. Cited on 16, 101, 139

[74] D. J. Berkeland and M. G. Boshier. Destabilization of dark states and optical spectroscopy in Zeeman-degenerate atomic systems. *Phys. Rev. A*, 65(033413), 2002. Cited on 18

[75] Harold J. Metcalf and Peter van. der. Straten. *Laser Cooling and Trapping.* Springer-Verlag New York, Inc., 1999. Cited on 19, 112, 116, 136, 201

[76] Christopher J. Foot. Oxford University Press, 2005. Cited on 19, 116

[77] F. Diedrich, J.C. Berquist, Wayne M. Itano, and D. J. Wineland. Laser cooling to the zero-point energy of motion. *Phys. Rev. Lett.*, 62(4):403, 1989. Cited on 21, 91

[78] Ch. Roos, Th. Zeiger, H. Rohde, H. C. Nägerl, J. Eschner, D. Leibfried, F. Schmidt-Kaler, and R. Blatt. Quantum state engineering on an optical transition and decoherence in a paul trap. *Phys. Rev. Lett.*, 83(23):4713, 1999. Cited on 21, 91

[79] C. Monroe, D. M. Meekhof, B.E. King, S.R. Jefferts, W. M. Itano, and D. J. Wineland. Resolved-sideband Raman cooling of a bound atom to the 3D zero-point energy. *Phys. Rev. Lett.*, 75(22):4011, 1995. Cited on 21, 91, 101

[80] J. Steinbach, J. Twamley, and P. L. Knight. Engineering two-mode interactions in ion traps. *Phys Rev A*, 56(6):4815, 1997. Cited on 21

[81] L. Deslauriers, P. C. Haljan, P. J. Lee, K.-A. Brickman, B. B. Blinov, M. J. Madsen, and C. Monroe. Zero-point cooling and low heating of trapped ^{111}Cd$^+$ ions. *Phys. Rev. A*, 70:043408, 2004. Cited on 21, 91, 139

[82] C.F. Roos, D. Leibfired, A. Mundt, F. Schmidt-Kaler, J. Eschner. Eschner, and R. Blatt. Experimental demonstration of ground state laser cooling with electromagnetic induced transparency. *Phys. Rev. Lett.*, 85(26):5547, 2000. Cited on 21

[83] Giovanna Morigi, Jürgen Eschner, and Christoph H. Keitel. Ground state laser cooling using electromagnetic induced transparency. *Phys. Rev. Lett*, 85(21):4458, 2000. Cited on 21, 24

[84] J. Eschner, G. Morigi, C. Keitel, C. Roos, D. Leibfried, A. Mundt, F. Schmidt-Kaler, and R. Blatt. Ground state laser colling of trapped atoms using electromagnetic induced transparency. *Proceedings of the XV International Conference on Laser Spectroscopy*, 2002. Cited on 21

[85] M. Johanning, A. Braun, N. Timoney, V. Elman, W. Neuhauser, and Chr. Wunder-lich. Individual addressing of trapped ions and coupling of motional and spin states using rf radiation. *Phys. Rev. Lett*, 102:073004, 2009. Cited on 21, 31, 147, 149

[86] I. Marzoli, J. I. Cirac, R. Blatt, and P. Zoller. Laser cooling of trapped three-level ions: Designing two-level systems for sideband cooling. *Phys. Rev. A*, 49(4):2771, 1994. Cited on 23

[87] Louis Deslauriers. Cooling and heating of the quantum motion of trapped cd$^+$ ions. *PhD thesis, University of Michigan*, 2006. Cited on 23, 27, 133, 146

[88] D. Leibfried, R. Blatt, C. Monroe, and D. Wineland. Quantum dynamics of single trapped ions. *Rev. Mod. Phys.*, 75:261, 2003. Cited on 27

[89] Patricia J. Lee. Quantum information processing with two trapped cadmium ions. *PhD thesis, University of Michigan*, 2006. Cited on 27, 133, 138, 170

[90] Florian Mintert and Christof Wunderlich. Ion-trap quantum logic using long-wavelength radiation. *Phy. Rev. Lett*, 87(25):257904, 2001. Cited on 31

[91] A. L. Schawlow and C. H. Townes. Infrared and optical masers. *Phys. Rev. Lett.*, 112, 1958. Cited on 33

[92] A. Sennaroglu, R. Paschotta, H. R. Telle, and U. Keller. Solid-state lasers and applications, 2007. Cited on 33

[93] Motoichi Ohtsu. Frequency stabilization in semiconductor lasers. *Optical and Qunatum Electronics*, 20:283–300, 1988. Cited on 33

[94] B. Dahmani, L. Hollberg, and R. Drullinger. Frequency stabilization in semiconductor lasers by resonant optical feedback. *Optics Letters*, 12:876–878, 1987. Cited on 33

[95] C.J. Cuneo, Jeffery J. Maki, and D.H. McIntyre. Optically stabilized diode laser using high-contrast saturated absorpotion. *Appl. Phys. Lett.*, 64:2625–2627, 1994. Cited on 33

[96] P. Wanninger, E.C. Valdez, and T.M. Shay. Diode-laser frequency stabilization based on the resonant Faraday effect. *IEEE Photonics Technology Letters*, 62:2593–2595, 1991. Cited on 33

[97] A.S. Arnold, J.S. Wilson, and M. G. Boshier. A simple exteneded-cavity diode laser. *Review of scientific instruments*, 69:1236–1239, 1998. Cited on 33

[98] Eugene Hecht. *Optics, fourth Edition.* Pearson Education, 2003. Cited on 39

[99] C.J. Myatt, N.R. Newbury, and C.E.Wieman. Simplified atom trap by using direct microwave modulation of a diode. *Optics Letters*, 18:649–651, 1993. Cited on 45, 121

[100] K. Odaka and S. Ueda. Dependence of outgassing rate on surface oxide layer thickness in type 304 stainless steel before and after surface oxidation in air. *Vacuum*, 47:689, 1996. Cited on 63

[101] M. J. Madsen, W. K. Hensinger, D. Stick, J. A. Rabchuk, and C. Monroe. Planar ion trap geometry for microfabrication. *Appl. Phys. B*, 78(5):639–651, 2004. Cited on 65

[102] W. W. Macalpine and R. O. Schildknecht. Coaxial resonators with helical inner conductor. *Proceedings of the IRE*, pages 2099–2105, December 1959. Cited on 66

[103] J. D Siverns, L. R. Simkins, S. Weidt, and W. K. Hensinger. On the application of radio frequency voltages to ion traps via helical resonators. *in preparation*, 2011. Cited on 66, 67

[104] W. Z. Zhao, J. E. Simsarian, L. A. Orozco, and G. D. Sprouse. A computer-based digital feedback control of frequency drift of multiple lasers. *Rev. Sci. Instr.*, 69(11):3737, 1998. Cited on 68, 71

[105] E. A. Donley, T. P. Heavner, F. Levi, M. O. Tataw, and S. R. Jefferts. Double-pass acousto-optic modulator system. *Review of Scientific Instruments*, 76(063112), 2005. Cited on 82

[106] Chih-Hao Chang, R. K .Heilmann, M. L. Schattenburg, and P. Glenn. Design of a couble-pass shear mode acosuto-optic modulator. *Review of Scientific Instruments*, 79(033104), 2008. Cited on 82

[107] A. G. Truscott. Trapping and cooling of rubidium atoms using stabilised diode lasers. *Doctor of Philosophy thesis, University of Queensland*, 1998. Cited on 82

[108] D. Hucul, M. Yeo, S. Olmschenk, W. K. Hensinger, J. Rabchuk, and C. Monroe. On the transport of atomic ions in linear and multidimenional ion trap arrays. *Quant. Inf. Comp.*, 8(6 & 7):0501, 1998. Cited on 86

[109] Jaroslaw Labaziewicz, Yufei Ge, Paul Antohi, David Leibrandt, Kenneth R. Brown, and Isaac L. Chuang. Suppression of heating rates in cryogenic surface-electrode ion traps. *Phys. Rev. Lett.*, 100(013001), 2008. Cited on 91

[110] J. Labaziewicz, Y. Ge, David R. Leibrandt, Shannon X. Wang, Ruth Shewmon, and Isaac L. Chuang. Temperature dependence of electric field noise above gold surfaces. *Phys. Rev. Lett.*, 101(180602), 2008. Cited on 91

[111] L. Deslauriers, S. Olmschenk, D. Stick, W. K. Hensinger, J. Sterk, and C. Monroe. Scaling and suppression of anomalous heating in ion traps. *Phys. Rev. Lett.*, 97:103007, 2006. Cited on 91, 98

[112] Q. A. Turchette, D. Kielpinski, B. E. King, D. Leibfried, D. M. Meekhof, C. J. Myatt, M. A. Rowe, C. A. Sackett, C. S. Wood, W. M. Itano, C. Monroe, and D. J. Wineland. Heating of trapped ions from the quantum ground state. *Phys. Rev. A*, 61:063418, 2000. Cited on 91, 96, 98

[113] R. J. Epstein, S. Seidelin, D. Leibfried, J. H. Wesenberg, J. J. Bollinger, J. M. Amini, R. B. Blakestad, J. Britton, J. P. Home, W. M. Itano, J. D. Jost, E. Knill, C. Langer, R. Ozeri, N. Shiga, and D. J. Wineland. Simplified motional heating rate measurements of trapped ions. *Phys. Rev. A*, 76:033411, 2007. Cited on 91, 95

[114] Marcus D. Hughes, Bjoern Lekitsch, Jiddu A. Broersma, and Winfried K. Hensinger. Microfabricated ion traps. *arXiv:1101.3207v1*, 2011. Cited on 100

[115] S. J. Park, P. J. Manson, M. J. Wouters, R. B. Warrington, M. A. Lawn, and P. T. H. Fisk. ^{171}Yb$^+$ microwave frequency standard. *IEEE International*, page 613, June 2007. Cited on 101

[116] P. J. Blythe, S. A. Webster, H. S. Margolis, S. N. Lea, G. Huang, S.-K. Choi, W. R. C. Rowley, P. Gill, and R. S. Windeler. Subkilohertz absolute-frequency measurement of the 467-nm electric octupole transition in ^{171}Yb$^+$. *Phys. Rev. A*, 67(2):020501, Feb 2003. Cited on 101

[117] N. Kjargaard, L. Hornekar, A.M. Thommesen, Z. Videsen, and M. Drewsen. Isotope selective loading of an ion trap using resonance-enhanced two-photon ionization. *Appl. Phys. B*, 71:207, May 2000. Cited on 101

[118] Z. W. Barber, J. E. Stalnaker, N. D. Lemke, N. Poli, C. W. Oates, T. M. Fortier, S. A. Diddams, L. Hollberg, C. W. Hoyt, A. V. Taichenachev, and V. I. Yudin. Optical

lattice induced light shifts in an Yb atomic clock. *Phys. Rev. Lett.*, 100(10):103002, March 2008. Cited on 101

[119] Sergey G. Porsev, Andrei Derevianko, and E. N. Fortson. Possibility of an optical clock using the $6^1S_0 \to 6^3P_0^o$ transition in ^{171,173}Yb atoms held in an optical lattice. *Phys. Rev. A*, 69(2):021403, Feb 2004. Cited on 101

[120] Tao Hong, Claire Cramer, Eryn Cook, Warren Nagourney, and E. N. Fortson. Observation of the $^1S_0 \to ^3P_0$ transition in atomic ytterbium for optical clocks and qubit arrays. *Opt. Lett.*, 30(19):2644, October 2005. Cited on 101

[121] Z. W. Barber, C. W. Hoyt, C. W. Oates, L. Hollberg, A. V. Taichenachev, and V. I. Yudin. Direct excitation of the forbidden clock transition in neutral ^{174}Yb atoms confined to an optical lattice. *Phys. Rev. Lett.*, 96(8):83002, Mar 2006. Cited on 101

[122] A. M. Bacon, H. Z. Zhao, L. J. Wang, and J. E. Thomas. Optical dipole noise of two-level atoms. *Phys. Rev. Lett.*, 75(7):1296–1299, Aug 1995. Cited on 101

[123] H. A. Klein, A.S. Bell, G.P. Barwood, and P. Gill. Laser cooling of trapped Yb$^+$. *Appl. Phys. B*, 50:13, Jan 1990. Cited on 101

[124] H. Lehmitz, J. Hattendorf-Ledwoch, R. Blatt, and H. Harde. Population trapping in excited Yb ions. *Phys. Rev. Lett.*, 62(18):2108–2111, May 1989. Cited on 101

[125] M. Roberts, P. Taylor, G. P. Barwood, P. Gill, H. A. Klein, and W. R. C. Rowley. Observation of an electric octupole transition in a single ion. *Phys. Rev. Lett.*, 78(10):1876–1879, Mar 1997. Cited on 101

[126] V. Enders, Ph Courteille, R. Huesmann, L. S. Ma, W. Neuhauser, R. Blatt, and P. E. Toschek. Microwave-optical double resonance on a single laser-cooled ^{171}Yb$^+$ ion. *Europhysics Letters*, 24(5):325, Nov 1993. Cited on 101

[127] K. Honda, Y. Takahashi, T. Kuwamoto, M. Fujimoto, K. Toyoda, K. Ishikawa, and T. Yabuzaki. Magneto-optical trapping of Yb atoms and a limit on the branching ratio of the $^1P_1$ state. *Phys. Rev. A*, 59(2):R934, Feb 1999. Cited on 101

[128] U. D. Rapol, A. Krishna, A. Wasan, and V. Natarajan. Laser cooling and trapping of Yb from a thermal source. *The European Physical Journal D - Atomic, Molecular, Optical and Plasma Physics*, 29(3):409–414, June 2004. Cited on 101

[129] R. Huesmann, Ch. Balzer, Ph. Courteille, W. Neuhauser, and P. E. Toschek. Single-atom interferometry. *Phys. Rev. Lett.*, 82(8):1611, Feb 1999. Cited on 101

[130] C. S. Edwards, P. Gill, H. A. Klein, A. P. Levick, and W. R. C. Rowley. Laser-cooling effects in few-ion clouds of ^{174}Yb. *Appl. Phys. B*, 59:179, May 1994. Cited on 101

[131] Das Dipankar and Natarajan Vasant. Laser cooling of ^{173}Yb for isotope separation and precision hyperfine spectroscopy. *Phys. Rev. A*, 76(6):062505, Dec 2007. Cited on 101

[132] T. Loftus, J. R. Bochinski, and T. W. Mossberg. Simultaneous multi-isotope trapping of ytterbium. *Phys. Rev. A*, 63(5):053401, Apr 2001. Cited on 101

[133] R. Maruyama, R. H. Wynar, M. V. Romalis, A. Andalkar, M. D. Swallows, C. E. Pearson, and E. N. Fortson. Investigation of sub-doppler cooling in an ytterbium magneto-optical trap. *Phys. Rev. A*, 68(1):011403, Jul 2003. Cited on 101

[134] W. F. Meggers and J. L. Tech. *J. Res. Natl. Bur. Stand*, 83:13, 1978. Cited on 101, 105, 106

[135] D. Das, S. Barthwal, A. Banerjee, and Natrajan. Absolute frequency measurement in Yb with 0.08ppb uncertainty: Isotope shifts and hyperfine structure in the 399 nm $^1S_0 \rightarrow ^1P_1$ line. *Phys. Rev. A*, 72:032506, September 2005. Cited on 101, 105, 106, 107, 108

[136] T. Loftus, R. Bochinski, and T. W. Mossberg. Optical double-resonance cooled spectroscopy. *Phys. Rev. A*, 63:023402, January 2001. Cited on 101, 106, 107

[137] K. Deilamian, J. D. Gillaspy, and D. E. Kelleher. Isotope shifts and hyperfine splitting of the 398.8-nm Yb I line. *J. Opt. Soc. Am. B*, 10(5):789, May 1993. Cited on 101, 106, 107

[138] R. Zinkstok, E. J. van Duijn, S. Witte, and W. Hogervorst. Hyperfine structure and isotope shift of transitions in Yb I using UV and deep-UV cw laser light and the angular distribution of fluorescence radiation. *Journal of Physics B: Atomic, Molecular and Optical Physics*, 35(12):2693, May 2002. Cited on 101

[139] E. W. Streed, T. J. Weinhold, and D. Kielpinski. Frequency stabilization of an ultraviolet laser to ions in a discharge. *Appl. Phys. Lett.*, 93:071103, 2008. Cited on 101, 115

[140] James J. McLoughlin, Altaf H. Nizamani, James D. Siverns, Robin C. Sterling, Marcus D. Hughes, Bjoern Lekitsch, Björn Stein, Seb Weidt, and Winfried K. Hensinger. Versatile ytterbium ion trap experiment for operation of scalable ion-trap chips with motional heating and transition-frequency measurements. *Phys. Rev. A*, 83(013406), 2011. Cited on 101

[141] Altaf H. Nizamani, James J. McLoughlin, and Winfried K. Hensinger. Doppler-free Yb spectroscopy with the fluorescence spot technique. *Phys. Rev. A*, 82(043408), 2010. Cited on 101, 114

[142] Yu. Ralchenko, A. E. Kramida, J. Reader, and NIST ASD Team (2008). *NIST Atomic Spectra Database (Version 3.1.5), [http://physics.nist.gov/asd3]*, 2010, August 24. Cited on 105

[143] M. M. Schauer, J. R. Danielson, D. Feldbaum, M. S. Rahaman, L.-B. Wang, J. Zhang, X. Zhao, and J. R. Torgerson. Isotope-selective trapping of doubly charged Yb ions. *Phys. Rev. A*, 82:062518, 2010. Cited on 106

[144] A. Braun, C. Paape, C. Balzer, W. Neuhauser, and C. Wunderlich. Resonance enhanced isotope-selective photoionization of Yb I for ion trap loading. *ArXiv e-prints*, December 2007. Cited on 106, 107

[145] Ch. Wunderlich and Ch. Balzer. Quantum measurements and new concepts for experiments with trapped ions. *Advances in Atomic, Molecular, and Optical Physics*, 49:295–376, 2003. Cited on 116

[146] C. S. Flether and J.D. Close. Extended temperature tuning of an external cavity diode laser. *Appl. Phys. B*, 78:305, 2004. Cited on 118

[147] A.-T. Nguyen, L.-B. Wang, M. M. Schauer, and J. R. Torgerson. Extended temperature tuning of an ultraviolet diodelaser for trapping and cooling single Yb^+ ions. *Rev. Sci. Instrum.*, 81:053110, 2010. Cited on 118

[148] Proivate communication with Nichia. Cited on 119

[149] Hugh D. Young and Rodger A. Freedman. *University Physics 11th Edition*. Addison WESLEY, 2004. Cited on 123

[150] R. Ozeri, C. Langer, J. D. Jost, B. DeMarco, A. Ben-Kish, B. R. Blakestad, J. Britton, J. Chiaverini, W. M. Itano, D. B. Hume, D. Leibfried, T. Rosenband, P. O.

Schmidt, and D. J. Wineland. Hyperfine coherence in the presence of spontaneous photon scattering. *Phys. Rev. Lett*, 95(030403), 2005. Cited on 136

[151] D.F.V. James. Quantum dynamics of cold trapped ions with application to quantum computation. *Appl. Phys. B*, 66:181–190, 1998. Cited on 137, 199, 200

[152] Christian Felix Roos. Controlling the quantum state of trapped ions. *PhD thesis, University of Innsbruck*, 2000. Cited on 139

[153] Gerhard Kirchmair. Quantum non-demolition measurements and quantum simulation. *PhD thesis, University of Innsbruck*, 2010. Cited on 139

[154] Chr. Tamm, D. Engelke, and V. Bühner. Spectoscopy of the electric-quadrupole transisiton $^2S_{1/2}(F{=}0)$-$^2D_{3/2}(F{=}2)$ in trapped ^{171}Yb$^+$. *Phys. Rev. A*, 61:053405, 2000. Cited on 139

[155] S. Ritter, A. Schoof, J. Grunert, and A. Hemmerich. Reducing the linewidth of a diode laser below 30Hz by stabilization to a reference cavity with a finesse above 10^5. *Opt. Lett.*, 26(20):1562–1564, 2001. Cited on 140

[156] M. Shahriar, A.V. Turukhin, T. Liptay, Y. Tan, and P.R. Hemmer. Demonstration of injection locking a diode laser using a filtered electro-optic modulator sideband. *Opt. Comm.*, 184(457), 2000. Cited on 142

[157] Peter Kohns and Wenko Süptitz. Injection-locking of laser diodes for multifrequency experiments. *Meas. Sci. Yechnol*, 6(979), 1995. Cited on 144

[158] D. Hayes, D. N. Matsukevich, P. Maunz, D. Hucul, Q. Quraishi, S. Olmschenk, W. Campbell, J. Mizrahi, C. Senko, and C. Monroe. Entanglement of atomic qubits using an optical frequency comb. *Phys. Rev. Lett.*, 104(140501), 2010. Cited on 147, 149

[159] W. C. Campbell, J. Mizrahi, Q. Quraishi, C. Senko, D. Hayes, D. Hucul, D. N. Matsukevich, P. Maunz, and C. Monroe. Ultrafast gates for single atomic qubits. *PRL*, 105(090502), 2010. Cited on 147, 149

[160] Eric Black. An introduction to Pound–Drever–Hall laser frequency stabilization. *Am. J. Phys.*, 69(1):79, 2001. Cited on 185, 187

[161] Eric Black. Notes on the Pound-Drever-Hall technique. *internal working note of the LIGO Project*, 1998. Cited on 185

[162] Jan Benhelm. Precision spectroscopy and qunatum information processing with trapped calcium ions. *PhD thesis, University of Innsbruck*, 2008. Cited on 201

Appendix A

Doppler Cooling Limit

Doppler cooling is the primary means for cooling trapped ions. The technique utilises the oscillatory motion of trapped ions to induce velocity dependent photon absorption to reduce the ion's energy. However, a small amount of energy is returned to the ion during photon emission. The limit of Doppler cooling is lowest steady state temperature, where the rate of energy loss due to photon absorption equals the heating rate due to photon recoil.

$$\frac{dE}{dt}|_{\text{cooling}} = \frac{dE}{dt}|_{\text{heating}} \tag{A.1}$$

Cooling Rate

Ion cooling is velocity dependent, where the rate of cooling is expressed as

$$\frac{dE}{dt}|_{\text{cooling}} = \bar{F} \cdot \bar{v} \tag{A.2}$$

where $\bar{F}$ is the velocity dependent damping force and $\bar{v}$ the ion velocity. This force is related to ion fluorescence via

$$\bar{F} = \hbar\bar{k}\frac{dN}{dt} = \hbar\bar{k}\frac{\Gamma s_0/2}{1 + s_0 + \left(\frac{2(\Delta - \Delta_{\text{D}})}{\Gamma}\right)^2} \tag{A.3}$$

where $\Delta_{\text{D}} = \bar{k} \cdot \bar{v}$ is the velocity dependent instantaneous Doppler shift of the transition frequency as a result of the ion motion. Assuming the ion velocity is small compared to the detuning $\Delta > \Delta_D$, the force applied to the ion can be Taylor expanded as

$$\bar{F} = \bar{F}_0 + \frac{d\bar{F}}{d\Delta}|_0 \cdot \bar{k}\bar{v} + ... \tag{A.4}$$

By setting $F_0 = 0$ the change in energy as a result of Doppler cooling is

$$\frac{dE}{dt}\Big|_{\text{cooling}} \approx \frac{4\hbar\bar{k}^2\Delta}{\Gamma} \frac{s_0\bar{v}^2}{\left(1 + s_0 + \left(\frac{2\Delta}{\Gamma}\right)^2\right)^2} \tag{A.5}$$

Heating Rate

The energy associated with each scatter event, recoil energy, is

$$E = \frac{(\hbar\bar{k})^2}{2m} \tag{A.6}$$

where $\bar{k}$ is the wavevector of the emitted photon and m the ion mass. Considering the scatter rate of an ion is

$$\frac{dN}{dt} = \frac{s_0\Gamma/2}{1 + s_0 + \left(\frac{2\Delta}{\Gamma}\right)^2} \tag{A.7}$$

where s_0 is the ion saturation parameter, Γ the natural linewidth of the ion, Δ the laser detuning. The ion, however, receives a momentum kick through both photon absorption and emission. The resulting ion heating rate is then

$$\frac{dE}{dt}\Big|_{\text{heating}} = \frac{1}{2m} \frac{\hbar^2\bar{k}^2 s_0\Gamma}{1 + s_0 + \left(\frac{2\Delta}{\Gamma}\right)^2} \tag{A.8}$$

Cooling Limit

In a steady state regime the heating rate and cooling rate are the same, and corresponds to the minimum ion velocity. Comparing equations A.8 and A.5 the ion velocity is expressed as

$$\bar{v}^2 = \frac{\hbar\Gamma^2}{8m\Delta}\left(1 + s_0 + \left(\frac{2\Delta}{\Gamma}\right)^2\right) \tag{A.9}$$

Assuming a small laser intensity, $s_0 \ll 1$, and relating ion temperature to ion energy $m\bar{v}^2/2 = k_B T/2$, the ion temperature can be expressed as

$$T = \frac{\hbar\Gamma}{4k_B}\left[\frac{\Gamma}{2\Delta} + \frac{2\Delta}{\Gamma}\right] \tag{A.10}$$

The minimum ion temperature, and hence the optimum cooling, is achieved when $\Delta = \Gamma/2$. The ion temperature is then

$$T_{min} = \frac{\hbar\Gamma}{2k_B} \tag{A.11}$$

Appendix B

Qubit Manipulation

Through the interaction with electromagnetic radiation it is possible to control the state of the qubit as well as couple to the motion of the harmonic oscillator. Presented here is the development of the Hamiltonian describing these interactions.

The interaction Hamiltonian in the interaction picture is expressed as

$$
\hat{H}_{int} = \frac{\hbar\Omega}{2}\left[e^{i\omega_0 t\hat{\sigma}_z/2}(\hat{\sigma}_+ + \hat{\sigma}_-)e^{-i\omega_0 t\hat{\sigma}_z/2}\right]
$$
$$
\left[e^{i\omega_i\hat{\alpha}^\dagger\hat{\alpha}}\left(e^{i(kr-\omega t+\phi)} + e^{-i(kr-\omega t+\phi)}\right)e^{i\omega_i\hat{\alpha}^\dagger\hat{\alpha}}\right] \quad\text{(B.1)}
$$

The terms in the first set of square brackets describe the spin state (qubit state), while the terms in the second set of square brackets describe the motional state of the ion. Since the spin and creation/annihilatin operators commute the two components can be treated separately. Considering first the spin component of equation B.1, these components can be simplified using the identities $[\hat{\sigma}_z, \hat{\sigma}_+] = 2\hat{\sigma}_+$ and $[\hat{\sigma}_z, \hat{\sigma}_-] = -2\hat{\sigma}_-$ and the relationship [?]

$$
e^{\alpha\hat{A}}\hat{B}e^{-\alpha\hat{A}} \approx \hat{B} + \alpha[\hat{A}, \hat{B}] + \frac{\alpha^2}{2!}[\hat{A}[\hat{A}, \hat{B}]] + \frac{\alpha^3}{3!}[\hat{A}[\hat{A}[\hat{A}, \hat{B}]]] \quad\text{(B.2)}
$$

The spin terms reduce to

$$
\begin{aligned}
e^{i\omega_0 t/2\hat{\sigma}_z}\hat{\sigma}_+ e^{-i\omega_0 t/2\hat{\sigma}_z} &= \hat{\sigma}_+ + \omega_0 t\hat{\sigma}_+ + \frac{(\omega_0 t)^2}{2!}\hat{\sigma}_+ + \frac{(\omega_0 t)^3}{3!}\hat{\sigma}_+ + \cdots \\
&= e^{i\omega_0 t}\hat{\sigma}_+ \quad\text{(B.3)}
\end{aligned}
$$

and

$$
\begin{aligned}
e^{i\omega_0 t/2\hat{\sigma}_z}\hat{\sigma}_- e^{-i\omega_0 t/2\hat{\sigma}_z} &= \hat{\sigma}_- - \omega_0 t\hat{\sigma}_- + \frac{(\omega_0 t)^2}{2!}\hat{\sigma}_- - \frac{(\omega_0 t)^3}{3!}\hat{\sigma}_- + \cdots \\
&= e^{-i\omega_0 t}\hat{\sigma}_- \quad\text{(B.4)}
\end{aligned}
$$

enabling the spin component of H_{int} to be written as

$$e^{i\omega_0 t\hat{\sigma}_z/2}(\hat{\sigma}_+ + \hat{\sigma}_-)e^{-i\omega_0 t\hat{\sigma}_z/2} = e^{i\omega_0 t}\hat{\sigma}_+ + e^{-i\omega_0 t}\hat{\sigma}_- \tag{B.5}$$

Turning now to the motional component in equation B.1. It can be rewritten as

$$e^{i\omega_i\hat{\alpha}^\dagger\hat{\alpha}}\left(e^{i(kr-\omega t+\phi)} + e^{-i(kr-\omega t+\phi)}\right)e^{-i\omega_i\hat{\alpha}^\dagger\hat{\alpha}}$$
$$= e^{i(kr_0-\omega t+\phi)}e^{i\omega_i\hat{\alpha}^\dagger\hat{\alpha}}e^{i\eta(\hat{\alpha}+\hat{\alpha}^\dagger)}e^{-i\omega_i\hat{\alpha}^\dagger\hat{\alpha}}$$
$$+ e^{-i(kr_0-\omega t+\phi)}e^{i\omega_i\hat{\alpha}^\dagger\hat{\alpha}}e^{-i\eta(\hat{\alpha}+\hat{\alpha}^\dagger)}e^{-i\omega_i\hat{\alpha}^\dagger\hat{\alpha}} \tag{B.6}$$

where the factor $e^{ik\cdot r}$ is separated into a phase factor, e^{ikr_0}, and a position operator, $e^{k\cdot z_t}$. The position operator is also rewritten as $k \cdot z_t = kz_0(\hat{\alpha} + \hat{\alpha}^\dagger) = \eta(\hat{\alpha} + \hat{\alpha}^\dagger)$, with $z_0 = \sqrt{\hbar/(2m\omega_z)}$ the spread of the ground state harmonic oscillator wavefunction. The exponent in $e^{i\eta(\hat{\alpha}+\hat{\alpha}^\dagger)}$ is then Taylor expanded and each term treated separately, yielding [89]

$$e^{i\omega_i\hat{\alpha}^\dagger\hat{\alpha}}(i\eta(\hat{\alpha} + \hat{\alpha}^\dagger))^n e^{-i\omega_i\hat{\alpha}\hat{\alpha}^\dagger} = (i\eta(\hat{\alpha}e^{-i\omega_i t} + \hat{\alpha}^\dagger e^{i\omega_i t})^n \tag{B.7}$$

then summing over all terms in the Taylor expansion produces [89]

$$e^{i\omega_i\hat{\alpha}^\dagger\hat{\alpha}}e^{i\eta(\hat{\alpha}+\hat{\alpha}^\dagger)}e^{-i\omega_i\hat{\alpha}\hat{\alpha}^\dagger} = e^{i\eta(\hat{\alpha}e^{-i\omega_i t}+\hat{\alpha}^\dagger e^{i\omega_i t})} \tag{B.8}$$

The motional part of $\hat{H}_{int}$ can then be written as

$$e^{i\omega_i\hat{\alpha}^\dagger\hat{\alpha}}\left(e^{i(kr-\omega t+\phi)} + e^{-i(kr-\omega t+\phi)}\right)e^{-i\omega_i\hat{\alpha}^\dagger\hat{\alpha}} = e^{i(kr_0-\omega t+\phi)}e^{i\eta(\hat{\alpha}e^{-i\omega_i t}+\hat{\alpha}^\dagger e^{i\omega_i t})} + c.c.$$

Combining the spin and motion components (equations B.5 and B.9 respectively) the interaction Hamiltonian in the interaction picture becomes

$$\hat{H}_{int} = \frac{\hbar\Omega}{2}\left[e^{i\omega_0 t\hat{\sigma}_z}\hat{\sigma}_+ + e^{i\omega_0 t\hat{\sigma}_z}\hat{\sigma}_-\right]\left[e^{i(kr_0-\omega t+\phi)}e^{i\eta(\hat{\alpha}e^{-i\omega_i t}+\hat{\alpha}^\dagger e^{i\omega_i t})} + c.c.\right] \tag{B.9}$$

Assuming the applied field is close to resonance ($\omega \approx \omega_0$) the Hamiltonian can be simplified by applying the rotating wave approximation (RWA). This approximation assumes that over the time scale required for the system to evolve all rapidly oscillating terms (i.e. those oscillating at $\omega + \omega_0$) average to zero. Applying the RWA the rapidly oscillating terms are removed and the interaction Hamiltonian can be written

$$\hat{H}_{int} = \frac{\hbar\Omega}{2}\left[\hat{\sigma}_+ e^{i[\eta(\hat{\alpha}e^{-i\omega_i t}+\hat{\alpha}^\dagger e^{i\omega_i t})+kr_0+\delta\omega t+\phi]} + \hat{\sigma}_- e^{-i[\eta(\hat{\alpha}e^{-i\omega_i t}+\hat{\alpha}^\dagger e^{i\omega_i t})+kr_0+\delta\omega t+\phi]}\right] \tag{B.10}$$

where $\delta\omega = \omega - \omega_0$ is the detuning of the laser from resonance. Depending upon the detuning the interaction Hamiltonian will couple specific internal and motional states. To determine the evolution of the two level system the generalised Hamiltonian (equation B.10) is inserted into Schrödinger's equation, along with the state vector $|\Psi(t)\rangle = \sum_{n=0}^{\infty}(c_{\uparrow,n}(t)|\uparrow,n\rangle + c_{\downarrow,m}(t)|\downarrow,m\rangle)$. The solution to the two-level system is [68]

$$\dot{c}_{\uparrow,n} = -i^{1+|n-m|}e^{-i(\delta t - \phi)}\frac{\Omega_{m,n}}{2}c_{\downarrow,m} \tag{B.11}$$

$$\dot{c}_{\downarrow,m} = -i^{1-|n-m|}e^{i(\delta t - \phi)}\frac{\Omega_{m,n}}{2}c_{\uparrow,n} \tag{B.12}$$

where $\Omega_{n,m} = \Omega_{m,n}$ is the Rabi frequency, or coupling strength, between $|\uparrow,n\rangle \leftrightarrow |\downarrow,m\rangle$. This expression for the Rabi frequency can then be further generalised [68]

$$\begin{aligned}
\Omega_{m,n} &= \Omega\langle m|e^{i\eta(\hat{a}+\hat{a}^{\dagger})}|n\rangle \\
&= \Omega e^{-\eta^2/2}\sqrt{\frac{n_<!}{n_>!}}\eta^{|n-m|}L_{n_<}^{|m-n|}\left(\eta^2\right) \tag{B.13}
\end{aligned}$$

where Ω is the coupling strength of the carrier transition ($|\uparrow,n\rangle \leftrightarrow |\downarrow,n\rangle$), $n_<$ and $n_>$ are the smaller and larger of n and m respectively, and $L_{n_<}^{|m-n|}$ is an associated Laguerre polynomial.

Appendix C

Laser Mount Drawings

The home built external cavity diode lasers used in the experiments is illustrated in figure C.1. Technical drawings for the individual components are shown in figures C.2 to C.11.
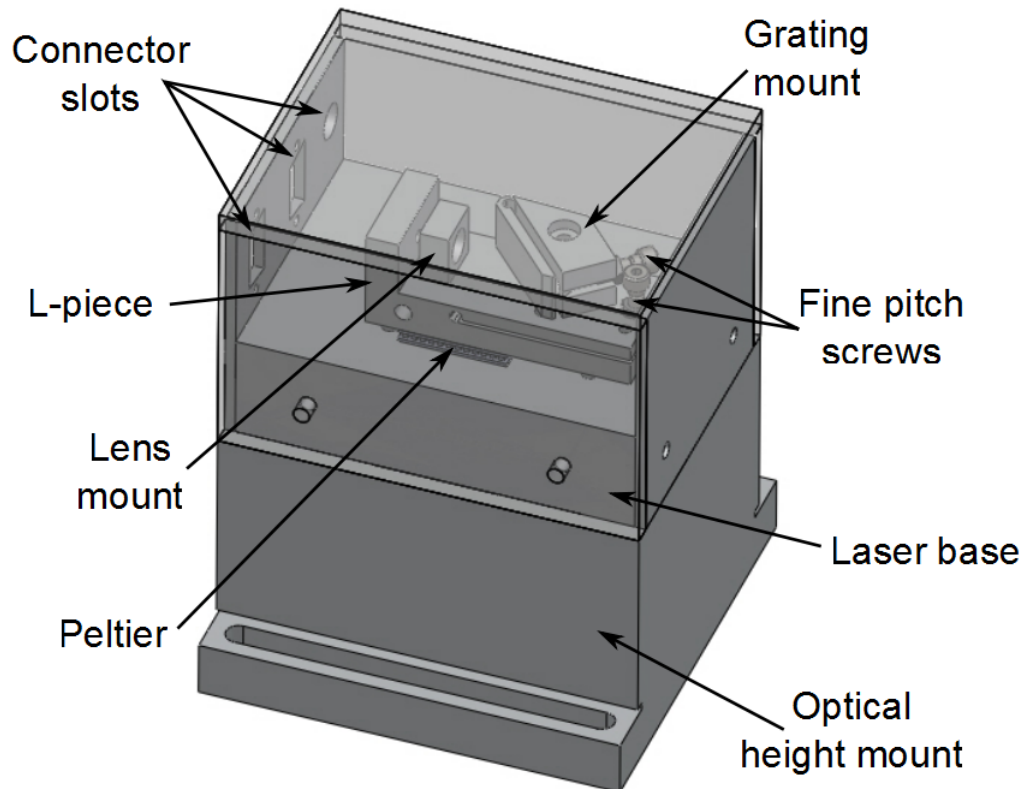

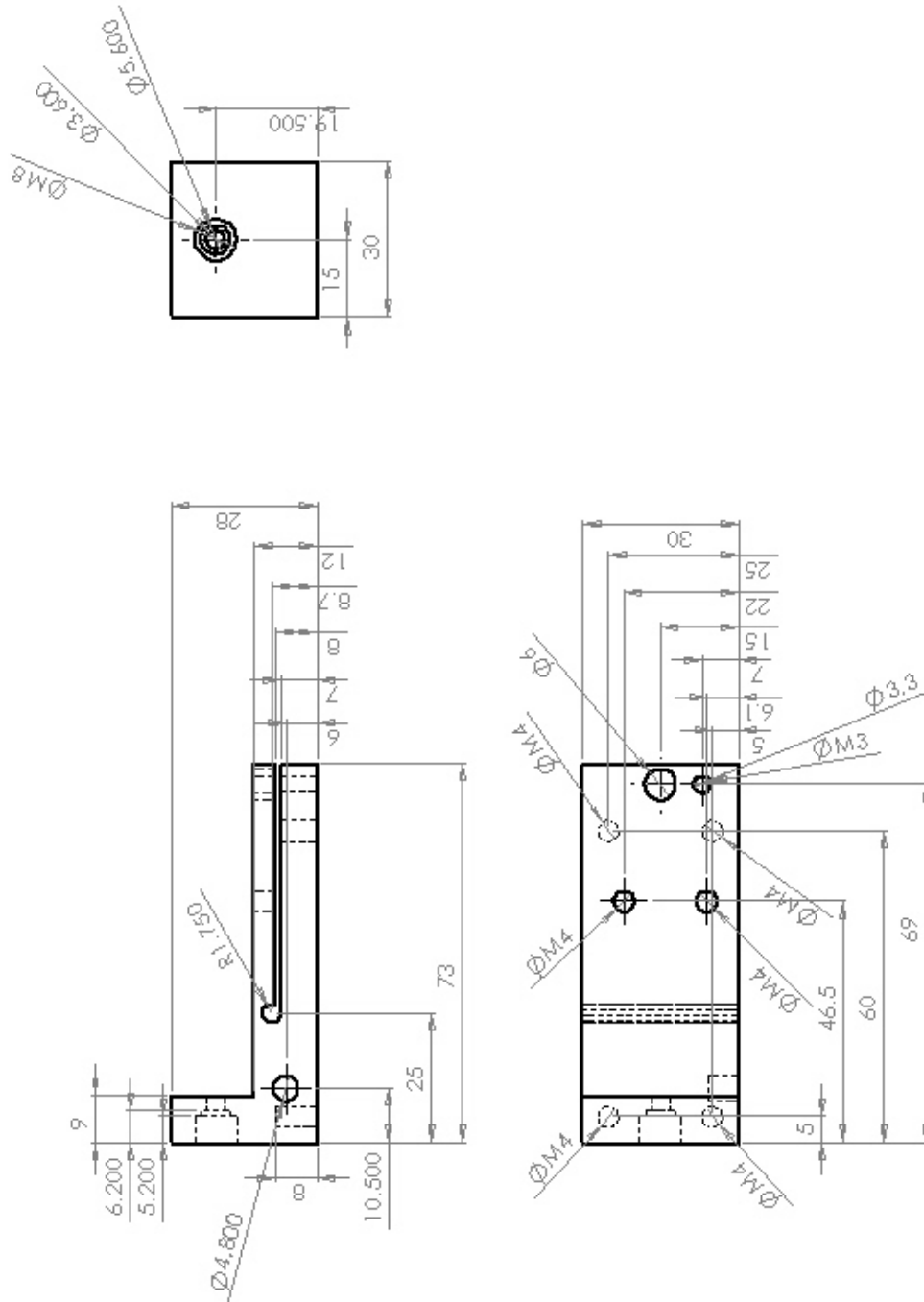Figure C.1: Overview of a constructed external cavity diode laser.

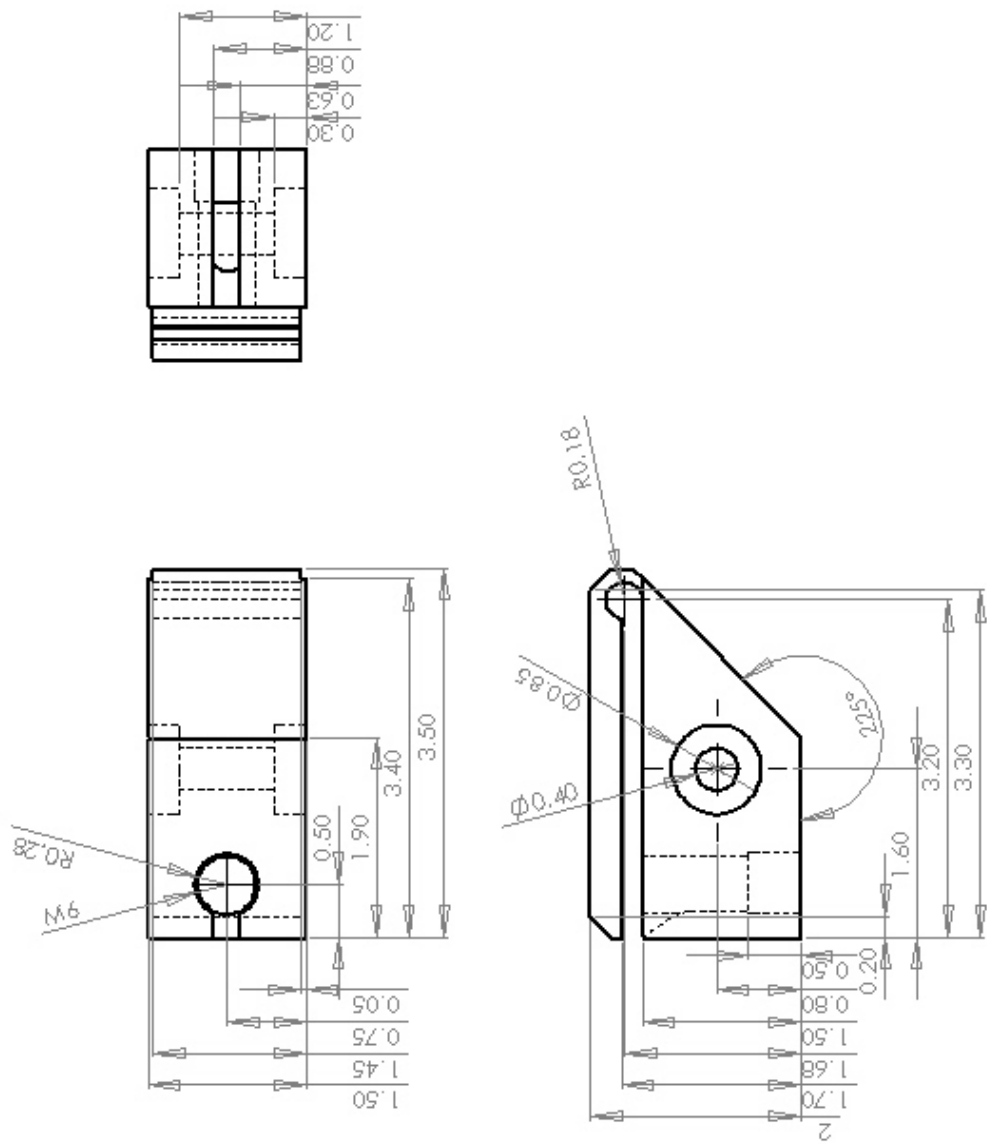Figure C.2: L-piece. Material: aluminium, quantity: x 1

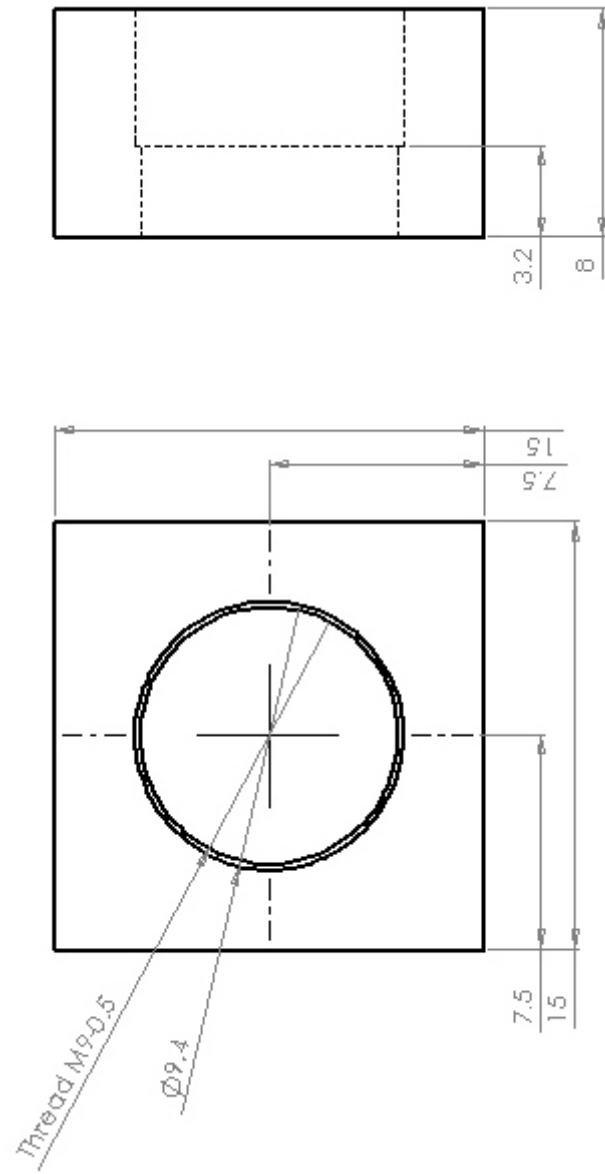Figure C.3: Grating Mount. Material: aluminium, quantity: x 1
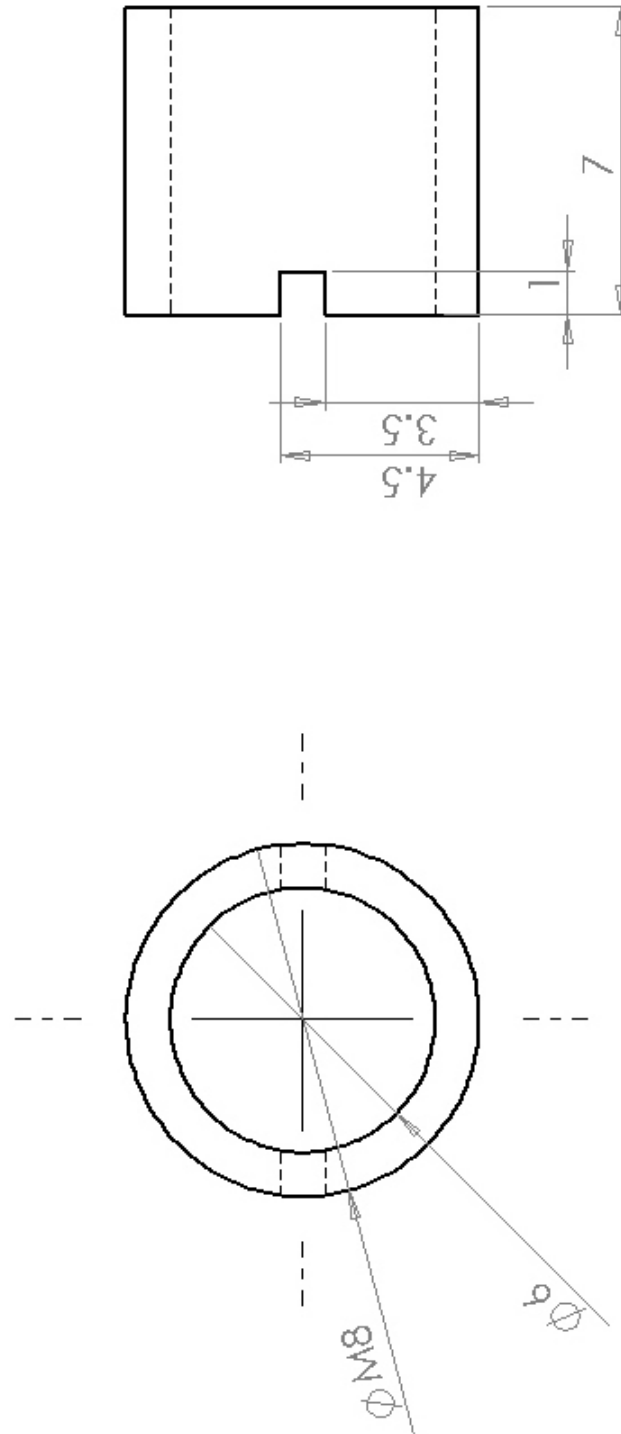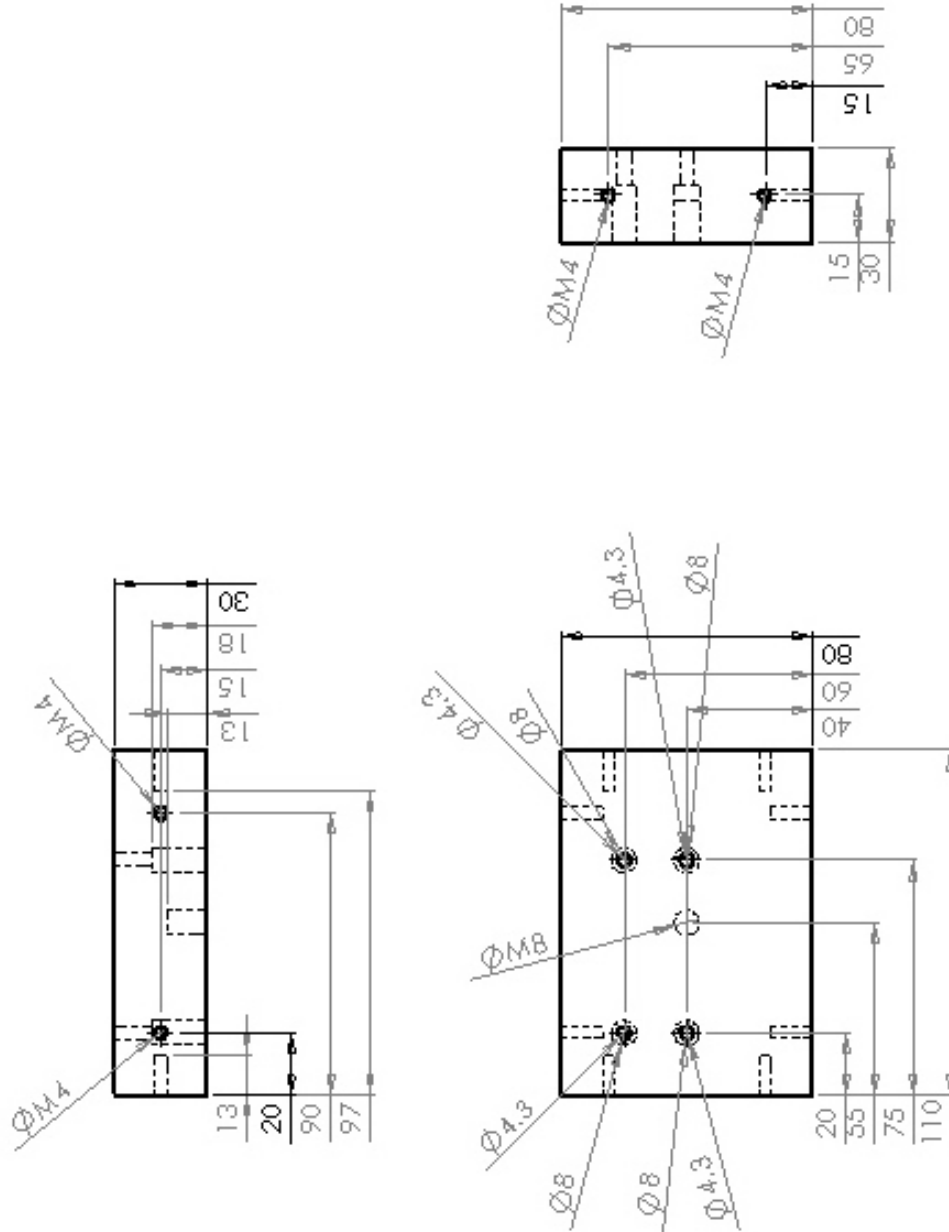
Figure C.4: Lens Mount. Material: aluminium, quantity: x 1

Figure C.5: Laser diode clamp. Material: brass, quantity: x 1

Figure C.6: Laser base. material: aluminium, quantity: x 1
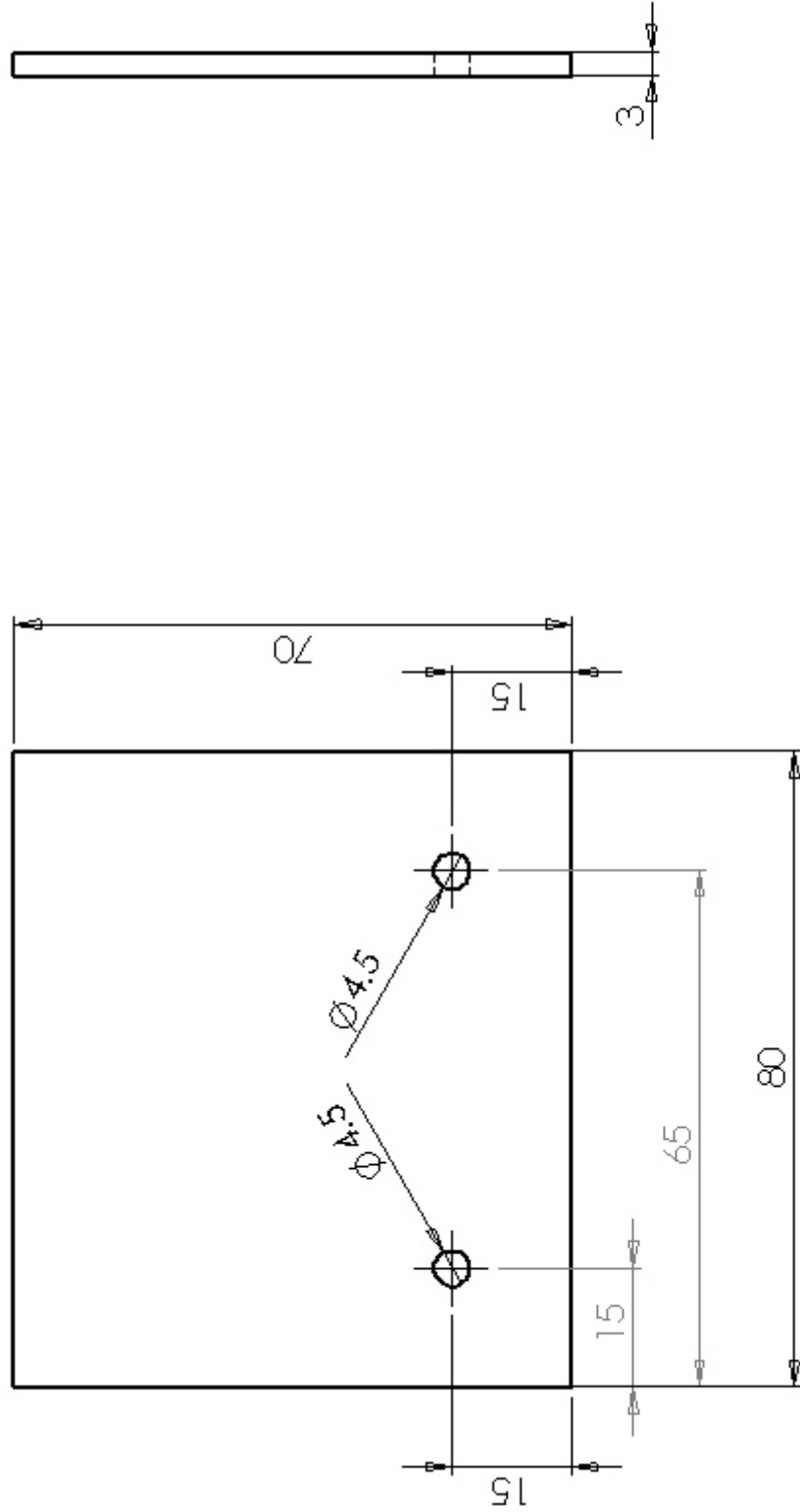
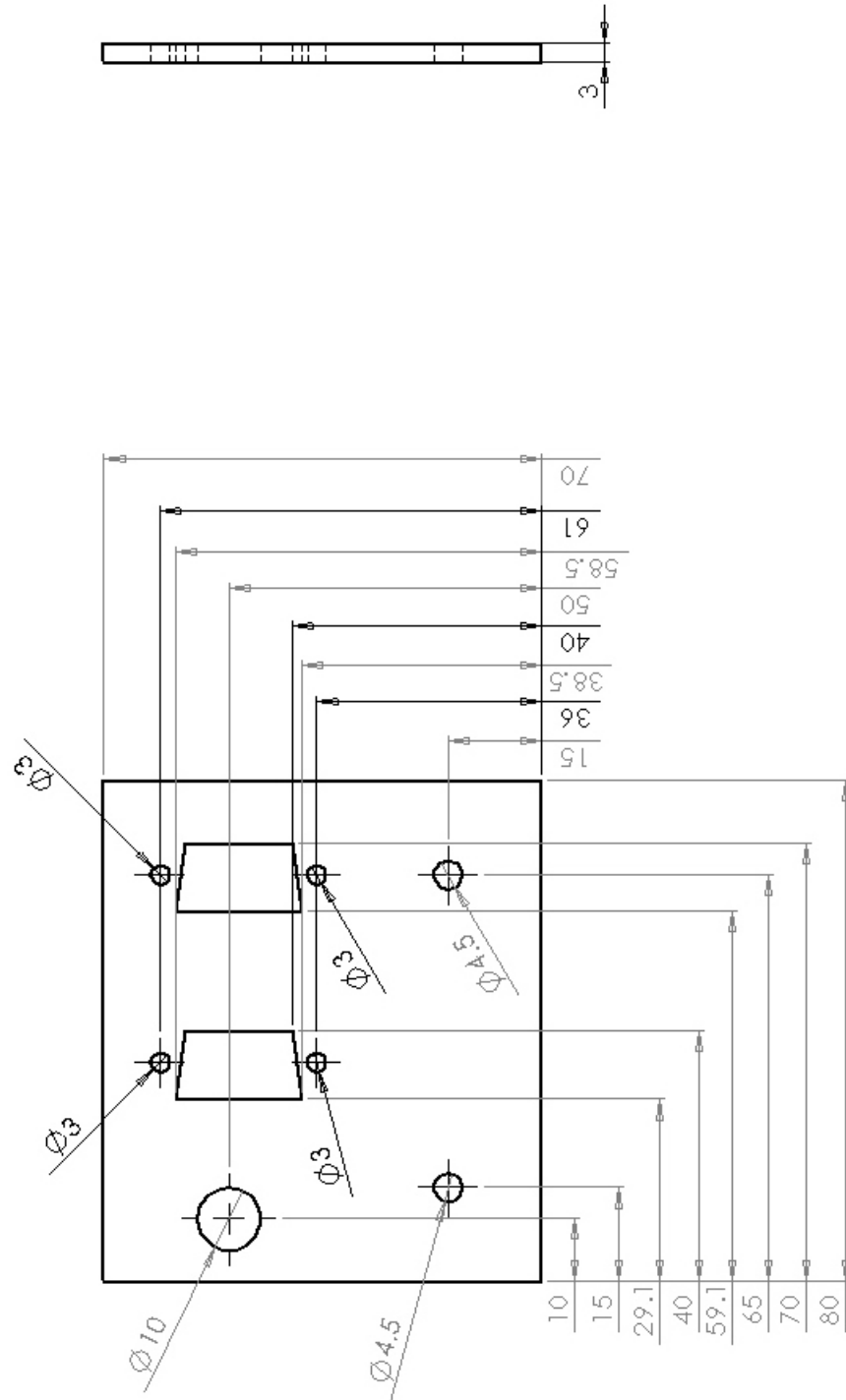Figure C.7: One side of the ECDL housing. Material: aluminium, quantity: x 1

Figure C.8: Side of the housing supporting electrical connections. The trapezoid through-holes are designed to accept sub-D9 connectors. Material: aluminium, quantity: x 1
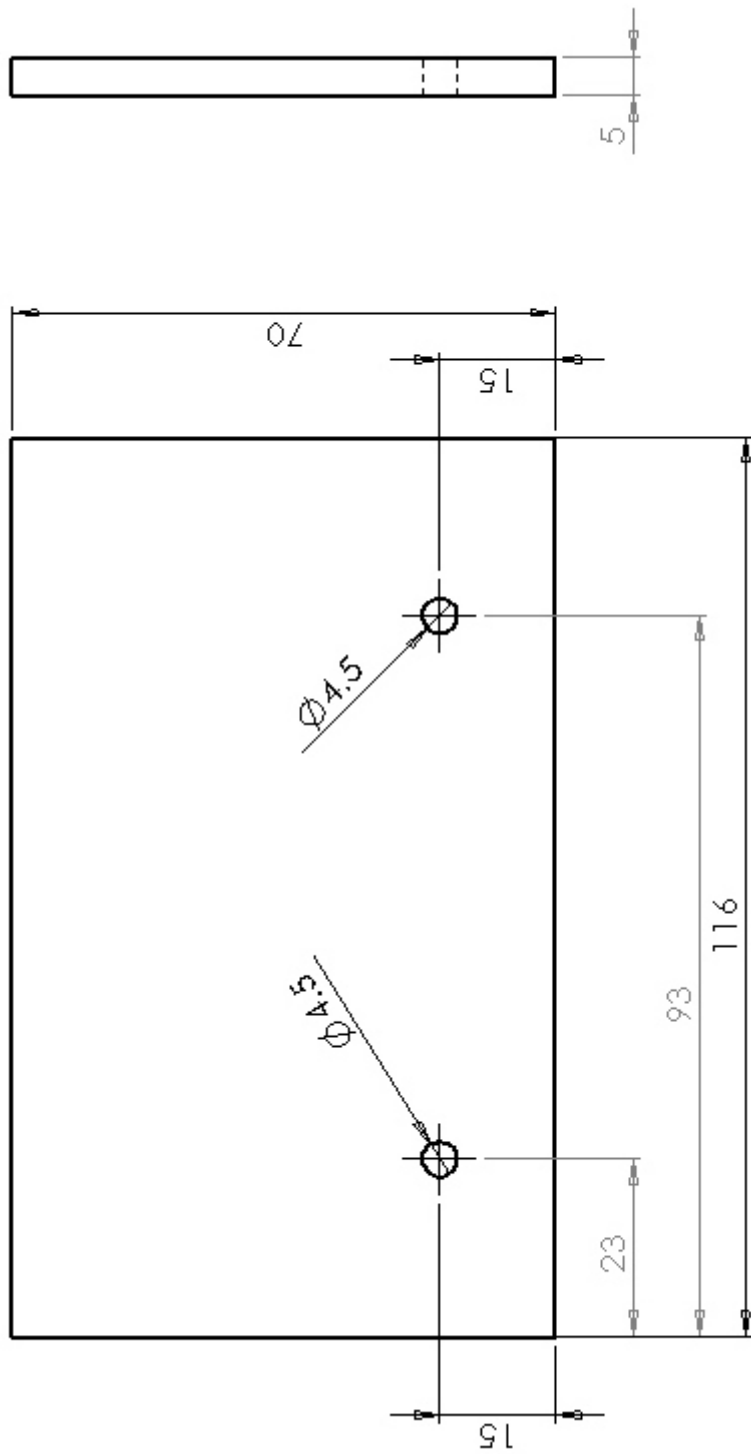
Figure C.9: Sidewalls of the ECDL housing. Hole used to allow beam to exit is not shown as hole changes location between lasers. Material: perspex, quantity: x 2
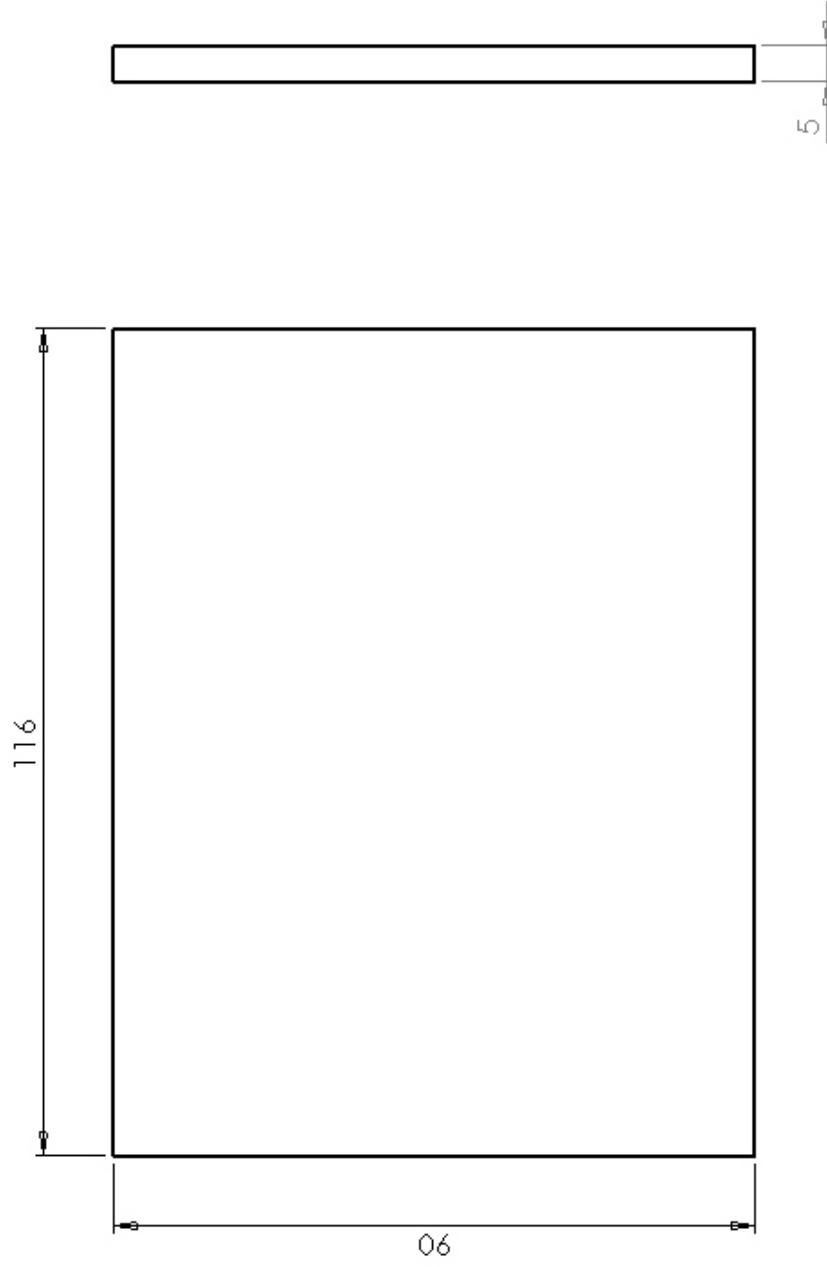
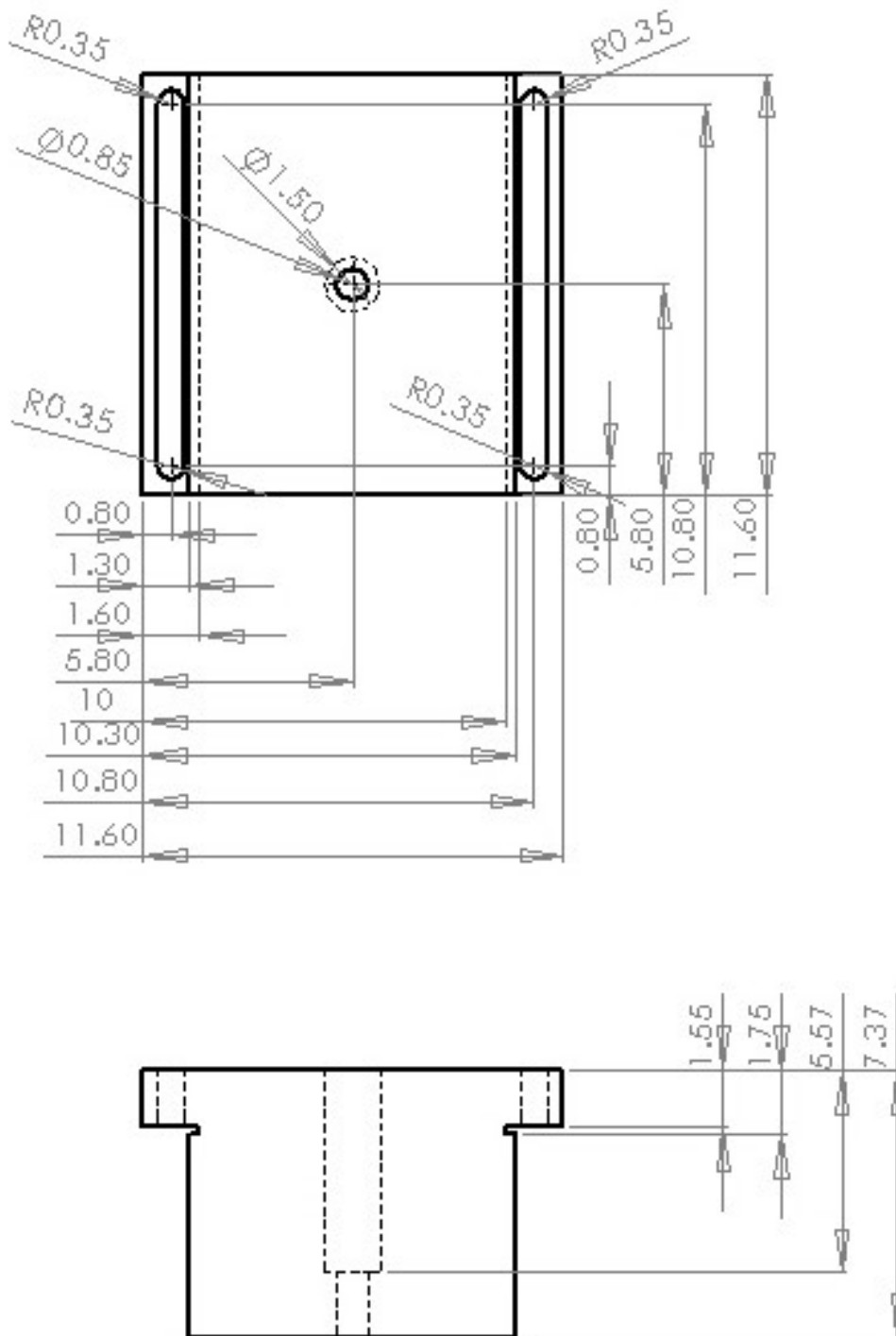Figure C.10: Lid covering the ECDL. Material: perspex, quantity: x 1

Figure C.11: Mount used to raise ECDL to the optical height of the table. Material: aluminium, quantity: x 1

Appendix D

Frequency Sideband Generation

To access the hyperfine states in $^{171}\text{Yb}^+$ frequency sidebands are applied to 739 nm (and 369 nm) and 935 nm beams via an electro optic modulator (EOM) and current modulation respectively, as discussed in chapter 3. Both of these approaches generate sideband by modulating the phase of the laser beam. Current modulation changes the refractive index of the laser diode, effectively changing the optical path length of the diode and hence the phase of the light propagating within the diode. Similarly the EOM uses a crystal with a voltage dependent refractive index, whereby a voltage across the crystal changes the optical path length within the crystal and the phase of light travelling through it.

To understand how modulating path length generates frequency sidebands first consider the electric field of the light of an unmodulated laser beam

$$E_\text{I} = E_0 \cos(\omega_0 t + \Phi) \tag{D.1}$$

where E_0 is the electric field amplitude, ω_0 the frequency of the unmodulated light, and Φ the phase of the beam. Modulating the optical path length, and phase of the electric field $\Phi = \phi \sin(\omega_\text{m} t)$, where $\omega_\text{m} t$ is the modulation frequency and ϕ is the modulation amplitude, the modulated electric field becomes

$$E_\text{m} = E_0 \cos(\omega_0 t + \phi \sin(\omega_\text{m} t)) \tag{D.2}$$

which can be rewritten as

$$
\begin{aligned}
E_\text{m} &= \frac{E_0}{2}\left[e^{i(\omega_0 t)}e^{i(\phi \sin(\omega_\text{m} t))} + c.c.\right] \\
&= \frac{E_0}{2}\left[e^{i(\omega_0 t)}e^{\frac{\phi}{2}(e^{i\omega_\text{m} t}-e^{-i\omega_\text{m} t})} + c.c.\right]
\end{aligned} \tag{D.3}
$$

Using the Bessel function relation

$$e^{(x/2)(t-1/t)} = \sum_{n=-\inf}^{\inf} J_n(x)t^n \qquad (D.4)$$

equation (D.3) can be rewritten as

$$E_m = \frac{E_0}{2}\left[e^{i(\omega_0 t)}\sum_{n=-\inf}^{\inf} J_n(\phi)e^{in\omega_m t} + c.c.\right] \qquad (D.5)$$

where n is an integer and $J_n(\phi)$ an ordinary Bessel function of order n. To drive the desired transition we are mostly interested in the carrier and first order sidebands, i.e. $n = 0, \pm1$. Under this consideration the resulting electric field can be written as

$$E_m \approx \frac{E_0}{2}\left[e^{i(\omega_0 t)} + J_1(\phi)e^{i(\omega_0 t + \omega_m)t} + J_{-1}(\phi)e^{i(\omega_0 - t\omega_m)t} + c.c.\right] \qquad (D.6)$$

which shows that the electric field consists not only of the carrier frequency, ω_0, but two extra frequencies at $\omega_0 + \omega_m$ and $\omega_0 - \omega_m$. It can therefore be seen that the frequency separation of the sidebands, from the carrier, is the same as frequency used to modulate the laser diode. Using current modulation 3.07 GHz (1.05 GHz) sidebands are applied to the 935 nm (739 nm) beam, while the EOM generates the 7.37 GHz sidebands on the 739 nm beam.

Appendix E

Derivation of Locking Error Signals

In section 3.3.5 the Pound Drever Hall technique is used to stabilise the frequency doubling laser, while in section 4.3.1 the 780 nm external cavity diode laser is stabilised using frequency modulated (fm) spectroscopy. In both techniques a modulated laser beam is directed towards a frequency reference and the frequency dependent beam intensity, relative to the resonance frequency of the reference, is measured. In the Pound Drever Hall lock the beam intensity corresponds to the proportion of the beam reflected from a cavity, which is a function of the laser frequency with respect to the cavity resonance. In fm spectroscopy the beam intensity is related to the amount of light transmitted through an atomic vapour, and therefore a function of the laser frequency with respect the atomic transition frequency. Although the mechanisms are different for both techniques the principle of generating an error signal using this frequency dependent beam intensity holds many similarities.

The following discussion describes how the error signal is generated via the Pound Drever Hall technique, so considers reflections from a cavity rather than transmission through an atomic reference. In both cases, however, the resulting error signals have the same profile. Following work by Eric Black [160, 161], the electric field of the modulated signal (considering up to first order sidebands only) is expressed as

$$E = E_0[J_0(\beta)e^{i\omega t} + J_1(\beta)e^{i(\omega+\Omega)t} - J_1(\beta)e^{i(\omega-\Omega)t}] \qquad \text{(E.1)}$$

where $J_n(\beta)$ is an ordinary Bessel function of order n, ω is the laser frequency and Ω is the modulation frequency. When the beam is incident upon the cavity, a proportion of the

beam is reflected, with the reflected portion given by $E_{\text{ref}} = F(\omega)E$. Where the reflection coefficient, for an ideal cavity, is

$$F(\omega) = \frac{r(e^{i\phi} - 1)}{1 - r^2 e^{i\phi}} \tag{E.2}$$

where r is the amplitude reflection coefficient of each mirror, and ϕ the phase gained after one round trip in the cavity. ϕ can be expressed as

$$\phi = \frac{\omega}{\Delta \nu_{\text{fsr}}} \tag{E.3}$$

where $\Delta \nu_{\text{fsr}}$ is the cavity free spectral range. The signal reflected from the cavity can therefore be expressed as

$$E_{\text{ref}} = E_0[F(\omega)J_0(\beta)e^{i\omega t} + F(\omega)J_1(\beta)e^{i(\omega+\Omega)t} - F(\omega)J_1(\beta)e^{i(\omega-\Omega)t}] \tag{E.4}$$

When the cavity is resonant with the laser frequency the reflection co-efficient goes to zero, corresponding to complete transmission through the cavity. The signal reflected from the cavity and measured by the photodiode is $P_{\text{ref}} = |E_{\text{ref}}|^2$. Using the relationships

$$P_0 = |E_0|^2 \tag{E.5}$$

$$P_{\text{c}} = J_0^2(\beta)P_0 \tag{E.6}$$

$$P_{\text{s}} = J_1^2(\beta)P_0 \tag{E.7}$$

where P_0 is the total power of the incident beam, P_{c} and P_{s} is the power in the carrier and first order sidebands. After some algebra the signal from the photodiode can be expressed as

$$
\begin{aligned}
P_{\text{ref}} = {} & P_{\text{c}}|F(\omega)|^2 + P_{\text{s}}\left(|F(\omega+\Omega)|^2 + |F(\omega-\Omega)|^2\right) \\
& + 2\sqrt{P_{\text{c}}P_{\text{s}}}(\Re[F(\omega)F^*(\omega+\Omega) - F^*(\omega)F(\omega-\Omega)]\cos(\Omega t) \\
& + \Im[F(\omega)F^*(\omega+\Omega) - F^*(\omega)F(\omega-\Omega)]\sin(\Omega t))
\end{aligned} \tag{E.8}
$$

where $F(\omega)$, $F(\omega+\Omega)$ and $F(\omega-\Omega)$ are the reflection coefficients at the carrier and sideband frequencies respectively, and the symbols $\Re$ and $\Im$ represent the real and imaginary components of the reflected signal. The shape of the error signal is then determined by the modulation frequency relative to the cavity linewidth.

When the modulation frequency is much greater than the linewidth of the cavity, such as

that used in the frequency doubling system, the frequency sidebands are assumed to be completely reflected. Black [160] has then shown that in this regime the cosine component of the signal reflected from the cavity, becomes negligible and the error signal can be written as

$$\varepsilon = -2\sqrt{P_c P_s}\,\Im([F(\omega)F^*(\omega + \Omega) - F^*(\omega)F(\omega - \Omega)]) \qquad \text{(E.9)}$$

Taking the example of the frequency doubling system where the modulation frequency Ω is approximately 10 times the free spectral range of the cavity. Plotting $\epsilon/2\sqrt{P_c P_s}$ as a function of ω and $\omega \pm \Omega$ generates the profile shown in figure E.1. Which can be seen to be the same as the error signal generated by the frequency doubling system as shown in figure 3.17.
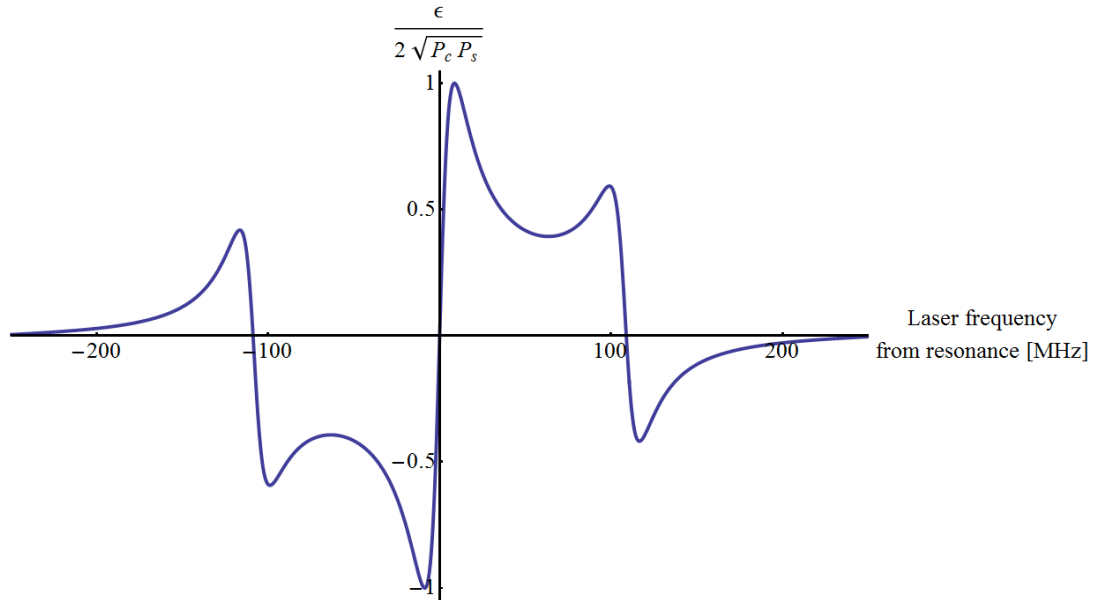

Figure E.1: Illustration of the locking error signal when Ω is greater than the cavity linewidth.

If however, the modulation frequency is small compared to the cavity linewidth, then the carrier and sidebands are all partially transmitted and partially reflected. In this case the power reflected from the cavity is $P_{ref} = P_0|F(\omega)|^2$, and Black has shown that only the cosine part of the reflected signal, equation E.8, survives [160]. The error signal is then

$$\varepsilon = -2\sqrt{P_c P_s}\,\Im([F(\omega)F^*(\omega + \Omega) - F^*(\omega)F(\omega - \Omega)]) \qquad \text{(E.10)}$$

Plotting $\epsilon/2\sqrt{P_c P_s}$ as a function of ω and $\omega \pm \Omega$, where Ω is approximately half a linewidth, yields the error signal shown in figure E.2.
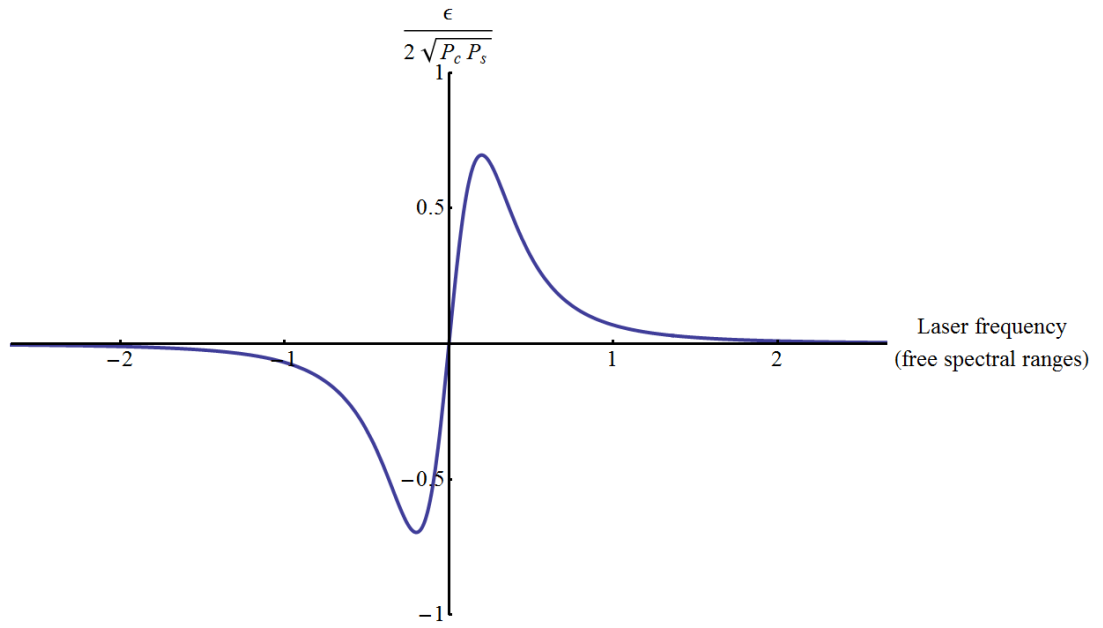
Figure E.2: Illustration of the locking error signal when Ω is less than the cavity linewidth.

This signal resembles the error signal obtained via fm spectroscopy as shown in figure 4.12. The resulting sideband features present in figure E.1 have now been swallowed into the linewidth of the cavity. It should be noted however that the gradient of the zero crossing in either case depends upon the linewidth of the cavity only and not the modulation frequency. The modulation frequency does however limit the speed of any feedback. Higher modulation frequencies enable faster feedback. For slow thermal feedback a lower modulation frequency would be used, while for faster feedback it is preferable to use higher modulation frequencies.

Appendix F

Scanning Fabry Përot Cavity Drawings

The confocal cavities used in the transfer locking scheme, described in section 4.3.2, are shown here. The combined cavity is illustrated in figure F.1, while technical drawings for the individual components are shown in figures F.2 to F.6.
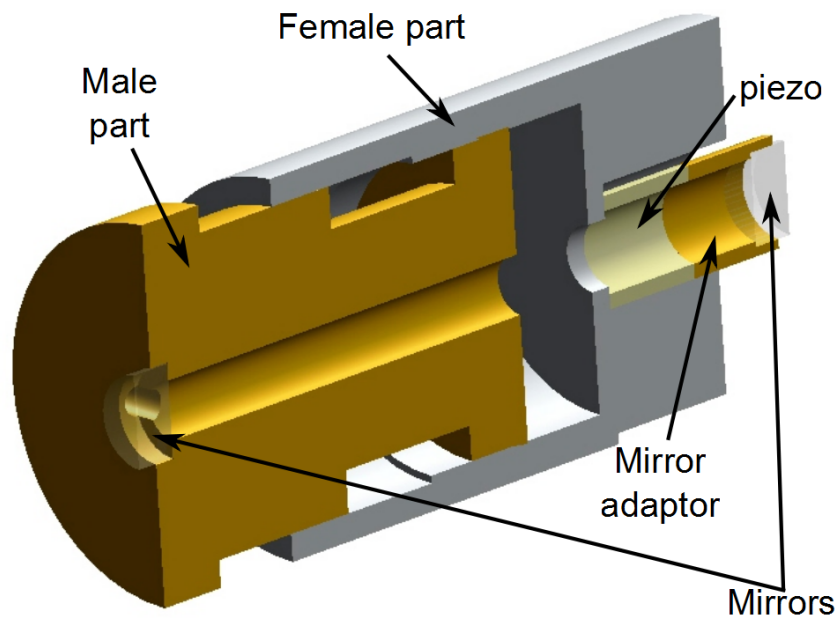

Figure F.1: Illustration of a scanning confocal Fabry-Pérot cavity used in the transfer locking scheme.
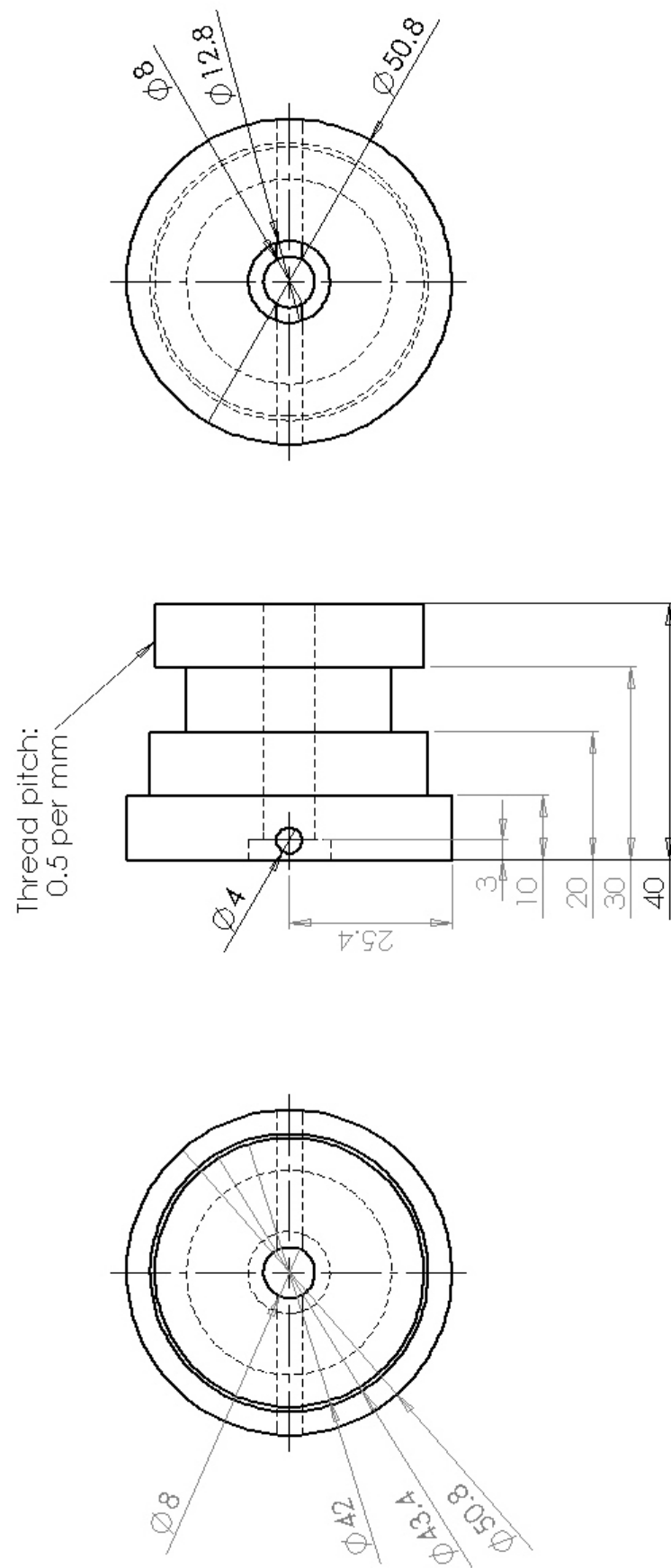
Figure F.2: Male part for the 780 nm / 739 nm cavity. Material: brass, quantity: x 1
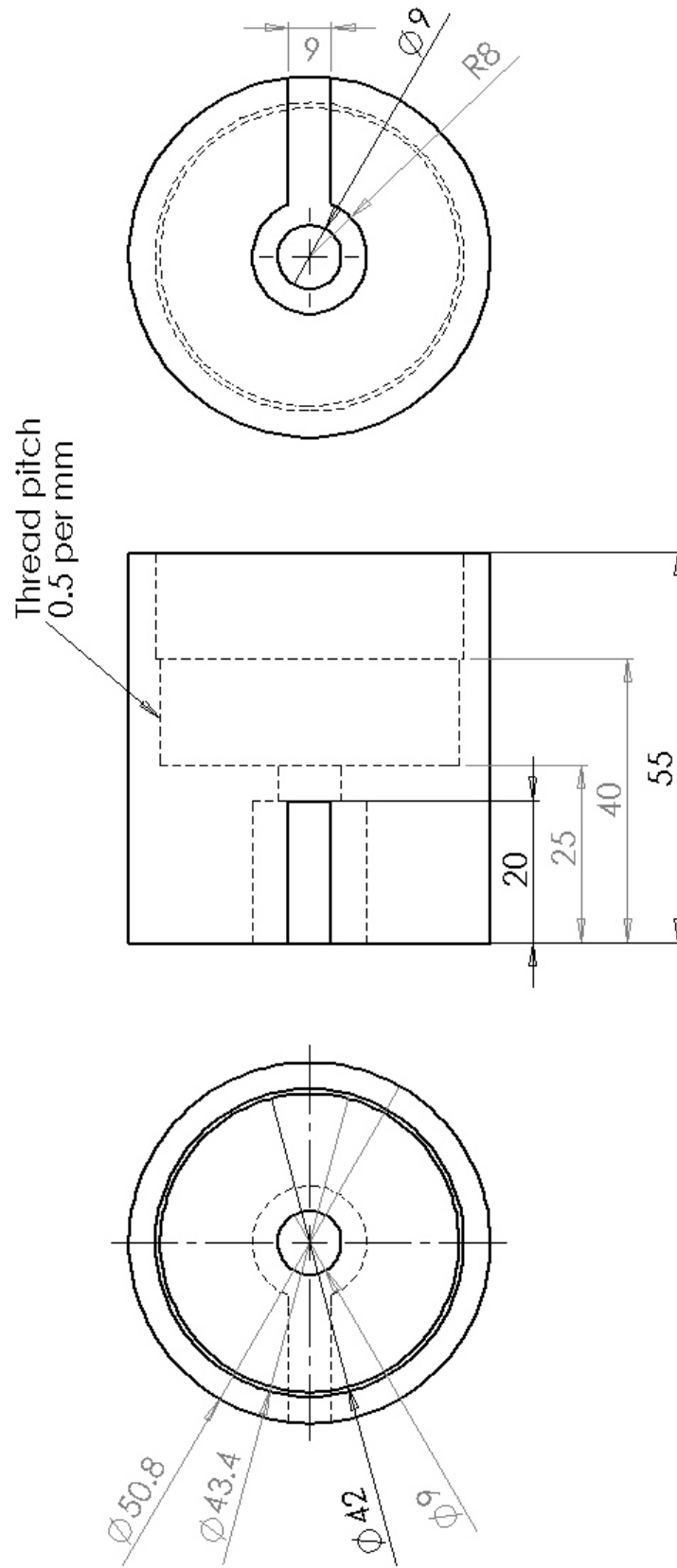
Figure F.3: Female part for the 780 nm / 739 nm cavity. Material: aluminium, quantity: x 1
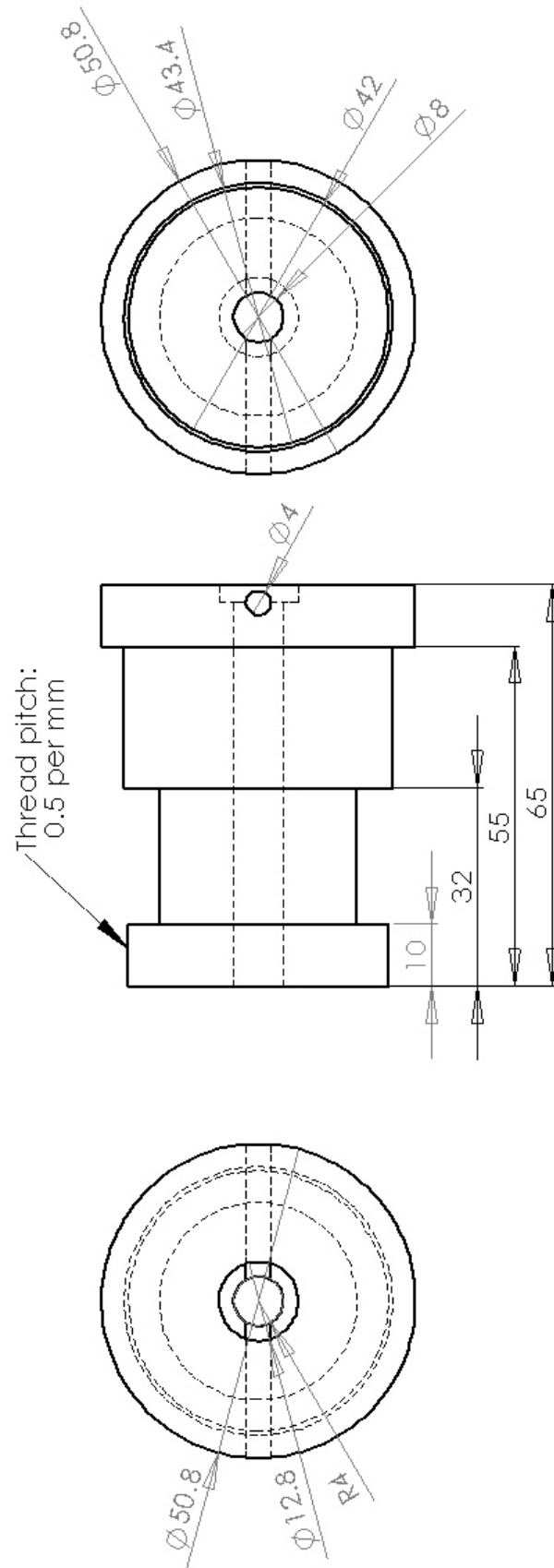
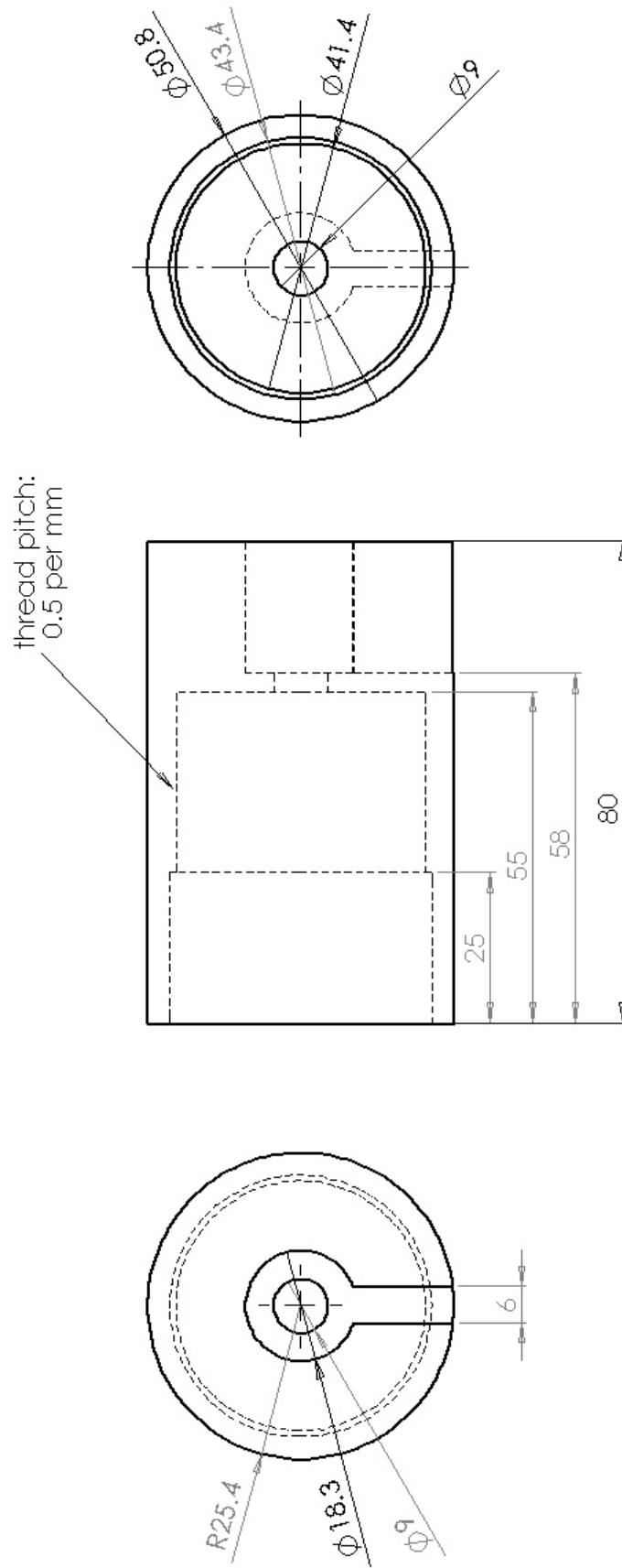Figure F.4: Male part for the 780 nm / 935 nm cavity. Material: brass, quantity: x 1

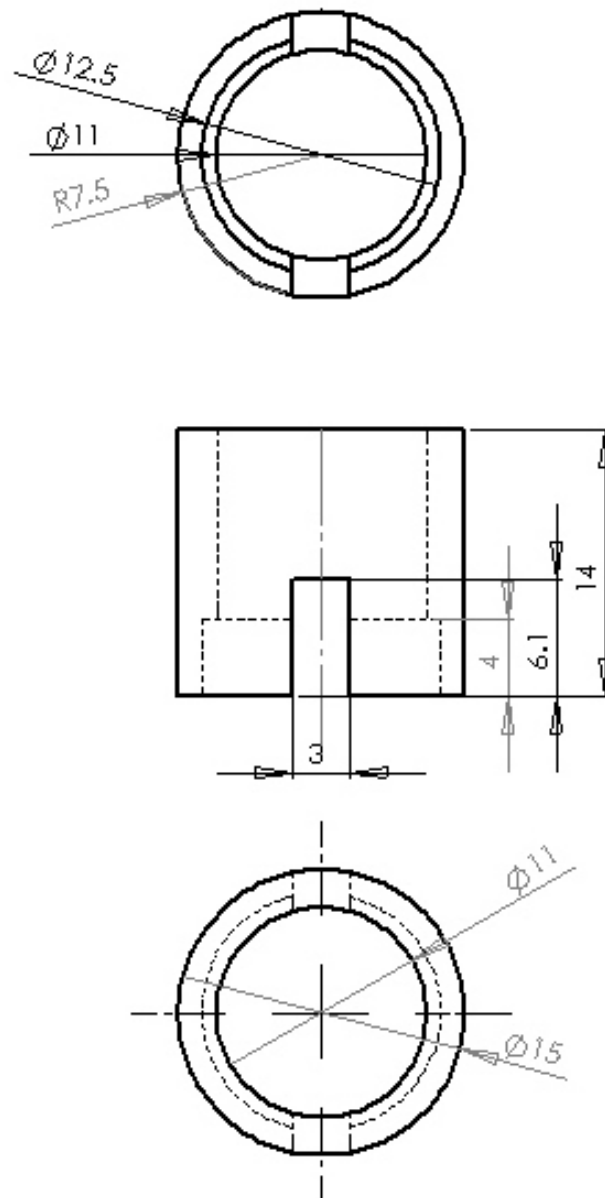Figure F.5: Female part for the 780 nm / 739 nm cavity. Material: aluminium, quantity: x 1

Figure F.6: Mirror holder for cavities. material: aluminium, quantity: x 1

Appendix G

Simplification of Ion Energy Evolution

The model proposed by Wesenberg *et al.* [1] discussed in chapter 5.1 describes the change in ion energy as a function of the scatter rate during Doppler cooling [1]. Expressions for the energy evolution and change in scatter rate are given by equations 5.8 and 5.9, but are somewhat complicated. The simplification of these expressions, following Wesenberg *et al.* [1], is presented here.

First of all the instantaneous scatter rate 5.2 and the probability density function 5.7 are simplified using the following substitutions

$$N = L_{/2} = \Gamma\sqrt{1+s}/2$$

$$T = \Gamma(s/2(1+s))$$

$$\Delta_{\max}/L_{/2} = \delta_{\max}, \qquad \Delta_{\mathrm{D}}/L_{/2} = \delta_{\mathrm{D}}, \qquad \Delta/L_{/2} = \delta$$

the instantaneous scatter rate and the probability density function then take the form

$$
\begin{aligned}
\frac{dN}{dt} &= \frac{\Gamma s/2}{1 + s + \left(\frac{2\Delta_{\mathrm{eff}}}{\Gamma}\right)^2} \\
&= \frac{\Gamma s/2}{1 + s + \left(\frac{2L_{/2}}{\Gamma}\right)^2 (\delta + \delta_{\mathrm{D}})^2} \\
&= \frac{\Gamma s/2}{1 + s + (1 + s)(\delta + \delta_{\mathrm{D}})^2} \\
&= T\frac{1}{1 + (\delta + \delta_{\mathrm{D}})^2}
\end{aligned}
\tag{G.1}
$$

$$
\begin{aligned}
P_{\mathrm{D}}(\Delta_{\mathrm{D}}) &= \frac{N}{2\pi\sqrt{\Delta_{\mathrm{max}}^2 - \Delta_{\mathrm{D}}^2}} \tag{G.2}\\
&= \frac{L_{/2}}{2\pi\sqrt{(L_{/2}\delta_{\mathrm{max}})^2 - (L_{/2}\delta_{\mathrm{D}})^2}} \\
&= \frac{1}{2\pi\sqrt{\delta_{\mathrm{max}}^2 - \delta_{\mathrm{D}}^2}} \tag{G.3}
\end{aligned}
$$

The time averaged scatter rate and energy evolution (eqns 5.8 and 5.9) become

$$
\left\langle \frac{dN}{dt} \right\rangle = T\int \frac{1}{\sqrt{\delta_{\mathrm{max}}^2 - \delta_{\mathrm{D}}^2}} \frac{1}{1 + (\delta + \delta_{\mathrm{D}})^2} \frac{d\delta_{\mathrm{D}}}{2\pi} \tag{G.4}
$$

$$
\left\langle \frac{dE}{dt} \right\rangle = -\hbar T L_{/2} \int \frac{\delta_{\mathrm{D}}}{\sqrt{\delta_{\mathrm{max}}^2 - \delta_{\mathrm{D}}^2}} \frac{1}{1 + (\delta + \delta_{\mathrm{D}})^2} \frac{d\delta_{\mathrm{D}}}{2\pi} \tag{G.5}
$$

From here it is more informative to work with $\langle dE/dt \rangle$ but the following approach can also be applied to $\langle dN/dt \rangle$. Equation G.5 can be simplified using $\delta_{\mathrm{D}} = \delta_{\mathrm{max}}\sin(\phi)$ and $d\delta_{\mathrm{D}}/d\phi = \delta_{\mathrm{max}}\cos(\phi)$

$$
\begin{aligned}
\left\langle \frac{dE}{dt} \right\rangle &= -\hbar T L_{/2} \int_0^{2\pi} \frac{\delta_{\mathrm{max}}\sin(\phi)}{\delta_{\mathrm{max}}\sqrt{1 - \sin^2(\phi)}} \\
&\quad \times \frac{\delta_{\mathrm{max}}\cos(\phi)}{1 + (\delta + \delta_{\mathrm{max}}\sin(\phi))^2} \frac{d\phi}{2\pi} \\
&= -\hbar T L_{/2} \int_0^{2\pi} \frac{\delta_{\mathrm{max}}\sin(\phi)}{1 + (\delta + \delta_{\mathrm{max}}\sin(\phi))^2} \frac{d\phi}{2\pi} \tag{G.6}
\end{aligned}
$$

To evaluate equation G.6, the following relation is used [1]

$$
Z(a, b) \equiv \int_0^{2\pi} \frac{1}{\sin(\phi) - z} \frac{d\phi}{2\pi} = -\frac{1}{z}\sqrt{\frac{z^2}{z^2 - 1}} \tag{G.7}
$$

By demonstrating the integrals in equations G.6 and G.7 are the same $\langle dE/dt \rangle$ can then

be described by the last part of equation G.7. To convert the integral in equation G.7 into the form in equation G.6 the substitutions $z = (a + i)/b$, $b = -\delta_{max}$ and $a = \delta$ are used. $Z(a, b)$ can then be written as

$$
\begin{aligned}
Z(a, b) &= \int_0^{2\pi} \frac{1}{\sin(\phi) - z} \frac{d\phi}{2\pi} \\
&= \int_0^{2\pi} b \frac{((b\sin(\phi) - a) + i)}{1 + (a - b\sin(\phi))^2} \frac{d\phi}{2\pi} \\
&= \int_0^{2\pi} -\delta_{max} \frac{(i - \delta - \delta_{max}\sin(\phi))}{1 + (\delta + \delta_{max}\sin(\phi))^2} \frac{d\phi}{2\pi}
\end{aligned}
\tag{G.8}
$$

The integral in equation G.6 can now be described in terms of real and imaginary components of $Z(a, b)$

$$
-\int_0^{2\pi} \frac{\delta_{max}\sin(\phi)}{1 + (\delta + \delta_{max}\sin(\phi))^2} \frac{d\phi}{2\pi} = \frac{\Re(Z) + \delta\Im(Z)}{\delta_{max}}
\tag{G.9}
$$

The expressions for $\langle dN/dt \rangle$ and $\langle dE/dt \rangle$ can then be expressed in terms of the real and imaginary components of $Z(a, b)$ as

$$
\left\langle \frac{dN}{dt} \right\rangle = \frac{T}{\delta_{max}} \Im(Z)
\tag{G.10}
$$

$$
\left\langle \frac{dE}{dt} \right\rangle = \frac{\hbar T L/2}{\delta_{max}} (\Re(Z) + \delta\Im(Z))
\tag{G.11}
$$

As equations G.6 and G.7 are equivalent the same substitutions as before: $z = (a + i)/b$, $b = \delta_{max}$, $a = -\delta$, along with $\sqrt{(-iz)^2} = -iz$. $Z(a, b)$ are inserted into the final term in equation G.7. $Z(a, b)$ can then be rewritten as

$$
\begin{aligned}
Z(a, b) &= -\frac{1}{z} \sqrt{\frac{(-iz)^2}{-i^2(z^2 + 1)}} \\
&= \frac{b}{\sqrt{(a + i)^2 - b^2}} \frac{i}{i} \\
&= \frac{i\delta_{max}}{\sqrt{\delta_{max}^2 - (i + \delta)^2}}
\end{aligned}
\tag{G.12}
$$

which shows the scatter rate, and energy evolution to be determined by the maximum Doppler shifts experienced, the laser detuning, and the transition linewidth. Considering the regime where the maximum Doppler shift is greater than the sum of the broadened linewidth L and detuning from resonance $\Delta_{max} \gg |L| + |\Delta|$, equation G.12 can be simplified. In this 'hot ion' regime

$$
\delta_{max} \gg \sqrt{1 + \delta}
\tag{G.13}
$$

and the expression for $Z(a, b)$ in equation G.12 can be reduced to $Z = i$. The average average scatter rate and energy evolution G.6 can then be reexpressed as

$$\left\langle \frac{dN}{dt} \right\rangle = \frac{T}{\delta_{\max}} \tag{G.14}$$

$$\left\langle \frac{dE}{dt} \right\rangle = \frac{\hbar \delta T L_{/2}}{\delta_{\max}} \tag{G.15}$$

which converting to the original terms are

$$\left\langle \frac{dN}{dt} \right\rangle = \frac{s\Gamma^2}{4\Delta_{\max}\sqrt{1 + s}} \tag{G.16}$$

$$\left\langle \frac{dE}{dt} \right\rangle = \frac{s\Gamma^2 \hbar \Delta}{4\Delta_{\max}\sqrt{1 + s}} \tag{G.17}$$

providing more manageable expressions of equations 5.8 and 5.9.

Appendix H

Re-expression of Raman Transition Rate

To help with the analysis of the Raman transition frequency the following derivation, provided by D.F.V. James [151] is used describe the Raman transition rate in terms of experimentally realisable parameters such as excited state lifetimes, coupling coefficients, laser power, and detunings etc. The general Raman transition rate, equation 8.13, is expressed as

$$\Omega_{Ram} = \frac{g_i^{(s)} g_j^{(s)*}}{2\Delta_{\mathrm{J}}} \tag{H.1}$$

where g is the Rabi frequency for an atomic transition, $s = 1, 2$ represents a dipole or quadrupole transition respectively, and i, j describe the $|\downarrow\rangle \leftrightarrow |e\rangle$ and $|\uparrow\rangle \leftrightarrow |e\rangle$ transitions respectively. For dipole and quadrupole transitions g is expressed as

$$g^{(1)} = \left| \frac{eE}{\hbar} \langle J, F, m_F | (\bar{\varepsilon} \cdot \bar{r}) | J', F', m'_F \rangle \right| \tag{H.2}$$

$$g^{(2)} = \left| \frac{eE\omega_{21}}{2\hbar c} \langle J, F, m_F | (\bar{\varepsilon} \cdot \bar{r})(\bar{k} \cdot \bar{r}) | J', F', m'_F \rangle \right| \tag{H.3}$$

where e is the electron charge, E the electric field amplitude, $\hbar$ the reduced plank constant, and c the speed of light, the terms in the bra-kets are the matrix elements describing the electric dipole (quadruople) transitions, and J, F, and m_F describe the electronic state with the primed terms describing the excited state. The matrix elements first in equations H.2 and H.3 can then be written as [151]

$$\langle J, F, m_F | (\bar{\varepsilon} \cdot \bar{r}) | J', F', m'_F \rangle = \langle J, F, m_F \parallel r C^{(1)} \parallel J', F', m'_F \rangle \sigma^{(1)} \chi^{\Delta m} \tag{H.4}$$

$$\langle J, F, m_F | (\bar{\varepsilon} \cdot \bar{r})(\bar{k} \cdot \bar{r}) | J, F', m'_F \rangle = \langle J, F, m_F \parallel r^2 C^{(2)} \parallel J', F', m'_F \rangle \sigma^{(2)} \chi^{\Delta m} \tag{H.5}$$

where the matrix elements in double bars indicate reduced matrix elements, and σ are the Clebsch-Gordan coefficients describing the relative coupling between specific Δm_F states. The term $\chi^{\Delta m}$ describes the direction and radiative patterns of the incident beam and orientations of the quantisation axis. As shown by D.F.V. James the reduced matrix elements are related to the spontaneous decay rates via [151]

$$\Gamma_{\mathrm{P}} = \frac{4c\alpha k_{\mathrm{P}}^3}{3(2J'+1)} |\langle J, F, m_F \parallel rC^{(1)} \parallel J', F', m'_F \rangle|^2 \sigma^{(1)} \chi^{\Delta m} \tag{H.6}$$

$$\Gamma_{\mathrm{D}} = \frac{c\alpha k_{\mathrm{D}}^5}{15(2J'+1)} |\langle J, F, m_F \parallel r^2 C^{(2)} \parallel J', F', m'_F \rangle|^2 \sigma^{(2)} \chi^{\Delta m} \tag{H.7}$$

where c is the speed of light, α the fine structure constant and k_{P} and k_{D} the wavevectors of the light resonant with the dipole and quadrupole transitions respectively. Combining equations H.2 to H.7 the Rabi coupling between either qubit state and the excited state become [151]

$$g^1 = \frac{eE}{2\hbar} \sqrt{\frac{3\Gamma_{\mathrm{P}}(2J'+1)}{c\alpha k^3}} \sigma^{(\mathrm{s})} \chi^{\Delta m} \tag{H.8}$$

$$g^2 = \frac{eE}{2\hbar} \sqrt{\frac{15\Gamma_{\mathrm{D}}(2J'+1)}{c\alpha k^3}} \sigma^{(\mathrm{s})} \chi^{\Delta m} \tag{H.9}$$

The effective Raman transition can then be written as

$$\Omega_{Ram} = \frac{e^2 E_i E_j}{8\hbar^2} \frac{\Gamma}{c\alpha k^3} \sum_{J=\frac{1}{2},\frac{3}{2}} \sum_{F=|I-J|}^{I+J} \sum_{m=-F}^{F} \left(\frac{\sigma_i^{(\mathrm{s})} \chi_i^{\Delta m} \sigma_j^{(\mathrm{s})} \chi_j^{\Delta m}}{\Delta_J} \right) \tag{H.10}$$

where the sums indicate that all transitions along all available channels are considered. The electric field amplitude, E, is related to the intensity of a Gaussian beam via $E = \sqrt{2P/(\pi r \varepsilon_0 c)}$, where P is the beam power, r the beam waist, ε_0 is the permittivity of free space, and c is the speed of light. Assuming that both beams have the same electric field strength the Raman transition frequency can be expressed as

$$\Omega_{Ram} = \frac{e^2 \Gamma}{4\hbar^2 c\alpha k^3} \frac{P}{\pi r \varepsilon_0 c} \sum_{J=\frac{1}{2},\frac{3}{2}} \sum_{F=|I-J|}^{I+J} \sum_{m=-F}^{F} \left(\frac{\sigma_i^{(\mathrm{s})} \chi_i^{\Delta m} \sigma_j^{(\mathrm{s})} \chi_j^{\Delta m}}{\Delta_J} \right) \tag{H.11}$$

Appendix I

Clebsch-Gordan Coupling Coefficients

The possibility of exciting Raman transitions via either dipole or quadruple transitions are discussed in section 8.2. Coupling is considered using dipole transitions via the $^2P_{1/2}$ and $^2P_{3/2}$ manifolds, and quadrupole transitions via the $^2D_{3/2}$ and $^2D_{5/2}$ manifolds. In all cases the both qubit states must couple to the same excited state to enable a Raman transition to be driven. To determine coupling between the qubit states and various excited m_F states the Clebsch-Gordan coupling coefficients are calculated using [75, 162]
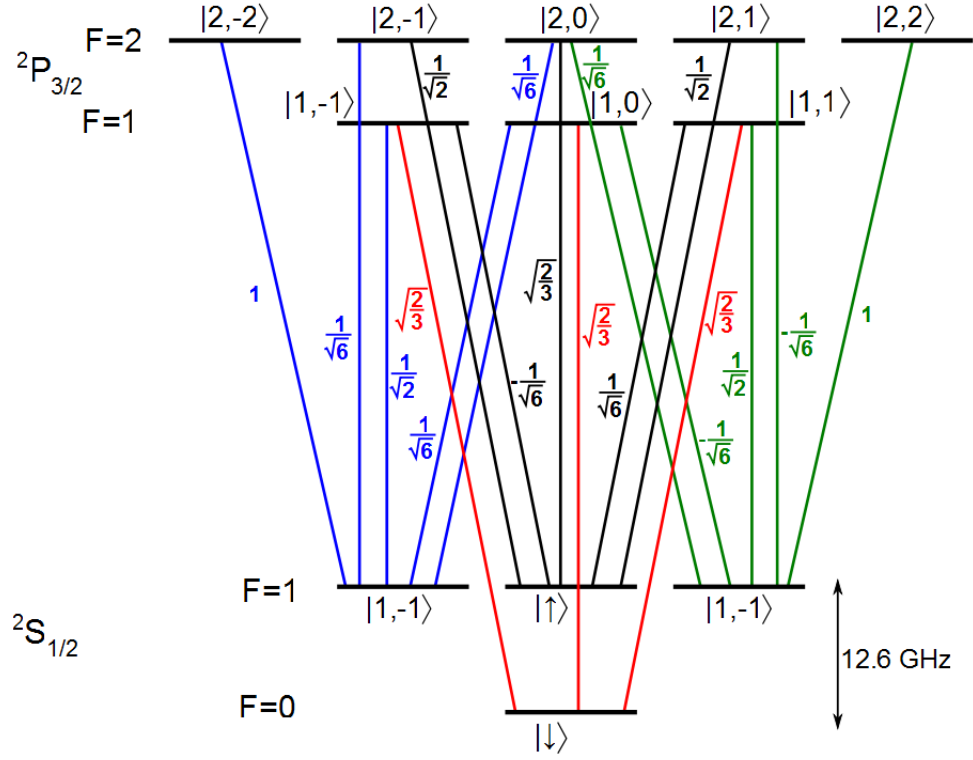
$$
\begin{aligned}
\sigma^{(s)} \;=\; & (-1)^{1+s+J+Jd+I-m'_F} \times \\
& \sqrt{(2F+1)(2F'+1)(2J'+1)} \begin{Bmatrix} J' & F' & I \\ F & J & 1 \end{Bmatrix} \begin{pmatrix} F & s & F' \\ m_F & q & -m'_F \end{pmatrix}
\end{aligned}
\tag{I.1}
$$

where the round (curly) brackets represent the Wigner 3(6)-j symbols with the integers $s = 1, 2$ represents the change of momentum during each transition (i.e. dipole and quadrupole transitions respectively), and q represents the momentum of the incoming photon. The Clebsch-Gordan coefficients are only non-zero when $q = m_F - m'_F$. The available transitions and coupling coefficients between the ground states and excited ^2P_J and ^2D_J manifolds are shown in figures I.1 to I.4. Due to the complexity of the possible quadrupole transitions the respective Clebsch-Gordon coefficients are only shown in the accompanying tables.
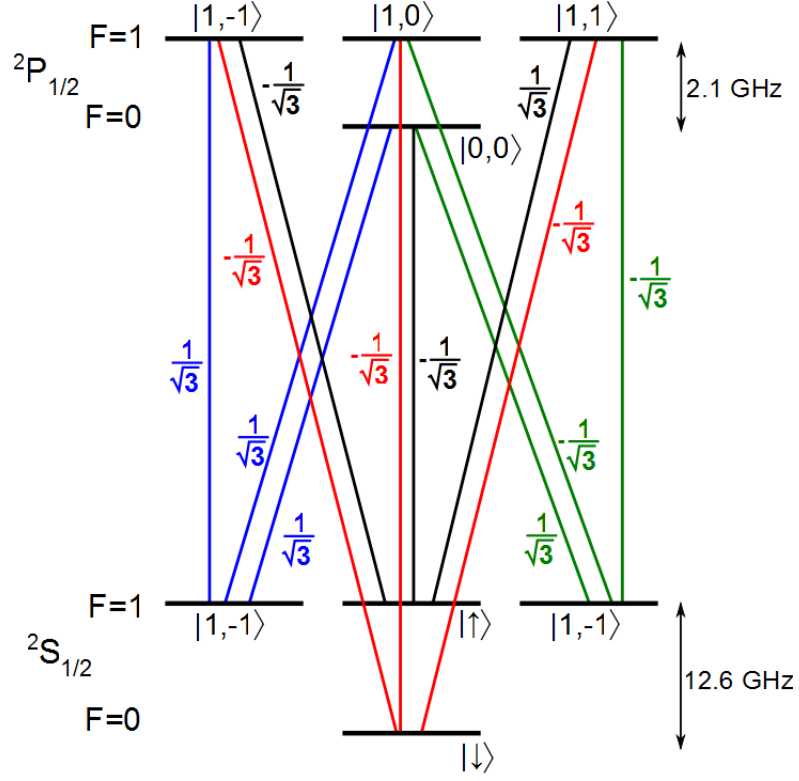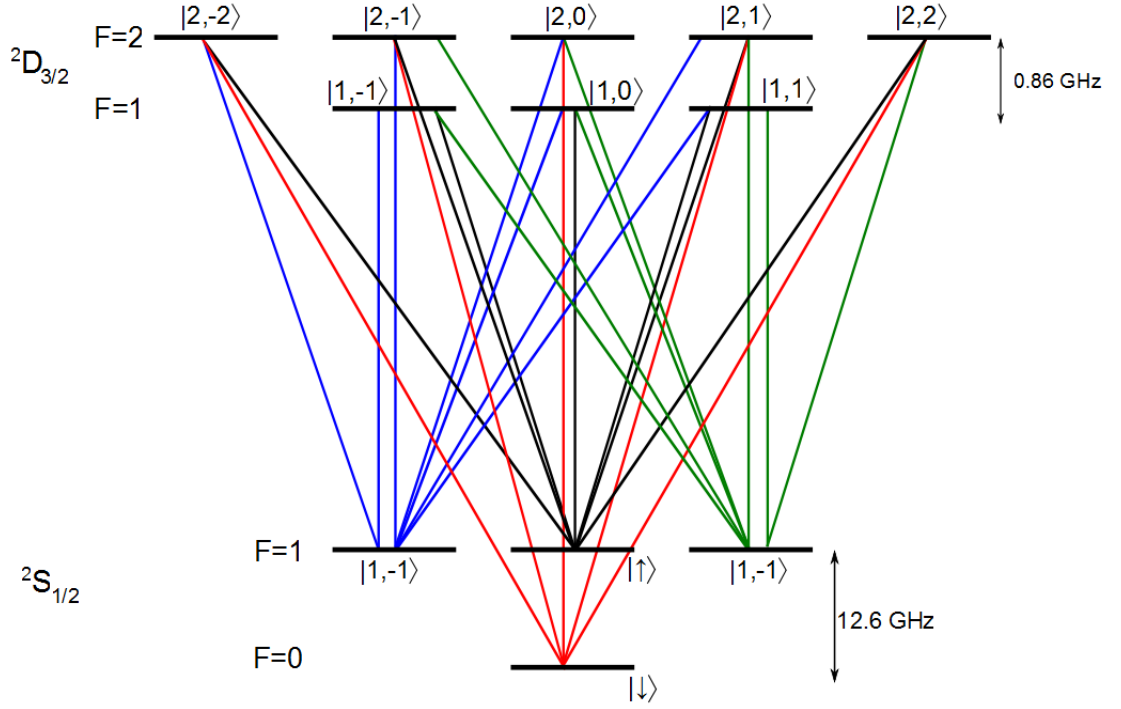
		$^2S_{1/2}\lvert F, m_F\rangle$			
		$\lvert 0,0\rangle$	$\lvert 1,-1\rangle$	$\lvert 1,0\rangle$	$\lvert 1,1\rangle$
$^2P_{1/2}\lvert 1, m_F\rangle$	$\lvert 0,0\rangle$	0	$\sqrt{\frac{1}{3}}$	$-\sqrt{\frac{1}{3}}$	$\sqrt{\frac{1}{3}}$
	$\lvert 1,-1\rangle$	$-\sqrt{\frac{1}{3}}$	$\sqrt{\frac{1}{3}}$	$-\sqrt{\frac{1}{3}}$	0
$^2P_{1/2}\lvert 1, m_F\rangle$	$\lvert 1,0\rangle$	$-\sqrt{\frac{1}{3}}$	$\sqrt{\frac{1}{3}}$	0	$-\sqrt{\frac{1}{3}}$
	$\lvert 1,1\rangle$	$-\sqrt{\frac{1}{3}}$	0	$\sqrt{\frac{1}{3}}$	$-\sqrt{\frac{1}{3}}$

Figure I.1 & Table I.1: Allows transitions between the $^2S_{1/2} \leftrightarrow {}^2P_{1/2}$ manifolds.
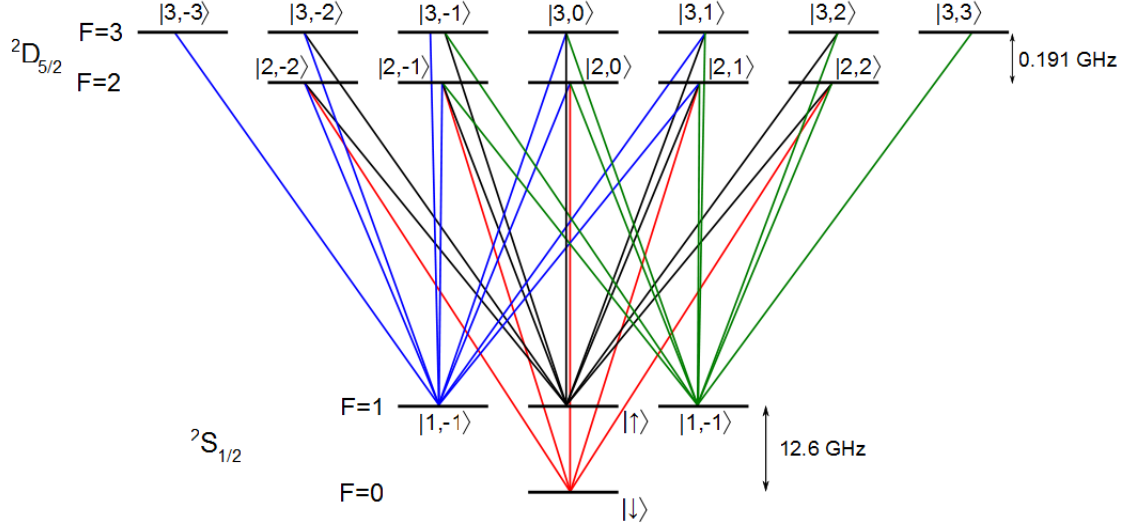
Figure I.2 & Table I.2: Allowed transitions between the $^2S_{1/2} \leftrightarrow {}^2P_{3/2}$ manifolds.

		$^2S_{1/2}\lvert F,m_F\rangle$			
		$\lvert 0,0\rangle$	$\lvert 1,-1\rangle$	$\lvert 1,0\rangle$	$\lvert 1,1\rangle$
$^2D_{3/2}\lvert 1,m_F\rangle$	$\lvert 1,-1\rangle$	$\sqrt{\frac{2}{3}}$	$\sqrt{\frac{1}{2}}$	$-\sqrt{\frac{1}{6}}$	0
	$\lvert 1,0\rangle$	$\sqrt{\frac{2}{3}}$	$\sqrt{\frac{1}{6}}$	0	$-\sqrt{\frac{1}{6}}$
	$\lvert 1,1\rangle$	$\sqrt{\frac{2}{3}}$	0	$\sqrt{\frac{1}{6}}$	$\sqrt{\frac{1}{2}}$
$^2D_{3/2}\lvert 2,m_F\rangle$	$\lvert 2,-2\rangle$	0	1	0	0
	$\lvert 2,-1\rangle$	0	$\sqrt{\frac{1}{6}}$	$\sqrt{\frac{2}{3}}$	0
	$\lvert 2,0\rangle$	0	$\sqrt{\frac{1}{6}}$	$\sqrt{\frac{2}{3}}$	$\sqrt{\frac{1}{6}}$
	$\lvert 2,1\rangle$	0	0	$\sqrt{\frac{1}{2}}$	$-\sqrt{\frac{1}{6}}$
	$\lvert 2,2\rangle$	0	0	0	1

Figure I.3 & Table I.3: Allowed transitions between the $^2S_{1/2} \leftrightarrow {}^2D_{3/2}$ manifolds.

	$^2S_{1/2}|F,m_F\rangle$			
	$|0,0\rangle$	$|1,-1\rangle$	$|1,0\rangle$	$|1,1\rangle$
$^2D_{5/2}|2,m_F\rangle$ $\quad$ $|2,-2\rangle$	$\sqrt{\frac{3}{5}}$	$-\frac{2}{\sqrt{15}}$	$-\frac{2}{\sqrt{5}}$	0
$|2,-1\rangle$	$\sqrt{\frac{3}{5}}$	$\sqrt{\frac{1}{5}}$	$-\sqrt{\frac{1}{15}}$	$-\sqrt{\frac{2}{15}}$
$|2,0\rangle$	$\sqrt{\frac{3}{5}}$	$\sqrt{\frac{1}{5}}$	0	$-\sqrt{\frac{1}{5}}$
$|2,1\rangle$	$\sqrt{\frac{3}{5}}$	$-\frac{2}{15}$	$\sqrt{\frac{1}{15}}$	$-\sqrt{\frac{1}{5}}$
$|2,2\rangle$	$\sqrt{\frac{3}{5}}$	0	$\frac{2}{\sqrt{15}}$	$-\sqrt{\frac{2}{15}}$
$|3,-3\rangle$	0	1	0	0
$|3,-2\rangle$	0	$\sqrt{\frac{2}{3}}$	$\sqrt{\frac{1}{3}}$	0
$|3,-1\rangle$	0	$\sqrt{\frac{2}{5}}$	$2\sqrt{\frac{2}{15}}$	$\sqrt{\frac{1}{15}}$
$^2D_{5/2}|3,m_F\rangle$ $\quad$ $|3,0\rangle$	0	$\sqrt{\frac{1}{5}}$	$\sqrt{\frac{3}{5}}$	$\sqrt{\frac{1}{5}}$
$|3,1\rangle$	0	$\sqrt{\frac{1}{15}}$	$2\sqrt{\frac{2}{15}}$	$\sqrt{\frac{2}{5}}$
$|3,2\rangle$	0	0	$\sqrt{\frac{1}{3}}$	$\sqrt{\frac{2}{3}}$
$|3,3\rangle$	0	0	0	1

Figure I.4 & Table I.4: Allowed transitions between the $^2S_{1/2} \leftrightarrow {}^2D_{5/2}$ manifolds.